A Study of the Solar Energy Systems and Storage Devices

PREPARED BY:
CHUKWUKA, CHUKWUBUIKEM OLUCHUKWU

This dissertation is submitted to the University of Cape Town in fulfilment of the academic requirements for the Master of Science degree in Electrical Engineering

SUPERVISOR:
PROF. K.A. FOLLY

UNIVERSITY OF CAPE TOWN
IDYUNIVESITHI YASEKAPA • UNIVERSITEIT VAN KAAPSTAD

DEPARTMENT OF ELECTRICAL ENGINEERING
UNIVERSITY OF CAPE TOWN
CAPE TOWN

Date: 21 November 2013

Declaration

I hereby declare that this is my own work. All alternative sources used have been identified and referenced. This thesis has not been submitted before for any degree at this or any other institution for any degree or examination.

Signature:

Mr. Chukwubuikem Chukwuka

Signed at the University of Cape Town

21 November 2013.

Acknowledgements

I thank the almighty God for His grace on the completion of this research work. Glory and honour be to Him forever more. I owe my greatest gratitude to my supervisor, Professor K. A. Folly for his guidance and instructions which were vital in producing this thesis. Special thanks to my research group, Intelligent Power and Energy Systems (IPES) group. Thanks to David Oyedokun, Paul Kehinde Olulope, Olaniyi Zaccheus Olaofe, Luyolo Nqobile Magangane, Famushu Tshina Mulumba, Dr Sandip Ghosh, Samuel Kibara, and Kehinde Awodele who contributed to the completion of this dissertation.

Synopsis

Following the 2008 severe electricity shortage in South Africa, domestic and industrial users faced incessant periods of blackouts. It is generally believed to be associated with lack of generation capacity. Since then research efforts have been directed towards boosting the generation capacity of the South African network by investing in a mix of power generation projects which include coal, nuclear and renewable energy schemes such as solar and wind. The renewable energy resources are considered a more viable option because of their many advantages such as lower greenhouse gas emissions, inexhaustible, reliable and even cheaper energy cost on the long term.

Africa has huge potentials of solar power because of the abundance of direct sunshine in most days of the year. The rising cost of the fossil electricity has made the solar power an attractive option bearing in mind that the cost of the solar power has plummeted steadily in the past few years. Two main technologies are prevalent in the solar power research.

These are photovoltaic (PV) systems and the concentrated solar power (CSP). The PV systems are made of solar panels and power electronic circuits. They are mostly economical in small residential units. The CSPs on the other hand which are made of solar field, thermal storage and steam turbine/generator units are economical only in large scale.

In this thesis, a 2.5 kW Residential PV system and a 100 MW Molten Salt Power Tower Concentrated Solar Power were developed. The technical model of the photovoltaic panel and the power electronic circuits that connect it to the grid were also developed with Matlab/Simulink while the economic simulation of the PV, as well as the Concentrated Solar Power were carried out with Systems Advisor Model (SAM) using the climate data of Cape Town.

The simulation results of this work compared the cost of PV electricity first with Renewable Energy Feed-in Tariff (REFIT) of National Energy Regulator of South Africa (NERSA), and then with the residential tariff charged by the City of Cape Town. Also the cost of electricity using CSP is compared NERSA`s REFIT. Finally the cost of PV electricity is compared with that of CSP. We therefore conclude that, with government incentives, CSP and PV are viable technologies however electricity produced by CSP is cheaper than that of the PV.

Table of Contents

List of Figures

List of Tables

Nomenclature

ACC	Air Cooled Condenser
AM15	15 is the coefficient of air mass
a-Si	Amorphous Silicon
a-Si:H	Hydrogenated Amorphous Silicon
Au-HTS	Gold-based High Temperature Superconductors
Bi-HTS	Bismuth High Temperature Superconductors
BSSCO	Bismuth Strontium Calcium Copper Oxide
BOP	Balance of plant
CdTe	Cadmium Telluride
CIGS	Copper Indium Gallium diSelenide
CPV	Concentrated Photovoltaics
CSC	Current Source Converter
c-Si	Mono-Crystalline Silicon
CSP	Concentrating Solar Power
CuPc	Copper pthalocyanine
C60	Fullerene
DFC	Dual Focus Cassegrainian Module
DNI	Direct Normal Irradiance
DSSC	Dye-Sensitized Solar Cells
EDLC	Electric Double Layer Capacitors
EPRI	Electric Power Research Institute
FACTS	Flexible AC Transmission System
GaAs	Gallium Arsenide
GWh	Gigawatt hour
Hc	Critical magnetic field
HCPV	High Concentration Photovoltaics
HTF	Heat Transfer Fluid

HCE	Heat Collecting Element
Hg-HTS	Mercury-based High Temperature Superconductors
HOMO	Highest occupied molecular orbital
HRSG	Heat Recovery Steam Generator
IMM	Inverted Metamorphic Multi-junction Solar Cells
IC	Incremental Conductance
ISCC	Integrated Solar Combined Cycle
InGaAsN	Indium Gallium Arsenide Nitride
InGaP	Indium Gallium Phosphorus
IPES	Intelligent Power and Energy Group
LCOE	Levelized Cost of Energy
LN_2	Liquified Nitrogen
LUMO	Lowest unoccupied molecular orbital
LSSCPV	Lateral Spectrum Splitting Concentrator Photovoltaic cells
LTS	Low Temperature Superconductors
MPPT	Maximum Power Point Tracking
mc-Si	multi-crystalline Silicon
MEG	Multiple Excitons Generators
MJ	Multi-junction Solar Cells
MWCNT	Multiwall Carbon Nanotube
MWe	Megawatt electric
NEC	Nantenna Electromagnetic Collectors
NREL	National Renewable Energy Laboratory
NPV	Net Present Value
OPVC	Organic photovoltaic cell
P3OT: CdTe	Poly 3-Octyl-thiophene on CdTe
PEAC	Power Electronics Application Centre
Pb-HTS	Lead-based High Temperature Superconductors
PCU	Power Conversion Unit
Poly-Si	Polycrystalline Silicon
PV	Photovoltaic
REFIT	Renewable Energy Feed in Tariff

R&D	Research and Development
SAM	System Advisor Model
SBSP	Space-based solar power
SF	Solar Field
SMES	Superconducting Magnetic Energy Storage
SRC	Steam Rankine cycle
SEGS	Solar Energy Generating Station
SCA	Solar Collector Assembly
SiO	Silicon oxide
SM	Solar Multiple
TBCCO	Titanium Barium Calcium Copper Oxide
Tc	Critical Temperature
TFSC	Thin Film Solar Cells
TES	Thermal Energy Storage
TPV	Thermo photovoltaic Cells
UTES	Underground Thermal Energy Storage
VSC	Voltage Source Converter
YBCO	Yttrium Barium Copper Oxide

Chapter 1

Introduction

The demand for energy to meet social and economic development and improve human welfare and health is increasing. Utilities around the world have embarked on the construction of a number of fossil fuel based power plants which led to the huge greenhouse gas (GHG) emissions such as carbon dioxide, nitrous, oxide and methane. The result is an increase in global average temperature [1, 12]. Recent data confirm that consumption of fossil fuels accounts for the majority of global anthropogenic GHG emissions.

There are multiple options for lowering GHG emissions from the energy system while still satisfying the global demand for energy services. These are alternative energy sources, energy efficiency and conservation schemes, carbon sequestration, and geo-engineering (which is the large scale intervention in the earth`s climatic system with the aim of reducing global warming).

Renewable energy systems, besides their potentials to mitigate climate change, have other benefits if properly implemented, such as social and economic development, energy access, secure energy supply, reducing negative impacts on the environment and health [12, 100]. Various renewable energy systems are capable of supplying electricity, heat, mechanical and clean fuels like solar fuels for residential, commercial and utility applications. Their outputs are variable but predictable (like wind and solar), constant or controllable (e.g. geothermal). Some of the common renewable energy technologies are biogas, biomass, solar, wind, geothermal, osmotic, wave energy and hydropower to name a few [4, 129].

Solar energy provides clean, abundant and renewable energy in places such as Africa where direct normal irradiance (DNI) is very high. The energy market is diversifying and vibrant. Governments and investors need relevant information in order to choose the most viable energy option for a given topology. This includes making informed decisions regarding the most viable energy option between solar, wind, and geothermal technologies for a given topology and energy market. Hence complex performance

characteristics and economics that vary with location need to be analysed using the most suitable tools [2, 3].

In Nigeria, as of the end of 2009, the installed electricity capacity was about 6000 MW but only a maximum of about 2000 MW is available at any time. This is made up of a mix of 36 % Hydro power, and 64 % thermal with no source of renewable energy systems yet. Although the federal government is investing heavily in expanding generation capacity, it is also encouraging investments in power production through joint ventures and IPPs with the hope of bringing the total installed capacity to about 17000 MW by 2015. The national power demand of Nigeria is about 9000 MW however the national utility is only able to provide about 2000 MW [4] .The effect is that, in a typical day, one can expect only two hours of electricity in urban areas like the commercial of Lagos. The two hours are often characterized by highly unstable voltage, which is very dangerous to appliances. The effect of the shortage of electricity on the general economy of the nation is enormous many people now resort to stand-alone diesel or petrol generators for their energy needs. Fossil fuel generators are neither environmentally friendly nor economical.

Here in South Africa, the total active generation capacity is approximately 41 000 MW [2]. As a result of economic growth since 1994 and increased power connections (84 % of the population is now connected). South Africa`s electricity demand has significantly increased. Due to South Africa`s ageing fleet of power stations and lack of new additions, reserve margins are significantly low by international standards and have dropped to as low as 5 % compared to the acceptable global average of 15 %, which has ultimately resulted in load shedding.

Government estimates are that the installed capacity will need to grow by 40 000 MW (i.e. double) in the next 20-25 years to meet current and forecasted demand. Approximately 42 % (or 17 800 MW) of all new generation is expected to come from renewable sources which includes 3 750 MW of new installation by 2016 costing between R70 bn and R80 bn at today`s prices [2, 147].

Coal fired plants comprise approximately 85 % of South Africa`s generating capacity and were built in the 1970`s with a intended life span of up to 40 years. Apart from their negative impact on the environment, there are significant inefficiencies in transmitting power from the Mpumalanga region where most of the power plants are located to the

Western and Eastern Cape provinces. It is estimated that the normal transmission and distribution losses are up to 20 % of the power generated [168].

To forestall these problems, renewable energy programme was introduced. The renewable energy systems are often equipped with energy storage facilities such as batteries and molten salt thermal storage. The advantage of the energy storage is to extend the capacity factor of the power plant. These renewable energy systems will see power being generated much closer to the end-users and utilize the abundance of natural resources in the country such as sun and wind. The renewable energy projects will be partnerships between the international developers and local firms that ensure high level of mentorships and skill transfer by the parties. Every project has a minimum BEE equity requirement and strong emphasis on investment by the projects into local socio-economic infrastructure and services such as employing local labour to build and maintain the plants.

1.1. Objectives of the Study

The objectives of this dissertation are:

- To explore common technologies for converting solar energy to useful energy such as electricity and heat
- To compare these technologies in cost, performance and adaptability to South Africa`s load profile and environment and facilitate identification of the most suitable for individual applications.
- To carry out an economic integration of the solar energy technologies with the existing grid infrastructures using SAM.

1.2. Research Methodology

There are a number of software applications in the market today; however, not all of them are suitable for modelling solar energy devices. Matlab and Systems Advisor Model (SAM) are chosen for this dissertation because they are proven. While Matlab is widely accepted software for engineering research, Systems Advisor Model (SAM) is one of the

few software applications that model the whole system including the economics and the technical aspects of the plant.

For each system modelled, we selected all the input parameters that characterize the system. Examples of the input parameters used to model the CSP farm and the PV system are the location climate, size of plant, type of technology and the type of market targeted. Having fed in the inputs, simulations are run. The simulations produce results which are analysed and discussed. Then, recommendations are made based on the results obtained

1.3. Scope and Limitation of this Work

The first part of this work involves the modelling and simulation of a 2.5 kW photovoltaic system using Matlab/Simulink/Simpowersystems which includes the photovoltaic module, DC-DC converter, MPPT system, full wave three-level inverter and the transformer stage.

The second part covers economic assessment of a 100 MW molten salt power tower type concentrated solar power farm and a 2.5kW photovoltaic system using the Systems Advisor Model. The result is used to determine the levelized cost of electricity (LCOE) produced by the CSP farm and the PV system over an analysis period of 20 years. The LCOE obtained is then compared with the NERSA Refit tariff and the City of Cape Town electricity tariff system. Hence, economic analysis in the context of South Africa was carried out to determine if these technologies are viable.

The modelling of energy storage devices such as batteries and molten salt thermal storage device as separate components are not included in this work. Modeling and simulation of the PV module as well as the power electronics required to produce a useful AC signal were developed. However, issues relating to integration are not covered in this dissertation. In the economic assessment of the CSP, the whole system modelling was conducted without attempting to model individual components of the CSP. Details of the theory and the working principles of the plant are also omitted for simplicity purposes.

1.4. Contribution of the Dissertation

This research attempts to model the CSP and PV with the same parameters and consequently compares the costs of the electricity produced by both technologies against the existing tariff structure of the South African utilities. The simulation of a 2.5 kW photovoltaic system could contribute to the technical integration of PV into the South African electrical grid. The economic simulation of a 100 MW Molten Salt Power Tower Concentrated Solar Power could contribute to the economic integration of CSP technology in the South African electricity tariff system. The 2.5 kW photovoltaic model developed provides some insight into the modelling of the photovoltaic module from the basic equations of the equivalent circuits of a solar cell. The economic models bring out the cost aspects of various systems within South African context. Hence, researchers can make informed decisions.

1.5. Outline of the Thesis

The dissertation is summarized as follows:

Chapter 1 Gives a background in solar energy systems and storage devices.

Chapter 2 Deals with literature reviews.

Chapter 3 Presents software packages used.

Chapter 4 Presents the theory development of the models developed.

Chapter 5 Modelling of photovoltaic module using Matlab Simulink.

Chapter 6 Modelling and simulation of the photovoltaic system using Simulink and SimPowerSystems toolboxes of Matlab

Chapter 7 Economic modelling of a 2.5 kW photovoltaic system and a 100 MW molten salt power tower concentrated solar farm

Chapter 8 Concludes the thesis and give recommendations as well as giving suggestions for future work.

References The references used in the thesis are presented in this section.

Appendix Contains further information on the true sine wave inverters

Chapter 2
Literature Review

2.1 Introduction

This chapter is a literature review of scientific advances in the area of energy storage devices, photovoltaic systems, concentrated solar power farms and the future of the solar power which is the nantenna electromagnetic collectors [5-6].

2.2 Energy Storage Systems

Energy storage has traditionally been seen as a way to shave peaks and improve the capacity factor of base-load generators [7]. But as the grid system is modernized, utilities are beginning to look at the other advantages of operating a storage plant more strategically. These advantages include increased transmission capacity through enhanced line stability, the spinning reserve of generators, levelling of renewable energy sources, voltage control, frequency control, sub-synchronous frequency damping, wide area generation control and black start [8].

In this section, energy storage techniques which are applicable to large-scale utilities and how they store energy either diurnally or inter-seasonally are reviewed. These techniques have been chosen not only because of the low cost per Watt stored but also for ecological reasons such as low carbon dioxide emissions. Batteries store energy in the form of electrochemical energy and are currently the most versatile form of energy storage. However, molten salt energy storage uses common salt which can be sourced almost everywhere cheaply. Superconducting magnetic energy storage offers high efficiency which could make a good economic sense on a large scale [9]. Super-capacitors have a very large number of cycles and hence longer life [10]. The Underground thermal energy storage (UTES) stores very large heat energy between seasons at minimal cost [11].

Here in South Africa and in the broader African continent, molten salt energy storage is the most promising because it could provide the cheapest (thermal) energy storage. It is

often used in conjunction with Concentrated Solar Power which could be a major component of the national energy mix [12].

2.2.1 Batteries

A battery is a device that converts chemical energy into electrical energy. It consists of a number of voltaic cells connected in series. Each cell contains a conductive electrolyte containing anions and cations. A redox reaction charges the battery by reducing the cations at the cathode and oxidizing the anions at the anode. Batteries are broadly classified as primary and secondary. Furthermore, they are classified according to the type of electrolytes used. These are acid based and alkaline based.

Primary cells are disposable. They cannot be recharged since the chemical reaction is irreversible. Examples of the first generation cells are voltaic pile, Daniel cells, grove cell, and atomic cell which can supply energy for over ten years before depletion [13]. The most recent primary batteries are the fuel cells that run as long as the fuel (such as Hydrogen) is refilled.

Secondary or rechargeable batteries are a group of one or more cells whose electrochemical reactions are electrically reversible. They can be recharged by applying current in the reverse polarity in order to reverse the chemical reaction that occurred during use. Examples are lead acid, nickel cadmium (NiCd), nickel metal hydride (NiMH), lithium-ion (Li-ion) and flow batteries.

N*uclear battery* is a primary battery which uses the emissions from a radioactive isotope to generate electricity. Like nuclear reactors they generate electricity from atomic energy but differ in that they do not go into a chain reaction. Nuclear accelerated generators have an added advantage of better scalability. They do not produce additional toxic waste since the fuel is sourced from the nuclear waste of an existing nuclear plant. Compared to other batteries they have extremely long lives (up to 400 years) and high energy densities but are very costly [14]. They are mainly used as power sources for equipment that must operate unattended for long periods of time, such as spacecraft. The following isotopes

have been tested for use with the atomic battery. These are tritium, nickel-63, promethium-147, and technetium-99 while the following has been used; plutonium-238, curium-242, curium-244, strontium-90 [15]. Other names of atomic batteries are nuclear battery, tritium battery and radioisotope generators. Beta-voltaics are made of radioisotope materials (such as potassium-40) that emit only the beta particles which are high energy, high speed electrons that could be stopped by an aluminium plate.

The first atomic battery was invented in 1913 by Henry Moseley [16]. It was called the beta cell. Since then, with the advent of nanotechnology and the new wide gap semiconductors, the atomic batteries have reached 2 % efficiency [17]. The energy conversion technology of the atomic batteries is classified into two types; thermal and non-thermal converters. The thermal converters are converters whose outputs are a function of temperature difference. Examples are; thermionic converters which are based on caesium vapour to optimize the work functions and radioisotope thermo-electric which combines thermocouple and thermo-photovoltaics to form an efficient thermal converter. Three thermal converters are thermocouple alloys, thermo-photovoltaics and silicon nanowires often united as a hybrid; Alkali-metal thermal to electric converter (AMTEC) is an electrochemical system which is based on the electrolyte used in sodium sulphur batteries [18]. The device is a sodium concentration cell which uses a ceramic polycrystalline β-alumina solid electrolyte (BASE) as a separator between a high pressure region containing sodium vapour at 1300 K and a low pressure region containing a condenser for liquid sodium at 700 K. Efficiency is about 16 % [18].

The non-thermal converters are converters whose outputs are not the function of the temperature difference. They extract a fraction of the nuclear energy as it is being degraded into heat. Examples of non-thermal converters are the direct charging generators. These converters use beta-particles or electrons betavoltaics made with tritium isotope. They are embedded into a direct gap semiconductor. As soon as the electrons are released, they are captured by the cell to generate electricity. Opto-electric nuclear battery is a device that converts nuclear energy into light which is then converted to electricity. The beta-emitter here is technetium which is used to stimulate an excimer which is a mixture of argon and xenon. In reciprocating electromechanical atomic

batteries use, the build-up of charge between two plates pull the bendable plates together until the two plates touch and discharge hence equalizing the electrostatic build-up. The mechanical motion produced could be used to produce electricity through a flexible piezoelectric material or a linear generator [17].

A *flow battery* is a form of rechargeable battery in which electrolyte containing one of the dissolved electro-active materials flows through an electrochemical cell that converts chemical energy into electricity. Additional electrolyte is stored externally in tanks and is pumped through a cell of the reactor. The flow batteries are recharged rapidly by refilling the tanks with the electrolytes while simultaneously recovering the spent material for re-energization. There are two types of flow batteries; redox flow batteries and hybrid flow batteries [19].

Redox flow batteries: in these batteries, the electro-active components are dissolved in the electrolyte. The energy of these flow batteries could be determined fully independent of the battery power since the energy is related to the electrolyte volume (tank size) and the power is related to the reactor size. The recharge time varies from minutes to days. Examples are vanadium, polysulphide bromide, and uranium flow batteries [20].
In hybrid flow batteries, one or more of the electro-active components are deposited as a solid layer. The recharge time is varied from several minutes to a few hours. The main advantages of flow batteries are flexible layouts, long life cycle (no phase changes), quick and responsive times, no harmful emissions, low maintenance and tolerance to overcharge and discharge. The disadvantages are those of low energy densities and complicated circuitry.

Flow batteries are applicable in large and stationary power installations (1 kWh-1 MWh) for load balancing, storing of renewable energy such as solar and wind, peak shaving, and power conversion [21]. Semisolid Lithium-ion fuel cells are the hybrid of the lithium-ion and flow batteries. They have a very high energy density [22]. This new flow battery design is made of lithium which has the advantage of low cost (made of abundant lithium), weight and hence high energy density. The issue of fast charging is also

addressed since the semi-solid material only needs to be refilled with the option of slowly recharging the electrochemical.

A *fuel cell* is a primary battery that converts chemical energy from fuel into electricity through a chemical reaction with oxygen or other oxidizing agent. Normally, this reaction does not involve combustion. The fuel cell was first discovered in 1838 by a German scientist Christian F. Schonbein [23]. The most common type of fuel cell is hydrogen based fuel cell however other hydrocarbons such as natural gas and alcohols (methanol) are also used. The basic architecture of a fuel cell is made up of a cathode, anode and an electrolyte that allows charges to move between the two sides of the fuel cell. The terminal voltage of a cell is about 0.7 V hence they are arranged in series and parallel in order to obtain the desired voltage. The efficiency is between 40-60 % and could reach 85 % if the heat output is utilized.

Types of fuel cells are proton exchange membrane fuel cell (PEMFC) which includes hydrogen, hydrocarbon (diesel), alcohol (methanol), and chemical hydrides. Other types are the high temperature fuel cells which are solid oxide fuel cell and molten carbonate fuel cell [24].

The proton exchange membrane fuel cell or polymer electrolyte membrane fuel cell is the type of fuel cell that transforms the chemical energy liberated during the electrochemical reaction of hydrogen and oxygen to electrical energy as opposed to the traditional combustion of hydrogen and oxygen to produce thermal energy. PEMFC is useful in both the stationary and mobile applications. Operating temperatures are between 50 to 100 $^{\circ}$C. A simplified diagram of the PEMFC is shown in figure 2.1. At the anode, hydrogen is catalytically split into protons and electrons in oxidation half-cell reaction as shown in the equation 2.1 [25]

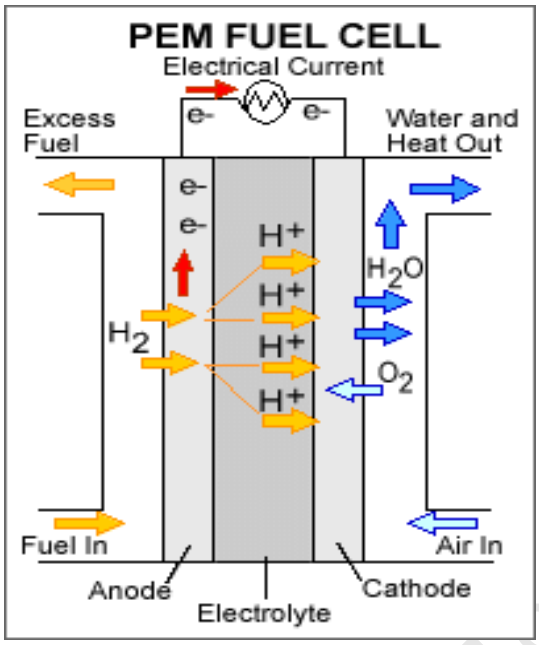

Figure 2.1: PEM Fuel Cell [11]

$$H_2 \rightarrow 2H^+ + 2e^- \quad ; \qquad E^0 = 0V \tag{2.1}$$

The protons permeate through the membrane to the cathode and the electrons travel through the external circuit. At the cathode, oxygen reacts with the protons and the electrons from the external circuit to form water as shown in the reduction half-cell reaction below.

$$\frac{1}{2}O_2 + 2H^+ + 2e^- \rightarrow H_2O; \quad E^0 = 1.229\ V \tag{2.2}$$

Overall Reaction

$$H_2 + \frac{1}{2}O_2 \rightarrow H_2O \quad ; \qquad E^0 = 1.229\ V \tag{2.3}$$

Splitting of hydrogen molecules is relatively easy using a platinum catalyst but the splitting of oxygen is not, iron, nitrogen and carbon have been tested [26]. Other challenges of the PEMFC are those of water management which could lead to flooding and high cost of platinum which makes the fuel cell expensive. A newer and cheaper catalyst to reduce oxygen from water molecules of a material known as perovskite was reported in nature chemistry [26]. Other types of fuel cells are zinc air, microbial,

regenerative, direct boro-hydride, alkaline, direct methanol, phosphoric acid, enzymatic biofuel cell and magnesium-air fuel cell.

Lithium Family Batteries: The term lithium batteries refers to a family of rechargeable/or disposable batteries with lithium metal or lithium compounds as the anode, iodine-polyvinyl pyridine cathode and electrolyte consisting of a thin layer of lithium iodide [27]. Because of the light weight of lithium, lithium batteries are characterized by very high energy densities. They are suitable for portable electronics, vehicular use and have recently been considered for grid scale applications. Typical efficiencies range between 80-90 %. There is a wide range of lithium batteries in both the market and laboratories.

Beltway batteries are a class of the lithium batteries invented by a scientist from Massachusetts Institute of Technology (MIT) that is characterized by fast charging [28]. They utilize a bypass system that allows the lithium-ions to enter and leave the battery at a speed great enough to fully charge in less than 5 minutes. By coating the electrode ($LiFePO_3$) in a glassy material called lithium pyrophosphate, ions bypass the channels and move faster than in other batteries. The typical charging times are between 10 - 20 seconds.

Lithium-titanate battery is a fast charging lithium battery in which the carbon surface of the lithium-ion anode is replaced with lithium titanate nano-crystals thereby producing a surface area in excess of 100 m^2 per gram. The average charging time is 10 minutes. An example is Toshiba super charge ion battery (SCIB) [29].

Lithium-air is a type of the lithium battery in which the lithium anode is coupled to atmospheric oxygen through an air cathode made of porous carbon nano-fibre. During discharge, lithium cations flow from the anode through an electrolyte and combine with oxygen at the cathode to form lithium oxide (Li_2O) or lithium peroxide (Li_2O_2) which is inserted into the cathode. They are known to possess a very high specific energy (up to 2500 Wh/kg) [30].

Lithium-ion batteries (LIB) belong to a family of rechargeable battery in which lithium-ions move from negative to the positive electrode during discharge [31]. They are one of the most popular types of the rechargeable batteries for portable electronics with one of the best energy densities, no memory effect and a slow loss of charge when not in use. The memory effect is an effect observed in batteries (esp. NiCd) that causes the batteries hold less charge if they are repeatedly charged after being only partially discharged. The specific energy of lithium-ion batteries is 250 Wh/kg. They have no memory effect, low loss of charge when not in use and large number of cycles (typically 1200).

2.2.2 Super-Capacitors

Super-capacitors are energy storage devices that are governed by the same fundamental equations as conventional capacitors but utilize higher surface area electrodes and thinner dielectrics to achieve greater capacitances (up to 5000 F). This allows for energy densities greater than those of the conventional capacitors and power densities greater than those of the batteries [32].

Energy is stored by the removal of the charge carriers typically electrons from one metal plate and depositing them on another. This charge separation creates a potential difference between the two plates. The amount of charge stored per unit voltage is essentially a function of size, the distance, and the material properties of the plates and the dielectric, while the potential between the plates is limited by the dielectric breakdown. Optimizing the material leads to a higher energy density for any given size of capacitor [33]. The formula for capacitance is given by**:**

$$C = \frac{A}{d}\epsilon_r\epsilon_o \qquad (2.4)$$

Where A is the area of the parallel plates, d is the distance between them,ε_0 is the relative permittivity or dielectric constant and ε_r is the permittivity of free space ($8.854x10^{-12}$ F/m). The energy stored by the capacitor is given by

$$E = \frac{1}{2}CV^2 \quad (2.5)$$

Where V is the voltage applied across the parallel plates

The energy can be increased in many ways. One way to increase the energy is to increase the applied voltage V, but this is limited by the maximum Energy Strength E_b at which the dielectric breaks down and starts conducting electricity which results in external component damage.

The internal components of a super-capacitor (e.g. current collectors, electrodes and dielectric material) also contribute to the resistance which is measured in aggregate by a quantity known as the equivalent series resistance (ESR). When measured at matched impedance (R = ESR), the maximum power P_{max} for a capacitor is given by

$$P_{max} = \frac{V^2}{4 \times ESR} \quad (2.6)$$

This relationship shows how ESR can limit the maximum power output of a capacitor. Super-capacitors are divided according to their unique mechanism for storing charges. These are Faradaic, non-Faradaic and Hybrid Super-capacitors.

The *Faradaic super-capacitors* are also known as pseudo capacitors. They are super-capacitors that charge faradaically through the transfer of charge between electrode and electrolyte. This is accomplished through electrosorption (absorption on the surface), reduction-oxidation and intercalation processes. Faradaic capacitors have greater capacitance and higher energy densities than the non-Faradaic capacitors. Two electrode materials are used here namely; conducting polymers and metal oxides [34]. Super-capacitors made by conducting polymers such as polyacetylene have relatively high capacitances and conductivities than the ultra-capacitors. They also cost less and they usually come in the form of p-type and n-type. The main disadvantage here is the mechanical stress which tends to reduce the cycle life of these devices. The pseudo capacitors made with metal oxides such as ruthenium oxide electrodes deliver high conductivities (or low internal resistance). Their capacitances, energy and power densities are higher than those of the conducting polymer and ultra-capacitors. The capacitance of

ruthenium oxide is obtained by the insertion and removal of protons into its amorphous structure. The main disadvantage here is that of prohibitive cost [35].

The non-Faradaic ultra-capacitors are constructed from carbon-based electrodes, an electrolyte and a separator shown in figure 2.2. They store charge electrostatically since there is no transfer of charges between the electrode and the electrolyte. When voltage is applied, ion in the electrolyte diffuses across the separator into the pores of the electrode of the opposite charge; however, the electrodes are designed to prevent the recombination of the ions. A double-layer of charge is produced [36]. The increase in surface area and decrease in the distance between electrodes allow EDLC to achieve higher energy density than conventional capacitors. Even though this device is electrochemical, no chemical reactions take place hence the process of charging is reversible.

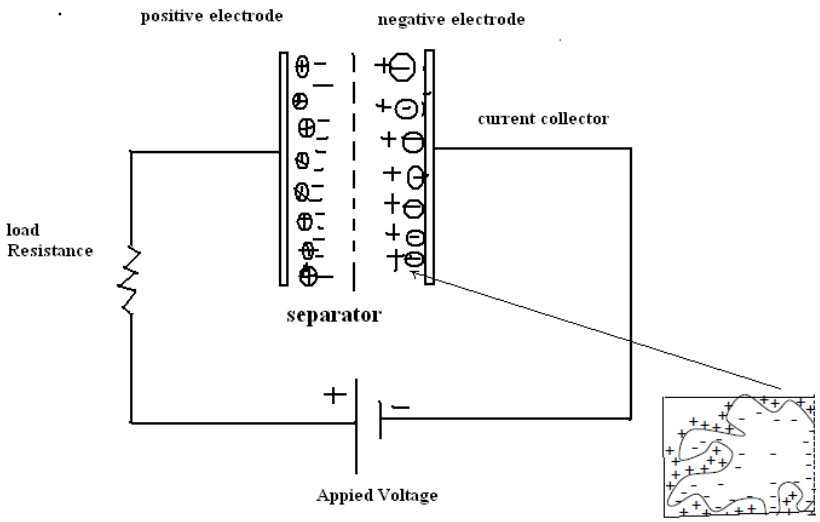

Figure 2.2: An electrochemical double-layer capacitor [36]

Very high cycle life is achievable in the order of 10^6 cycles. The two types of electrolytes used here are the aqueous and organic electrolytes. Examples of aqueous electrolytes are H_2SO_4 and KOH which are characterized by lower breakdown voltage, lower internal resistance and minimum pore size requirements compared to organic electrolytes such as acetonitrile. Shown in figure 2.2 is the diagram of the EDLC.

The following are different types of carbon based electrodes used; graphene, activated carbons, carbon aerogels, carbon nanotubes, carbon black, and carbon cloth. Graphene is

an allotrope of carbon whose structure is a one-atom-thick planar sheets of carbon atoms that are densely packed in a honeycomb crystal lattice. It has an excellent surface area per unit of volumetric densities. It is highly conductive and can be produced in various labs but not available in production quantities. The ultra-capacitors made with graphene electrode have energy densities comparable with that of a nickel metal hydride battery. Aerogel is a manufactured material with low bulk density of any known porous solid. It is a very good thermal insulator. Aerogel provides an extremely high surface area density of about 400-1000 m^2/g. Aerogel super-capacitors are small sized, and can only work at few Volts. Higher voltages ionize the carbon and damage the capacitor. Energy and power densities are 90 W.h/kg and 20 W/g respectively [37]. Carbon nanotubes have excellent nano-porosity properties, allowing tiny spaces for the polymer to sit in the tube and act as a dielectric. The mesopores in carbon nanotubes are interconnected, allowing a continuous charge distribution that uses almost all of the surface area.

Hybrid super-capacitors attempt to exploit the relative advantages and mitigate the disadvantages of EDLCs and pseudo-capacitors to realize better performance achieving energy and power densities greater than EDLCs without sacrificing the cost and cycle life [38]. There are three types of hybrid configuration based on their electrode configuration. Composite electrode integrates carbon based and polymer/metal oxide materials to achieve a higher capacitance. This attributed to the accessibility of the entangled structure which allows a uniform coating of poly-pyrole and a three dimensional distribution of charge hence a longer cycle life is achieved. Asymmetric hybrid capacitors couple two electrodes of EDLC and polymer pseudo-capacitors to circumvent the limitation of negatively charged conducting polymer thereby achieving higher energy and power densities than the EDLC. Like the asymmetric hybrids, battery-type hybrid couple two different electrodes. However, the battery-type is unique in coupling a super-capacitor electrode with a battery electrode. This specialized configuration reflects the demand for higher energy super-capacitors and higher power batteries, combining the energy characteristics of batteries with the power, cycle life and charging times of super-capacitors. Nickel hydroxide, lead dioxide serves as one electrode while activated carbon as the other.

Disadvantages include lower energy per unit weight, the output voltage decreases with energy stored so a control circuit would be needed, higher dielectric absorption, higher self- discharge, requires voltage balancing when three or more capacitors are connected in series, very low internal resistance and high output power could lead to health hazard such as electric shock. As of now more research is needed before super-capacitors could replace batteries. Advantages are very long cycle life up to 10^6 cycles, lower cost per cycle, fast charging and discharge, good reversibility, very low internal resistance, no corrosive chemical, high cycle efficiency (up to 95 %), no moving parts, modular design, compatibility with existing source-voltage inverters, excellent low temperature performance, can provide VAR and kW support and low toxicity materials [39].

Super-capacitors are commercially available for automotive motor racing, computer electronics and renewable energy; the larger test bed Electric Power Research Institute/Power Electronics Application Centre (EPRI/PEAC) 1MJ super-capacitor is capable of holding 100 kW for 10 seconds [40].

2.2.3 Molten Salt Energy Storage

The molten salt energy storage will be used in Eskom 100 MW Concentrating Solar Thermal Turbine project which will be located in Upington, Northern Cape, South Africa. This project is poised to be completed in 2014 as part of Eskom's commitment to renewable energy [41]. It is made of 200 m high tower surrounded by 6000 heliostats which are arranged in an elliptical formation around the focal point. The central receiver is situated on top of the central tower which in essence is a heat exchanger consisting of thin walled tubing which absorbs the concentrated beam radiation and transfers the heat to the working fluid (the molten salt circulated through it) which in turn is used to generate superheated steam. Electrical power is generated through a Rankine cycle (steam turbine process) [42]. The molten salt which is a mixture of 60 % sodium nitrate and 40 % of potassium nitrate commonly called saltpetre is a non-flammable and non-toxic material used in chemicals and metals industries as heat transport fluid. It melts at 221 °C (430 °F). It is kept liquid at 288 °C (550 °F) in an insulated "cold" storage tank [43]. The liquid salt is pumped through panels in a solar collector where the focused sun

heats it to 566 °C (1,051 °F). It is then sent to a hot storage tank. This is so well insulated that the thermal energy can be usefully stored for up to a week [44].

When electricity is needed, the hot salt is pumped to a conventional steam-generator to produce superheated steam for a turbine/generator as used in any conventional coal, oil or nuclear power plant. A 100 MW turbine would need tanks of about 9.1 m (30 feet) tall and 24 m (80 feet) in diameter to drive it for four hours by this design. The main disadvantage of molten salt energy storage is low energy densities compared to ordinary lithium batteries [45].

2.2.4 Superconducting Magnetic Energy Storage (SMES)

SMES is an energy storing device that stores electromagnetic energy in a magnetic field which is created by a flow of direct current through a large coil of superconducting material which is cooled down below its transition temperature. The amount of energy (E) in Joules stored is given by

$$E = \frac{1}{2} LI^2 \tag{2.7}$$

where L is the inductance of the coil measured in Henries and I is the current measured in Amperes.

Superconductivity is the ability of certain materials to conduct electrical current with no resistance and extremely low losses. Superconducting cables can carry hundred times the amount of current a regular copper cable of the same size can carry. When superconducting materials are cooled down to their critical temperatures, the ohmic resistance of these materials tends to zero; a perpetual current begins to flow. The temperature where this begins to happen is called the transition temperature [46]. Other conditions that affect superconductivity are critical current density and magnetic flux intensity. The architecture of SMES is shown in figure 2.3 and it is made up of the superconducting coil, the power conditioning system, cryocoolers/ refrigerators and control system.

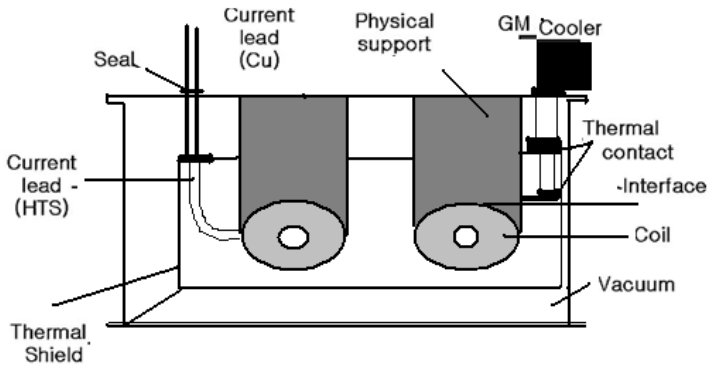

Figure 2.3: Basic architecture of SMES [25]

The *superconducting coil* is the heart of SMES systems. Most practical SMES installed to date use alloy of Niobium and Titanium (Nb-Ti) which require operational temperature near the boiling point of liquid helium, 4.2 K [47]. However the development of these materials today is such that they are not cost effective. Other superconducting materials are discussed below in two classes namely; type 1 and type 2 superconductors.

The type 1 superconductors are those conductors which are not penetrated by magnetic flux lines (Meissner-Ochsenfeld effect). This Meissner effect breaks down when the applied magnetic field exceeds a certain critical point, H_C and the material ceases to super conduct. Hence type 1 materials have only one H_C. Most pure elements and metals which include aluminium, lead and mercury are type 1 superconductors. These are not used for SMES

Type 2 superconducting materials are developed as a result of the enormous cost involved in the cooling down the SMES to absolute zero Kelvin. These are new in the market and are currently being researched. Type 2 superconductors are characterized by a gradual transition from the superconducting state to a normal state within an increasing magnetic field. Parameters to be considered here are T_{C1} and T_{C2}, H_{C1} and H_{C2} which are the range of temperatures and magnetic fields respectively when super conduction begins and ends. Type 2 superconductors exhibit higher critical currents at higher critical temperatures which are useful for strong electromagnetism. Apart from pure elements such as Niobium, vanadium and Technetium most type 2 materials are alloys. The alloys

include cuprate materials because they contain copper oxide, others are perovskites, iron-arsenides, skutterudites (contains no rare elements) etc.

The first set of type 2 superconductors was discovered in 1986, called Yttrium Barium Copper Oxide (YBCO) family. An example is the $Yba_2Cu_3O_7$ which is able to exhibit superconductivity at a temperature of 93 K attainable with liquid nitrogen which is much cheaper than liquid hydrogen and helium that were used in the LTS [48].

Shortly, after that the Bismuth Strontium Calcium Copper oxide (BSSCO or Bi-HTS) family was discovered in 1988 with the critical temperature of 133 K much higher than the liquid nitrogen (LN2) temperature, other classes were discovered such as titanium barium calcium copper oxide (TBCCO), Au-HTS, Pb-HTS, Hg-HTS Gold, Lead and Mercury HTS respectively to name but few [49]. The transition temperature of any one of these materials is higher than 100 K. This created an opportunity to use cryocoolers instead of liquid nitrogen for a much reduced cost [50]. SMES are also classified according to their operating temperatures. The low temperature SMES, LTS (T_C<10 K) are available commercially [51]. The high temperature SMES, HTS (T_C>100 K) are commercially available and still being researched. One of the disadvantages of HTS is the fact that they are mainly ceramics and cannot be drawn into wires. However, they are laid as thin layers on other materials such as stainless steel.

Besides the properties of the wire itself the configuration of the coil is an important issue because of the mechanical properties which are; inferior strain tolerance, thermal contraction upon cooling and Lorentz forces in a charged coil. Among these the strain tolerance is the most important because it determines how much structural material is needed to keep the SMES from breaking. Two types of connections in use are toroidal geometry and solenoid configuration [52]. The toroidal geometry is always under compression by the outer hoops and two disks one of which is on top and the other is on the bottom to avoid breakage. Toroidal SMES is used to lessen the external magnetic forces and therefore reduce the size of the mechanical support hence toroidal SMES can be located near a utility or customer load. The toroidal SMES are used for larger scale SMES while the solenoid configuration is used for the smaller systems [53].

A *cryogenic refrigerator* or cryocoolers are devices used to reach cryogenic temperatures (below 100 K) by cycling certain gases (such as helium) in a

thermodynamic cycle. Thermodynamic cycles such as ideal, Rankine, Stirling and Carnot cycles are reversible, external combustion engines are operated by cyclic compression and expansion of the working fluid at different temperature levels such that there is a net conversion of heat to work. The LTS SMES uses the liquefied helium gas to reach the transition temperature of the LTS SMES. Since the cost of helium gas is high it added to the high cost of the SMES. The HTS super conducts above 100 K were cooled with liquid nitrogen which provided a reduced cost of cooling. However future advances in technology led to the invention of the cryogenic refrigerator or cryocoolers which could simply be adjusted to reach desired temperature down to 20 K. They provide economical and efficient cooling. These coolers are already in mass production with different capacities costing about R30, 000 ($3, 000) per unit depending on the size [54]. Examples include Gifford-McMahon, Joule Thomson, Stirling engine, Pulse-Tube and room temperature magnetic coolers [55-57].

Power conditioning system (PCS) is the interface between the SMES storage coil and the utility grid or load. It has the function of converting the high current in the coil to the high voltage of the utility grid. The design challenge for the PCS is to find the best combination of controllability, reliability, efficiency, and cost [58]. The PCS use conventional components as shown in figure 2.4. According to the topology of configuration, there are three kinds of PCS for SMES namely; thyristor, voltage source converter (VSC) and current source converter (CSC) based SMES.

The *thyristor based SMES* can control mainly the active power and has little or no control over the reactive power [59]. Its control of both the active and reactive components of power is not independent. On the other hand, both the VSC and CSC based SMES can control both the active and reactive components of power independently and simultaneously. Therefore in applications which mainly require active power control, the thyristor-based SMES is used while applications in which reactive power controls are required VSC or CSC-based is used.

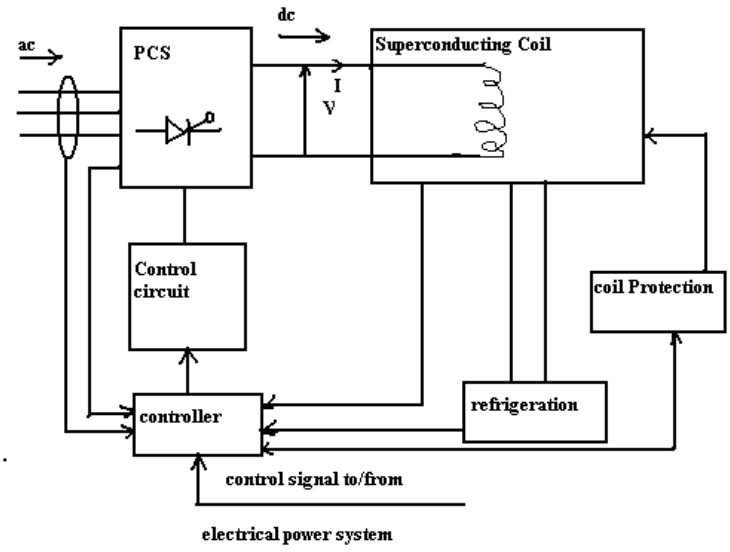

Figure 2.4: Thyristor based power conditioning system [58]

The control system sets up a link between power demands from the grid network and power flow to and from the superconducting coil. It receives dispatch signals from the power grid and status information from the coil. The integration of the dispatch request and charge level determines the time response of the SMES unit. The control system also measures the condition of the SMES coil, the cryo-coolers and other equipment. It maintains system safety and sends status information to the operator. SMES systems provide remote observation and control via internet connections [60]. Small scale devices (~1 MJ or smaller) with short duration charge/discharge in few seconds are used for power conditioning and stabilization of critical manufacturing equipment and computer facilities. Medium-scale SMES units (1-10,000 MJ) with duration of few minutes can be built with self-supporting containment structures. This size category encompasses load levelling for electric transmission lines, maglev trains, pulse power and renewable energy applications [61]. Large-scale diurnal energy storage systems (>10,000 MJ) with a duration of a few hours would be used by electric utilities for load levelling in regions where large hydro-pumped storage is not feasible. Large-scale SMES systems require earth support to counteract the magnetic forces acting on the coils and would be constructed below grade in bedrock [62]. Studies have shown that large-scale SMES devices, 5000-10000 MWh could provide the most economical form of storage the design of which consist of a low-aspect-ratio solenoid magnet about 1000 m in diameter and 20

m high, buried in a trench in earth or rock [63]. The estimated cost of such project would be about US$1 billion and approximately 1 million litres of helium would be needed. In 1992, the Japanese built a 5 GJ (1.4 MWh) SMES test facility [63]. The magnet is about 5 m in diameter. Most of the cost associated utility-scale SMES are related to the mechanical structure required to contain the very large Lorentz structure and the path to dissipate the energy stored should a fault develop within the coil.

SMES are compact having a low aspect ratio (ratio of this diameter to its height about 1000 m to 20 m for a 5000 MWh). SMES has the highest efficiency (typically 95 %) of all other utility scale storage devices [64]. They have unlimited charging and discharge cycles. They have very short charging and discharge times hence power is immediately available and high reliability because SMES contain no moving parts. The disadvantages include large current in conductors, high magnetic field which suppresses superconductivity in type 2 materials. Other disadvantages are large cooling losses and fairly large investment costs [65].

The cost of an SMES system can be divided into two: the cost of energy storage and the cost of power handling capability. The storage related costs include capital and construction costs of conductor, coil structure components, cryogenic vessel, refrigeration, protection, and control equipment. Power related cost includes the capital and construction costs of the PCS. The cost of the storage is between US$85,000-125,000 per mega-joule while the cost of the power conversion system depends on the configuration of the system [66]. For example, if an SMES is connected to an AC system, a DC-DC chopper and a VSC or a CSC is needed, but if the SMES is connected to an existing flexible AC transmission system (FACTS) device with a DC bus, only the DC-DC chopper is required [67].

2.2.5 Underground Thermal Energy Storage (UTES)

Underground thermal energy storage is also known as seasonal thermal or Interseasonal thermal or thermal bank. This slightly differs from the other energy storage techniques discussed in this dissertation. UTES is purely a thermal storage hence it is the cheapest

method [68]. It is a new concept in that it makes use of the earth as the thermal mass. It is based on the fact that at a depth of 20 m below ground surface, temperature is steady round the year. Energy is collected as heat using solar collectors, stored underground either in underground aquifers (underground water reservoirs) or underground heat bank and then extracted using heat exchangers in winter for space heating. Normally, temperature is usually below 100 degrees Celsius [69]. This is an efficient and economical way of storing excess heat produced in the summer for use in the winter. In the desert, it could also be used for space cooling thereby taking the load of heating and cooling off the grid. Different types of UTES include the duct, aquifer and the borehole thermal energy storage [70].

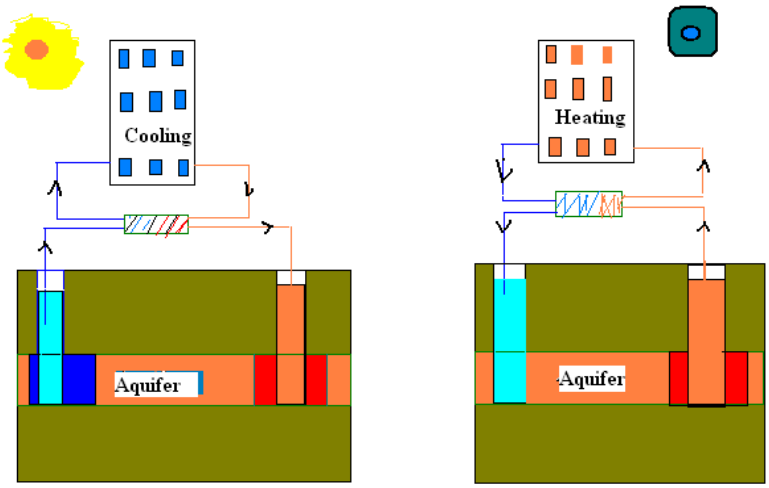

Figure 2.5: Underground Thermal Energy Storage [43]

Aquifer thermal energy storage uses underground water reserves called aquifers [71]. There are two wells as shown the figure 2.5 either side with hydraulic coupling. One well is for the warm water and the other one is for the cold. In the winter, warm water is cooled and passed to the cold well. Energy is extracted by the heat exchanger for heating purposes. In summer, the process is reversed and cold water is used for cooling. Once heated, the water is stored in the warm well. The advantage of this system is that it is environmentally safe; the water which circulates from underground to the heat exchangers and back cannot be contaminated as it always remains in the system. Moreover, there is no net loss of water from underground [72]. The only problem is that this system can only be used in areas that are above aquifers [73].

2.3 Photovoltaic Cells

Photovoltaic cells are classified as direct converters because they convert solar energy directly to electricity. The physical process whereby light is converted to electricity is known as the photovoltaic effect and was first studied by a French physicist known as Alexandre-Edmond Becquerel in 1839 [74][75]. Low energy light striking a silicon crystal causes atoms of silicon to vibrate and twist in their bound position. The electrons in bonds also gain more energy and attain a higher energy level. However, the atoms and the electrons soon lose their energy and return to their original energy levels and give away heat. Light of greater energy upon collision with the silicon crystal releases an electron to move around in the crystal thereby creating a hole. A pair of electron and hole created as a result of the light is called the light-generated electron-hole pair. The electron-hole pairs generated, on their own, cannot set up a current flow unless a potential barrier is set up within the cell. This charge separation is what sets up a voltage difference at the ends of the cell. Hence, electric current is driven in an external circuit. This process is referred to as the photovoltaic effect [76]. Research efforts in the field of the photovoltaics are geared towards reducing the cost while increasing the efficiencies of the PV. Other researchers are developing new materials, new architectures with better light absorption and charge carrier capabilities [77]. The major advantages of the photovoltaic cells are: clean and no harmful gases are produced; free energy from the sun; solar energy is very compatible with the distributed power generation; the global cost of the solar panels has plummeted continually, governments and other bodies also provide incentives and the solar panels are easy to install [78].

The main disadvantages of solar cells are: intermittent nature of sunlight; difficulties in the predicting the sunlight. In addition, they require additional components such as inverters, maximum power point tracking (MPPT) system and batteries; they require large land space. Solar cells could be classified as the silicon, thin films, highly efficient multi-junctions and the thermo-photovoltaic solar cells.

2.3.1 Silicon Solar Cell

The highly efficient solar cell was first developed by Daryl Chapin, Calvin Souther Fuller and Gerald Pearson in 1954 at Bell`s telephone laboratories using a diffused silicon p-n junction [79], [80]. The silicon solar cells control about 80 % of the solar market. As the name implies they are made of silicon which makes up about 26 % of the earth`s crust and it is the second most abundant element after oxygen. The four valence electrons play an important role in the photovoltaic effect.

Because the amount of power produced by a single solar cell is relatively small, one or two watts, designers group solar cells together to form modules (panels) that supply a more useful level of voltage, current and power. Solar cells may be connected in series to produce higher voltages and in parallel to produce a higher current. This kind of solar cell is called a crystalline silicon (c-Si) cell. Their efficiencies range from 15 % to 23 %. The crystal size of the ingot, ribbon or wafer can determine the way these cells are classified

The basic structure of a photovoltaic solar cell is shown in figure 2.6.

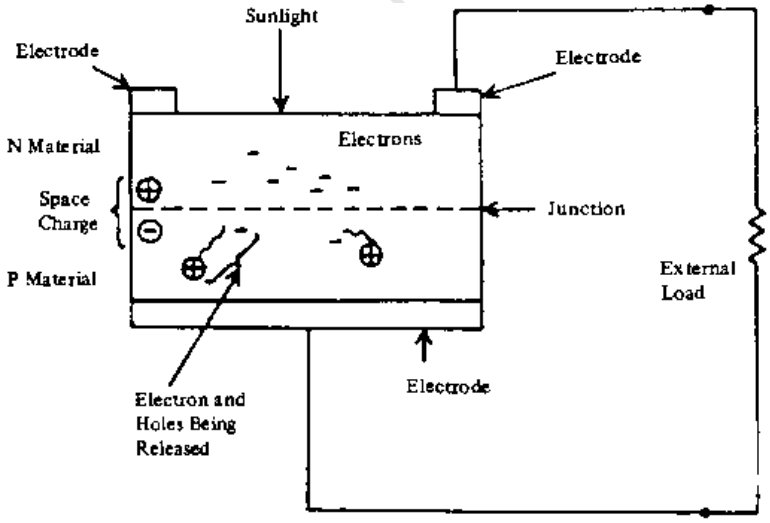

Figure 2. 6: Basic structure of a silicon based solar cell [81]

Mono-Crystalline Silicon (c-Si) has an ordered crystal structure, with each atom ideally exhibiting predictable and a uniform behaviour. This process is called Czochralski named after a polish scientist Jan Czochralski [82]. This means that this type of Silicon goes

through several cycles of slow and energy intensive filtration and separation processes and thus is the most expensive type of silicon. They are usually circular shaped or 'square-without-corners' when they are grown from an ingot. The only way to create high purity crystal structures is to extrude the molten liquid and the cylindrical shape of block is created by force of gravity. From the cylindrical block, smaller cells are cut [83].

*Poly-Si or multi-crystalline silicon (*mc-Si*)* is made from several regions of crystalline silicon kept together through covalent bonding and are separated by 'grain boundaries'. This means that the poly-Si goes through a lower number of cycles of energy intensive filtration and separation processes that mono crystalline cells do and are therefore less expensive. They are grown in a square shape because the molten liquid in the (square) ingot does not need to be extruded hence efficiency is lower [84].

Micro-morph (μc-Si: H) is the short form of nano-crystalline or microcrystalline silicon. It was first introduced by Veprek and Marecek [85] to describe a new form of thin film silicon deposited by glow discharge technique. This material is essentially a polycrystalline form of silicon obtained at relatively low deposition temperatures (<300 $^{\circ}$C). The micro morph is a hybrid of a-Si and c-Si. It contains small crystals which are capable of absorbing broader spectrum of light [86]. Efficiencies have reached 10 %.
Black silicon solar cells are made from ordinary silicon solar cells but in this case, the colour is changed to black to enable the solar cells to capture the full range of the solar spectrum. Researchers at NREL showed that these cells which are made of nano-islands of silver on a silicon wafer and immersed briefly in liquids to make billions of nano-sized holes in each square inch of silicon wafer surface are cheaper because they do not require an anti-reflective surface [87]. The black solar cells have demonstrated an efficiency of 1 % higher than ordinary solar cell. RIE is an etching technology used in micro fabrication [88], [89].

2.3.2 Thin Film Solar Cells

The recent boom in the demand for the photovoltaic modules has created a silicon supply shortage [90]. This provided an opportunity for thin-film photovoltaic modules to enter the market. The thin film solar cells (TFSC) are solar cells made by eliminating the expensive silicon wafers that account for about 50 % of the cost. TFSC are made by depositing one or more thin layers of photovoltaic material on a substrate. The TFSC are less than a few micrometers thick. They constitute less than 20 % of the market today [91]. They are the second generation solar cells and are classified as follows: amorphous Silicon (a-Si), Cadmium Telluride (CdTe), Copper Indium Gallium diSelenide (CIGS), Dye-Sensitized Solar Cell (DSSC) and Organic Solar Cells.

Amorphous silicon (a-Si) or hydrogenated amorphous silicon (a-Si: H) are made from the non-crystalline allotrope of silicon at temperatures below 70 °C. They are mostly used for light power devices such as calculators. However, by cascading them in multi-junctions, their efficiencies could be enhanced. They offer advantages of higher energy absorption, ability to be deposited on a wide range of substrates, flexibility, light weight and lower cost. Maximum efficiency is less than 10 % [92].

Cadmium Telluride (CdTe) solar cells emerged as a new electronic material in 1947 when Frerichs synthesized CdTe crystals by the reaction of Cd and Te vapors in a hydrogen atmosphere and measured their photoconductivity [93]. In 1954, Jenny and Bube reported that p-type and the n-type conductivity could be obtained in CdTe by doping them with foreign impurities and that the conductivity type could also be changed by varying the Cd-Te stoichiometry. Cd excess yields n-type and Te excess yields p-type conductivity. The properties of the CdTe thin film include optimum bandgap, optical absorption co-efficiency and the ability to be doped and arranged in n-i-p configuration [94]. CdTe thin film solar cells have demonstrated overall efficiency exceeding 17% while the typical module price is about R6.45/ kW [95]. They are cheaper than the Silicon solar cells; good match with the sun and cadmium is abundant. The main disadvantages are toxicity of cadmium and the scarcity of tellurium [96].

Copper Indium Diselenide (CIS) solar cells are a precursor to copper indium gallium selenide (CIGS) [97]. In fact, the acronym CIS is sometimes used interchangeably with

CIGS. The two types of cells are very similar in makeup. The CIS family is a group of I-III-VI direct bandgap semiconductor materials discovered as a replacement of the toxic CdTe solar materials. The most popular of the CIS family being copper indium gallium diselenide ($CuIn_{1-x}Ga_xSe_2$) or CIGS: Where x can vary from 1 (pure Copper Indium Selenide) to 0 (pure Copper Gallium Selenide). They consist of two semiconductor layers made up of CIS and CIGS [98]. That light generates electrons upon absorption, which are herded into an electric current to produce usable electricity. Their efficiencies vary between 14 to 19 % while the band gaps range between 1 to 1.7 eV. The CIS could be fabricated in a continuous roll-to-roll process without going through the vacuum evaporation process [99]. Light weight, low cost, high flexibility, and low toxicity, non-crystalline nature of the CIS makes them very attractive to a wide range of solar applications [100].

Dye-sensitized solar cell (DSSC) was invented by Micheal Gratzel and Brian O`Regan at the Ecole Polytechnique Federal de Lausanne (EPFL) in 1991and is therefore also known as "Gratzel cells" [101]. DSSCs are electrochemical devices comprising a light-absorbing molecule anchored onto semiconducting titanium dioxide (TiO_2) nanoparticles, which make use of sunlight to generate electricity. What makes the DSSC differ from other PV technologies is their ability to separate the function of charge absorption and charge transport. The major benefits of the DSSC technology are: the use of non-vacuum based and simpler manufacturing process; the use of non-toxic and abundant materials; superior performance in low and diffuse light; very low capital expenditure required relative to other PV technologies. The function of charge absorption and transport which were originally performed by the same unit in the junction cells are separated in the DSSC. The main parts of a DSSC are: a mechanical support coated with transparent conductive oxide; the semiconductor film, usually TiO_2; a sensitizer adsorbed onto the surface of the semiconductor; an electrolyte containing a redox mediator and a counter electrode capable of regenerating the redox mediator like platine. The maximum efficiency is about 11 % [102]. This solar cell is still subject to basic research in the areas of chemical and thermal stability; hence it is not yet fully commercialized. Advantages of DSSC are low cost and robustness while the main disadvantage of the DSSC is they are made with

liquid electrolyte such as ruthenium (R_U) hence their durability is reduced. Research efforts are directed at making DSSCs with solid electrolytes like quantum dot

Organic Photovoltaic Cells (OPVC) technology which converts sunlight into electricity by employing thin films of organic semi-conductors have been the subject of active research over the past 20 yrs. The OPVC are the third generation photovoltaic cells that are based on organic electronics which deals with conductive polymers for light absorption and charge transport [103]. These cells are still under basic research hence their prices are not determined. However, since their manufacturing process involves roll-to-roll printing at low temperatures, their prices could be comparable to those of household plastic product. Organic electronics is a branch of electronics that deals with conductive organic polymers or small organic molecules for light absorption and charge transport. In the organic molecules or hydrocarbons, the valence band is equivalent to the lowest unoccupied molecular orbital (LUMO) while the conduction band could be compared to the highest occupied molecular orbital (HOMO). The separation between the LUMO and the HOMO is called bandgap and this is typically 1-4 eV. When these materials are exposed to the sunlight and excitons (electron-hole pairs) are formed. These excitons are separated by an electric field created by the junction of two dissimilar materials known as the acceptor and donor materials.

Organic solar cells are easily manufactured due to molecular nature of the material by methods such as solution processes, high throughput printing techniques, roll-to-roll technology all at low energy and low temperature hence they are low cost compared to the silicon solar modules. They are highly compatible with a wide range of substrates, portable, lighter, and rollable. The manufacturing methods of the organic solar cells are environmentally friendly. The organic solar cells find application in the portable electronics like cell phones, laptops etc. Another advantage of the organic solar cell is that of the high absorption coefficient. The major disadvantages are low efficiency, lower thermal stability and lower strength [104]. Single layer organic photovoltaic cells; Bi-layer organic photovoltaic cells; Bulk hetero-junction photovoltaic cells; Graded hetero-junction photovoltaic cells are various types of the organic solar cells.

Single layer organic photovoltaic cells are the most basic of the four and they are fabricated by sandwiching a layer of organic semi-conductor between two metallic conductors. An example is a layer of indium tin oxide (ITO) with high work function and a layer of low work function metal such as Al, Mg or Ca. External quantum efficiency, (EQE), of 0.17 % at 0.4 V has been observed [105].

Bi-layer Organic Photovoltaic Cells also referred to as planar donor-acceptor hetero-junctions. They are more advanced than the single layer OPVC. The bilayer organic PV cells have two different layers in between the conductive electrodes resulting in improved electron affinity and ionization energy. Consequently, the electrostatic force is set at the junction of the two layers which acts as a separator of the excitons between the acceptor and the donor [106]. An example is the derivative of fullerene C_{60} which has a high affinity, hence is a good electron acceptor and poly 2-mthoxy-5-(2-ethyl-hexyloxy)-1, 4-phenylene vinylene (MEH-PPV) as the donor. EQE of 9 %, overall power efficiency of 1 % and fill factor (FF) 0.48 have been observed in PPV/C_{60} [107].

In *bulk Hetero-junction Photovoltaic Cells*, light generates excitons with subsequent separation of charges in the interface between an electron donor and acceptor blend within the device`s active layer. These charges then transport to the device`s electrodes where these charges flow outside the cell, perform the work and re-enters the device on the opposite side. C_{60} fabricated with poly (3-octylthiophene-2, 5-diyl) (P3OT) and carbon nanotube (CNT) composite produced a quantum yield of 45 % under reverse bias. The peak monochromatic power efficiency is 1 % [108].

In *Graded Hetero-junction Photovoltaic Cells*, the blends of the acceptors and the donors are annealed in order to optimize film morphology and enable efficiency for small molecule materials without utilizing a thermal treatment [109]. This is accomplished through the use of a highly tunable, continuously graded acceptor-donor hetero-junction material. Consequently, a gradual gradient is formed at the acceptor-donor interface. The architecture combines the short electron travel distance in the dispersed hetero-junction with the advantage of the charge gradient of the bi-layer technology. Example is a solar

cell blended with copper pthalocyanine (CuPc) and fullerene (C_{60}) EQE of 50 % and power conversion efficiency of 2.1 % at 1.5 G irradiation were observed [110].

Hybrid solar cells combine the organic and inorganic materials with the aim of utilizing the lower cost cell production of organic photovoltaics as well as obtaining other advantages such as tunable absorption spectra, from inorganic component [111]. The hybrid of nanoparticle-polymer cells contain photoactive layers consisting interconnected semiconducting nanoparticles/quantum dots (such as CdSe, PbSe and TiO_2) in a solid semiconducting polymer phase (like P3HT, MEH-PPV). Other advantages of the hybrid solar cells are low cost, efficient electron transport and strong optical absorption. Others are efficient excitons dissociation, ease of fabrication (with cheap wet chemical synthesis) and possibility of tailoring the properties by varying the size of the nanoparticles. Typical power conversion efficiency of 2 % has been reported [112].

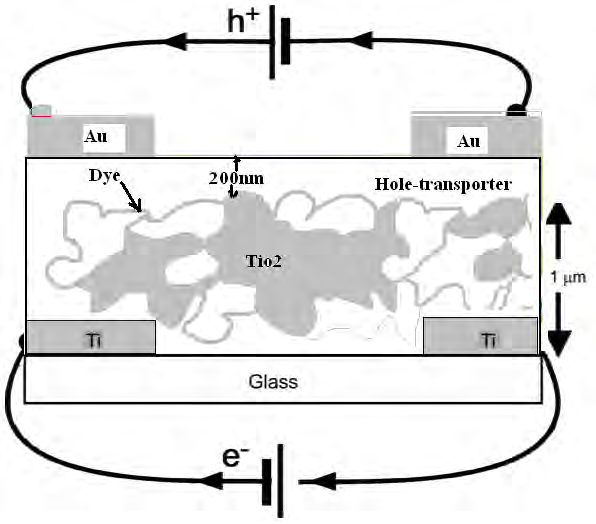

Figure 2.7: Polymer-nanoparticle composite [113]

Types of organic hybrid solar cells are polymer-nanoparticle composite, carbon nanotube solar cells and the dye-sensitized solar cells. The polymer nano-particle composites are characterized by large surface area to volume ratio. The size control creates quantum confinement which allows for tuning of the optoelectronic properties such as band gaps and electron affinity [113]. The diagram of polymer-nanoparticle composite is shown in

figure 2.7. Dye and TiO_2 form the polymer/nanoparticle interface through which electron transport occurs.

Carbon nanotubes are nano-materials which are known for their high strength, hardness, kinetic, electrical, optical, EM wave absorption, thermal conductivities and flexibility [114].

2.3.3 Highly Efficient Photovoltaic (PV) Cells

The following concepts describe novel ways of achieving very high efficiencies in the design of a photovoltaic cell. These are multi-junctions, multi-gap, multiple excitons generators (MEG) and hot carrier solar cells.

Multiple Gap Photovoltaic Cells also referred to as the multi-gap PV. The researchers at Berkeley Laboratories in 2002 discovered that indium gallium nitride (InGaN) absorbs different wavelengths of light if the amount of the indium alloy is slightly changed. This led to the invention of a new type of solar cell known as the multi-gap that is capable of absorbing the entire solar spectrum [115], [116]. Also by replacing some of the molecules of GaInAs with a highly electronegative atom like oxygen, highly mismatched alloys are produced which might be stacked together to form a multiple band-gaps well below the conduction band. This device is predicted to show an efficiency of 50 % [117].

Multiple Excitons generation (MEG) simply refers to the generation of multiple electron-hole pairs from the absorption of a single photon. This phenomenon is capable of boosting the internal quantum efficiency of a nano-crystal based solar cell. However, because of the short lives of the excitons, the harvest of energy could be difficult. MEG was demonstrated in a Lead Sulphide (PbS) quantum dot solar cell where photons whose energies equal to two times the energy of the PbS particles were released on the solar cell. It was observed that one photon liberated two electron-hole pairs [118]. This however should not be confused with impact ionization which occurs in bulk materials under an electric field. Light excites a high-energy exciton (X) which decays irreversibly into a quasi-continuum of multi-exciton (multi-X) states available at this energy. The model requires only the density of states of multi-excitons to be very high, while the Coulomb

coupling between X and multi-X can be quite small [119]. Under concentrated light of air mass 1.5 (AM 1.5), MEG cell has a potential to reach 41 % power conversion efficiency.

Hot carriers solar cells offer the possibility of very high efficiencies (up to 68 % under 1sun) with structures that are simpler than other solar cells with comparable efficiencies.1 sun is equivalent to a solar insolation of 1 kW/m^2. The basic concept underlying hot carrier cell operation is as follows: in the normal cell operation, a lot of energy is lost through the relaxation of the photo-excited carriers by a process known as thermalization which leads to the degradation of the solar cell. But in the hot carrier solar cells, the relaxation is avoided allowing energy in the excess of the band gap to be stored in the photo excited carriers populations. The hot carrier solar cells tend to capture these hot carriers before they thermalize by including a special layer of SiO to capture these hot carriers [120], [121].

2.3.4 Multi-junction Solar Cells

The single junction silicon solar cells are limited by the Shockley-Quiesser efficiency limit of 30 %. The multi-junctions however attempt to exceed this limit by cascading two or more single junction solar cells one on another. This device is referred to as the multi-junction (MJ) solar cell. In 1990, Boeing`s Spectrolab developed a GaInP/GaInAs/Ge on Germanium substrate with a record efficiency of 40.6 % under 325 suns [122]. Ever since then, other kinds of MJ have been built in a more cost efficient manner.

The multi-junctions are designed to split the solar spectrum with many junctions. Here, thermalization losses are minimized. Two junctions have two energy layers typically, 1.6 and 0.9 eV. The materials used here could range from amorphous silicon, micro crystalline silicon, dye-sensitized, CIGS or organic semiconductors [123]. Triple junction solar cells split the solar spectrum into three energy bands (1.8, 1.2, 0.7 eV). Their maximum efficiency is 42 %. Four to six junctions are already practically achieved. Infinite junctions have theoretical efficiencies tending to 85 %, which is the thermodynamic limit. General limitations of solar cells include surface reflection, series

resistance at contacts and recombination losses. Limitations specific to tandem solar cells are: (1) they are in series connection hence there is the need for current matching, (2) variations of solar spectrum throughout the day, (3) resistance in intermediate recombination layer, and (4) transmittance of top cells and light management with textured substrates [124].

Metamorphic Multi-junction Solar Cell: In 1999, Fraunhofer ISE developed an MJ using groups III-V semiconductor compounds [125]. These cells are made out of thin $Ga_{0.35}In_{0.65}P$ and $Ga_{0.83}In_{0.17}$ (band gaps 1.92 eV and 1.87 eV respectively) as layers on GaAs (1.42 eV) or Ge (0.67 eV) substrates. These are grown by a method known as metamorphic growth on either germanium or gallium/arsenide substrate. In contrast to the conventional cells, these cells do not have the same lattice constant (i.e. the distance between the atoms in a crystalline structure are not the same) [126]. This makes it difficult to grow the III-V semiconductor layers with a high crystal quality since at the interface of materials with different lattice constants, strain is present. This strain causes dislocation and other crystal defects. The researchers at Fraunhofer then localized the defects in a region not electrically active and the active region remains relatively free of defects [127].

Metamorphic Crystal Growth enables the use of a much larger range of III-V semiconductors. Different layers of the cell generate the same amount of current resulting in an efficient cell of about 41.1 % efficiency at 454 suns [128].

Inverted Metamorphic Multi-junction (IMM) is an improvement on the metamorphic cells which tends to improve the efficiency of the cell by reducing the band gaps of the GaInP and GaInAs [129]. But this causes a mismatch between the alloys and the Ge substrate thereby reducing the efficiency. Here, growth is inverted relative to the conventional MM. The process used here is organo-metallic chemical vapour phase deposition (MOCVD). The top two layers are lattice matched. Growing the third metamorphic layer on the first two layers leads to cell misfit and dislocation and mismatch reduces the performance of the entire system. The inverted metamorphic multi-junction, shown in figure 2.8, solves the problem by disposing a transparent step graded

composition (AlGaInP) buffer in-between the second layer and the metamorphic third layer.

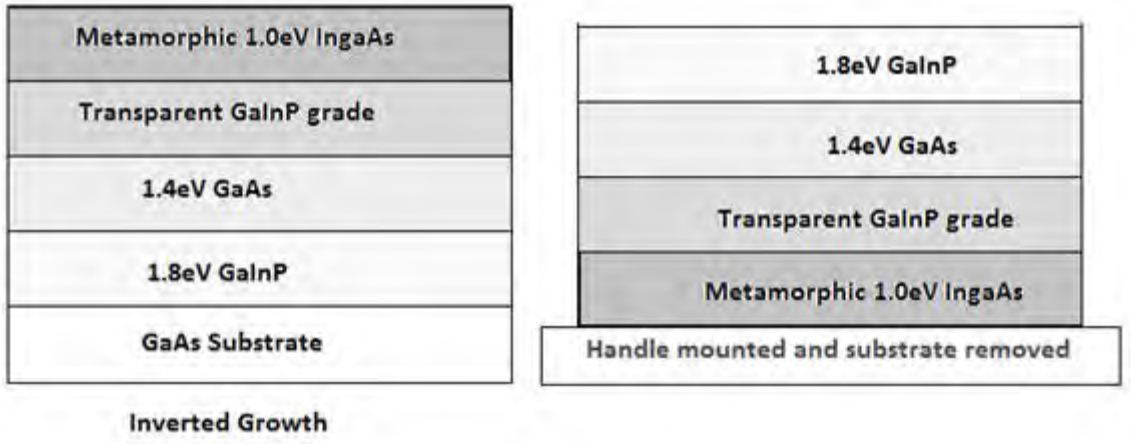

Figure 2.8: Inverted Multi-junction Solar Cell [129]

The grade is engineered to achieve a nearly strain-free metamorphic junction. Afterward the GaAs substrate is then removed and then reused as a template to grow another cell. Finally, MgF_2/ZnS antireflective coating (ARC) is deposited by thermal evaporation and mounted on a handle. This method of growing an inverted solar cell creates room for adding more junctions using the same template. The following are the advantages of the IMM: strain free metamorphic bottom layer without damaging the top lattice-combination; possibility of lower cost by the reuse of the removed substrate; flexible and lightweight and rejection of unused infrared light for reduced heating [130].

Multiple Quantum Well (MQW) Structure: A 'quantum well' is a potential well that confines particles in two dimensions that are otherwise free to move in three dimensions [131]. Both electrons and holes can be confined in semiconductor quantum wells. The effect is to increase the gain and efficiency of the solid state device such as lasers in CD or DVD players, infrared imaging, and more recently, solar cells. A quantum well is basically a semiconductor with a small energy gap (or band gap) sandwiched between two thicker layers of semiconductor(s) with a large energy gap, such as gallium arsenide (GaAs) as shown in figure 2.9.

12	P+GaAs		Cap layer
11	P+AlGaAs		Window layer
10	p+GaAs		Emitter
9	AlGaAs"I"		Spacer layer
8	AlGaAs"I"		Barrier
7	GaAs"I"		Well
6	AlGaAs"I"		Barrier
5	GaAs"I"		Well
4	AlGaAs"I"		Spacer layer
3	n+ GaAs		Base
2	n+ GaAs		Buffer layer
1		Substrate GaAs n+	
bottom Electrode			

Figure 2.9: Multiple Quantum Well Solar Cells [131]

Quantum well solar cells are built with multiple nano-scale semiconductors layered on top of one another with a lateral conduction layer between the substrate and n region to allow contact between the three layers. They are special multiband gap devices with intermediate properties between the hetero-junctions (the sum of the currents generated in different materials is the lower of the two) and tandem cells (sum of the voltages is determined by the worst of the two cells. It is known that quantum well solar cells (QWSCs) can enhance short circuit current and power conversion efficiency in comparison with similar, conventional solar cells made from the quantum well (QW) barrier material alone. Some designs have multiple quantum wells in the I-region of the p-i-n cells; hence they are referred to as the multiple quantum well solar cells (MQWSC). Professor Keith Barnham of Imperial College London invented the quantum well solar cell in 1989 [132]. The solar cells developed by Barnham operate at high current. The i-region consists of alternating layers of indium gallium arsenide (InGaAs) and gallium arsenide phosphide (GaAsP), while the p and n layers of the solar cell are made from gallium arsenide (GaAs). A “strain balance” technique is used to grow the different layers, which matches the lattice structures of the different semiconductor materials, preventing defects. This method allows more than 65 wells to be grown on top of one

another without dislocation [133]. MQW has a theoretical efficiency over 50 % but in practice only 29 % has been realized.

III-V/Silicon lattice-Matched Tandem Solar Cell: The newly discovered GaNPAs can be grown lattice matched to the silicon substrate with very low structural defect densities and a band gap ideally suited for a high-efficiency multi-junction solar cell [134].

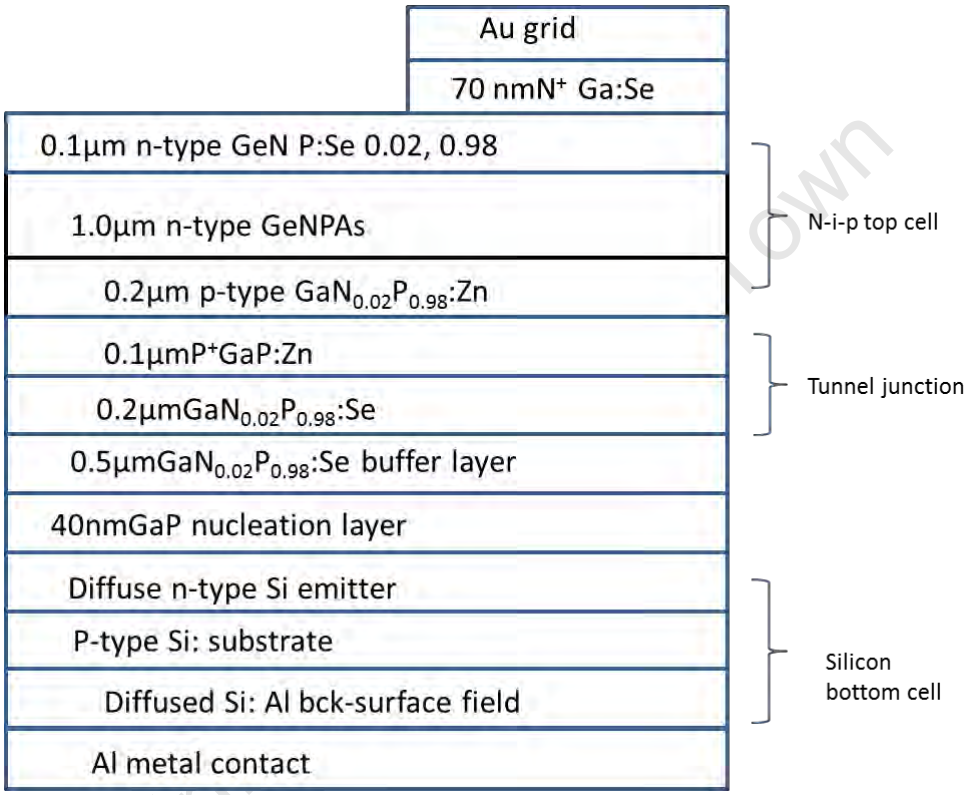

Figure 2.10: III-V-on-Silicon Tandem Solar Cell [134]

A two-junction device consisting of a 1.7 eV GaNPAs junction on a 1.1e V silicon junction has the theoretical potential to achieve nearly optimal efficiency for a two-junction tandem cell. In the monolithic III-V-on-silicon tandem solar cell, elements of groups III-V layers are nearly lattice-matched to the silicon substrate. The cell includes a 1.8 eV GaNPAs top cell, a GaP-based tunnel junction (TJ), and a diffused silicon junction formed during the epitaxial growth of GaNP on the silicon substrate. This tandem on

silicon has an efficiency of 5.2 % in AM1.5 G without any antireflection coating. Low currents in the top cell are the primary limitation to higher efficiency at this point.

The III-v/Silicon latticed-matched tandem solar cell is shown in figure 2.10. Silicon junction is formed during epitaxial growth of high crystalline quality lattice–matched GaNPAs on silicon by metal-organic vapour phase epitaxy (MOVPE). Two junction solar cell devices using this approach have the potential to reach efficiencies of 35 % under the direct spectrum or 37 % under the global spectrum. So far, efficiency of 7 % has been realized [135].

2.3.5 Thermo-photovoltaic (TPV) Cells

A different approach for the conversion of solar energy into electricity is thermo photovoltaic systems [136]. Potential applications include combined heat and power, portable and auxiliary power, radioisotope space power, industrial waste heat recovery and concentrated solar power. The TPV first absorbs the solar radiation and re-emits the thermal radiation before illuminating the solar cell. The absorption in the radiator and the re-radiation reduce the quality of the radiation by reducing its temperature. The theoretical efficiency however is estimated using the following optimization parameters: sunlight concentration ratio, TPV cell parameters, absorber/emitter temperature /efficiency and the photon recirculation efficiency. It has been found that emitter temperature exceeding 2000 K, absorber/emitter efficiency of 90 % and TPV system`s efficiency exceeding 30 % can be obtained at sunlight concentration ratio exceeding 8000 suns using gallium antimony (GaSb). The theoretical efficiency limit is 85 %. Other research means of increasing the efficiency are: use of nano-structured receiver/emitter assembly to absorb very wide spectrum of light and emit a very narrow band of photon with energy of about 0.7 eV. The parts of a TPV system are: a source of heat (e.g. a flame, radiative isotope or the sun); a radiator; filter; a solar cell; a means of re-circulating the sub-bandgap photons to conserve energy; a power conditioning system [137].

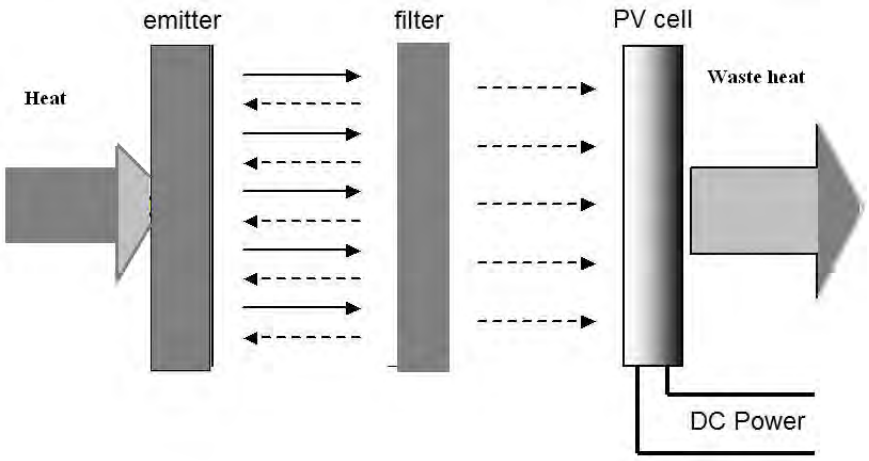

Figure 2.11: Thermo-photovoltaic Solar Cell [137]

The *TPV materials* are classified as follows: (1) the metals and alloys of metals such as Polycrystalline silicon carbide, tungsten, rare-earth oxides and photonic crystals*;* (2) photovoltaic cells such as Silicon (Si), Germanium (Ge), Gallium Aersenide (GaAs), Indium Gallium Arsenide antimony (InGaAsSb), Indium Gallium arsenide (InGaAs), Indium Phosphorous Arsenide Antimony (InPAsSb)*;* (3) bulk nano-structured semiconductor groups III-V elements like Bi_2Te/Sb_2Te_3 thin film superlattics or embedded PbSeTe quantum dot superlattices and Silicon Nanowires [138]. They are grown by organo-metallic vapor-phase epitaxy or molecular-beam epitaxy, GaInAs is lattice matched to Indium Phosphorus (InP) substrate. When the atomic proportions of Gallium to Indium are in the ratio 47:53, the bandgap of 0.73 eV is observed. This bandgap is too large and corresponding efficiency is low. However when InGaAs is lattice-mismatched to InP substrate with relatively low defect bandgap is improved to 0.5 eV. A quartenary alloy of GaInAsSb produces the bandgap between (0.38-0.7) eV [139].

An *absorber/emitter* is an intermediate structure that absorbs the sun's rays in a TPV, heats up and emits a narrow-banded spectrum directly above the bandgap of the solar cell. Emitter could be either broadband or narrow band. Narrow band emitters such as ytterbia, erbia and holmia radiate energies of 1.1, 0.7 and 0.5 eV respectively. The most frequently used broad band emitter is the silicon carbide whose emittance is 0.9 and can withstand temperatures up to 1900 K and spectral emittance close to one. Other broad band emitters are tungsten photonic crystal, rare-earth metals and photonic crystals [140].

The *Silicon Nanowires* (SNW) typical dimensions of the SNW are 10 nm x 20 nm. They are another class of TPV which are more efficient than the bulk Silicon. The performances of the SNW are controlled by adjusting their sizes and impurity levels [141]. The silicon nanowire solar cells come in two designs; p-i-n co-axial nanowire solar cells and core/sheath nanowire solar cells. The SNWs are applicable in providing an on-chip power for nano-electronic devices, biological systems, and numerous microscopic robots. Efficiency of 3.4 % at 1sun and peak power of 200 pW has been reported. The University of Houston TPV Radioisotope power conversion technology development effort is aiming at combining TPV with thermocouple for four fold improvement in system overall efficiency [142], [143].

2.4 Concentrated Photovoltaics (CPV)

The CPV is based on using an optical device to focus a large area of sunlight onto a relatively small but efficient solar cell [144]. This technology has the advantage of replacing most of the expensive photovoltaic materials with cheap optical materials (glass and plastic) without necessary compromising the overall performance of the system. Because the size of the photovoltaic cell is minimal compared to the system, the most efficient solar cell (such as the tandem solar cell) could be used here without much increase in the overall cost of the entire installation. One major disadvantages of the CPV is its inability to operate in diffuse light as a result of cloudy weather and the need for tracking devices which makes it only economical for large scale power generation. The major components of the CPV are the tracking system, the non-imaging light concentrators, solar cell and the cooling system. The basic architecture of the CPV is shown in figure 2.12.

2.4.1 Non-Imaging Light Concentrators

Non-Imaging optics is a branch of optics concerned with the optimal transfer of light from source to the target. The non-imaging light concentrators are optimized to transfer the maximum solar power from the source to the target rather than transfer image. They contrast conventional imaging optical devices that are optimized to transfer image [145]. The non-imaging light concentrators are used not only for the maximum power transfer but also for the uniform distribution of light at a specified area and a complete blocking of light on the rest of the surface. For the purposes of optimization, the following parameters are optimized: total radiant flux, angular and spatial distribution of light. The advantages of these concentrators include higher tolerances (as larger angle of acceptance), reduced thermal losses, higher concentration (requiring smaller cells) and better distribution of illumination at target. Some of the common concentrators are optical light guides, reflectors, lenses, or a combination of reflectors and lenses. Practical applications are car headlamps, LCD backlights and fiber optic illumination lights. The optical concentrators are classified as follows: active concentrators; passive concentrators and hybrid concentrators. There are many different design methods for the non-imaging concentrators however the most popular methods are the flow-line or Winston-Welford method, the simultaneous multiple surface (SMS) or Minano-Benitez method and Minano method using Poisson brackets. The following are 2D designs [146]:

- Refractive and Reflective (RX)
- Refractive and Reflective and internal Reflection (RXI)
- Total Internal Reflection and Refraction (TIR-R)
- Single mirror two stage (SMTS)
- Dielectric single mirror two stage (D-SMTS)

Passive Concentrators use geometrical optics or a change in index of refraction to increase the illumination on a surface above the incident solar level [147]. Hence concentration is shown as a function of the index of refraction and angular collection range. The geometric concentration ratio is the ratio of the collector aperture to the receiver active area. These concentrators could be engineered to optimize the acceptance angle which eliminates the need for tracking at the same time minimizing the size of the

photovoltaic cell. A passive concentrator could focus light up to 1000 suns (1 sun = 1 kW/m^2) on to a cell of about 1 mm^2.

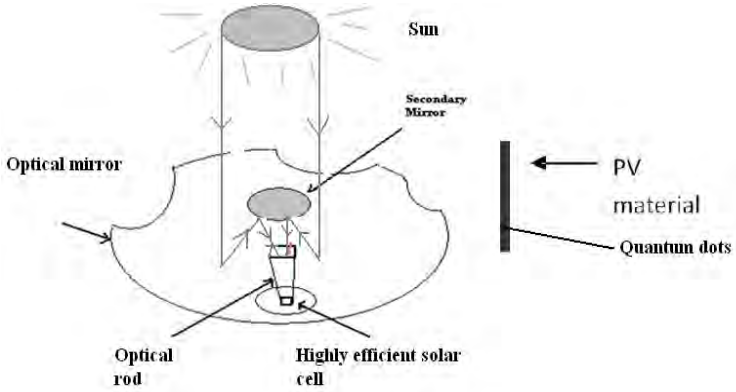

Figure 2.12: Compound parabolic concentrator [147]

An example of a passive concentrator is the compound parabolic concentrator (CPC) which focuses light on the photovoltaic cell for the production of steam or hydrogen [148], [149]. Others are the Hyperboloid, central power tower concentrators which use reflectors, Fresnel lens concentrator which uses refractors.

Active Concentrators are fluorescent or luminescent concentrators that concentrate light

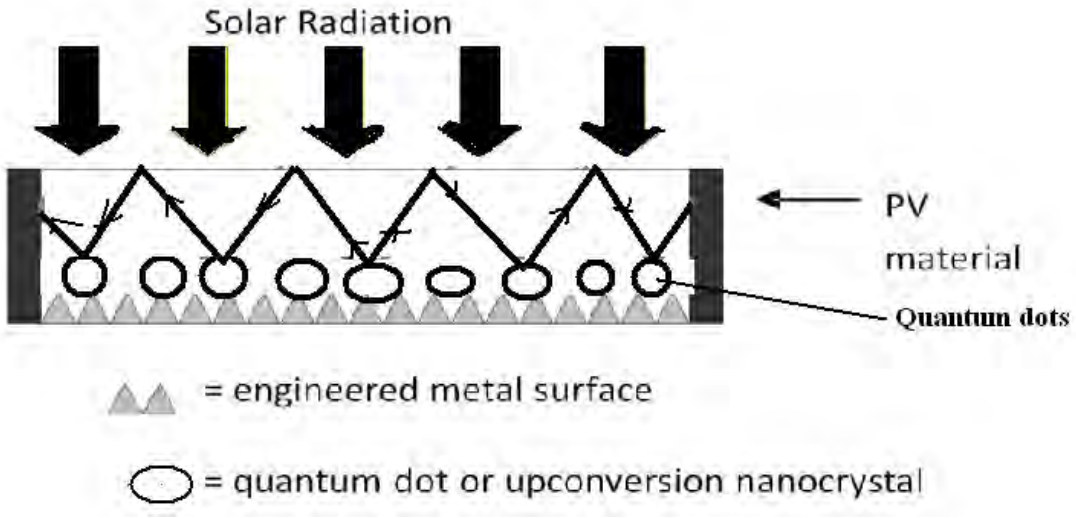

Figure 2.13: Luminescent Solar Concentrator [151]

by Stokes shift or by shifting the frequency of the solar radiation from high to low frequency [150]. Lumagen dye or quantum dots nanoparticle are the most common materials used to absorb the solar high velocity photons and emit them at a lower predetermined frequencies. Total internal reflection is used to guide the re-emitted light to the solar cell [151]. The diagram of luminescent solar concentrator is shown in figure 2.13. An example is the Quantum Dot Concentrator. One advantage of these concentrators is that they do not require tracking devices.

The *hybrid concentrators* combine the active and passive concentrators in cascade to produce ultrahigh flux regime for the production of the solar laser. Other designs of non-imaging optic include the simultaneous multiple surface method (SMS 3D or 2D). An example is the Dielectric Totally Internally Reflecting Concentrator (DTIRC). Each of these concentrators is capable of focusing the sun up to one thousand times unto an efficient PV of area of between 1 mm^2 to 1 cm^2 delivering up to 100 W. The large acceptance angle eliminates the need of a tracking system. Solfocus is a pioneer producer of cheap concentrated photovoltaic solar cell [152].

2.4.2 Lateral Spectrum Splitting Concentrator Photovoltaics (LSSCPV)

The Spectral Beam splitting devices try to make a more efficient use of the broad solar spectrum by dividing it into different energy ranges [153]. The LSSCPV are fitted with special concentrators like dichroic filters which split the Sun`s spectrum into two or more parts. This device usually has a wide acceptance angle therefore they require only low level tracking systems. The LSSCPV are very thin about 1 cm therefore they are useful for domestic and portable devices.

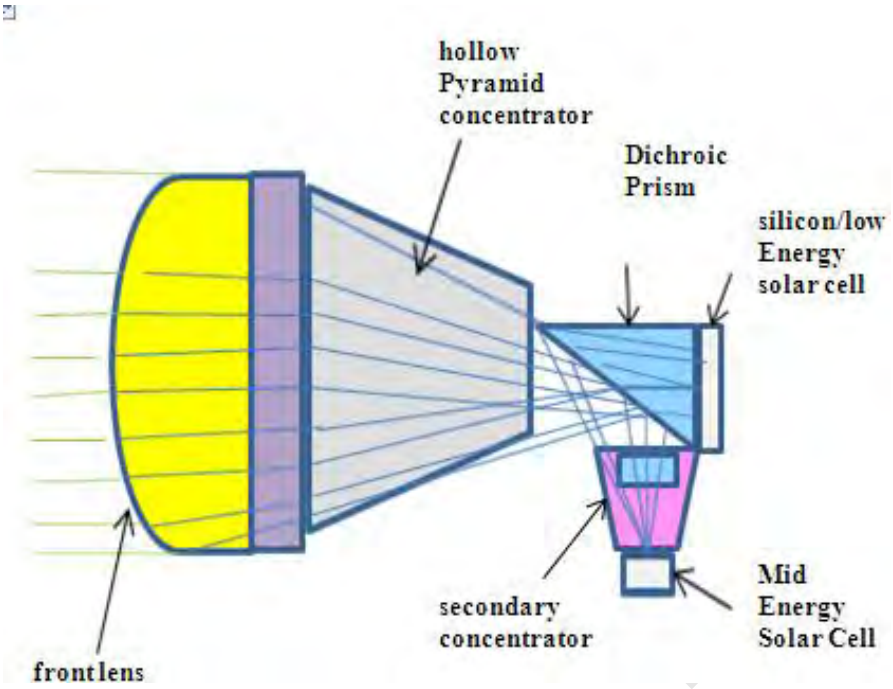

Figure 2.14: Lateral Spectrum Splitting Concentrator Photovoltaic [153]

Figure 2.14 shows the LSSCPV system. The major parts are: a front lens array using non-spherical lenses (toroids or crossed cylinders); a hollow pyramidal reflective concentrator array which increases the performance of the system for light which is not normal to the module; a non-imaging solid concentrator on the solar cell converting photon energies between 1.4 and 2.4 eV (called mid-energy solar cells); and Dichroic or trichroic prism which reflects the light above 1.4 eV and passes light below this energy. Further research suggests the use of InGaN for increased bandwidth (0.7-2.4 eV) collection and improved efficiency [154]. Because the cells are separate from each other the constraints of current and lattice matching do not apply. It allows the use of low cost materials such as silicon. The LSSCPV reduces the need for tunnel diodes and buffer layers. No need for tracking system when static concentrators are used. The system is portable and light suitable for rooftop. The best efficiency is 42.9 % at 20 suns with 93 % optical efficiency. A typical cell composition for a three cell system are GaInP (31.7 %), GaInAs/GaInAs (bottom filtered by Si) (6.2 %), silicon (filtered by GaAs) 5 %. The total efficiency is 42.9 % [155].

2.4.3 Dual Focus Cassegrainian (DFC) module

DFC is very similar to LSSCPV except that the dichroic mirror only isolates the low infra-red (IR) waves from the rest of the radiation [156]. This low IR is captured with the Gallium Antimonide (GaSb) or InGaAs/InP. These are thermo photovoltaic (TPV). The TPV has an added advantage of diverting the heat away from the IMM. The rest of the radiation is captured with the normal IMM cell. Here the expected efficiency is 46 % [157]. The figures 2.15 and 2.16 show the spectral response the basic architecture of the DFC respectively.

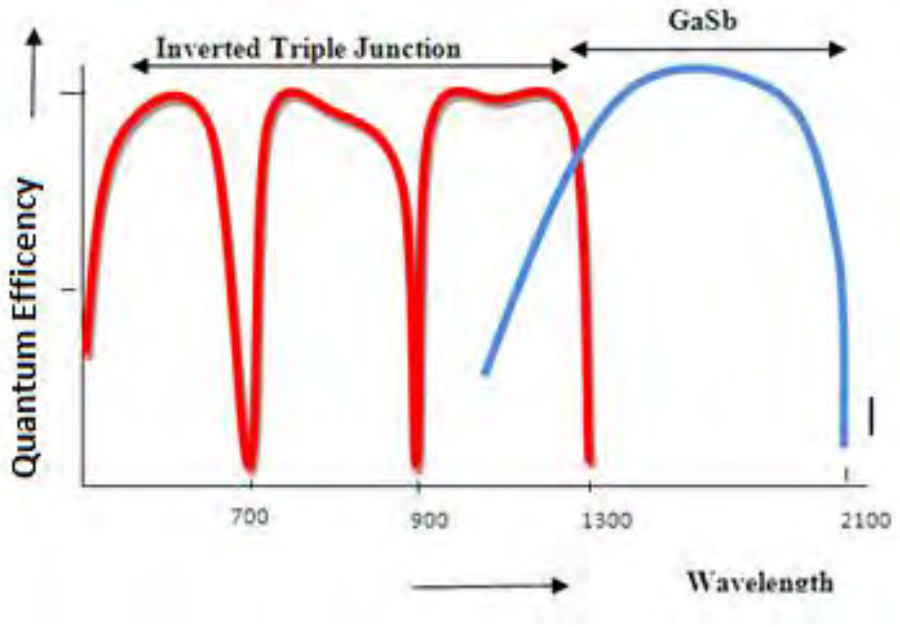

Figure 2.15: **DFC Spectral responses** [157]

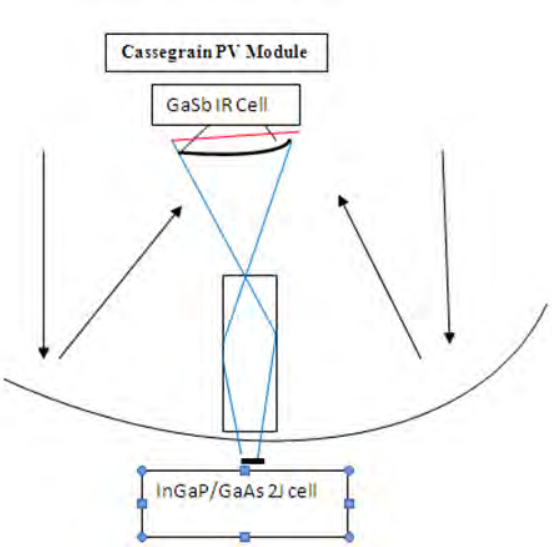

Figure 2.16: Dual-Focus Cassegrainian Module [157]

2.4.4 Key Features of a CPV which are geared towards Cost Reduction

The CPV utilizes the most efficient solar cells such as MM, IMM, MQW, III-V on silicon, LSSCPV or Cassegrainian CPV, these cells guarantee superior output and because the sun is concentrated this set up occupies less land space. Effective thermal management is applied to ensure uniform distribution of heat for absorption by the TPV. Hence the temperature of the system is always kept low (less than 40 $^{\circ}$C). This eliminates the need of heat sink or an elaborate cooling system, all of which add to the cost of the installation. Some systems are designed with static concentrators having a wide angle of acceptance in order to cut the cost of trackers [158].

Finally, to roll out the CPV in mass production, 6-axis robots and high speed material handling methods are used. The CPV module costs at Solfocus over volumes are summarized in the chart below. These costs do not include the trackers or other balance of system items. It is projected within five years that the cost of 1GW CPV farm would be less than R4/W ($0.5/ W) from the current R12/ W ($1.5/ W) [159].

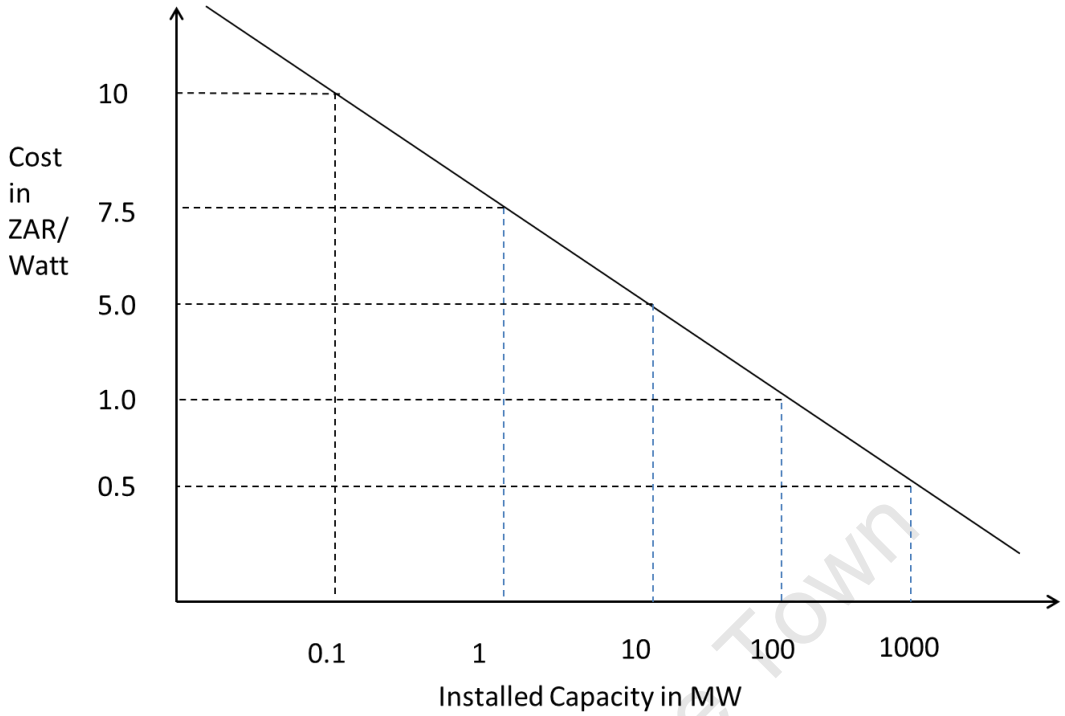

Figure 2. 17: Solfocus Second Generation CPV cost/installed capacities [159]

2.5 Thermal Solar Power

The thermal solar power is a term used to describe systems that convert solar energy primarily to heat [160]. They are also often referred to as the thermal converters because their efficiencies depend on temperature. When their final output is electricity the thermal solar power systems are called the indirect solar power systems because they convert solar energy first to heat and then to electricity. The thermal solar power devices could be classified according to their operating temperatures [161].

2.5.1 Low Temperature Collectors (LTC)

LTC are used to collect low level heat for the swimming pools, space cooling/heating devices such as solar ventilators and solar updraft towers. They can be used to provide

80-90 % of the energy necessary to heat a residential pool which would normally be heated using natural gas. The solar thermal pool heating is so effective needing only about 3 years to pay for itself. They operate below 50 $^{\circ}$C [162].

Solar Updraft Tower: The solar updraft tower is a renewable energy power plant for generating electricity from the sun. The sun shining on the greenhouse-like collector structure around the base of the tall chimney heats up the air within the chamber which rises up the chamber thereby setting up a convection current in the plant. This convection air current is what drives the blades of the turbine located at the base of the chimney as shown in figure 2.18. A 200 MW solar updraft plant is planned in the state of Arizona, USA which was created by Enviromission, Australia. The budget for this project is about $700 million [163]. The small experimental solar updraft tower plant, built in Manzanares, Spain in 1982 by Schlaich and Bergermann is shown in figure 2.18.

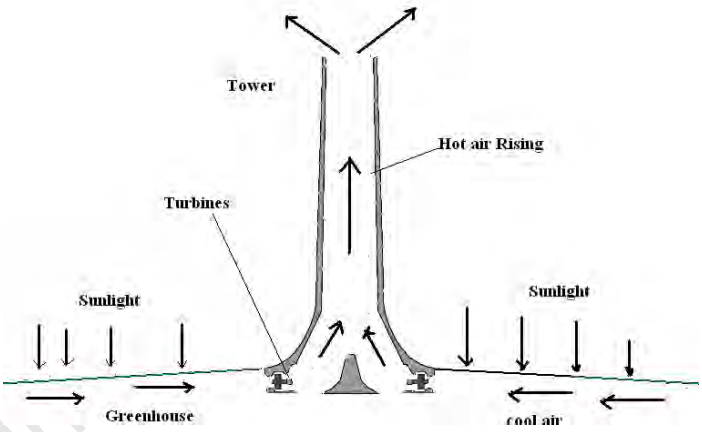

Figure 2.18: Solar Updraft Tower [164]

At night, the difference in temperature between the ground and the air allows this effect to continue. Some designs equip the updraft system with thermal storage to smoothen the day time and night time difference in temperature [164].

2.5.2 Medium Temperature Collectors

The medium temperature collectors are mostly the solar water heaters (SWH). These are divided into the low pressure and high pressure heaters. It is shown that over 40 % of the energy consumption of typical households is related to water heating hence many utilities including Eskom of South Africa is subsidizing solar water heaters for private consumers. The high pressure heater which boils water at 9 Bar provides more efficient water heating than the ordinary solar heater [165]. The three types of collectors used here are the flat plate, evacuated tubes and the integral collector-storage systems. The circulation systems come in form of the direct, indirect and drain back circulation systems. Details of the solar water heater are not covered in this dissertation [166].

2.5.3 Concentrated Solar Power (CSP)

The concentrated solar power is a type of the high temperature solar collector. It operates at temperatures between 400 °C and 1500 °C and is the most popular type of the high temperature converters. Another name for the concentrated solar power is the concentrated solar thermal power plant. Some of the common technologies of CSP are parabolic trough, linear Fresnel, molten salt power tower and Stirling Dish. The emphasis of this section will be on the molten salt power tower CSP. The experimental CSP farms called the solar one and two were built in the Mojave Desert in California [167]. Globally, there are up to 600 MW of installed CSP capacity up and running by 2009 and 15 GW being planned and under construction. SEGS I-IX were developed in the Mojave desert in California after the first oil crisis in the early 70s and this marked the beginning of modern development of CSP plants worldwide. SEGS I-II (1984-85) is located in Daggett, with capacity of 44 MW; SEGS III-VII (1986-88) is located in Kramer Junction, with a capacity of 150 MW; SEGS VIII-IX (1989-90) is located in Harper Lake, and its capacity is 160 MW. They operate at an annual efficiency of about 15 %. Others are in Spain, Italy, China and India [168].

Here in South Africa, plans are underway to build a massive 100 MW CSP near Upington, Northern Cape Province by the South African utility, Eskom, year of commissioning is 2016 [169]. About 14 farms under the Independent Power Producer (IPP) have received approval from the National Department of Environmental Affairs of South Africa for the development of solar projects using different technologies such as the CSP, CPV and PV [170]. Most of these projects would be in the Western Cape, Northern Cape and in the Eastern Cape Provinces of South Africa. Examples of these IPP projects are Group five 650 MW plant at Kalahari Nature Reserve, Ilangalethu 125 MW plant at Karoshoek and a 310 MW farm in Pofadda [171]. There are three designs of CSP and these are the parabolic trough, Dish/Stirling engine and the power tower. The parabolic trough is the most developed and the cheapest while the power tower is the newest and the most efficient. The power tower has the capability of reaching very high temperatures and very high concentration. The advantage of the CSP is its ability to store energy in the form of heat in the molten salt tanks and dispatch the energy during peak periods while the main disadvantage of the CSP is low efficiency, about 15 %. The major parts of a CSP are the solar collector field made up of the heliostats and the receiver tower; the molten salt tanks; turbine and generator block. The block diagram is shown in figure 2.19.

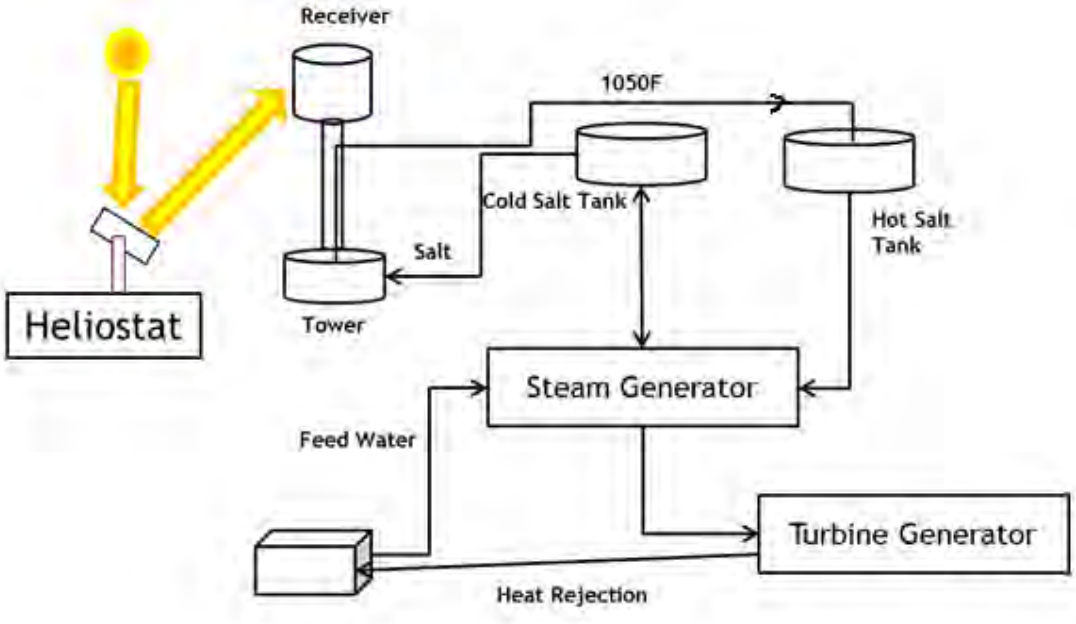

Figure 2.19: A block diagram of a CSP plant [169]

At the solar field are the heliostats which are arranged in an elliptical formation to concentrate the solar rays onto a small receiver located on top of a tower which is about 200 meters high. The concentrated solar rays heat up the receiver to some 400 °C. At the receiver, heat transfer fluid absorbs the heat and transfers it to the storage tanks. From the thermal storage tanks, the steam is generated which turns the turbine at the steam plant. The typical efficiencies of these plants range from 8 % to 16 % [172]. The overall efficiency of a solar power plant is a function of the efficiencies of three subsystems; optics, receiver and the power block.

The *Solar Field* or the heliostat field is also called the solar collector. Heliostats are motorized mirrored devices that move to compensate for the changing angle of the Sun as it moves across the sky, reflecting its rays onto a fixed target such as a central receiver [173]. In a solar tower system, the heliostats are the most important cost element of the solar tower constituting 50 % of the total cost of the plant so cost saving here would contribute immensely to a unit cost of energy produced by this plant.

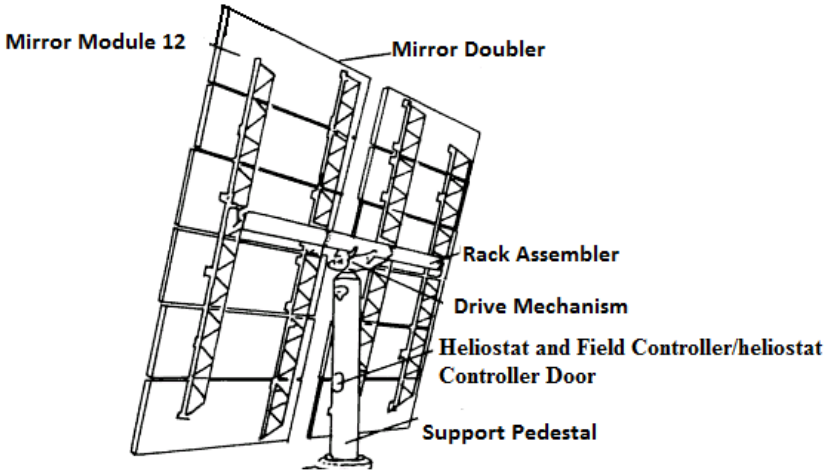

Figure 2.20: Pedestal mounted heliostat [173]

The various designs of heliostats are:

Pedestal mounted – shown in figure 2.20 consists of a joint mounted to a pedestal which is able to move both azimuth and elevation of more than 90 degrees.

Bubble-enclosed membrane heliostats are those heliostats whose glass mirrors are replaced with stretched membrane reflectors suitable for optical splitting. Due to their

simplicity and light weight they promise a significant reduction in cost over conventional glass heliostats [174].

Ganged Heliostats refer to an array of heliostats controlled by a single mechanism such that each heliostat is able to redirect the rays of the sun towards a common fixed target area over the course of the day and thereby concentrate rays of the sun received over a large area to a much smaller area.

Caroused heliostat has a large single mirror (100 m^2) instead of small units. They have several points of support and therefore are more stable and rigid. The driving system is not a part of the structure. The lever arm is longer because the movement is not done from the centre. They are more accurate and can track the sun continuously without stops.

Rotating field heliostats- are the most advanced heliostat with accurate tracking systems. Extensive evaluation shows that pedestal mounted (100 m^2 size) heliostat have a cost advantage over others. The cost is about R1260 (or $126) if 50,000 units are produced per year. Azimuth drive pedestal account for 30 % of the total cost [175].

Spectral Splitting Solar Fields: One way to boost the efficiency of the solar field is by installing a spectral splitting filter. This can also be achieved by either of these two methods. First, at the heliostats and then at the central receiver:

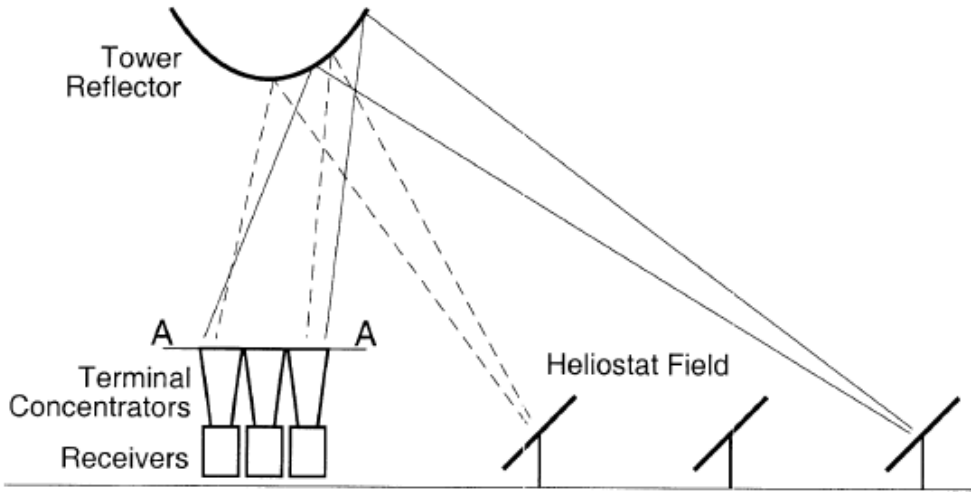

Figure 2.21: Reflector beam optics [174]

The first method involves splitting of the solar spectrum at the heliostats and this could be achieved by placing narrow band pass filters to isolate waves corresponding to the bandwidth of silicon which is between 600 to 900 nm. An example of a narrow band-pass

filter is a stretched micro structured Mylar membrane. This membrane is laid over the mirrors as described by Heijnandi [176]. The silicon solar cells can convert a narrow band (600-900 nm) wave with over 60 % efficiency. About 6000 cells, heat sinks and optical filters would be needed. Beam down optics is another method shown in figure 2.21.

Here, the hyperboloid-shaped tower replaces an ordinary receiver. The hyperboloid-shaped tower reflector is used as the spectrum splitter. Its mirror can be made of transparent fused silica glass, coated with a dielectric layer, functioning as a band pass filter. Higher energy waves over 1.4 eV could be filtered out and routed to Ultraviolent optimized solar cell [177]. The lower reflector mirror, A-A, is made of silvered borosilicate. The rest of the spectrum passes through a fibre optic cable for further concentration instead of a Heat transfer fluid (HTF) otherwise Compound parabolic concentrator is used to increase the concentration up to 10, 000 suns producing a temperature of about 2000 °C. This system is popularly known as concentrated photovoltaic or thermal hybrid system.

An ideal blackbody is a physical body that absorbs all incident electromagnetic radiation. Because of this perfect absorptivity at all wavelengths a blackbody is also the best possible emitter of thermal radiation which it radiates incandescently in a characteristic continuous spectrum that depends on the body`s temperature. Graphite and lampblack are close to blackbodies with emissivities greater than 0.95. Other blackbodies include cylindrical blackbody solar receiver and black fluid with antireflective device. Here, the receiver consists of an annular cylindrical tube with an aperture parallel to the axis of the cylinder. To reduce the radiative losses, the tube is surrounded by a layer of a thermal insulator [178]. There are two types of receiver namely; external and cavity receiver. The external receivers are designed to absorb rays coming from all directions, they have very simple designs. The size is determined by the amount of radiation it is meant to absorb and the amount of heat loss. Common losses are by radiation and convention. They are shaped either tubular or spherically. The cavity receivers are used in most of the commercial large scale solar plants. They have an aperture through which internal reflection ensures the majority of the radiation that has entered the cavity is absorbed on

the internal surface thus their heat losses are minimal but they are more expensive. Once the heat is absorbed in the cavity it is transferred to the working fluid [179]. The cavity blackbody can convert incident radiation to heat at 2000 $^{\circ}$C with the efficiency of 90 %.

Heat Exchanger/Storage/Transport Facilities: What makes the CSP electricity unique and cost effective is the ability of the plant to store and despatch energy at times when demand is highest. A number of energy storage techniques have been studied and these include mechanical energy systems which are pumped hydro storage, compressed air storage, flywheels; chemical energy storage such as electrochemical batteries and organic molecular storage [180]. Others are biological energy and superconducting magnetic energy storage (SMES) but so far thermal energy storage have been shown to be the cheapest and one of the most efficient (in excess of 90 %). They have a fixed value of R1120/ kW ($140/ kW) and a variable cost of R184/ kW-hour ($23/ kW-hour) storage, derived from National Renewable Energy Laboratory (NREL). Once the heat has been realized from the central receiver, it has to be transmitted from the tower to the heat bank which is located at the ground hence heat transfer fluid is used [181]. Whether the heat exchanger is needed depends on the design and the type of materials used. High temperature storage concept could be studied in two parts: the type of storage which could be active or passive storage, the materials used as the storage medium which could be solid, liquid or gases of salt.

Active storage systems are mainly characterized by forced convection heat transfer into the storage material. The storage medium itself circulates through a heat exchanger (this heat exchanger can also be a solar receiver or a steam generator). This system uses one or two tanks as storage media [182]. Active systems are further divided into direct and indirect systems. In a direct system, the heat transfer fluid serves also as the storage medium, while in an indirect system, a second medium is used for storing the heat.

Passive storage systems are generally dual media storage systems: the HTF passes through the storage only for charging and discharging a solid material. The HTF carries energy received from the energy source to the storage medium during charging and receives energy from the storage when discharging (these systems are also called

regenerators). The main disadvantage of regenerators is that the salt temperature decreases during discharging as the storage material cools down [183]. The second disadvantage is that the heat transfer is low since there is no contact between the HTF and the storage material.

Other designs include two-tank direct, two-tank indirect and single tank thermocline. The single tank thermocline is a form of an active indirect storage system where the hot and the cold fluids are stored in the same tank. A thermocline also known as a metalimnion is a thin but distinct layer in a large body of fluid (an example is the ocean) in which temperature changes more rapidly with depth than it does in the region above or below it. This system provides one possibility of further reducing the cost of a direct two-tank storage system. Here the hot and cold fluids are separated because of the stratification. The zone between the hot and the cold fluids is called the thermocline. A filler material is used to help the thermocline effect. Sandia National Laboratories identified two filler materials as quartzite rock and silica sands [184].

Thermal storage materials are classified into three main categories namely: sensible heat materials, phase change materials and chemical heat storage materials.

Sensible heat storage materials are defined as a group of materials which undergo no change in phase over the temperature range encountered in the storage process. The amount of thermal energy, Q, stored in joules is given by

$$Q = \rho \bullet \hat{c}_p \bullet V\Delta T. \quad (2.8)$$

Where ρ is the density of the storage material in Kg/L, $\hat{c}_p$ is the specific capacity over the temperature range of operation in J/KgK, V is the volume of the storage material used in L, and ΔT is temperature range of the operation in $^{\circ}$C. The following physical properties are considered for a material to be useful as a sensible heat material; thermal conductivity, cost, thermal diffusivity and low melting point. The sensible heat store could either be liquid or solid. Liquids are less common because at higher temperature they evaporate hence pressure containers add to the cost of the system. Examples of sensible heat materials include ceramics, reinforced concrete, cast iron, magnesia fire

bricks and molten salt. In CSP, eutectic mixture of salts is commonly used [185]. An eutectic mixture is a mixture that contains two or more salts whose melting point is lower than the melting point of the individual salts. An example is 60 % $NaNO_3$ and 40 % KNO_3. Sometimes, HTF and the storage material are same.

Phase change materials (PCM) also known as latent heat storage media refer to those materials that store thermal energy isothermally as latent heat of fusion or evaporation as they change phase from solid to liquid or from liquid to gas. Examples of PCM are paraffin (RT110), HITEC salt (KNO_3-$NaNO_3$-$NaNO_3$), Hydroxides, $CaCO_3$, Fe_2CO_3. Organic materials are preferred because their operating temperature could be close to room temperature [186]. An advantage of PCM is that they have higher energy density hence lower cost. Disadvantages of PCM are higher complexity of the system, uncertainty of the life time cycle, poor conductivity.

Chemical Heat Storage is the technology of utilizing the heat of chemical reaction to store thermal energy with the possibility of realizing higher energy process than any other thermal energy storage technologies. Examples of Chemical Heat Storage materials are shown in table 2.1.

Table 2.1: Chemical heat storage materials

Compound	Energy/density	Temperature
Ammonia	67 kJ/mol	400-500 $^{\circ}$C
MgO	3.3 GJ/m^3	250-400 $^{\circ}$C

The research and development in chemical heat storage is focused on heat transformer, chemical heat pump (CHP) in the following aspects: Reaction-Phase Change, Reaction – Reaction and Reaction Separation. Heat transformers are absorption pumps that boost the temperature of industrial waste heat. Currently, the limit of this heat transformation is about 100 $^{\circ}$C. Solutions of lithium bromide (LiBr), Sodium Hydroxide-water (NaOH) are commonly used [187]. Advantages of Chemical heat storage are: energy density higher than those of sensible materials and PCM; they are suitable for long term storage; they have wide and flexible operating temperatures. The PCM and CHS are still under basic

research and are not yet used on any CSP farm. A novel hybrid storage material made of the PCM-Sensible-PCM is developed by DLR-ZSW. The advantages of hybrid thermal storage are increased storage capacity, better use of PCM storage capacities, reduction in the cost of storage and improved storage ratio.

The *power conversion unit* is basically made up of the thermodynamic cycle(s), the turbine and a generator. The content of which varies according to the design of an individual plant. Most heat engines are based on the Carnot cycle which operates with an efficiency which is dependent on the steam temperature. The Carnot cycle is a theoretical thermodynamic cycle produced by Nicolas Clement and Sadi Carnot in 1824 [188]. It is the most efficient cycle of converting a given amount of thermal energy into work or creating a temperature difference by doing a given amount of work [189]. The Carnot efficiency is given by

$$\eta = 1 - \frac{T_C}{T_H} \tag{2.9}$$

Where T_C is the condenser temperature and T_H is the input temperature. In practice, other thermodynamic cycles in use are the Rankine cycle and the Brayton cycle.

The *Rankine cycle* is a thermodynamic cycle that converts heat into work. It is sometimes called the practical Carnot cycle. The difference between the Rankine cycle and the Carnot cycle is that the heat addition into the boiler and heat rejection in a condenser are isobaric in Rankine and isothermal in the theoretical Carnot cycle. There are four processes in a Rankine cycle as follows: the working fluid (water) is pumped from low to high pressure; the high pressure liquid enters a boiler where it is heated at constant pressure by an external heat source to become a saturated vapour; the dry saturated vapour expands through a turbine generating power [190]. This decreases the temperature and pressure and condensation may occur; wet vapour then enters the condenser where it is condensed at a constant temperature to become liquid. Other variations of a basic Rankin cycle for better performance are: Rankine with reheat, Regenerative Rankine Cycle and Organic Rankine Cycle. In Rankine with reheat, the turbines work in series, the first accepts vapour from the boiler at high pressure while the second accepts the

vapour from the first boiler reheats it and then sends it through the second boiler at a lower pressure. Higher efficiency is expected here. In Regenerative Rankine Cycle, the working sub-cooled liquid from the condenser is heated by the steam tapped from the hot portion of the cycle (in-between the turbines) to end up with the saturated liquid [191]. If the steam does not mix with the compressed water from the pump it is called closed feedwater heaters. The Organic Rankine Cycle uses an organic fluid such as n-pentane or toluene in place of water/steam. This allows the use of lower temperature heat source (70-90 °C).

The *Brayton cycle* also known as Joule cycle is a thermodynamic cycle that describes the working of a gas turbine. It is mostly run as an open system, external combustion engine as in jet engines; however it could also be run as a closed-loop cycle if the exhaust gas is recycled [192]. The basic components of a Brayton cycle are a gas condenser, a mixing chamber, an expander and turbine as shown in figure 2.22.

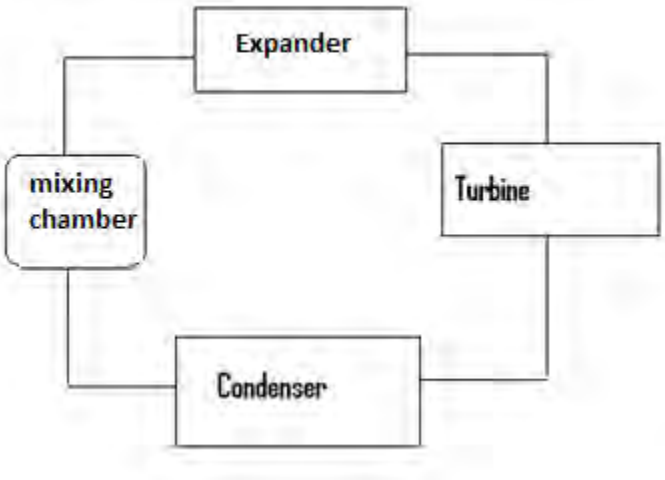

Figure 2.22: Brayton Cycle [192]

A typical Brayton cycle consists of an adiabatic process in which air is drawn for compression, heat is added for combustion (Isobaric process), adiabatic expansion of gasses and an isobaric rejection in atmospheric pressure. The efficiency of the system could be increased by reheating to increase the temperature, increasing the pressure and by regeneration.

Magneto hydrodynamic (MHD) generator is a dynamo that converts thermal/kinetic energy directly into electricity. MHD produces electricity by passing a magnetic field across a hot (about 2000 $^{\circ}$C) fluid such as an inert gas (Helium or Caesium seed) which is usually in plasma forms. MHD is a very reliable device because there are no moving parts [193]. The start-up time is short. It could be used as a topping generator in a combined cycle plant because the output is a flame. Efficiency is over 50 % and it is suitable for a large scale power production [194].

Thermo-electric generators also known as thermo generators are devices which convert heat (temperature differences) directly into electrical energy, using a phenomenon known as the Seaback effect. Classes of materials that have been used for thermo electrics are ordinary alloys of metals (like Bi_2Te_3), complex crystals (semiconductors like GaAs) and multiphase nano-composites such as silicon nanowires. The thermo-electrics have not been used as generators because of their high internal resistance which makes them ideal for temperature measuring instruments. Recently, scientists have considered the use of thermo-electrics as generators because they are less complex, have no moving parts. Currently their efficiency is about 15 % [8, 195]. Micro pelt are manufacturers and vendors of novel thin film thermo-electric components.

Nantenna Electromagnetic Converters (NEC) are solar converters that harvest solar energy based on the wave-particle duality nature of the light. Sunlight had been seen as photons which carry pockets of energies and photovoltaic cells have been optimized to capture various energy levels of photons except that these photovoltaic cells have been characterized by low efficiency because of the very wide band of the solar radiation. The nantennas are nano antennas which are equipped with the nano or molecular diodes. They are often tuned to the frequency of light hence they are also known as the optical antennas. They capture the solar radiation and convert it to DC signal via the diodes. Now these antennas have been shown to absorb heat waves (or the infrared waves) at about 60 % efficiency [196]. It is proposed that the future power plant could reduce cost, durability and increase efficiency by replacing the power conversion unit with the NEC. Within the solar energy spectrum the infrared (heat) waves possess the longest wavelength hence they are most easily harvested with nano-diodes. The NECs currently are targeted for thermal to electricity conversion and if they are successfully developed commercially

they would be ideal for the thermal conversion unit of the CSP. More details of NEC would be discussed in section 2.6.

Hybrid (fossil/solar) Power Plant or the Integrated Solar combined-cycle System (ISCCS) configuration could reduce the cost of solar power by as much as 22 % [197]. Hybridizing with fossil fuel can be done in various ways: using an auxiliary system to heat the HTF during low insolation; introducing the fossil back up in the steam cycle – the evaporation, superheat or reheat zones. Advantages of the ISCCS are: solar to electricity conversion is more efficient; incremental costs for a larger steam turbine are less than the overall unit cost in solar plant only; inefficiencies associated with the daily steam turbine start up and shut down are reduced. There are other designs that attempt to replace the fossil backup turbine with Biomass combustion plants [198].

Triple Cycle Power Plant was proposed by Kribus [199] and it is composed of three conversion steps; a topping MHD cycle, an intermediate Brayton cycle and a bottoming steam Rankine cycle. Using a simple model, the efficiency of the entire plant for a range of temperatures could be optimized and the performance of a two level solar combined cycle and a new triple cycle could be compared [200].

Power Cycle Integration Concepts: The heat generated in the solar absorbers is subsequently used for electric power generation. Different concepts for integration of the solar collector into conventional power cycles are presented and the difference between these concepts is the collector integration within the thermodynamic cycle and the degree of hybridization with fossil power generation (solar share).

Option 1: Solar Live Steam in hybrid Rankine plants or Solar augmented steam cycle for natural gas plants shown figure 2.23 is used in SEGS plants in California [201]. Coupling a solar field with a conventional coal-fired power plant can lead to lots of savings in CO_2 production whenever solar steam is available.

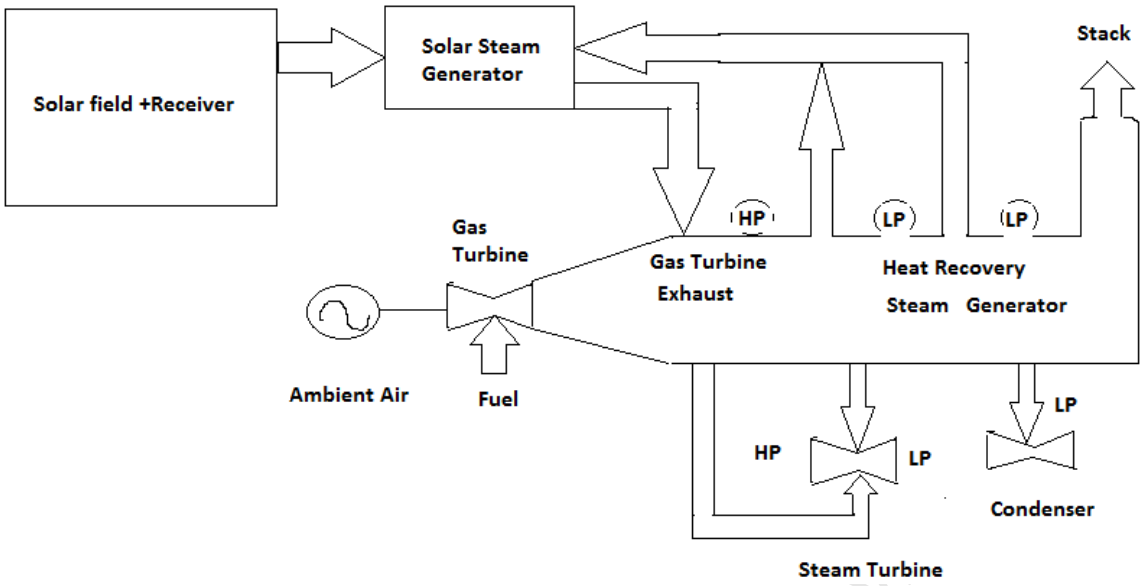

Figure 2.23: Solar augmented steam cycle for natural gas plants [202]

Option 2: 'Solar-only" Rankine plant has the same underlying power-block concept as the hybrid plant but without the fossil-fuel steam generator. The disadvantage of this is the large cost of storage.

Option 3: Solar gas turbine combined cycle option has the possibility of high efficiencies in the medium term cost saving in field investment.

Option 4: Combined heat and power solar plant is similar to the combined heat and power, however, in this option a solar thermal electricity application such as sea water desalination or air-conditioner co-firing is possible. Due to double use solar heat and power efficiency of 80 % is possible. Any type of thermal plant could be designed to capture the waste heat.

Option 5: Integrated solar combined cycles (ISCC) are based on the high temperature gas turbine and a bottoming steam turbine. The size of the steam turbine in ISCCS is larger than it would be in a conventional combined cycle. Advantages of ISCCs are higher solar shares in solar feed water preheating, no solar energy losses due to daily plant start-up and shut- down and the incremental costs for a larger steam turbine are less than the overall unit cost of a solar-only plant.

Option 6: Solar feed water preheating; the solar thermal heat is used for preheating feed-water in large scale conventional Rankine plants, substituting steam that would otherwise be bled from the turbine. Additional electricity can be generated, or fossil fuel be saved depending on the operation mode. This concept is well suited for market introduction of new collector types since it reduces the risk of increase the investment costs that would otherwise be needed for a new steam cycle [202].

Option 7: Solar process heat application such as space cooling of buildings and refrigeration are ways to dynamically cut the initial cost of investment in CSP [203].

2.6 Nantenna Electromagnetic Converters (NEC)

Nantenna or nano-antenna is a nano-scopic rectifying antenna made of Multi-walled carbon nanotubes (MWCNT). It is an electromagnetic collector designed to absorb specific wavelengths which are proportional to the size of the antenna. The nantennas are not yet commercially available but Idaho National laboratories in USA have designed a nantenna to absorb wavelengths in the range of 3-15 micrometers which correspond to photon energies of 0.08-0.4 eV [204].

The current photovoltaic technologies rely on the quantum nature of light and semiconductors which are fundamentally limited by the bandgap energies. Nantenna or the nano scale antenna was first suggested by Professor Robert Bailey of the University of Florida and Fletcher, J.C. of NASA in 1972 [205]. The study of NEC revolves around the wave nature of light. The patent describes the concept as a device for converting electromagnetic wave energy into electric power. NEC consists of a number of relatively close-spaced electromagnetic wave absorber elements with tapered portions responsive to wideband electromagnetic wave radiation. They suggested that broadband rectifying antennas could be used for solar to D.C. electricity conversion. The efficiencies of these nantennas would not be limited by band gaps as in the traditional semiconductors solar panels.

2.6.1 Wave-Particle Duality Nature of Light

Thomas Young first investigated the wave nature of light in 1803 using the double-slit interferometer [206]. Sacha Kocsis performed a modernized version of the same experiment using the laser beams [207]. The sun is mainly composed of hydrogen and helium. Thus, within the sun, a thermonuclear fusion converts the hydrogen and helium releasing huge amounts of energy. The energy created by the fusion reaction is converted to thermal radiation and transmitted in the form of electromagnetic waves in the free space. Solar radiation occurs over a wide range of wavelengths, nevertheless the main range of this radiation includes ultraviolet (UV; 0.001-0.4 μm), visible light (0.4-0.7 μm), and infrared radiation (IR; 0.7-100 μm). Part of the solar radiation is scattered and reflected by clouds and a part is absorbed by the atmosphere and by the surface of the earth. By absorbing the incoming solar radiation, the earth warms up and its temperature rises. In general, all heated objects emit electromagnetic radiation. The amount of emitted radiation can be calculated through the Stephan-Boltzmann`s law [208]. Stephan-Boltzmann`s law is applicable to perfect black bodies, i.e. an object that absorbs and emits radiation uniformly with 100 % efficiency. Moreover, the total (overall wavelengths) energy radiated from a blackbody is proportional to the fourth power of its absolute temperature. The ratio between the reflected and the incoming energies is named as Planetary Albedo [209]. The average albedo of the earth is about 0.3. This is the fraction of the incoming radiation reflected back to space while 0.7 is absorbed. Since the incoming solar radiation is an electromagnetic wave radiation at terahertz wavelengths, it can be collected by using optical antennas [210].

2.6.2 Properties of Light

The properties of light are: intensity, propagation direction, frequency or wavelength spectrum, polarization and speed in a vacuum (which is 300,000 km/s). Light which is emitted and absorbed in tiny packets called photons exhibits properties of both waves and particles and the study of light is known as optics. Light could in fact be slowed down and accelerated to normal speed [211].

2.6.3 Theory of Nantennas

The size of the antenna is dependent on the wavelength of light it is meant to capture. The incident electromagnetic flux produces a standing-wave electrical current in the finite antenna array structure and absorption occurs at the resonant frequency. The induced cyclic plasma movement of free electrons flows along the antenna generating alternating current at the resonant frequency. The angular reception characteristic of the nantennas results in a wider angle of incidence exposure to thermal radiation hence the need for a mechanical tracker is reduced. Efficiency could also be increased by increasing the radial field. The virtual large surface area antenna focuses the electromagnetic energy onto the nano-sized energy conversion material fabricated at the antenna feed-point. Theoretical efficiency is improved by the enhanced radiation capture area. The nantenna consists of the following: the ground plane (which reflects the light back to the antenna); the optical resonance cavity (absorbs the electromagnetic wave); the optical resonance cavity (which bends and concentrates the light back towards the antenna via ground plane) [212][213]. An example is the multiwall carbon nanotube (MWCNT) [214]. Factors which were critical to the successful implementation of the Nantenna Electromagnetic Collectors: Frequency-dependent modelling of antenna elements; Selection of materials with proper THz properties; novel manufacturing methods that enable economical large-scale manufacturing.

2.6.4 Energy Conversion Methods

To capture infrared wave at THz region the normal Schottky diodes would not work without enormous losses. One promising method requires embedding a rectifier diode such as the metal-insulator-insulator-metal (MIIM) tunnelling diode element into the antenna structure. This device consists of a thin barrier layer and two dielectric layers (oxide) sandwiched between two metal electrodes with different work functions. The output of the rectifiers can be DC-coupled together allowing arrays of antennas to be networked together to further increase the output power capacity [215].

The metal loops give inductance to the NEC as thermally-excited radiation induces the current. The gaps between the metallic loops and the gap within the loop compose the capacitors with a dielectric fill. A resistance is present because the antenna is composed of lossy metallic elements on a dielectric substrate. The resulting RLC circuit shown in figure 2.24 has resonance 'tuned' filter behaviour.

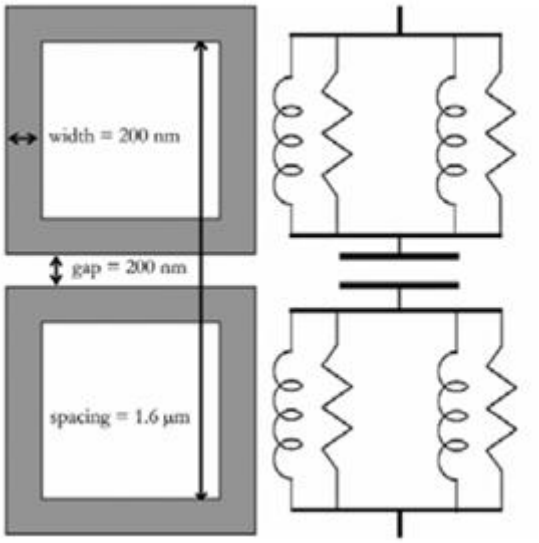

Figure 2.24: Square FSS elements and the RLC circuit analogy [216]

2.6.5 Proof of Concept

A 1.0 cm^2 array of loop antennas fabricated on a silicon substrate was tested with infrared wave (3 to 15 microns). The peak emissivity was found to be centred at 6.5 microns and reaches 1micron. An emissivity of 1 micron means the antenna absorbs all the photons of a specific wavelength that is incident on it. Spectral surface characteristics of IR FSS prototype were studied using spectral radiometer. It was elevated to 200 °C and the maximum contrast is over 90 % between emission of near 4nm and emission resonance [216].

2.6.6 Applications

The Nantenna electromagnetic collectors could be integrated into all consumer electronics and green energy sustainable buildings to charge the batteries as well as cooling devices. Double-sided panels could be used to absorb the broad spectrum during the day while the other side could absorb radiated heat from the earth`s surface and other industrial heat waves. The efficiencies of the CSP plant could be enhanced by integrating the NEC technology at the central receiver block [217].

2.6.7 Advantages and Disadvantages of NEC over Photovoltaic Panels

The Nantenna Electromagnetic Collectors can be configured as a frequency selective surface to efficiently absorb the entire solar spectrum. Rather than generating single electron–hole pair as in the PV, the incoming electromagnetic field from the sun induces a time-changing current in the antenna. Efficient collection of the incident radiation is dependent upon proper design of the antenna resonance and impedance matching of the antenna. The discovery of nanotechnology has made this a reality. The biggest advantages of an antenna are the high theoretical efficiency which is over 85 % compared with the photovoltaics of about 30 %. This efficiency is not limited by the Carnot efficiency. Another advantage is that the nantennas could be designed to absorb any frequency of light. An example is the Archimedean spiral microwave RF antennas, and frequency independent within their bandwidth [218].

The main disadvantage is that the frequency within which they operate makes the typical Schottky diodes impractical although metal-insulator-metal (MIM) diodes show more promise. The other disadvantage is that the current electron beam lithography that is currently used for production is costly. Another promising method is the roll-to-roll and photolithographic technique. The new artificial molecules have been observed, by a team of researchers at Birmingham University UK, to switch states in the terahertz range [219].

Chapter 3
Overview of Software Packages

3.1 Introduction

Two software applications were used in this work. They are Matlab, a product of Mathworks [220] and Systems Advisor Model (SAM) which is a product of the National Renewable Energy Laboratories [221]. Matlab, which is the parent software application, has toolboxes like Simulink, SimPowerSystems and Simscape. Matlab is used to model the photovoltaic module. SAM is used for the overall system model which includes the performance and economic aspects of the concentrated solar power.

3.2 Overview of Matlab

The source of the information discussed in this section is Matlab library. Matlab, a product of Mathworks, is a high-level language and interactive environment for algorithm development, data analysis, visualization, and numerical computation that enables you to perform computationally intensive tasks faster than with traditional programming languages, such as C, C++, and FORTRAN. Matlab can be used in a wide range of applications, including signal and image processing, communications and control design, test and measurement, financial modelling and analysis, and computational biology. For millions of engineers and scientists in industry and academia, Matlab is the language of technical computing. Add-on toolboxes (collections of special-purpose Matlab functions) extend the Matlab environment to solve particular classes of problems in these application areas. Matlab provides a number of features for documenting and sharing resources. Matlab codes can be integrated with other languages and applications, and distributed as standalone applications [220].

The Matlab language supports the vector and matrix operations that are fundamental to engineering and scientific problems. It enables fast development and execution. With the Matlab language, you can program and develop algorithms faster than with traditional

languages because you do not need to perform low-level administrative tasks, such as declaring variables, specifying data types, and allocating memory. In many cases, Matlab eliminates the need for 'for' loops. As a result, one line of Matlab code can often replace several lines of C or C++ code. At the same time, Matlab provides all the features of a traditional programming language, including arithmetic operators, control flow, data structures, data types, object-oriented programming (OOP), and debugging features. Matlab lets you execute commands or groups of commands one at a time, without compiling and linking, enabling you to quickly iterate to the optimal solution. For fast execution of heavy matrix and vector computations, Matlab uses processor-optimized libraries. For general-purpose scalar computation, Matlab generates machine code instructions using its JIT (just-in-time) compilation technology. This technology is available in most platforms. It provides execution speeds that rival those of traditional programming languages.

Matlab includes developmental tools that help you implement your algorithm efficiently. These include a Matlab editor for standard editing and debugging features such as setting breakpoint and single stepping; code analyser, checks your code for problems and recommends modification to maximize performance and maintainability; Directory reports scan all the files in a directory and report on code efficiency, file differences, file dependencies and code coverage. Graphical user interface development environment (GUIDE) could be used to layout, design and edit user interfaces. GUIDE lets you include list boxes, pull-down menus, push buttons, radio buttons, and sliders, as well as Matlab plot and Microsoft ActiveX control [220].

Matlab supports the entire data analysis process, from acquiring data from external devices and data bases, through pre-processing, visualization and numerical analysis, to producing presentation-quality output. The interactive tools and command-line functions for data analysis operations include; interpolating and decimating, extracting sections of data, scaling, and averaging, thresholding and smoothing, correlation, Fourier analysis and filtering, 1-D peak, valley, and zero finding, basic statistics, curve fitting and matrix analysis. Matlab is an efficient platform for accessing data from files, other applications, databases, and external devices. It can read data from popular file formats such as Excel, ASCII text or binary files; image, sound and video files. It can acquire data from hardware devices such as computer serial port or sound card. It can stream live, measured

data directly into Matlab for analysis and visualization using a Data Acquisition toolbox. Instrument control toolbox enables communication with GBIB and VXI hardware.

3.2.1 Visualizing Data

All the graphic features that are required to visualize engineering and scientific data are available in Matlab. These data are 2-D and 3-D plotting functions, 3-D volume visualization functions, tools for interactively creating plots and the ability to export results to all popular graphic formats. It can customize plots by adding multiple axes; changing line colours and markers; adding annotation, LaTEX equations and legends; and drawing shapes.

3.2.2 Performing Numeric Computation

Matlab contains mathematical, statistical, and engineering functions to support all common engineering and science operations. These functions developed by experts in mathematics are the foundation of the Matlab language. The core math functions use the LAPACK and BLAS linear algebra subroutine libraries and the FFTW Discrete Fourier Transform library. Because these processor-dependent libraries are optimized to the different platforms that Matlab supports, they execute faster than the equivalent C or C++ code. Matlab provides the following types of functions for performing mathematical operations and analysing data: matrix manipulation and linear algebra, polynomials and interpolation, Fourier analysis and filtering, data analysis and statistics, optimization and numerical integration, ordinary differential equations (ODEs), partial differential equations (PDEs), sparse matrix operations. It can perform arithmetic on a wide range of data types, including doubles, singles and integers. Add-on toolboxes provide specialized mathematical computing functions for areas including signal processing, optimization, statistics, symbolic math, partial differential equations solving and curve fitting.

3.2.3 Publishing Results and Deploying Applications

Matlab provides a number of features for documenting and sharing your work. Matlab codes could be integrated with other language applications, codes and algorithms could be deployed as standalone programs or software modules. The results could be exported as plots or complete reports in all popular formats. The editor can also publish Matlab codes in other formats. To create more complex reports like simulation results and multiple parameter tests, Matlab Report Generator could be used [220].

3.2.4 Matlab Toolboxes

The complete list of all Matlab toolboxes installed in any copy of Matlab is displayed using the Matlab command "ver". The toolbox used in this work is Simulink, and Simscape and SimPowerSystem found under Simulink have been used.

3.2.5 Simulink

Simulink is an environment for multi-domain simulation and Model-based Design for dynamic and embedded systems. It is a commercial tool for modelling, simulating and analysing multi-domain dynamic systems. Its primary interface is a graphical block diagramming tool and a customizable set of block libraries. It offers tight integration with the rest of the Matlab environment and can either drive Matlab or be scripted from it. At the Matlab command prompt Simulink could be loaded by typing Simulink.

Key Features of Simulink

- Extensive and expandable libraries of predefined blocks.
- Interactive graphical editor for assembling and managing intuitive block diagrams.
- Ability to manage complex designs by segmenting models into hierarchies of design components.
- Model Explorer to navigate, create, configure and search all signals, parameters, properties and generate code associated with your model.

- Application programming interfaces (API) that let you connect with other simulation programs and incorporate hand-written code.
- Matlab Function blocks for bringing Matlab algorithms into Simulink and embedded system implementations.
- Simulation modes (Normal, Accelerator, and Rapid accelerator) for running simulations interpretively or at compiled C-code speeds using fixed- or variable-step solvers.
- Graphical debugger and profiler to examine the simulation results and then diagnose performance and unexpected behaviour in designs.
- Full access to Matlab for analysing and visualizing results, customizing the modelling environment and defining signal, parameter and test data.
- Model analysis and diagnostics tools to ensure model consistency and identify modelling errors.

The Simulink environment is made of sub-toolboxes such as Simscape and SimPowerSystems [220].

3.3 Overview of Systems Advisory Model (SAM)

The issues discussed in this chapter are obtained from NREL SAM reference book [221].

3.3.1 Software Development History and Users

SAM, originally called the 'Solar Advisory Model' was developed by the National Renewable Energy Laboratory in collaboration with Sandia National Laboratories in 2005. It was first used internally by the U.S. Department of Energy`s Solar Energy Technologies Program for systems-based analysis of solar technology improvement opportunities within the program. The first public version was released in August 2007 as version 1, making it possible for solar energy professionals to analyse photovoltaic systems and concentrated solar power parabolic trough systems in the same modelling platform using consistent financial assumptions. Since 2007, two new versions have been

released each year. Adding new technologies and financing options. In 2010, the name changed to 'Systems Advisor Model' to reflect the addition of non-solar technologies.
The DOE, NREL and Sandia continue to use the model for program planning and grant programs. Since the first public release, over 35,000 people representing manufacturers, project developers, academic researchers and policy makers have downloaded the software. Manufacturers use the model to evaluate the impact of efficiency improvements or cost reductions in their products on the cost of energy from installed systems. Project developers use SAM to evaluate different system configurations to maximize earnings from electricity sale. Policy makers and designers use the model to experiment with different incentive structures.

3.3.2 What is SAM?

- SAM is a free application for personal computer or Macintosh prepared by a collaboration between the National Renewable Energy Laboratory (NREL) and Sandia National Laboratory (SNL) in Golden Colorado and in partnership with the U.S. Department of Energy in 2006 [221].
- It is an open source performance and economic model designed to facilitate decision making for people involved in the renewable energy industry, ranging from project managers and engineers to incentive program designers, technology developers and researchers.
- SAM makes performance predictions for grid-connected solar PV, small wind and geothermal power systems and economic estimates of distributed energy and central generation projects.
- SAM is a highly intuitive interface. Users can explore in real time how variations in technology parameters, finance options and performance affect project outcomes across residential buildings and utility-scale markets.
- SAM`s individual models for photovoltaic modules and inverters, CSP solar fields and thermal storage were validated against measured data and the overall model was validated against actual performance data
- It helps to analyse efficiency and cost.

- SAM is used to design an energy production facility.
- It produces a year`s worth of hour-by-hour data, e.g. incident radiation, kWh or $/kWh.

3.3.3 How SAM Works

SAM calculates a system's total electricity production in kilowatt-hours for the first year based on hourly weather data for a particular location, and physical specifications of the power system components. It then calculates the total production for subsequent years based on an annual degradation factor, and annual cash flows based on financial and economic inputs to determine the levelized cost of energy and other economic metrics. Figure 3.1shows the basic architecture of SAM.

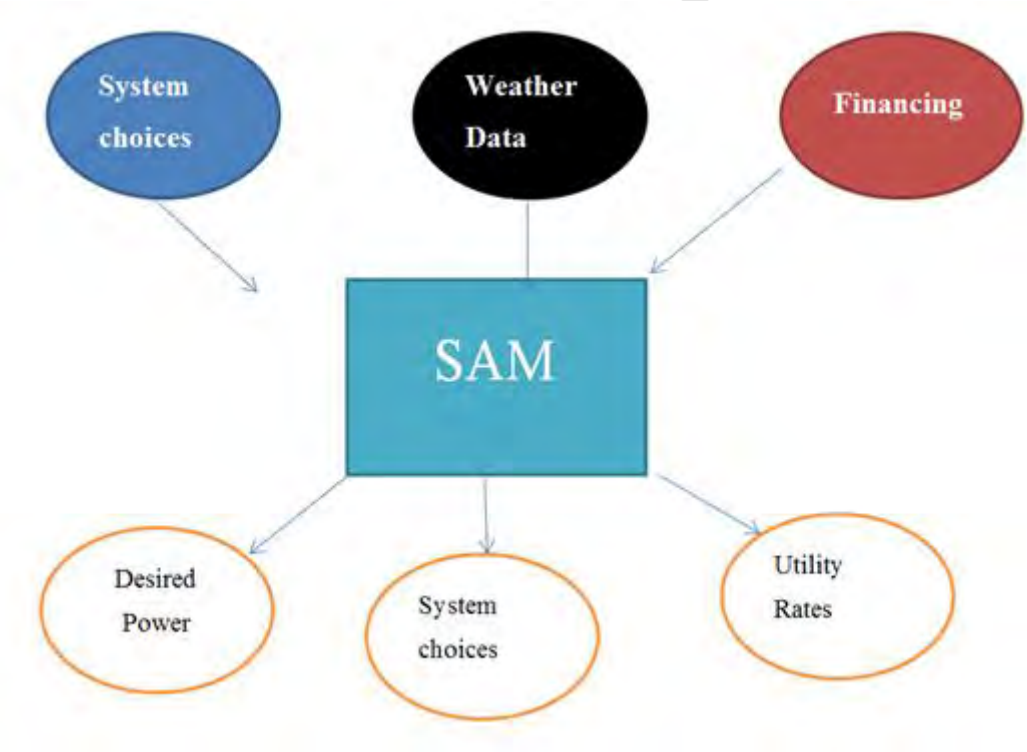

Figure 3.1: How SAM works [221]

3.3.4 Inputs and Outputs

SAM requires inputs describing the weather at a system`s location, information about the project`s cost and financial assumptions, and specifications of the system`s performance characteristics. SAM input variables are populated with sample default values.

Weather data: SAM`s simulation engine uses data from hourly weather files to model the solar resource at a given location. The weather file supplies radiation data for energy calculations, and wind speed, temperature, snow cover and other data to model the effects of temperature and ground reflectance on the system`s performance. Weather data is supplied in TMY2, TMY3, or EPW (Energyplus weather data). TMY2 are comma-delimited text file format (.csv) which represents average weather data over a range of years from 1961-1990, available for 239 locations. TMY3 are non-delimited text file format (.tm2) which represents average weather data over a range of years from 1991-2005 and it's available for over 1020 U.S. locations. EPW is comma-delimited text file format (.epw) is used for weather data for locations around the world.

Financial and economic inputs: SAM`s cash flow calculations depend on a set of inputs variables describing the project`s finances such as the analysis period equivalent to the system lifetime, discount rate , inflation rate, loan amount and loan rate. SAM provides different financing options that use different sets of input variables.

Incentives: SAM models two types of incentives, tax credits and incentive payments. Tax credits can be provided by a state or federal government, utility, or other entity. An investment-based incentive or tax credit is a one-time payment for the project made in year one of the project cash flow that is either a fixed amount, percentage of total installed costs, or a function of the system size. A production-based incentive or tax credit is an annual payment based on the amount of energy produced by the system in each year. Incentive payments may or may not be taxable by the Federal or state government.

System performance: SAM stimulates the hourly performance of the power system using algorithms developed at the National Renewable Energy laboratory, Sandia National laboratory, and the University of Wiscousin to convert hourly weather date into hourly AC electrical output estimates. SAM adds the 8760 hourly values to calculate the system`s total annual output.

Costs: SAM calculates the cash flow and the resulting economic metrics based on two categories of costs. Capital accounts for the cost of installing modules, inverters, balance-of-system components. Operation and maintenance costs accounts for recurring costs for maintenance, repair and replacement of equipment. For residential and commercial projects, SAM allows operation and maintenance costs to be assigned to specific years, which makes it possible to analyse projects with periodic inverter replacements or other periodic costs.

3.3.5 Outputs

- ✓ Levelized cost of energy
- ✓ Power purchase price, rate of return and other financial targets for utility-scale projects,
- ✓ Payback period and net present value of residential and commercial projects,
- ✓ Hourly, monthly and annual average predictions of the system performance, including net electric output and component efficiencies
- ✓ Annual cash flow table with cost details
- ✓ Customizable graphs,
- ✓ Capacity factor,
- ✓ Efficiency.

3.3.6 Typical Uses of SAM

1) Installers use SAM to determine the effects of orientation and tilt on the rooftop solar array in their city.
2) Developers use SAM`s hour-by-hour weather files to determine if a concentrating solar power project makes a financial sense for a specific location and electricity rate structure.
3) Developers use SAM analyses to show bankers that their project is comparable to projects that have proven to be sound investments.

4) Manufacturers show SAM-generated graphs to potential lenders to demonstrate their understanding of the main cost drivers of their renewable energy technology.
5) Research and development companies use SAM to analyse the performance benefits versus the financial costs of improving various system components.
6) Project managers at the US department of Energy use SAM to evaluate the effect of the solar energy research investment on the cost of the technologies and to analyse applications for loan guarantees and to carry out feasibility studies,
7) Utilities, graduate students, and federal energy managers use SAM for feasibility studies.
8) Software developers use SAM`s application programming interface to integrate parts of SAM with their own models.
9) Engineering due-diligence firms and utilities use SAM to check assumptions having to do with solar field conditions as well as the projected hourly and annual energy generation of a proposed project.

3.3.7 Starting a Project with SAM

SAM is designed to handle analysis of the following technologies: photovoltaics, concentrated solar power, solar water heating, wind power, biomass and geothermal plants as shown in the figure 3.2.

Figure 3.2: Select a technology page [221]

Photovoltaics

This is the direct conversion of sunlight to electricity using solar cells and it is subdivided into three technologies shown in figure 3.3.

- Flat plate PV
- High-X Concentrating PV
- PVWatts System Model

Figure 3.3; Types of Photovoltaics Technology [221]

Concentrating Solar Power

CSP systems use mirrors or lenses to focus sunlight to generate the heat source for conventional type of power plant. It is also subdivided into parabolic trough (physical and empirical model types), molten salt power tower, direct stream power tower, linear Fresnel, dish Stirling and generic solar system as shown in figure 3.4.

Financial Model

SAM`s financial model calculates financial metrics for various kinds of power projects based on a project`s cash flows over an analysis period that you specify.

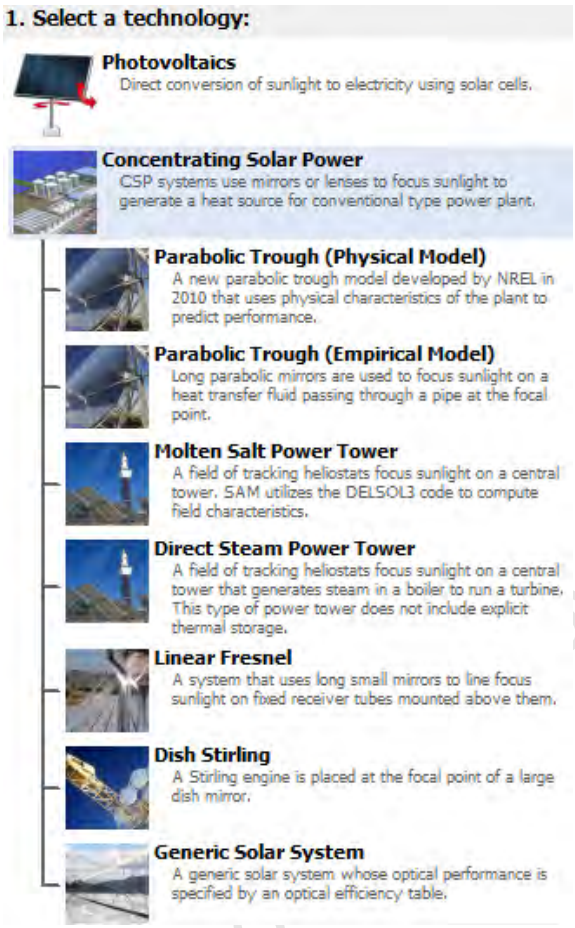

Figure 3.4: Concentrated Solar Power Technologies [221]

The financial model uses the system`s electrical output calculated by the performance model to calculate the series of annual cash flows.

SAM includes financial model for the following kinds of projects:

- Residential rooftop (retail electricity rates)
- Commercial rooftop (retail rates or power purchase agreement)
- Utility-scale (power purchase agreement):
    - Single owner
    - Leveraged partnership flip
    - All equity partnership flip
    - Sale leaseback

Residential and Commercial Projects

Residential and commercial projects are financed through either a loan or cash payment, and recover investment costs by selling electricity through either a net metering or time-of-use pricing agreement. For these projects, SAM reports the following financial metrics:

- Levelized cost of energy
- Revenue with and without renewable energy system
- Payback Period

Power Purchase Agreement (PPA) Projects

Utility and commercial PPA projects are assumed to sell electricity through a power purchase agreement at a fixed price with optional annual escalation and time-of-delivery factors. For these projects, SAM calculates:

- ✓ Levelized cost of energy
- ✓ PPA price (electricity sale price)
- ✓ Internal rate of return
- ✓ Net present value
- ✓ Debt fraction or debt service coverage

SAM can either calculate the internal rate of return based on a power price you specify or calculate the power price based on the rate of return you specify.

Levelized Cost of Energy and Cash Flow

SAM calculates the Levelized cost of energy (LCOE) after-tax cash flows for projects for using retail electricity rates, and from the revenue cash flow for projects selling electricity under a power purchase agreement. The project annual cash flows include:

- Revenues from electricity sales and incentive payments
- Installation costs
- Operating, maintenance, and replacement costs
- Loan principal and interest payments
- Tax benefits and liabilities (accounting for any tax credits for which the project is eligible)
- Incentive payments

- Project and partner`s internal rate of return requirements (for PPA projects)

Incentives

The financial model can account for a wide range of incentive payments and tax credits:

- Investment-based incentives (IBI)
- Capacity-based incentives (CBI)
- Production-based incentives (PBI)
- Investment tax credits (ITC)
- Production tax credits (PTC)
- Depreciation (MACRS, Straight-line, custom)

The following financing options have been modelled by SAM across all the technologies in SAM as shown in figure 3.5.

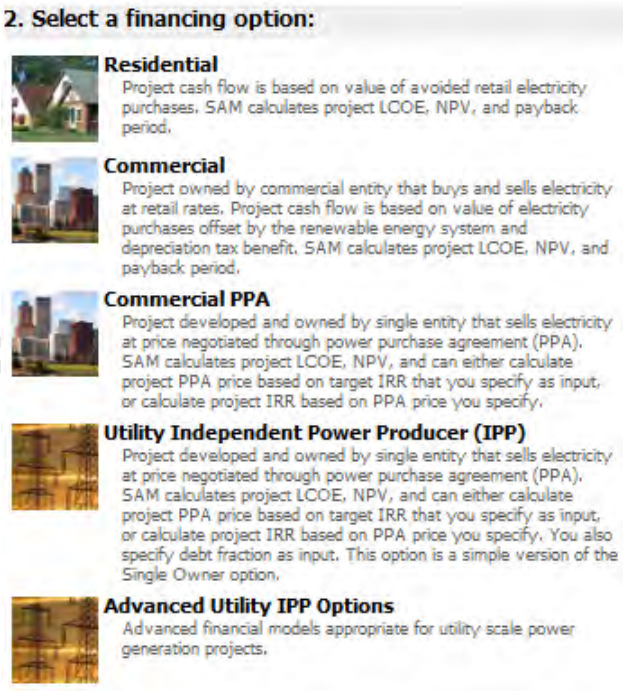

Figure 3.5: Financing Options page [221]

3.3.8 Functions of SAM

SAM calculates the energy system`s hourly energy output over a single year, and calculates the cost of energy for a renewable energy project over the life of the project.

- ✓ The performance model makes energy output calculations
- ✓ The financial model makes cash flow calculations.
- ✓ And the default values help us to get started.

3.3.9 Creating a SAM file

The first step in creating a SAM file is to choose a technology and financing option for your project. SAM automatically populates input variables with a set of default values for the type of project. It is your responsibility as an analyst to review and modify the input data as appropriate for each analysis. Next, you provide information about a project`s location, the type of equipment in the system, the cost of installing and operating the system, and the financial and incentive assumptions. It includes several databases of performance data and coefficients for system components such as photovoltaic modules and inverters, parabolic trough receivers and collectors, or biopower combustion systems. For those components, you simply choose an option from a list. SAM can automatically download data from an online database of retail electricity rates and structures for US utilities.

For the remaining input variables, you either use the default value or change its value. Some examples of input variables are:

- Installation costs including equipment purchases, labour, engineering and other project costs, and land costs and operation and maintenance cost.
- Number of modules and inverters, tracking type, derating factors for photovoltaic systems.
- Collector and receiver type, solar multiple, storage capacity.

3.3.10 Run Simulations

After reviewing and modifying inputs on the input pages, click the run all simulation button to run simulations shown in figure 3.6

Figure 3.6: Run all Simulations [221]

SAM runs simulations based on the values of input variables that appear on the input pages and reports those as 'base case' results.

In addition to the base case, SAM runs simulations for any additional simulations you may have set up on the configure simulations pages, such as parametric or sensitivity analyses as shown in figure 3.7. You can also run simulations from the case menu.

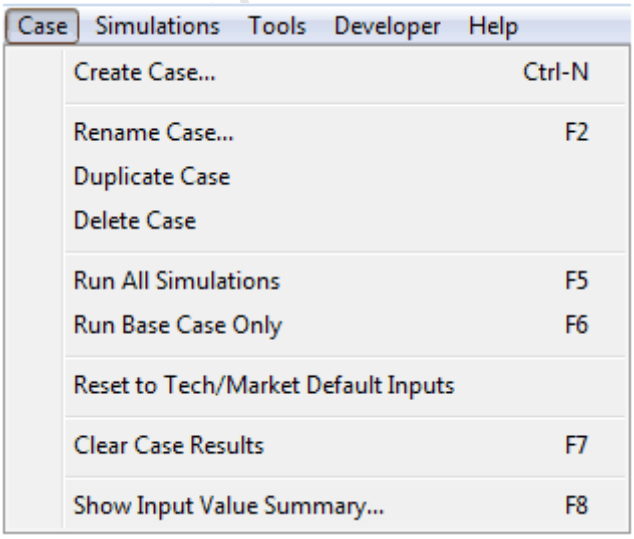

Figure 3.7: Selecting cases [221]

3.3.11 Run all Simulations

Runs all of the simulations configured in the current case. Equivalent to clicking the run button, this option does not save hourly results. Run base case only: runs a single simulation based on the input values shown on the input pages, ignoring any parametric, sensitivity, optimization or other configuration requiring multiple simulation runs, and does not save hourly results.

3.3.12 Result Page

The result page displays data from both the performance model and financial model. You export data from any graph or table displayed on the result page to excel or text files.
Or click switch for results to show the result page without running simulations as shown in figure 3.8.

Figure 3.8: To switch to graphs and results viewer [221]

3.3.13 Performance Model Results

When you run simulations based on inputs you specify on the system pages in SAM, the performance model creates a file of hourly data called the simulation results files. There several options in SAM for viewing data from this file

- The Metrics display key metrics that summarize the performance model results, such as total annual electrical output, capacity factor, etc.
- Graphs, and charts displays monthly electrical output and an annual energy flow graph and allows you to create your own graphs.

- The data tables allow you to build custom tables of hourly, monthly and annual results on the result page.
- The Base Case Time Series displays time series and statistical graphs of hourly data.

3.3.14 Financial Model Results

SAM`s financial model uses the sum of the performance model`s 8760 hourly output values in kWh as an input representing the system`s total annual electrical output in kWh. The financial model calculates the project`s cash flow based on the inputs you specify on the Costs and financing pages. SAM displays financial model results in the following places:

- The Metrics table displays key metrics such as the LCOE, PPA, IRR and payback period.
- The Base Case Cash Flow table shows details of the projects` cash flow.
- The Data Tables allow you to build custom tables of cost flow data along with metrics.

3.3.15 Export Data and Graphs

SAM provides a several options for exporting images of graphs and results data to other applications for further analysis or inclusion in reports and other documents.
Result Page View Graph and Charts: when the results page is in the view graph and charts mode, you can export the data in the graph using one of the following methods: Click Copy Graph Data to copy data from the graph to your computer`s clipboard. You can then paste the data into a spreadsheet or other programs as shown in figure 3.9.

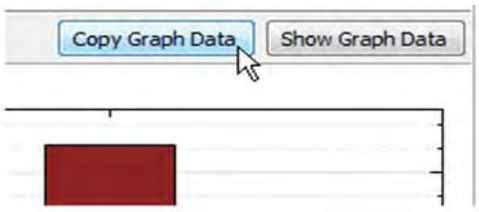

Figure 3.9: Copying the graph data [221]

Right click the graph to copy either data from the graph or an image of the graph to the clipboard, or export it to a file as shown in figure 3.10.

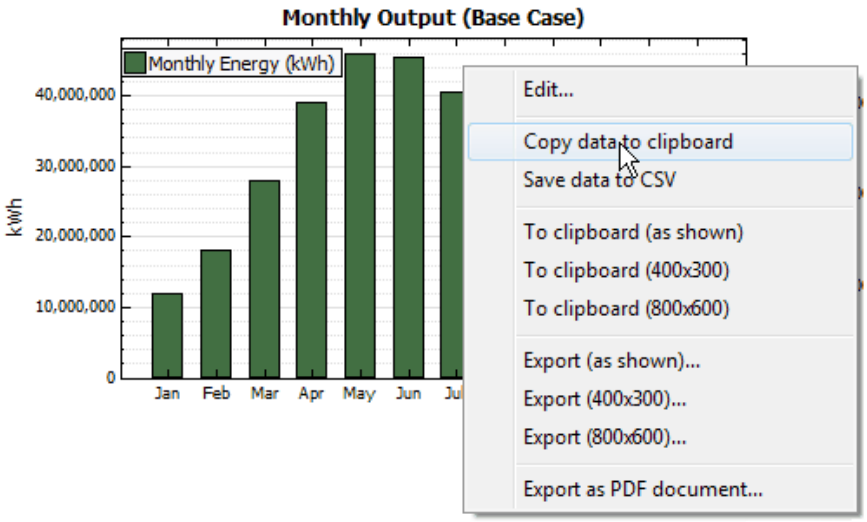

Figure 3.10: Copying to the clipboard [221]

On the results menu, click graph data to view a list of options for exporting graph data as shown in figure 3.11.

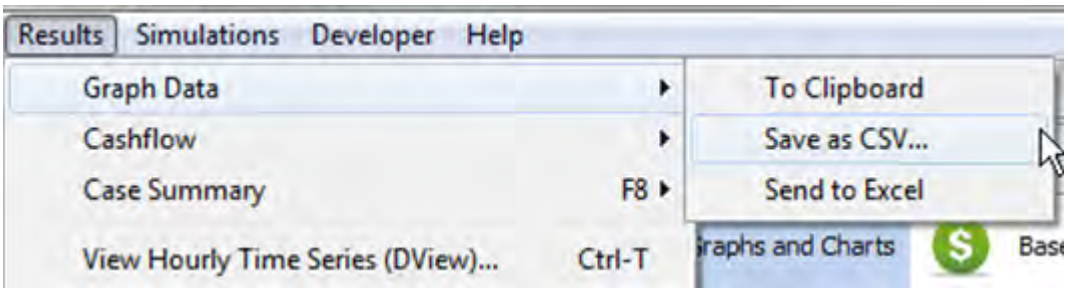

Figure 3.11: Saving a file [221]

3.3.16 Manage Cases

A case is a complete set of input data and results. A project file contains at least one case. SAM uses tabs to display each case in the project, analogous to the way Excel displays worksheets in a workbook. SAM indicates the active case name in bold type as shown in figure 3.12.

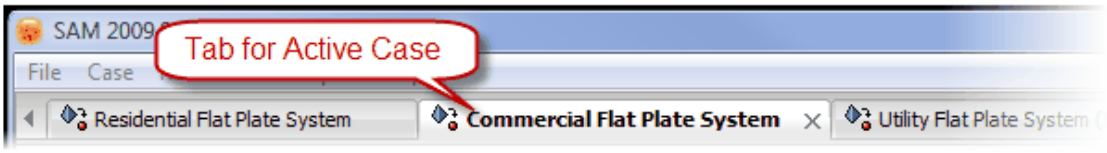

Figure 3.12: Managing cases [221]

By creating more than one case in a file, one can easily compare the assumptions and results of different analysis scenarios. For example, you could use cases to compare the cost and performance of a residential photovoltaic system in several locations by defining a separate case for each location, or you could compare utility-scale photovoltaic and concentrated solar power systems.

3.3.17 Creating and Deleting Case

To add, remove and rename cases, use the four commands on the case menu shown in figure 3.13.

*Create Case***:** Adds a new case to the project file. SAM displays the technology and the market window for you to choose options for the case.

Rename Case: Change the label identifying the case that appears on the case tab.

Duplicate Case: Creates a copy of the active case, with a duplicate set of input parameters and results.

Delete Case: Deletes the active case. You can also delete a case by clicking the 'x' on the case`s tab.

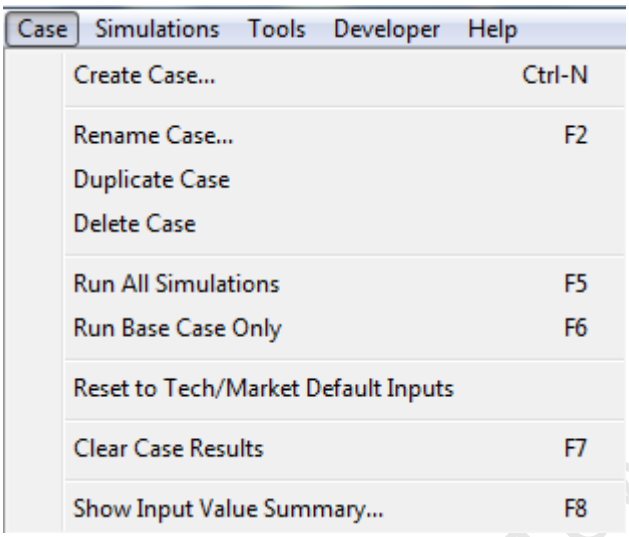

Figure 3.13: Creating and Deleting cases [221]

Chapter 4
Theory Development of Solar Energy Systems

4.1 Theory of Solar Cells

The simplest equivalent circuit of a solar cell is a current source in parallel with a diode is shown in figure 4.1. The output of the current source is directly proportional to the light falling on the cell (photocurrent, I_{ph}). During darkness, the solar cell is not an active device; it works as a p-n junction of a diode [222]. It produces neither a current nor a voltage. However, if it is connected to an external supply (large voltage) it generates a current I_0, called diode current or dark current. The diode determines the I-V characteristics of the cell. The series resistance (R_S) and the shunt resistance (R_{SH}) are resistance of the external circuit of the PV.

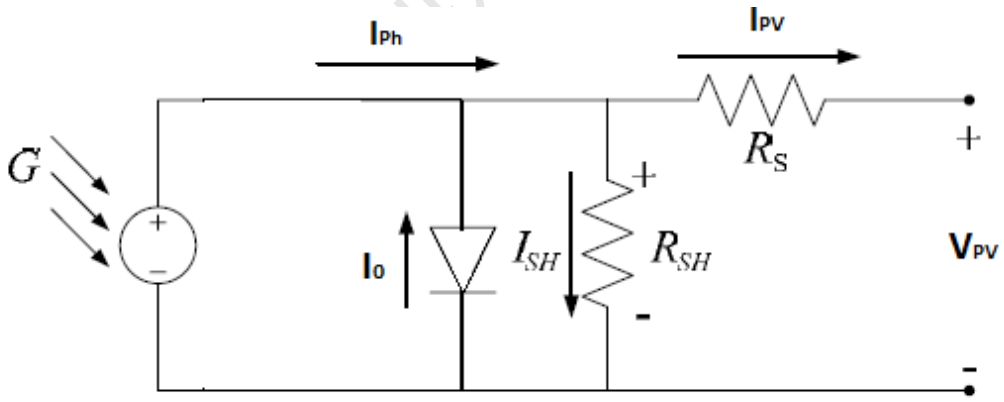

Figure 4.1: Equivalent Circuit of a PV [222]

The theory of solar cells explains the physical processes by which light is converted into electrical current when striking a suitable semiconductor device. The theoretical studies are of practical use because they predict the fundamental limits of solar cell performance,

and give guidance on the phenomena that contribute to losses and solar cell efficiency. Simple explanations are:

1. Photons in sunlight hit the solar panel and are absorbed by semiconducting materials, such as silicon.
2. Electrons (negatively charged) are knocked loose from their atoms, allowing them to flow through the material to produce electricity. Due to the special composition of solar cells, the electrons are only allowed to move in a single direction.
3. An array of solar cells converts solar energy into a usable amount of direct current (DC) electricity.

When a photon hits a piece of silicon, one of three things can happen:

1. The photons can pass straight through the silicon-this (generally) happens to lower energy photons,
2. The photon can reflect off the surface,
3. The photon can be absorbed by the silicon, if the photon energy is higher than the silicon band gap value. This generates an electron-hole pair and sometimes heat, depending on the band structure [223].

When a photon is absorbed, its energy is given to an electron in the crystal lattice. Usually this electron is in the valence band, and is tightly bound in covalent bonds between neighbouring atoms, and hence unable to move far. The energy given to it by the photon "excites" it into the conduction band, where it is free to move around within the semiconductor. The covalent bond that the electron was previously a part of now has one fewer electron. This is known as a hole. The presence of a missing covalent bond allows the bonded electrons of neighbouring atoms to move into the "hole," leaving another hole behind, and in this way a hole can move through the lattice. Thus, it can be said that photons absorbed in the semiconductor create mobile electron-hole pairs.

A photon need only to have greater energy than that of the band gap in order to excite an electron from the valence band into the conduction band. However, the solar frequency spectrum approximates a black body spectrum at about 5,800 K, and as such, much of the solar radiation reaching the Earth is composed of photons with energies greater than the band gap of silicon. These higher energy photons will be absorbed by the solar cell, but

the difference in energy between these photons and the silicon band gap is converted into heat (via lattice vibrations - called phonons) rather than into usable electrical energy.

4.1.1 Charge Carrier Separation

There are two main modes for charge carrier separation in a solar cell:

1. The drift of carriers, driven by an electric field established across the device
2. Diffusion of carriers due to their random thermal motion, until they are captured by the electrical fields existing at the edges of the active region.

In thick solar cells there is no electric field in the active region, so the dominant mode of charge carrier separation is diffusion [224]. In these cells the diffusion length of minority carriers (the length that photo-generated carriers can travel before they recombine) must be large compared to the cell thickness. In thin film cells (such as amorphous silicon), the diffusion length of minority carriers is usually very short due to the existence of defects, and the dominant charge separation is therefore drift, driven by the electrostatic field of the junction, which extends to the whole thickness of the cell.

4.1.2 The p-n Junction

The most commonly known solar cell is configured as a large-area p-n junction made from silicon. As a simplification, one can imagine bringing a layer of n-type silicon into direct contact with a layer of p-type silicon. In practice, p-n junctions of silicon solar cells are not made in this way, but rather by diffusing an n-type dopant into one side of a p-type wafer (or vice versa) [225].

If a piece of p-type silicon is placed in intimate contact with a piece of n-type silicon, then a diffusion of electrons occurs from the region of high electron concentration (the n-type side of the junction) into the region of low electron concentration (p-type side of the junction). When the electrons diffuse across the p-n junction, they recombine with holes on the p-type side. The diffusion of carriers does not happen indefinitely, however, because charges build up on either side of the junction and create an electric field. The electric field creates a diode that promotes charge flow, known as drift current that opposes and eventually balances out the diffusion of electrons and holes. This region

where electrons and holes have diffused across the junction is called the depletion region because it no longer contains any mobile charge carriers. It is also known as the space charge region. It is formed by deposition of one material on the surface of an extrinsic semi-conductor by spray method.

4.1.3 Connection to an External Load

Ohmic metal-semiconductor contacts are made to both the n-type and p-type sides of the solar cell, and the electrodes are connected to an external load. Electrons that are created on the n-type side, or have been "collected" by the junction and swept onto the n-type side, may travel through the wire, power the load, and continue through the wire until they reach the p-type semiconductor-metal contact. Here, they recombine with a hole that was either created as an electron-hole pair on the p-type side of the solar cell, or a hole that was swept across the junction from the n-type side after being created there.
The voltage measured is equal to the difference in the quasi Fermi levels of the minority carriers, i.e. electrons in the p-type portion and holes in the n-type portion [226].

4.1.4 Photovoltaic Module

The general mathematical description of the I-V output characteristics of a PV cell has been studied in the past few decades. This model consists mainly of the photo current, a diode, a parallel (shunt) resistor with a leakage current and a series resistor which represents the internal resistance to the flow of current as shown in figure 4.2 [227].

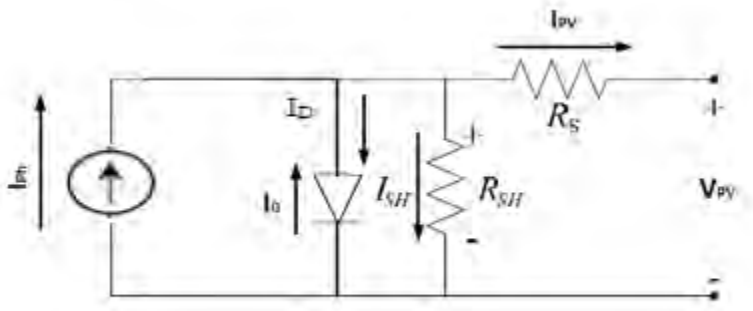

Figure 4.2: The Equivalent Circuit of a PV [227]

In an ideal PV cell, there is no series loss and no leakage to the ground hence $R_S = 0$ and $R_{SH} = \infty$. The voltage-current characteristic equation of a solar cell is given by

$$I_{PV} = I_{SCr}\left\{\exp\left(\frac{(q(V_{PV}+IV_{PV}))}{kRTA}\right) - 1\right\} - \frac{V+IR_S}{R_{SH}} \quad (4.1)$$

Where I_{ph} is a light-generated current or photocurrent, I_D is the voltage-dependent current lost to recombination, I_{SCr} is the cell saturation or dark current, ($q = 1.6x10^{-19}$ C) is an electron charge, T is the cell`s working temperature. A is an ideal factor and the k (=1.38 x $10^{-23}$ J/K) is the Boltzmann`s constant. The photocurrent depends on the solar insolation and cell`s working temperature which is described in equation 4.2

$$I_{ph} = [I_{SCr} + k(T - 298)] * \lambda/1000 \quad (4.2)$$

Where I_{SC} is the cells short-circuit current at 25 $^{\circ}$C and 1 kW/m^2, k_{SC} is the cell`s short circuit current temperature coefficient, T is the cell`s reference temperature, and λ is the solar insolation in kW/m^2.

Intrinsic Carrier concentration in Semiconductors: Like other semiconductor devices, solar cells are sensitive to temperature. Increase in temperature reduces the band gap of the semiconductor thereby affecting most of the semiconductor material parameters and vice versa. The saturation I_o from one side of the p-n junction is given by

$$I_0 = qA\frac{Dn_i^2}{LN_D} \quad (4.3)$$

where:
q is the electric charge;
D is the diffusivity of the majority carrier for silicon as a function of doping;
N_D is the doping;
A is the ideality factor which is 1.6;
n_i is the intrinsic carrier concentration for silicon.

The equation for the intrinsic carrier concentration is :

$$n_i^2 = PT^3 \exp(-\frac{qE_{G0}}{BkT}) \quad (4.4)$$

Where:

T is the temperature;

P is a temperature dependent constant

E_{G0} is the band gap linearly extrapolated to absolute zero

B is a temperature dependent constant.

Equation 4.5 is obtained by substituting n_i in equation 4.3

$$I_0 = qA\frac{D}{LN_D} PT^3 \exp(-\frac{E_{G0}}{kT}) = P'T^3 \exp\left(-\frac{qE_{G0}}{BkT}\right) \quad (4.5)$$

Where,

P' is a temperature dependent constant with a typical value of 3.9 x 10^{16}.

We define the saturation current at a reference temperature (T_r) as shown in equations 4.6 and 4.7

$$I_{rs} = P'T_r^{\,3} \exp(-\frac{qE_{G0}}{BkI_{ref}}) \quad (4.6)$$

Where T_r is the reference temperature

Equation 4.7 is obtained by solving equations 4.5 and 4.6;

$$I_0 = I_{rs}[\frac{T}{T_r}]^3 \exp[\frac{q*E_{G0}}{Bk}\left\{\frac{1}{T_r} - \frac{1}{T}\right\}] \quad (4.7)$$

Where

I_{rs} is the cell`s reverse saturation current at a reference temperature and a solar radiation

E_{g0} is the band gap energy of the semiconductor used in the solar cell.

In general, the solar cell efficiency is insensitive to the variation in R_{SH} and the shunt-leakage resistance can be assumed to approach infinity without leakage current to the ground. A small change in R_S will affect the output power of the panel [227]. Hence equation 4.1 could be modified as follows

$$I_{PV} = I_{ph} - I_0\left[\exp\left\{\frac{q*(V_{PV}+I_{PV}R_S)}{AkT}\right\} - 1\right] \quad (4.8)$$

If $R_s = 0$ then equation 4.8 is rewritten as equation 4.9

$$I_{PV} = I_{ph} - I_0 \left[\exp\left\{\frac{q*(V_{PV})}{AkT}\right\} - 1\right] \quad (4.9)$$

4.1.5 Levelized Cost of Electricity

The Levelized Cost of Energy (LCOE) is the total cost of installing and operating a project expressed in Rand per kilowatt-hour of electricity generated by the system over its life. It accounts for installation costs, financing costs, taxes, operation and maintenance costs, salvage value, incentives, revenue requirements and quantity of electricity the system generates over its life [221].

The LCOE in SAM depends on the following assumptions:

- The quantity of electricity generated by the system for each year in the analysis period
- Installation and operating costs
- Financing assumptions
- Depreciation assumptions

The real LCOE is a constant Rand, inflation-adjusted value while the nominal LCOE is a current rand value.

The levelized cost of energy (LCOE) which is given by equation (4.10)

$$\text{Real LCOE} = \frac{\sum_{N-1}^{N} \frac{R_n}{(1+d_{nominal})^n}}{\sum_{N=1}^{N} \frac{Q_n}{(1+d_{real})^n}} \quad (4.10)$$

where,

Q_n is the electricity generated in year n in (kWh),

n is the analysis period in years,

R_n is the projected revenue from electricity sales in year n,

d_{real} is the discount rate,

$d_{nominal}$ is the nominal discount rate.

4.2 Power Electronics

Power electronics provides a link or buffer that connects the solar panel to the load or the electrical power grid. It is the application of solid-state electronics for the control and conversion of electric power. It also refers to a subject of research in electrical engineering which deals with design, control, computation and integration of nonlinear, time varying energy processing electronic systems with fast dynamics. The power electronics could be found anywhere it is required to change voltage, current or frequency values of electric power [228]. The power range of these converters is from some milliwatts (as in the mobile phones) to hundreds of megawatts in HVDC transmission lines. With 'classical' electronics, the electric signals carry information whereas in the power electronics they carry power.

4.2.1 Converters

In the early days, mercury-arc valves were used but these days, semiconductor materials such as diodes, thyristors, and transistors have replaced the valves. R.D Middlebrook and his colleagues are the pioneers of power electronics in the mid-sixties [229].
The power electronics could be classified as

- ✓ AC to DC (rectifiers)
- ✓ DC to AC (inverters)
- ✓ DC to DC (converters)
- ✓ AC to AC (converters)

4.2.2 DC-AC Inverters

The DC /AC converters produce AC output waveform from a DC source. Applications include adjustable speed drives (ASD), uninterruptible power supplies (UPS), static VAR compensators, active filters, flexible AC transmission systems (FACT), voltage

compensators and photovoltaic generators [230]. Topologies for these converters can be separated into two distinct categories:

- Voltage source inverters
- Current source inverters.

Voltage source inverters (VSIs) are named so because the independently controlled output is a voltage waveform. Similarly, current source inverters (CSIs) are distinct in that the controlled AC output is a current waveform. DC-AC power conversion is the result of controllable semiconductor power switching devices. The output waveforms are however made of discrete values (like square waves) which produce fast transitions rather than smooth sinusoidal waveforms. In order to produce near sinusoids around the fundamental frequency modulating techniques such as

- Carrier-based techniques
- Pulse width modulation
- Space-vector techniques
- Selective-harmonic techniques

Voltage source inverters have practical uses in both single-phase and three-phase applications. The single-phase VSIs utilize half-bridge and full-bridge configurations and are widely used for power supplies, single-phase UPSs and elaborate high-power topologies when used in multi-cell configurations. Three-phase VSIs are used in applications that require sinusoidal waveforms such as ASDs, UPSs, FACTs and VAR compensators where arbitrary voltage is required as in active filters and voltage compensators [231].

Multilevel inverters are relatively new class of inverters which are useful for applications where high quality voltage waveforms are required. The normal operation of CSIs and VSIs can be classified as two level inverters because power switches connect to either the positive or negative DC bus. If more than two voltage levels were available to the inverter output terminals, the AC output could provide a better sine wave. Hence multilevel inverters are better even though they are more complex and more costly.

There are three main types of VSIs:

- Single-phase half-bridge inverter
- Single-phase full-bridge inverter
- Three-phase voltage source inverter

a) Single-Phase Half-Bridge Inverter

The single-phase voltage source half-bridge inverters are meant for lower voltage applications and are commonly used in power supplies. Shown above is the schematic of this inverter. Low-order current harmonics get injected back to the source voltage by the operation of the inverter [232]. This means that two large capacitors are needed for filtering purposes in this design. As shown in the figure 4.3, only one switch can be on at a time in each leg. If both switches in one leg are on at the same time, the DC source will be shorted out.

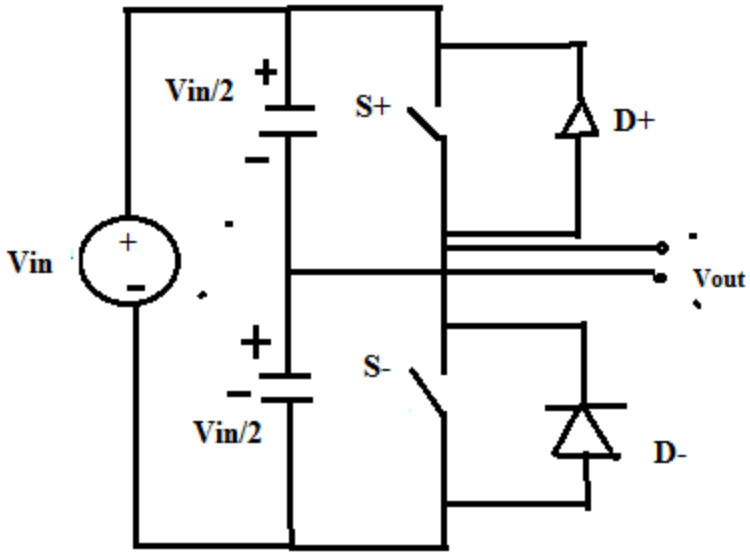

Figure 4.3: Single-Phase Half-Bridge Voltage-Source inverter [232]

Therefore, the AC output voltage is not controlled by the inverter, but rather by the magnitude of the DC input voltage of the inverter. Using selective harmonic elimination (SHE) as a modulation technique allows the switching of the inverter to selectively eliminate intrinsic harmonics. The fundamental component of the AC output voltage can also be adjusted within the desirable range. Since the AC output voltage obtained from

this modulation technique has odd half and odd quarter wave symmetry, event harmonics do not exist. Any undesirable odd (N-1) intrinsic harmonics from the output waveform can be eliminated.

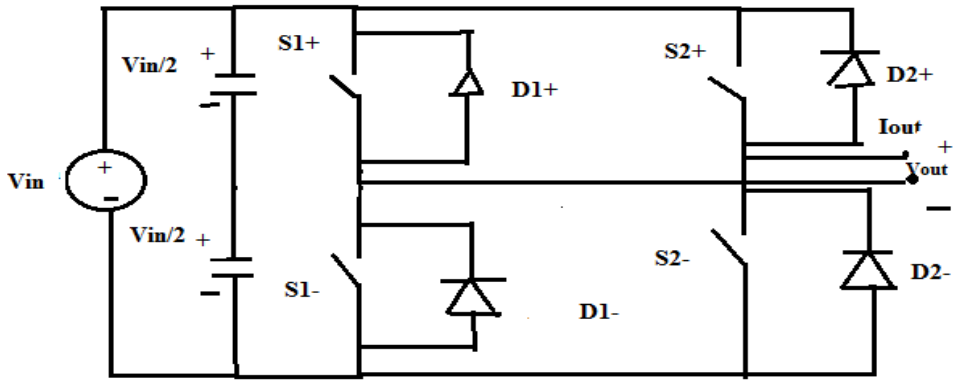

Figure 4.4: Single-Phase Voltage source Full-bridge Inverter [232]

b) Three- phase Inverter

Single-phase VSIs are used primarily for low power range applications, while three-phase VSIs cover both medium and high power range applications. Switches in any of the three legs of the inverter cannot be switched off simultaneously due to this resulting in the voltages being dependent on the respective line current's polarity [233]. States 7 and 8 produce zero AC line voltages, which result in AC line currents freewheeling through either the upper or the lower components. However, the line voltages for states 1 through 6 produce an AC line voltage consisting of the discrete values of V_i, 0 or $-V_i$. Further studies of the multi-level inverters are found in the appendix.

4.2.3 DC-DC Converters

A DC-DC converter is a power electronic device under the class of power converter whose function is to convert a source of DC from one voltage to another. There are two classes of DC-DC converters; the linear mode and the switched-mode conversion [234]. Linear regulator output lower voltages from the input hence efficiency is low but the switched-mode converters convert one DC voltage to another by storing the input energy temporarily and then releasing it to the output at different voltages.

Boost Converters are a class of switched-mode step-up converter with an output greater than its input. It contains at least two semiconductor switches (diode and transistor) and at least one energy storing element; a capacitor, inductor or a combination of the two as shown in figure 4.5 [235].

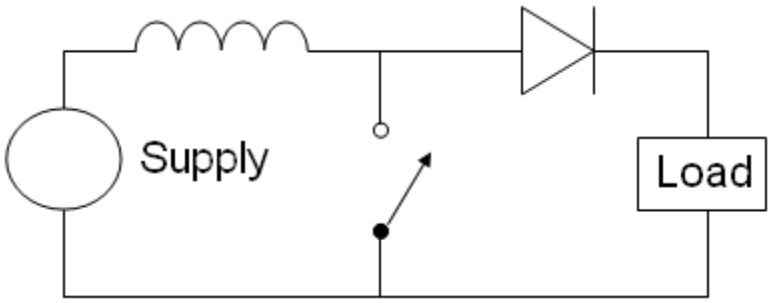

Figure 4.5: B**oost Converter basic diagram [235]**

A more practical circuit would replace the switch with a semiconductor switch such as a diode and IGBT as shown in the figure 4.6.

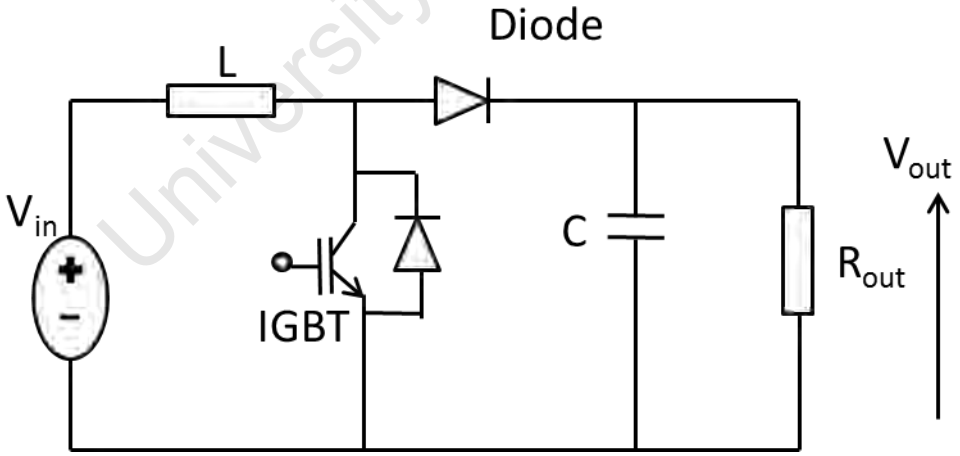

Figure 4.6: DC-DC boost converter [235]

The boost converter above with a switching period of T and a duty cycle of D is given. A duty cycle meanwhile is the ratio of on-time to the period of the wave. Assuming continuous conduction mode of operation, the state space equations when in switched mode of operation is ON are shown by equation 4.11.

$$\begin{cases} \frac{di_0}{dt} = \frac{1}{L}(V_{in}) \\ \frac{dV_{out}}{dt} = \frac{1}{C}\left(-\frac{V_{out}}{R_{out}}\right) \end{cases}, 0 < t < dt, Q: ON \quad (4.11)$$

And when the switch is OFF

$$\begin{cases} \frac{di_L}{dt} = \frac{1}{L}(V_{in} - V_{out}) \\ \frac{dV_{out}}{dt} = \frac{1}{C}\left(i_L - \frac{V_0}{R_{out}}\right) \end{cases}, dT < t < T, Q: OFF \quad (4.12)$$

A boost converter can be constructed when the switch and inductor are connected as shown in figure 4.7. This converter produces an output voltage V_0 that is of greater magnitude than the input voltage, V_{in} and its conversion ratio is by equation 4.13

$$D = \frac{1}{1-D} \quad (4.13)$$

Where D is the duty cycle

The critical inductance is calculated according to the formula:

$$L_{crit} = \frac{RT}{2}(1-D)^2 D \quad (4.14)$$

And the voltage ripple is given equation 4.15:

$$\Delta V = \frac{DV_{out}}{R_{out} Cf} \quad (4.15)$$

Buck converters are used to step down high voltages to low voltages. This circuit is realised by swopping the positions of diode and the inductor as shown in figure 4.7 [236].

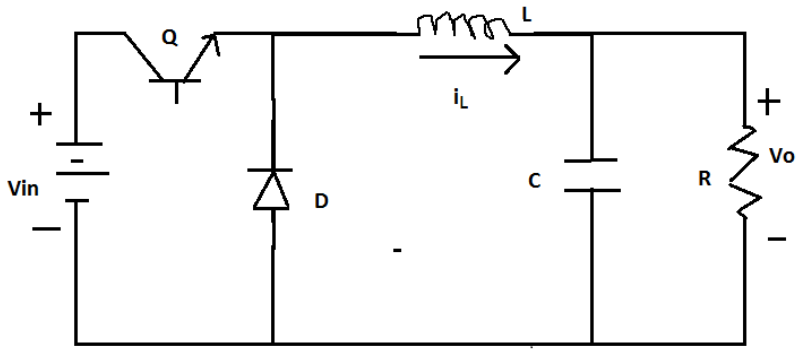

Figure 4.7: Equivalent Circuit of a Buck Converter [236]

4.3 Theory of Concentrated Solar Power

The source the information discussed here is found in reference [221]. The solar field module calculates the solar field thermal output $Q_{SF,}$ thermal and optical losses, solar field warm-up energy and freeze protection energy based on weather data from the weather file and solar field parameters. The storage and dispatch module calculates energy flow into and out of the thermal energy storage system and into the power block based on the solar field thermal output. Q to TES and out of storage Q from thermal energy storage (TES), the thermal energy delivered to the power block, Q to PB.

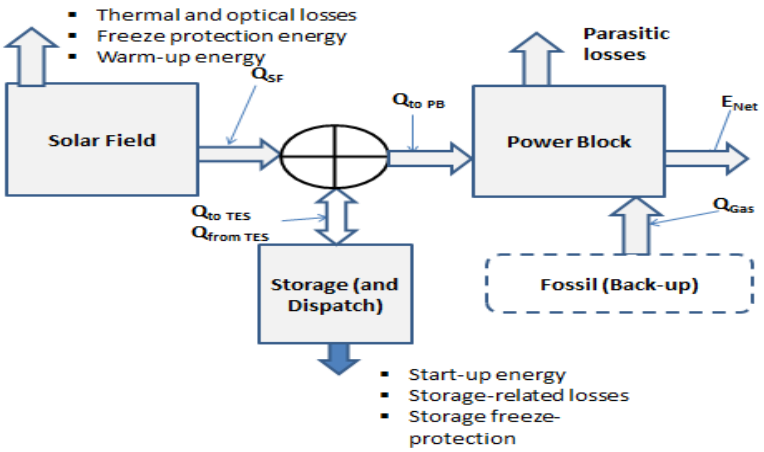

Figure 4.8: Block Diagram of CSP Energy Flow [221]

The storage and dispatch module also determine the timing of the storage and power block energy flows. The power block module calculates the system`s net electric output E_{net} based on the thermal energy input from the storage and dispatch modules and

parameters. It also calculates parasitic losses, and backup system thermal input as shown in figure 4.8.

4.3.1 The Input Variables

The solar field input variables determine the size and orientation of the solar field, heat transfer fluid type and solar field optical efficiency and heat loss parameters. The design point variables describe the reference weather conditions, equipment design parameters and thermal losses under reference conditions for calculating the solar field size. The definition of the Solar multiple is the solar field area for a solar multiple which is equivalent to the solar field area that under reference conditions and accounting for heat losses, generates sufficient energy to drive the power block at design turbine thermal input level [SAM 2011].

Table 4..1: The Input Variables

Name	Units	Symbol
Solar Multiple (calculated)		$F_{SolarMultiple}$
Solar Field Area (calculated)	m^2	$A_{SolarField}$
Ambient Temperature	$^{\circ}C$	$T_{AmbientRef}$
Direct Normal radiation	W/m^2	Q_{NIRef}
Wind Velocity	m/s	$v_{WindRef}$
Optical efficiency		$F_{SFOpticalEffD}$
Design Turbine Thermal Input	MW_t	$Q_{PBDesign}$
Solar Field Piping Heat Losses	W/m^2	$Q_{SFPipeLossD}$

4.3.2 Solar Multiple Reference Conditions

The three reference condition variables, ambient temperature, direct normal radiation, and wind velocity are the ambient conditions at which the solar field thermal output is equal to the power block`s design thermal input multiplied by the solar multiple. The reference direct normal radiation value does not have a significant impact on the solar field size calculations. Factors that affect the choice of the reference direct normal radiation value for a given system are location, storage capacity, maximum storage charge rate and

variability of the solar resource over the year which is determined by the weather data [SAM 2011].

4.3.3 Heat Transfer Fluid

The heat transfer fluid (HTF) parameters describe solar field properties that affect the HTF temperature calculations for the hour-by-hour simulation calculations. The HTF input variables are the Solar Field HTF and Solar Field inlet Temperature (T_{SFinD}) given in $^{\circ}C$, Solar Field Outlet temperature (T_{SFoutD}) in $^{\circ}C$, Solar Field Initial Temperature ($T_{SFinInit}$) $^{\circ}C$, Solar Field piping losses @ Design T (Q_{PHLD}) in W/m^2, Piping heat loss coefficients (FPHL), minimum HTF temperature ($THTF_{min}$), HTF gallons per area (V_{HTF}) in gal/m^2 [SAM 2011]. More literature regarding the working principles of the CSP and photovoltaic systems as well as their simulations are found in the users' manual of SAM.

Chapter 5
Photovoltaic Model

5.1 Simulink Model

The Current source represents the cell photocurrent while R_{sh} and R_S are the shunt and series resistances. Usually, R_{sh} is very large and R_S is very small hence they are neglected to simplify the analysis. The cells are grouped to form the module and interconnected either in parallel or in series shown in figure 6.12. In this work, Solkar solar panel made in India is used as the reference module. The values shown in Table 5.1 are obtained under standard test conditions (STC) [237].

Table 5.1: Solker Solar Module

Rated Power	37.08 W
Voltage at maximum Power (V_{mp})	16.56 V
Current at Maximum power (I_{mp})	2.25 A
Open circuit voltage (V_{oc})	21.24 V
Short circuit Current (i_{scr})	2.55 A
Total number of cells in series (N_s)	36
Total number of cells in parallel (N_p)	1

Note: The electrical specifications are under test conditions of irradiance of 1 Kw/m^2, air mass 1.5 and cell temperature of 25 $^{\circ}$C

5.1.1 Converting Operating Temperature in Celsius to Kelvin

The Simulink models of temperatures T_{aK} and T_{rK} of equation 4.1 are presented. From the Simulink library menu click and drag the blocks and connect the blocks to form the circuits as shown in figure 5.1. The model converts Celsius to Kelvin using equations 5.1 and 5.2 which are the equations of the reference and operating temperatures respectively:

$$T_{rK} = 273 + 25 \quad (5.1)$$

$$T_{aK} = 273 + T_{op} \quad (5.2)$$

Where T_{rk} is the reference temperature in Kelvin

And T_{ak} is the operating temperature in Kelvin

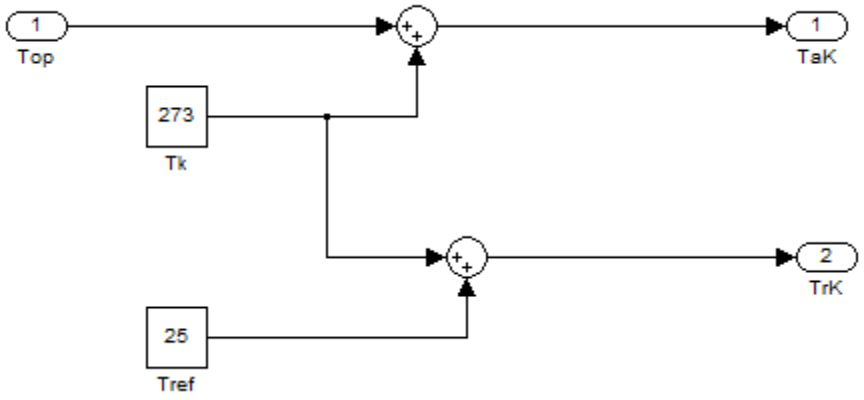

Figure 5.1: Converting Celsius to Kelvin

A subsystem in Simulink is a simplified block/module that contains all the circuits in question. A subsystem is created by selecting all the components you want to put in the subsystem and then right clicking to open a menu that contains the subsystem. When subsystem is clicked the circuits and all its components are hidden in the subsystem as shown in figure 5.2. To view the content of the subsystem, simply double click on the subsystem block.

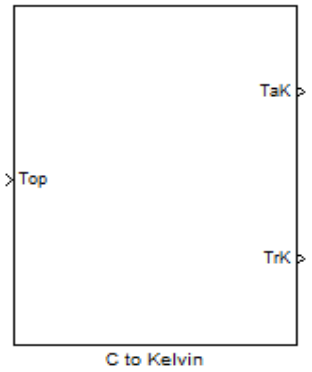

Figure 5.2: Subsystem to convert Celsius to Kelvin

5.1.2 Modelling the Photocurrent

Insolation (G/1000) = 1 kW/m^2

Module operating temperature, T_{ak} = 30 to 70 $^{\circ}$C

Module reference temperature, T_{rk} = 25 $^{\circ}$C

Figure 5.3 and 5.4 are used to model equation 5.3. This model calculates the short circuit current (I_{SC}) at a given operating temperature. Light generated photon.

Current, I_{Ph}

$$\text{Iph} = [\text{Isc} + \text{Ki}(\text{Tak} - \text{Trk})] * \text{X} \quad (5.3)$$

Where X is the irradiation

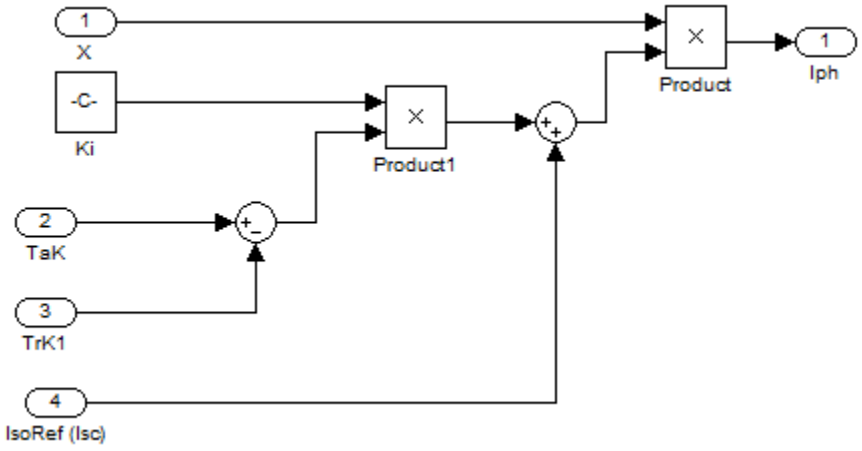

Figure 5.3: Modelling equation 4.1

The whole model on the page is selected by drawing a selection box over them. Right clicking on the model and selecting "create subsystem" from the pull-down menu, all the components could be grouped together in a single subsystem block. This is named "Photo Current" as shown in figure 5.4. The terminals of the module are Insol, T_{ak}, T_{rk}, I_{soRef} and I_{ph} respectively.

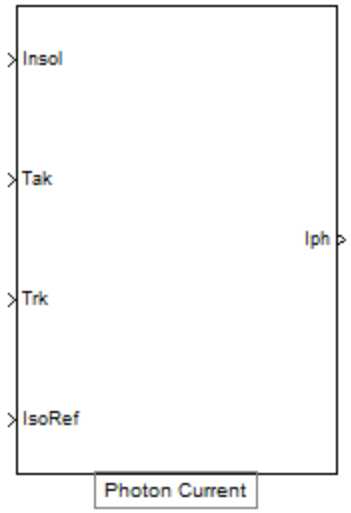

Figure 5.4: **Photon current subsystem**

5.1.3 Modelling the Reverse Saturation Current

Here, the reference temperature, I_{SC} = 2.55 A, and module reference temperature, T_{rk}= 25 °C are the input to the equation (5.4). Reverse Saturation Current of the diode from the equation 4.2 is calculated as follows.

$$I_{rs} = I_{SC}/[\exp\left(\frac{qVoc}{NsKATK}\right) - 1] \quad (5.4)$$

The Product block is configured to compute the scalar product of all six input variables Ns, k, q, V_{OC}, A, T_{ref} and the output is fed into a three pin Mux as shown in figure 5.5. The Mux converts the three input variables Iso Ref, the output of the Product block and the constant to u(1), u(2) and u(3) respectively. This forms the input of Matlab function block (fcn). The fcn uses the formula in equation 5.4 which was programmed into its block to calculate I_{rs} which is the output.

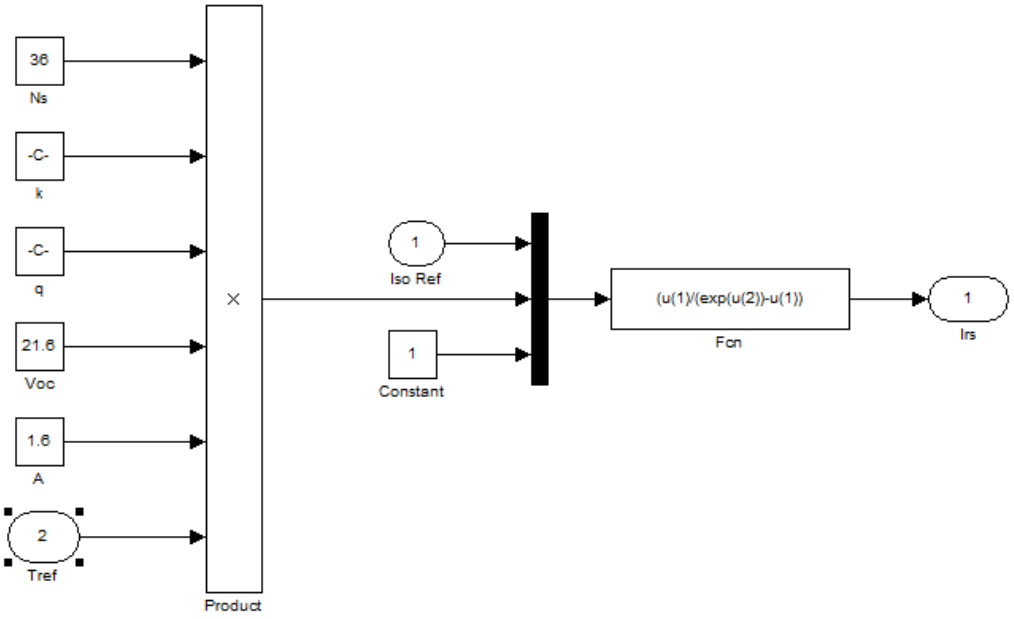

Figure 5.5: Reverse saturation current model for equation 5.4

The whole model on the page is selected by right clicking on the model. The "create subsystem" found in pull-down menu is used to group all the components in a single subsystem block. This is named "Reverse sat Current" as shown in figure 5.6. The three terminals of this subsystem are T_{ref}, iso Ref, and I_{rs}.

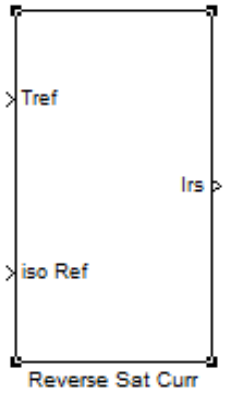

Figure 5.6: Reverse Saturation Current subsystem

5.1.4 Modeling the Module Saturation Current

To model the saturation current, Is, the module reference temperature, T_{rK} is 25 $^{\circ}$C, the reverse saturation current, (I_{rs}) and the operating temperature, T_{ak} are fed in as the input and the module saturation current is calculated as shown in the figure 5.7.

$$I_0 = I_{rs}[\frac{T}{T_r}]^3 \exp[\frac{q*E_{g0}}{Bk}\{\frac{1}{T_r} - \frac{1}{T}\}] \quad (5.5)$$

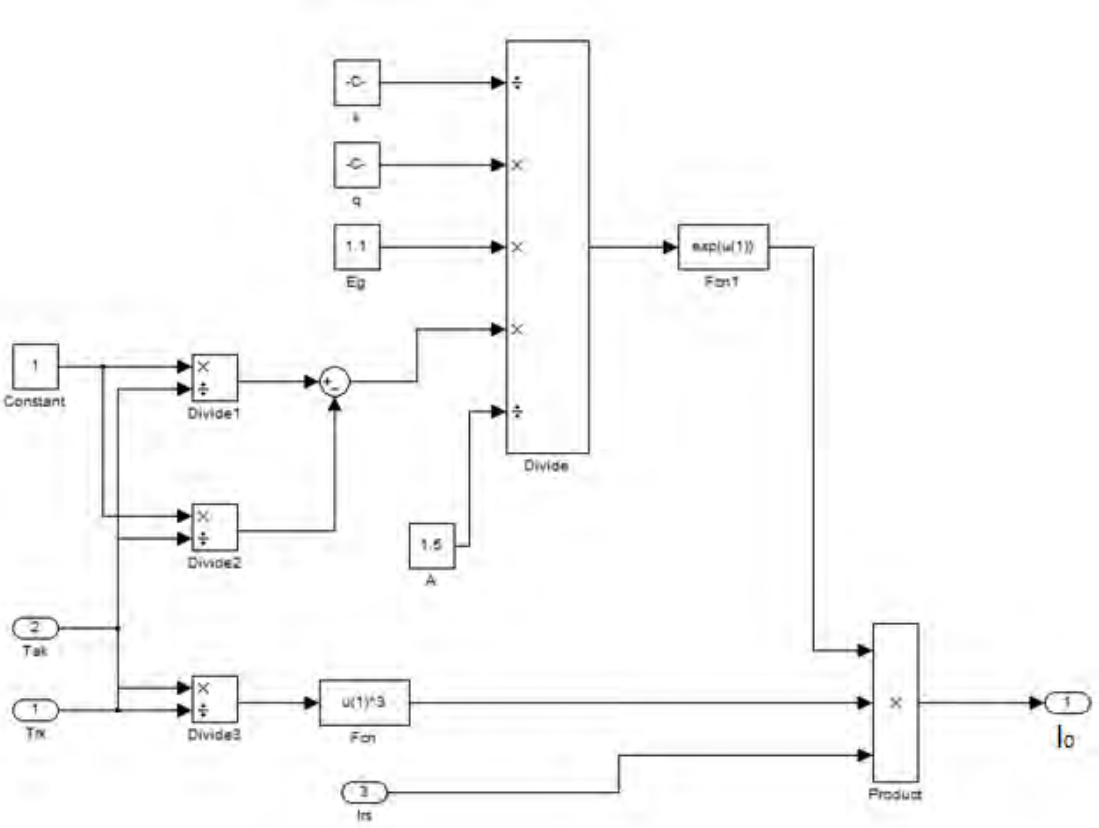

Figure 5.7: **Modelling the saturation current**

The subsystem is shown in figure 5.8. By drawing a select box over the model in figure 5.9, the whole model on the page is selected. Right clicking on the model and selecting "create subsystem" from the pull out menu, the entire components could be grouped together in a single subsystem block which is named Sat Current as shown in figure 5.8. The input terminal is T_{rK}, T_{ak} and I_{rs} while the output terminal is I_s.

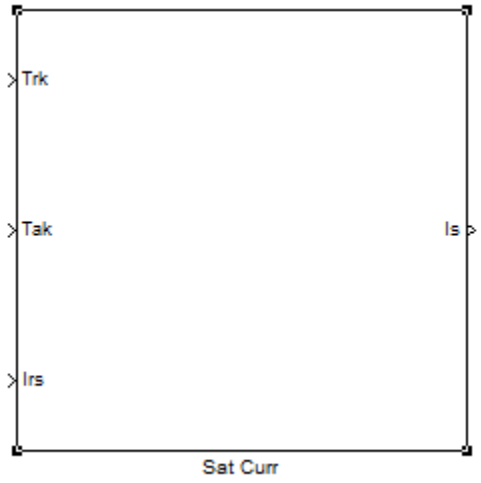

Figure 5.8: **Subsystem for the saturation current of the PV from equation 4.12**

5.1.5 Modelling the Temperature Dependent Constant (NsAkT)

To model the product NsAkT, which the denominator of the exponential function in equation (4.2), the operating temperature, N_S, A and T_{ak} are fed in as the input and the output is NsAkT as shown in figure 5.9.

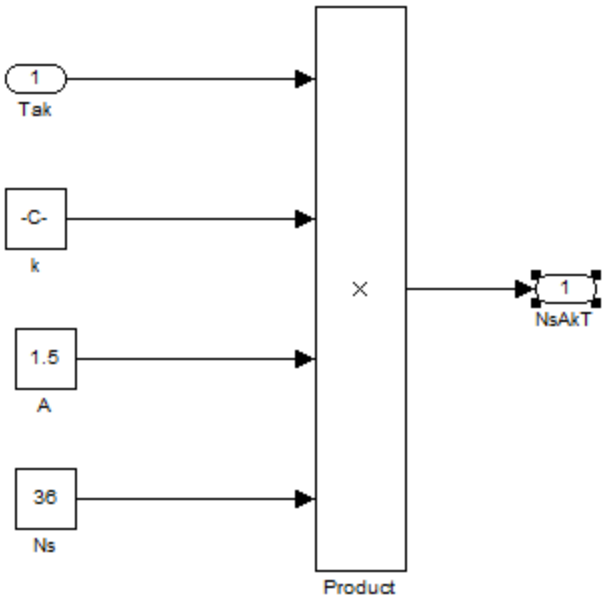

Figure 5.9: **Modelling NsAkT**

By drawing a select box over the model in figure 5.9, the whole model on the page is selected. Right clicking on the model and selecting "create subsystem" from the pull down menu, the entire components could be grouped together in a single subsystem block. This is named "NsAkT" as shown in figure 5.10. The input terminal is T_{ak} while the output terminal is NsAkT, where N_S is the number of panels in series.

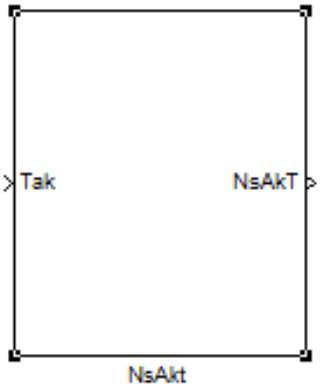

Figure 5.10: **NsAkT subsystem**

5.1.6 Modeling Module Output Current

Figure 5.11 models I_{PV} from equation 5.6 which is given by

$$I_{PV} = I_{ph} - I_0 \left[\exp\left\{\frac{q*(V_{PV}+I_{PV}R_s)}{AkT}\right\} - 1\right] \quad (5.6)$$

A Mux (like a mini busbar) with 6 input terminals is used to convert V_{PV}, q, I_{ph}, I_S, NsAkt and the output of the feedback loop to u(1), u(2), u(3), u(4), u(5) and u(6) respectively. The output of the Mux is passed through a function block, fcn, which has been programmed to compute the output I_{pv} using the formular "u(3)-u(4)*(exp((u(2)*(u(1)+u(6)))/(u(5)))-1)" rewritten from equation (5.6). The output i_{pv} is fed back to the mux through another function block fcn1 and a gain (R_S).

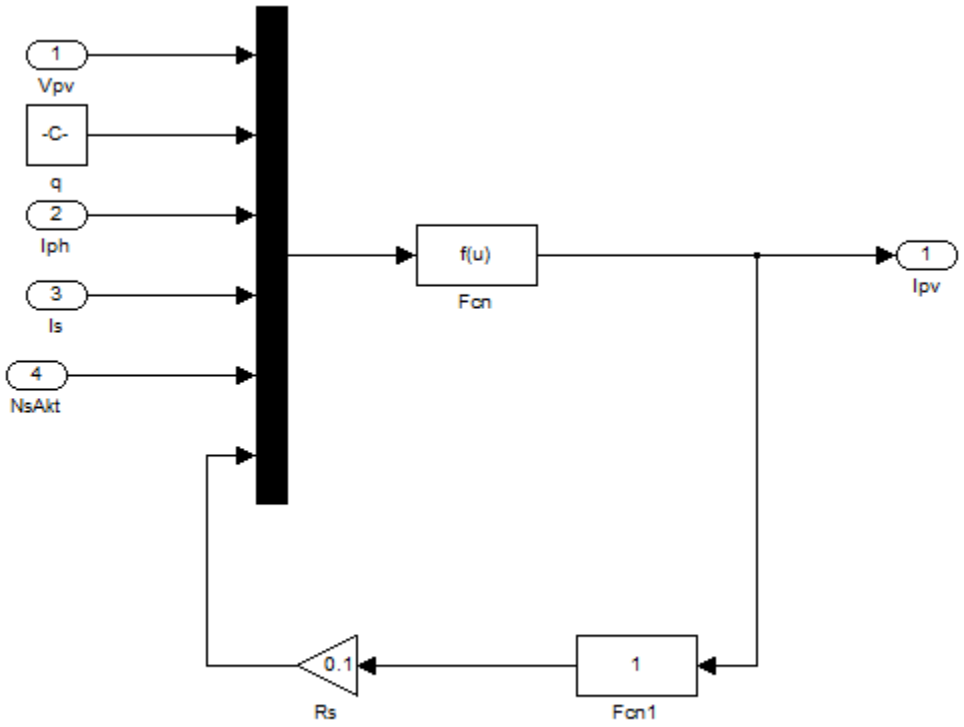

Figure 5.11: **PV output current model**

The whole model on the page is selected by drawing a select box over them. Right clicking on the model and selecting subsystem from the pullout menu, the entire components could be grouped together in a single subsystem block. This is named "Module Output Current" as shown in figure 5.12. The input terminals are V_{PV}, I_{ph}, I_S, and NsAkT while the output terminal is I_{PV}.

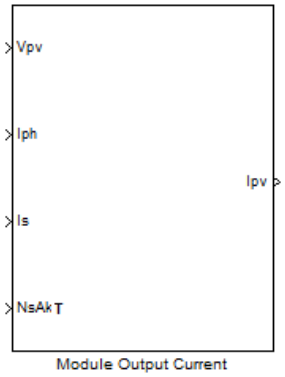

Figure 5.12: **Subsystem of Module Output Current**

5.1.7 Overall PV Module

All six models are connected as shown figure 5.13. The V_{PV} is connected as both the input and the output for ease of measurement.

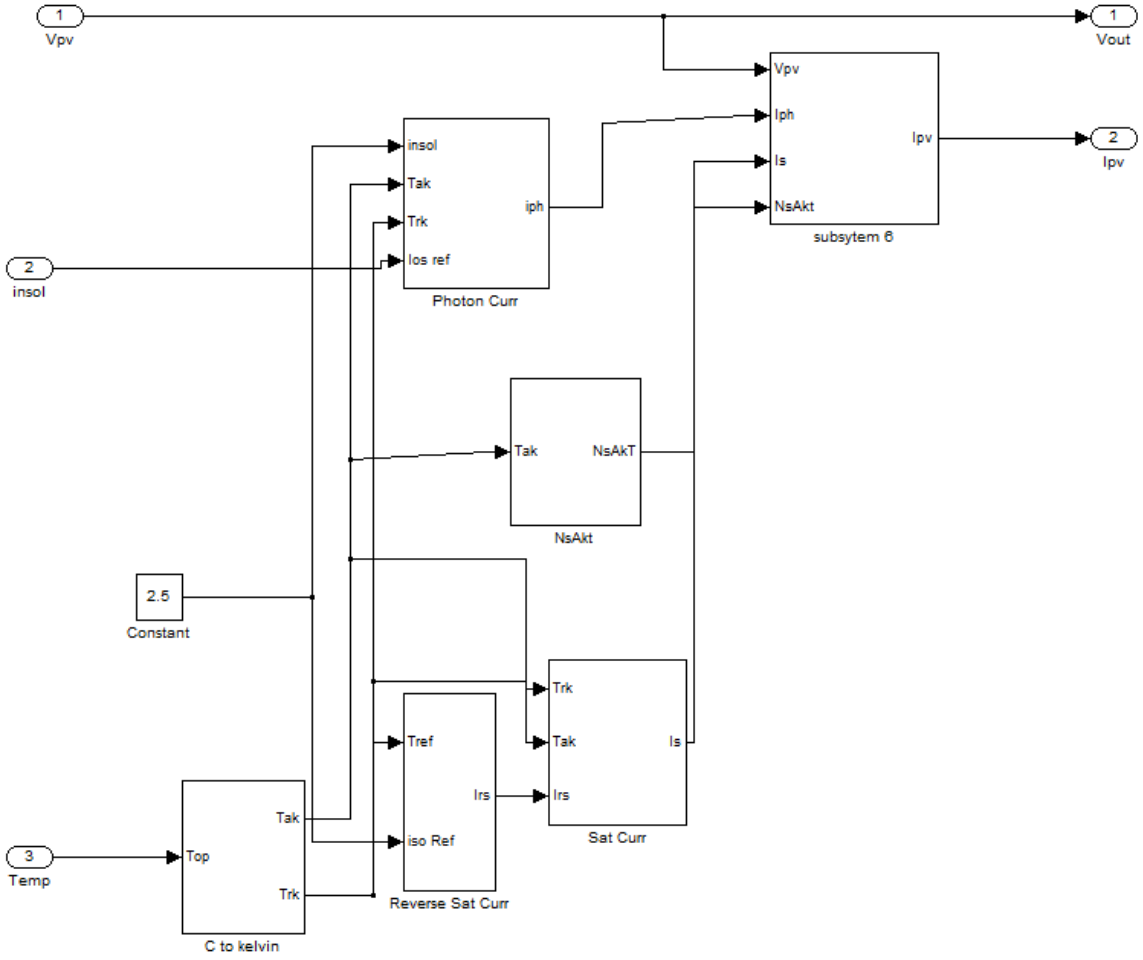

Figure 5.13: **An overall PV module**

The whole model on the page is selected by drawing a select box over them. Right clicking on the model and selecting subsystem from the pull out menu, the entire components could be grouped together in a single subsystem block. This is named "PV module" as shown in figure 5.14. The input terminals are V_{PV}, insol, and Temp while the output terminals are V_{out} and I_{PV}.

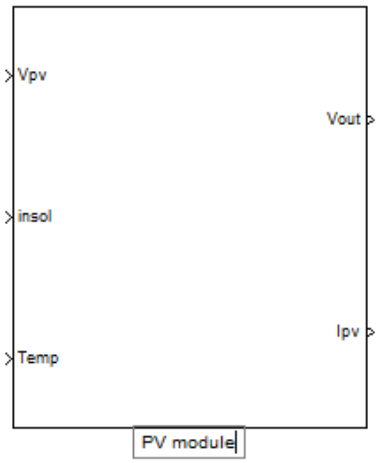

Figure 5.14: **Subsystem of the Photovoltaic Module**

Chapter 6
Simulation of the Photovoltaic System

This chapter covers the simulation of the photovoltaic module which was modelled in chapter 5. The details of the characterization which include the voltage current characteristics of the module with varying irradiation intensities, the thermal characteristics, voltage power charts at varying temperatures and irradiation levels are also discussed. Furthermore, physical model of the photovoltaic module is built with the aid of the SimPowerSystems of the Matlab. The power electronic circuits that connect the PV model to the load and eventually to the grid are all discussed in this chapter.

6.1 PV Module Results

The photovoltaic module is connected as shown in figure 6.1

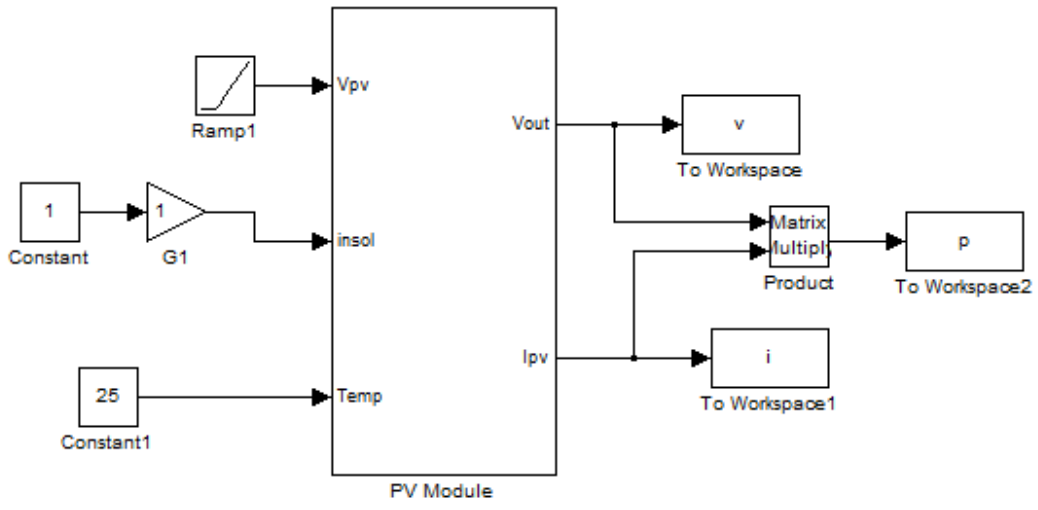

Figure 6.1: Simulink Model of PV ready for export to Matlab main window

The output of the Simulink PV module is exported to the Matlab workspace by exporting the variables power, current and voltage as p, i, v respectively using 'to workspace' block from the Simulink library and labelling as shown in the figure 6.1. Then run the simulation and the results automatically appear in the Matlab pane. Having modelled the PV module the following results are obtained with 30 seconds simulations. Figure A.1 in Appendix A shows the code that iterates the I-V characteristics for insolation ranging from 200 to 1000 W/m^2 at 25 $^{\circ}$C.

The I-V characteristics of the PV is plotted in figure 6.2 which shows that by increasing the solar irradiation levels from 200 W/m^2 to 1000 W/m^2 in steps of 200 W/m^2 the PV module output current increases from 0.5 A to 2.7 A. This shows that for this module, the PV output current is proportional to the solar irradiation at voltages up to 14 V.

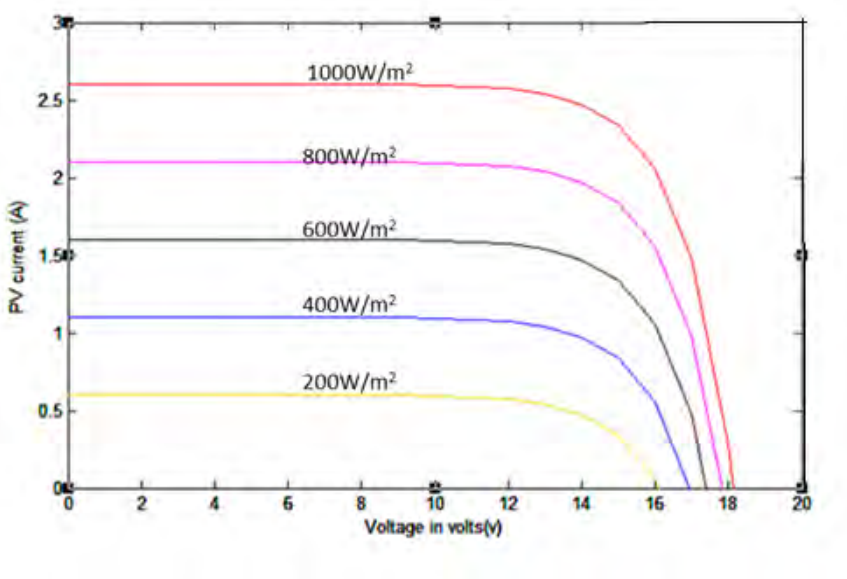

Figure 6.2: I-V characteristics of PV module at irradiation levels (200-1000 W/m^2)

When irradiation increases, the output current and the voltage increase. Figure A.2 of Appendix A shows the code that iterates the Power (P) –Voltage (V) characteristics for insolation ranging from 200 to 1000 W/m^2 at 25 $^{\circ}$C. The solar intensity is increased from 200 W/m^2 to 1000 W/m^2 in steps of 200 W/m^2. The chart in figure 6.3 shows that output power is minimal with solar intensity of 200 W/m^2 while the power output is maximal at solar intensity of 1000 W/m^2.

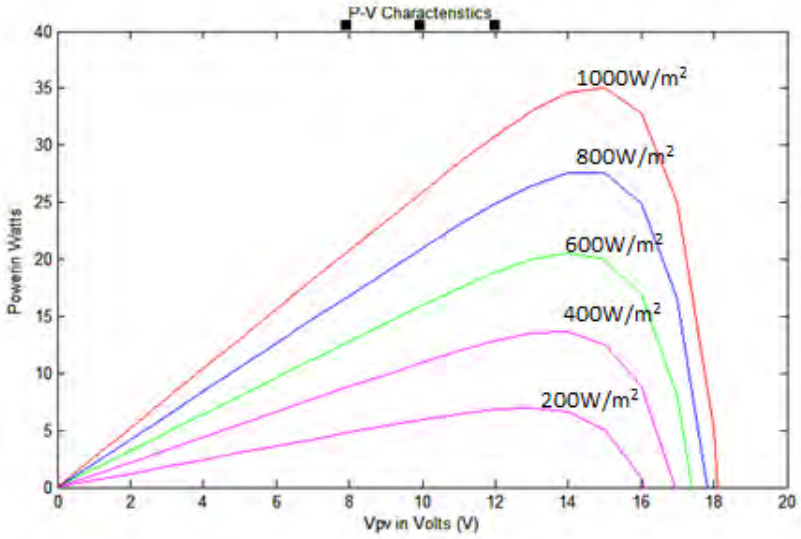

Figure 6.3: Power/Voltage curve of the photovoltaic module

Figure A.3 in Appendix A shows the matlab code that iterates the voltage/current characteristics of the photovoltaic module at temperature ranging from 25 to 75°C in steps of 25 °C. The command set_param ('PV/G2', 'Gain', gvalStr) sets the value of the gain block of Simulink to the pre-determined temperature. The output power of the PV module is also plotted against the output voltage at different temperatures as shown in figure 6.4.

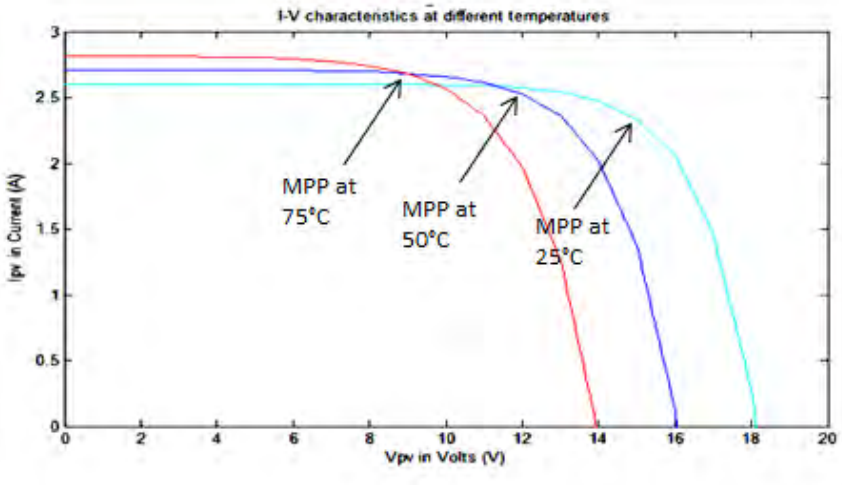

Figure 6.4: V-I chart of the PV module at temperatures 25, 50, 75°C

At higher temperatures such as 75 °C, Maximum power point (MPP) of the PV is lower (23.4W). At reduced temperatures, (25 °C), maximum power point is higher (30.8W). The MPP is obtained by multiplying the current and voltage at the neck of the PV graph shown in figure 6.4. Figure A.4, in Appendix A, shows the iteration code written in Matlab m-file. When the simulation is run the result is shown in figure 6.5. At the temperature of 25 °C, the PV module shows at higher output power up to 35 W, while at a higher temperature of 75 °C the power output is lower, about 25 W_{peak}.

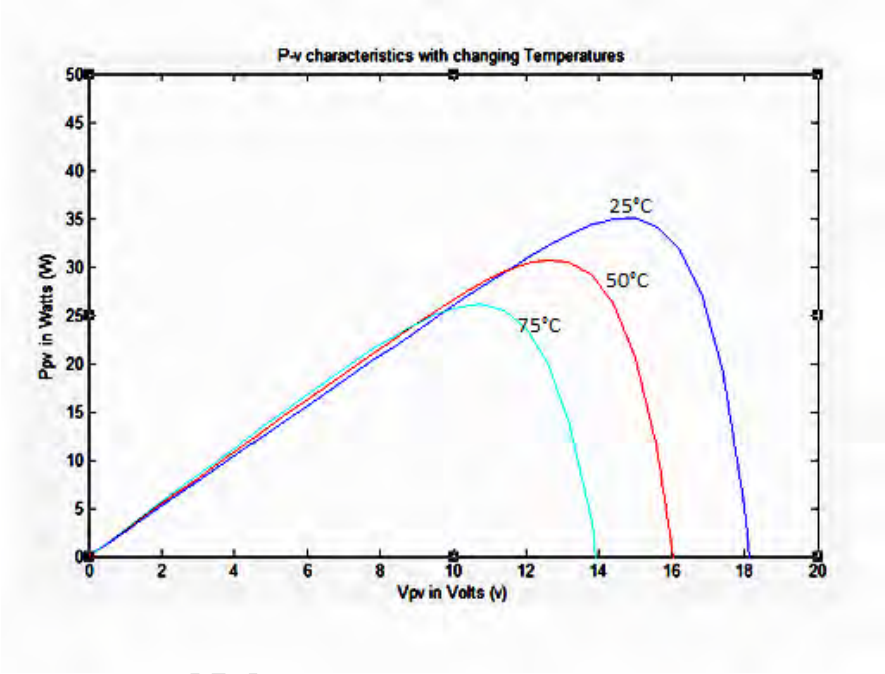

Figure 6.5: Power/Voltage Characteristics of a PV module

6.2 Series Connected PV

It is often necessary to increase the current, voltage and the power of the photovoltaic panel to a required value. Equation 6.1 simplifies calculation of the photovoltaic current [238].

And the graph in figure 6.6 shows the current/voltage chart of five PV modules which are connected in series. The maximum voltage is therefore increased to 90 V.

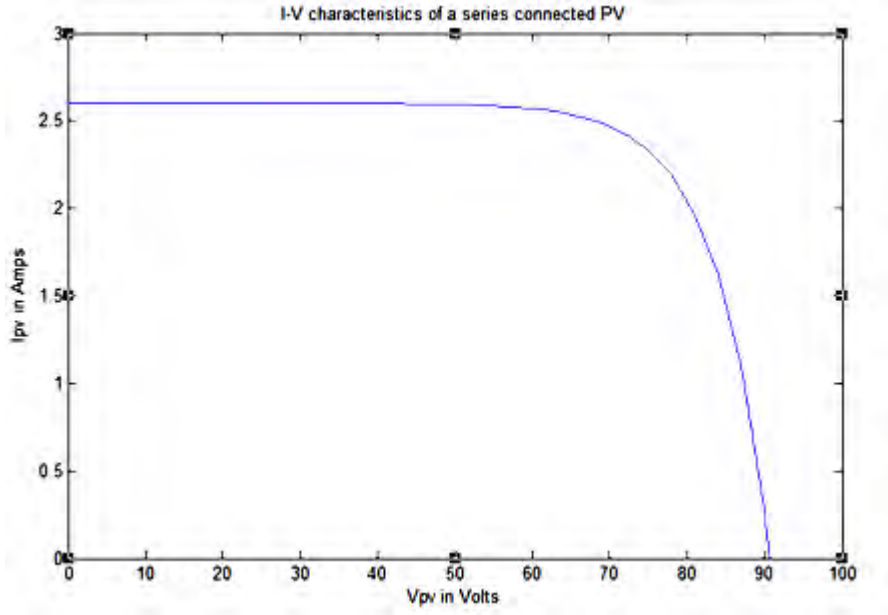

Figure 6.6: Current/Voltage characteristics of the five PV modules connected in series

The power-voltage characteristic of the 5 PV modules connected in series is shown in figure 6.7.

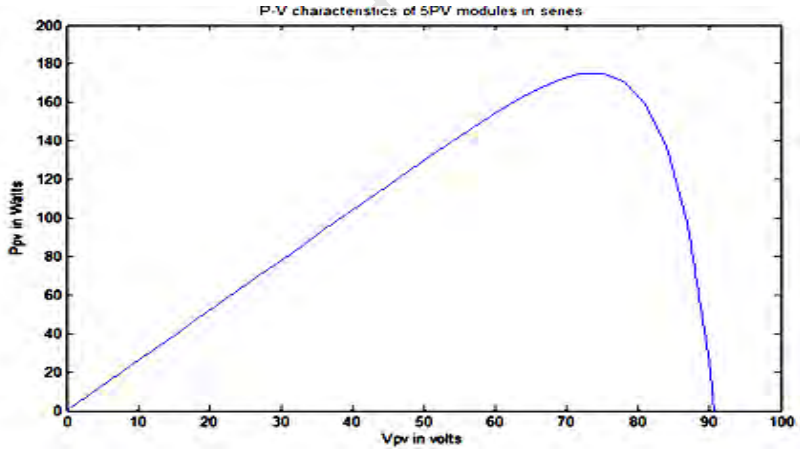

Figure 6.7: The Power-Voltage chart five PV modules connected in parallel

6.3 Parallel Connection of PV Modules

The photovoltaic modules often come with fixed manufacturer`s specifications. In order to achieve the desired current level the modules are connected in parallel as shown in figure 6.8 [239].

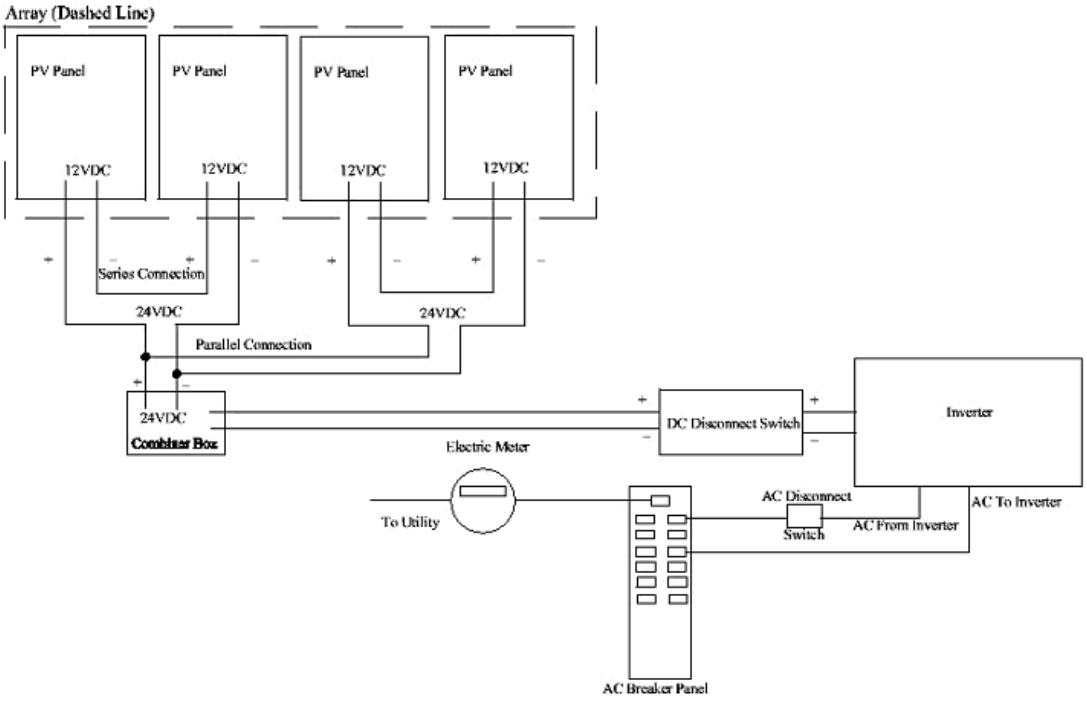

Figure 6.8: Parallel PV connection [239]

6.4 SimPowerSystems

The SimPowerSystems as already discussed in chapter 3 is used to model the physical circuit as it is in the real life. Simulink is used to model the equivalent circuit equation(s) of physical circuits. The SimPowerSystems model shown in figure 6.9 illustrates the means of integrating the PV module built in chapter 5 using the Simulink toolbox into the physical circuit.

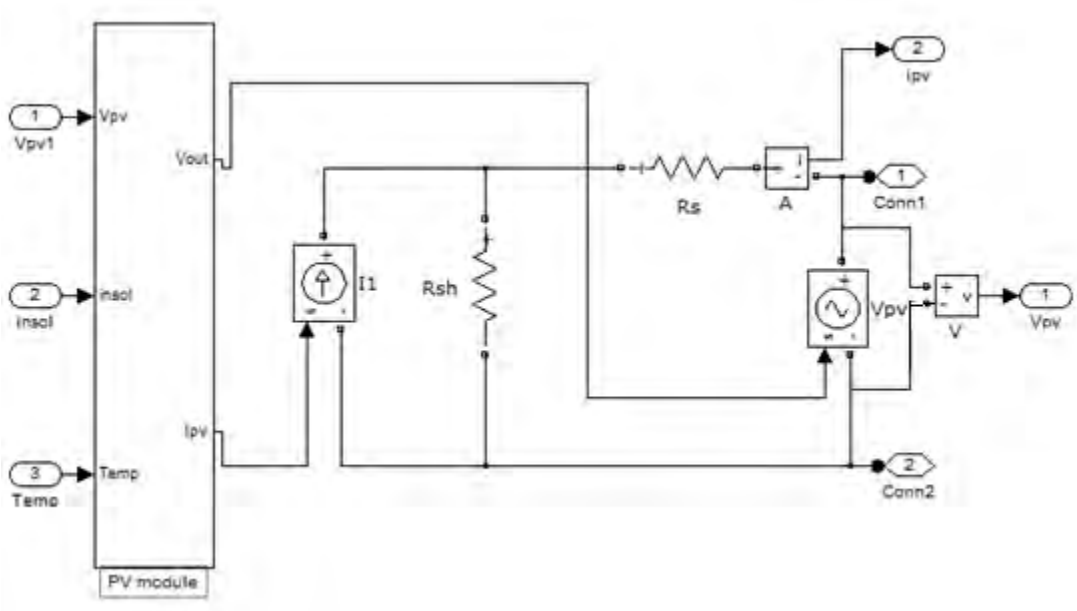

Figure 6.9: The SimPowerSystems model of the Photovoltaic Circuit

The Controlled current source I_1 and the Controlled voltage source V_{PV} are used to connect the Simulink PV module to the SimPowerSystems circuit. The current measurement A and the Voltage measurement V are also used to connect the output signals of the current and voltage to the Simulink scope.

6.5 Maximum Power Point Tracking (MPPT)

Maximum power point tracking (MPPT) is a technique that grid-tie inverters, solar battery chargers and similar devices use to get maximum possible power from one or more solar panels. Solar cells have a complex relationship between solar irradiation, temperature and total resistance that produces a non-linear output efficiency known as the I-V curve. It is the purpose of the MPPT system to sample the output of the cells and apply the proper resistance (load) to obtain maximum power for any given environmental conditions. Controllers usually follow one of two types of strategies to optimize the power output of an array [239]. Maximum power point trackers may implement different algorithms and switch between them based on the operating conditions of the array.

6.5.1 Perturb and Observe

This is the most common method of MPPT due to its ease of implementation. The controller adjusts the voltage by a small amount and measures the power, if the power increases, further adjustments in that direction are tried until the power no longer increases. This is often called hill climbing method because it depends on the rise of the curve of power against voltage below the maximum power point and often results in oscillation of the power output. The flow chart is shown in figure 6.10.

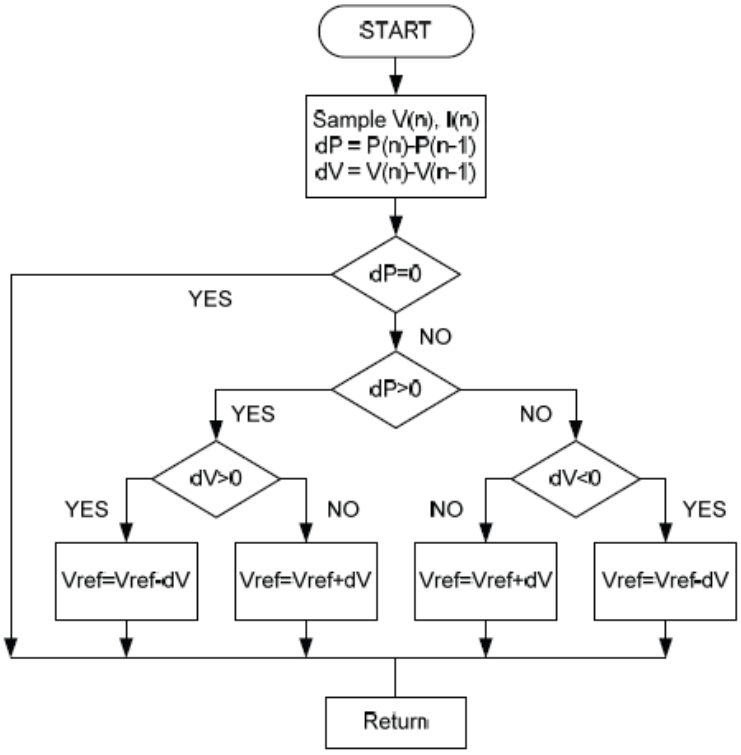

Figure 6.10: Flow Chart Perturb and Observe [238]

6.5.2 Incremental Conductance

Here, the controller measures incremental changes in array current and voltage (dI/dV) to compute the sign of the change in the power with respect to the voltage (dP/dV). This method requires more computation in the controller but can track changing conditions more rapidly than P & O. It can also produce oscillations in the power output. When the

incremental conductance is zero, the output voltage is the MPP voltage. The controller maintains this voltage until the irradiation changes and the process is repeated [240]. The flow chart is shown in figure 6.11.

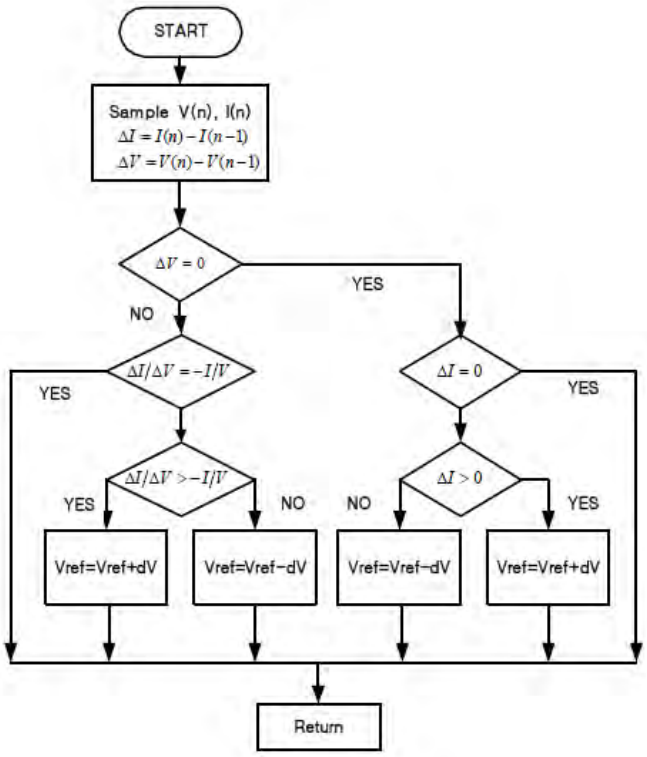

Figure 6.11: Flow chart of incremental Algorithm [240]

The incremental conductance (IC) algorithm is based on the observation that the following equations 6.2 and 6.3 hold for the MPPT. The principle of this method is to judge whether the system works at MPP or works on the left or right.

$$\frac{\mathrm{dP}}{\mathrm{dV}} = \frac{\mathrm{d(IV)}}{\mathrm{dV}} = \mathrm{I} + \mathrm{V}\frac{\mathrm{dI}}{\mathrm{dV}} = \mathrm{I} + V\frac{\Delta \mathrm{I}}{\Delta \mathrm{V}} = 0;$$
$$-\frac{I}{V} = \frac{\Delta I}{\Delta \mathrm{V}} \qquad (6.2)$$

Therefore, by analysing the derivative, one can test whether the PV generator is operating at its MPP or far from it using equations (6.2).

$$\frac{\mathrm{dP}}{\mathrm{dV}} > 0 \text{ for } \mathrm{V} < \mathrm{V_{MPP}} \qquad (6.3)$$

$$\frac{dP}{dV} = 0 \text{ for } V = V_{MPP} \quad (6.4)$$

$$\frac{dP}{dV} < 0 \text{ for } V > V_{MPP} \quad (6.5)$$

Figure 6.12 shows the SimPowerSystems model of PV module, MPPT and the DC-DC converter. This model transfers maximum power from the photovoltaic module to load or battery via the inverter stage. The validation of the DC-DC boost converter using a steady state input signal is shown in appendix C.

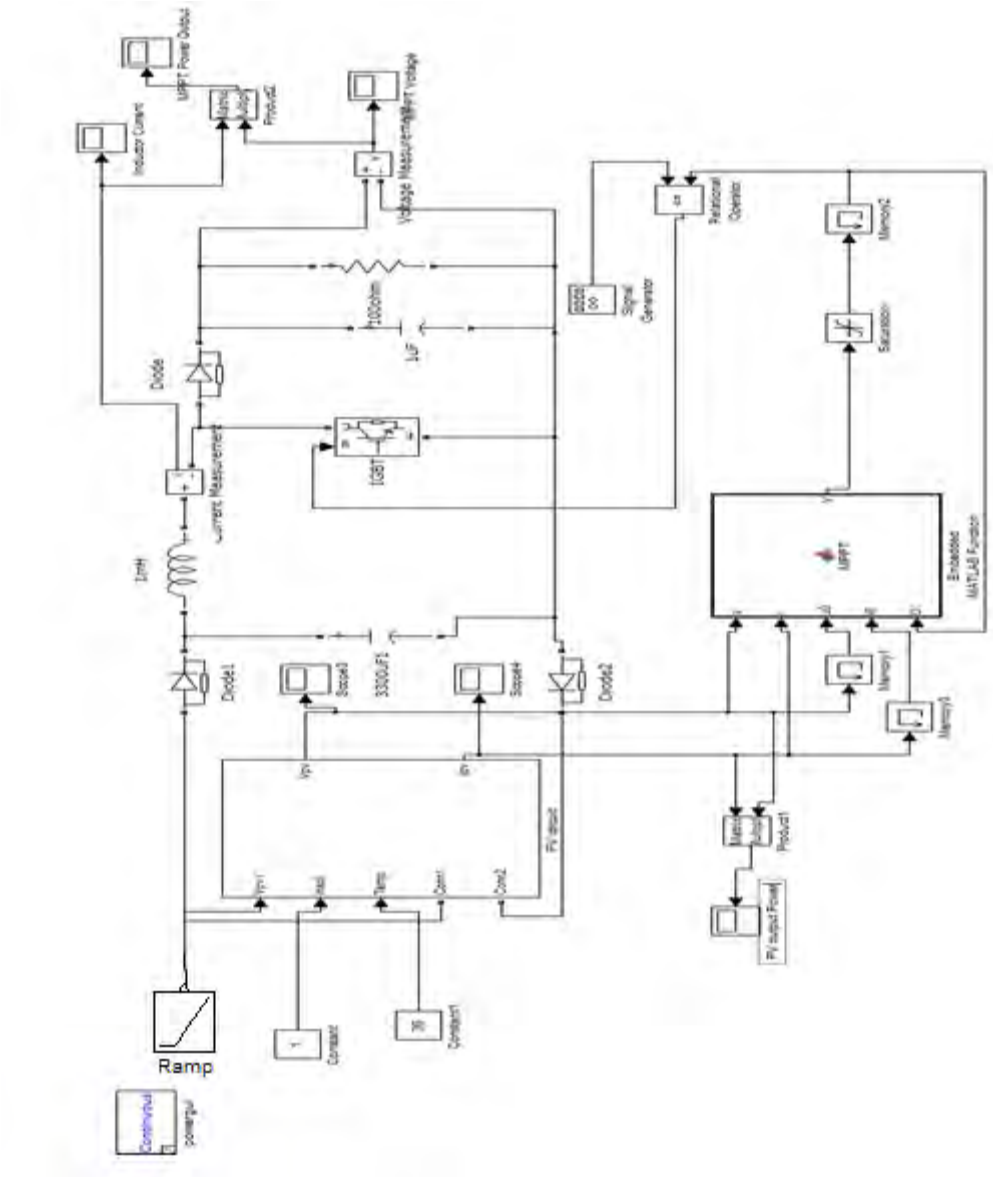

Figure 6.12: MPPT charge controller, DC-DC boost converter and the PV module

The MPPT can thus be tracked by comparing the instantaneous conductance (I/V) to the incremental conductance ($\frac{\Delta I}{\Delta V}$). The V_{ref} is the reference voltage at which the PV array is forced to operate. Once the MPP is reached, the operation of the PV array is maintained at this point unless a change in ΔI *is* noted, indicating a change in the atmospheric conditions and the MPPT. The proposed integrated maximum power point tracker (MPPT) has been used to force the PV array to work around the maximum power point. For this reason, the MPPT is required to track the maximum power available in the PV array. The need for MPPT is the power output of the solar. The code for the MPPT is found in Figure A.5, Appendix A.

The PV is however connected with the DC-DC boost converter and the MPPT for an enhanced battery charging experience as shown in figure 6.13 while the boost converter steps up the voltage from the current 20 V to about 200 V the MPPT ensures that maximum power is transferred from the PV to the batteries or inverters in this case [240]. The time series power output of the PV/MPPT circuit is shown in figure 6.13.

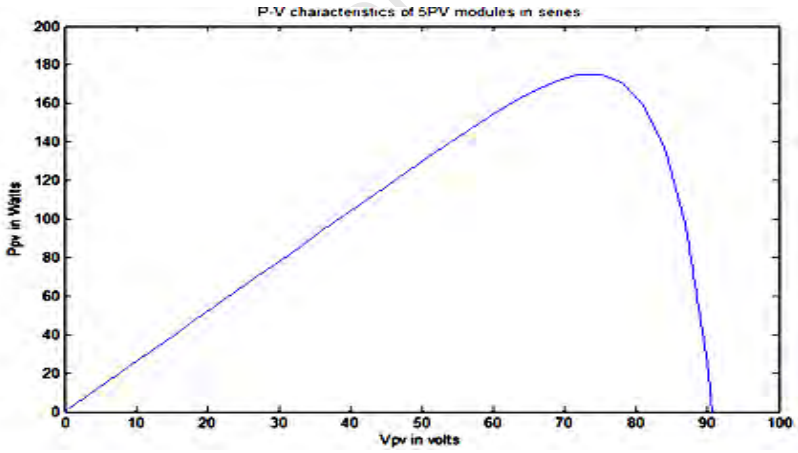

Figure 6.13: PV output power

Time series of the PV current chart is shown in figure 6.15

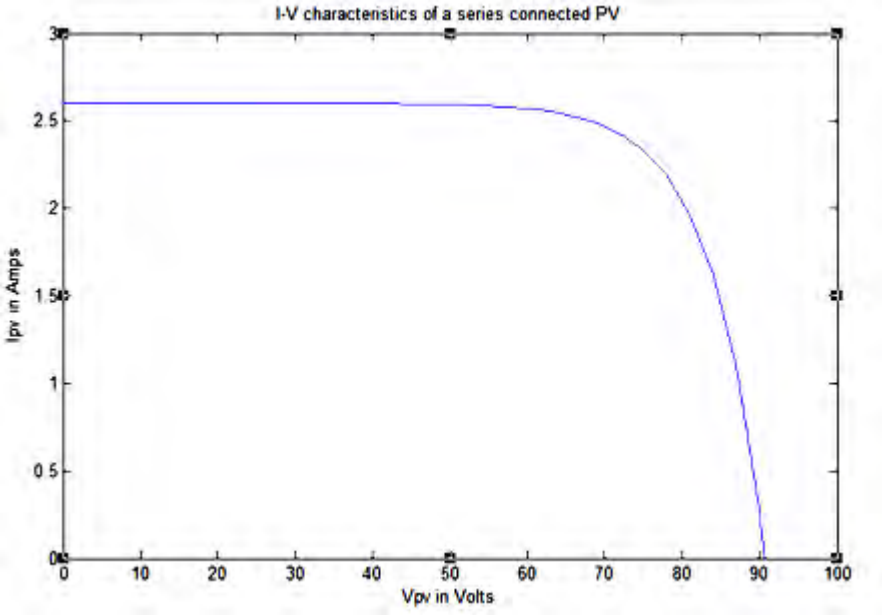

Figure 6.14: The input current of the MPPT

Here, we have the output of the pulse generator in figure 6.16 which is set to the frequency of 10,000 Hz. The pulse is square waveform from the pulse generator which is set maximum and minimum values of 1 and -1.

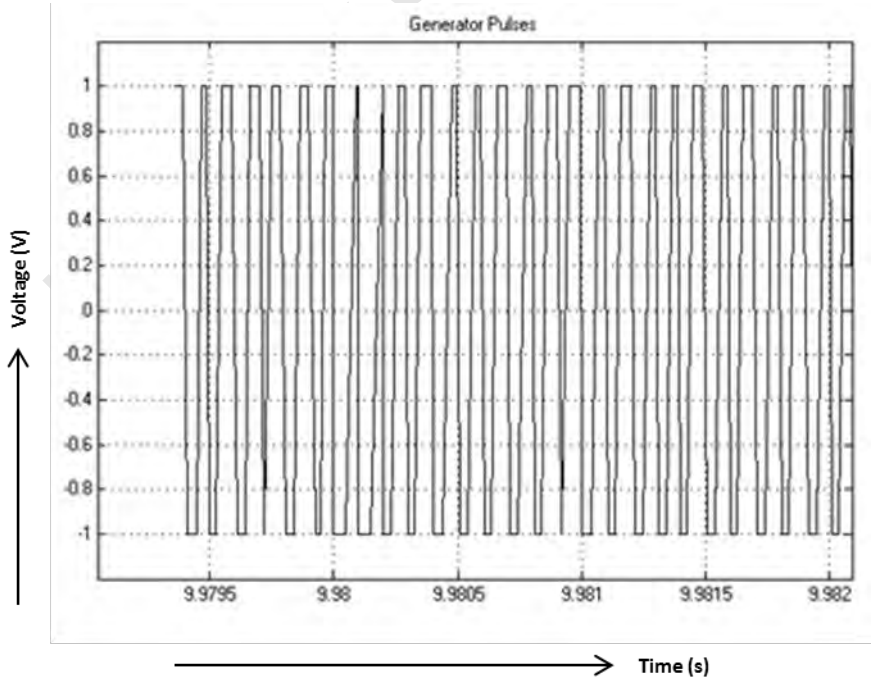

Figure 6.15: Pulses from the pulse generator

Figure 6.17 shows the output current of the PV module with the MPPT and the boost converter. The MPPT allows maximum power to be transferred only at designated times when the output is maximum.

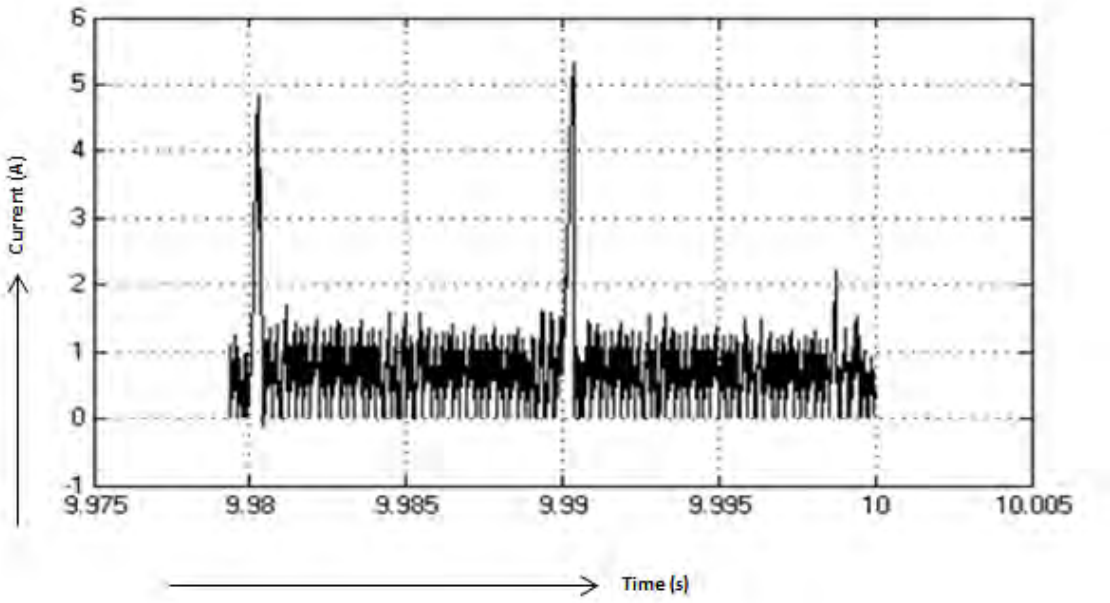

Figure 6.16: Inductor Current

The MPPT allows the only the maximum power to be transferred to the battery or the output for optimum power transfer. Hence the MPPT is working satisfactorily. Figure 6.18 shows the output voltage of the PV module MPPT and the boost converter.

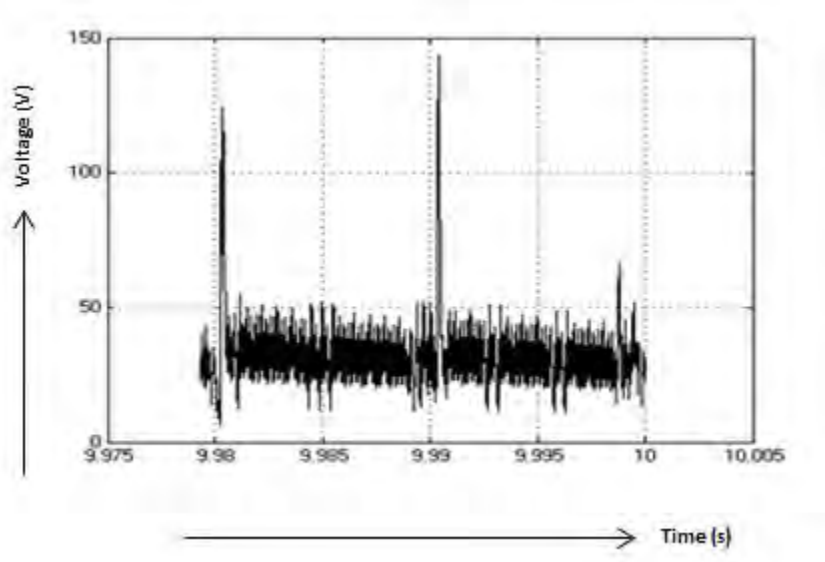

Figure 6.17: Output voltage of boost DC-DC converter

At the maximum power point high output voltages are delivered at 9.98 and 9.998 Sec The power output of the MPPT/Converter is shown in figure 6.19.

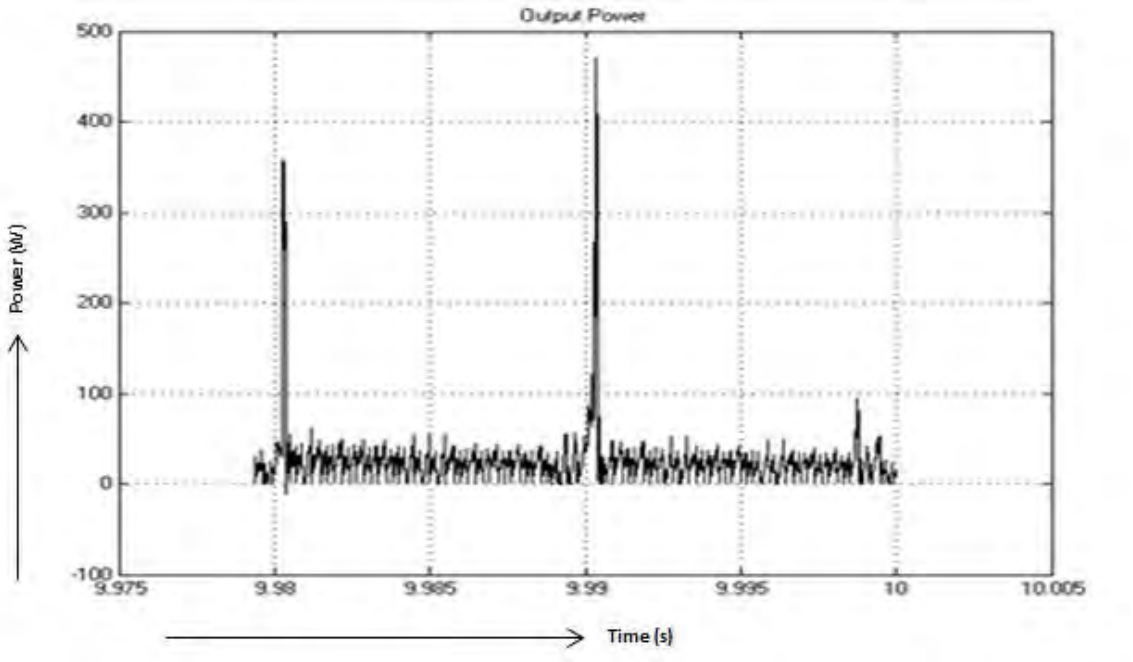

Figure 6.18: The output power of the MPPT/PV/converter

These results are very interesting because they show that power is only delivered at the maximum power point at 9.90 and 9.99 sec the rest is cut off.

6.6 The inverter Stage

In recent years, industry has begun to demand higher power requirement which now reaches the megawatt level. Controlled AC drives in the megawatt range are usually connected to a medium-voltage network. Today, it is hard to connect a single power semiconductor switch directly to medium voltage grids (such as 2.3, 3.3, 4.16, or 6.9 kV). For these reasons, a new family of multilevel inverters has emerged as the solution for working with higher voltage levels [241].

Types of inverters are single phase inverters and three phase inverters. Three step inverters are the simplest types however, in situations where sensitive appliances like the computers are used; these inverters are not desirable because of their tendencies to produce disadvantages such as low efficiencies and harmonics. These problems have been addressed by the multi-level inverters such as the seven level inverters and the true sine wave inverters but these inverters have the disadvantage of high circuit complexity and high cost. A novel type of inverter is currently being developed which is the current source inverter (CSI). All the previously discussed inverters are the voltage source inverters (VSI). The CSI has much less complicated circuitry, cheaper and are not sensitive to voltage fluctuations [242].

Up to this level, the output signal is direct current however because most appliances are still operating in the AC current we would need an inverter to transfer this signal to the alternating current. And for the purposes of this simulation, we would only model the three level single phase inverter which is the simplest type of inverter. Note also that the subsystem dubbed the PV module is now a subsystem containing the PV, MPPT and the DC-DC boost converter. The periods of the pulse generators 0 and 1 is set are out of phase, 0 and 3 are in phase and pulse generators 1 and 2 are in phase. The frequency of the pulse generators is set to 50 Hz which gives the period of 0.02 Sec [243]. The circuit diagram of a three level full-wave inverter with the energy storing capacitor, 0.15F is shown in figure 6.20.

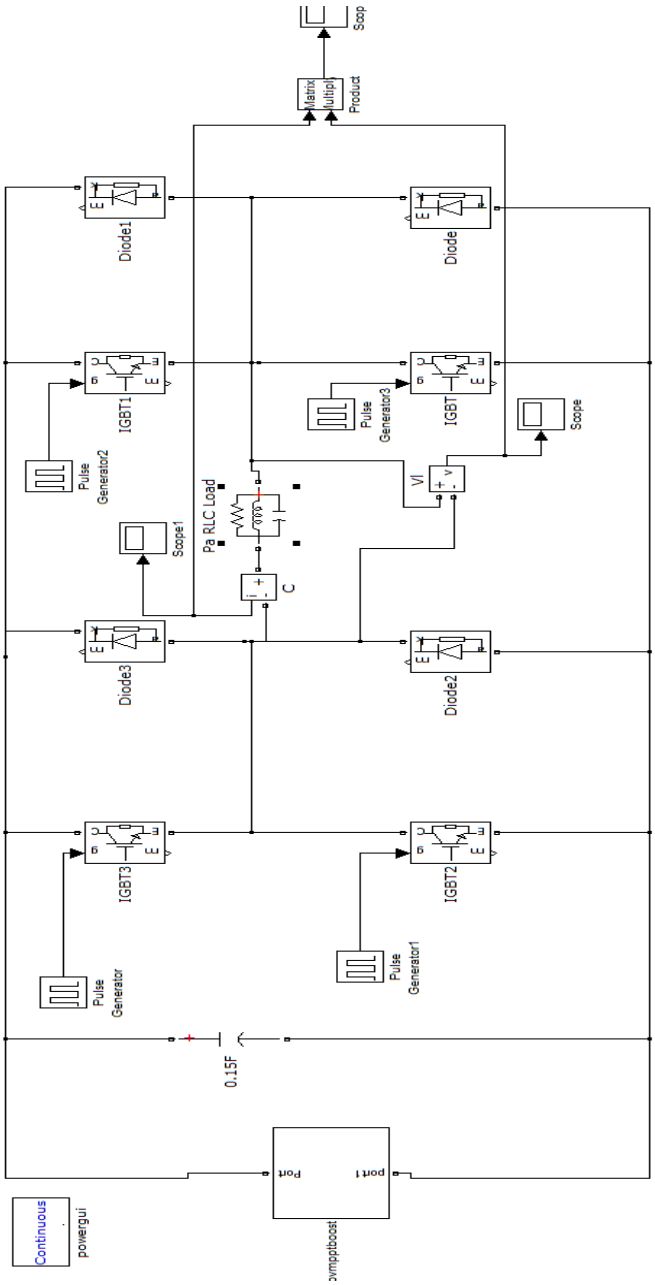

Figure 6.19: PV module and Full wave three-level inverter

The block properties of the RLC load showing the nominal voltage, nominal frequency, active power, inductive reactive power, and capacitive reactive power are all set to their respective values as shown in figure 6.21.

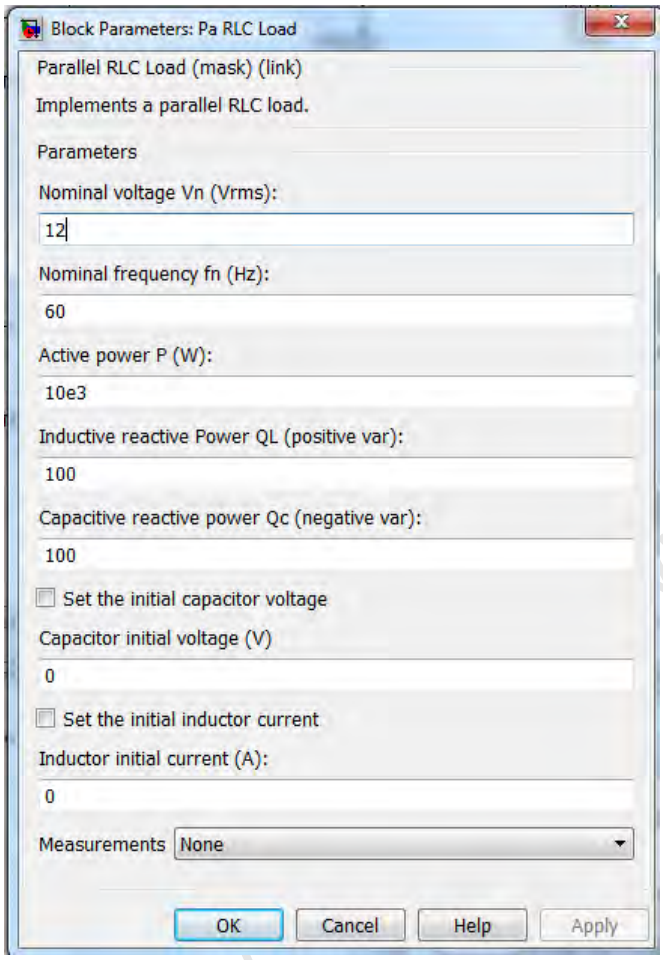

Figure 6.20: The configuration of the load

6.7 Transformer Stage

The output of the inverters is about 6 V so a step up transformer is used to step up the voltage to 220 V which is the distribution voltage. Filters are used to remove some of the harmonics as shown the figure 6.21. The PV module, MPPT, DC-DC converter and the inverters are wrapped up in a subsystem and labelled the PV module. This output is sent to the load and the grid. The output of the transformer needs to be passed through an anti-islanding circuit before being sent to the grid however the simulation of the anti-islanding circuit is not covered in this dissertation.

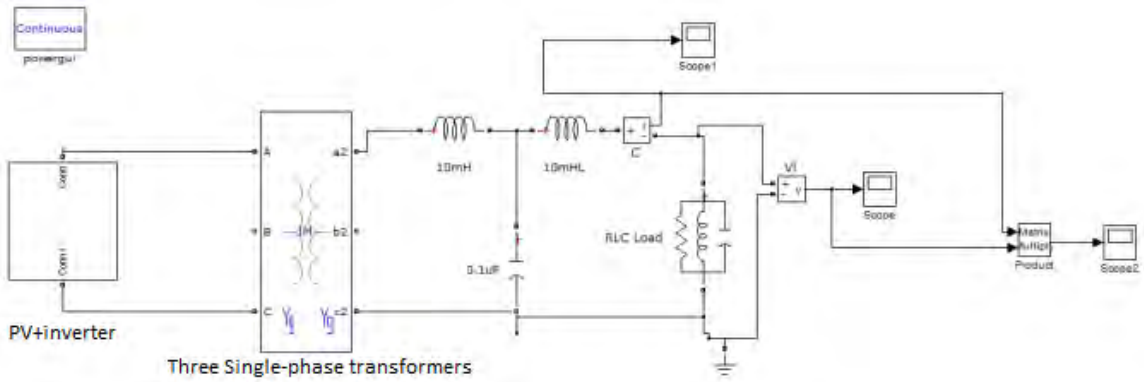

Figure 6.21: PV modules (PV, converter, MPPT and inverter) and the transformer

6.8 Simulation Results of the PV System

The signals in figures 6.22, 6.23 and 6.24 are the power, voltage and current of the PV panel sent to the grid and to power the load.

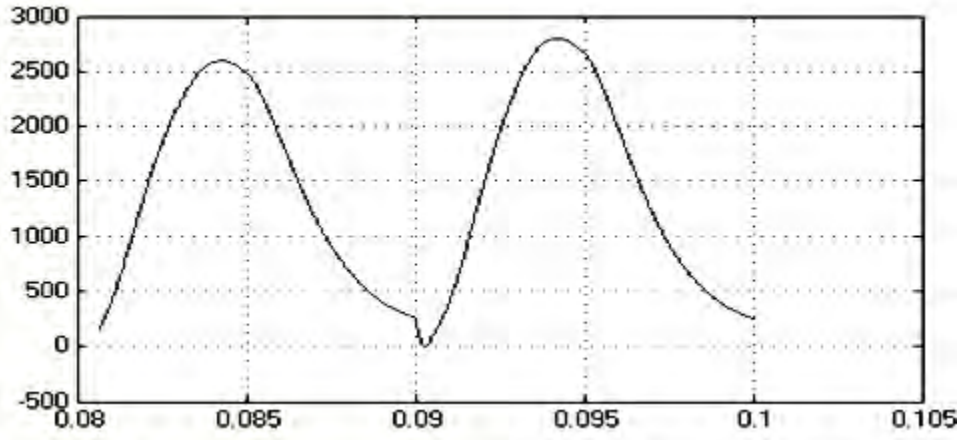

Figure 6.22: Power Output of the panel

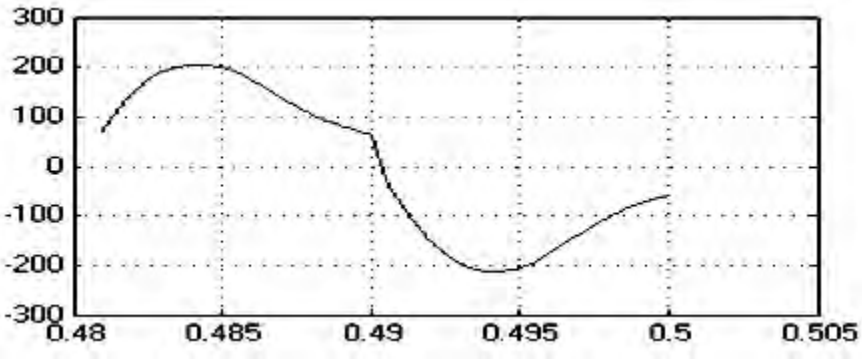

Figure 6.23: PV Output Voltages

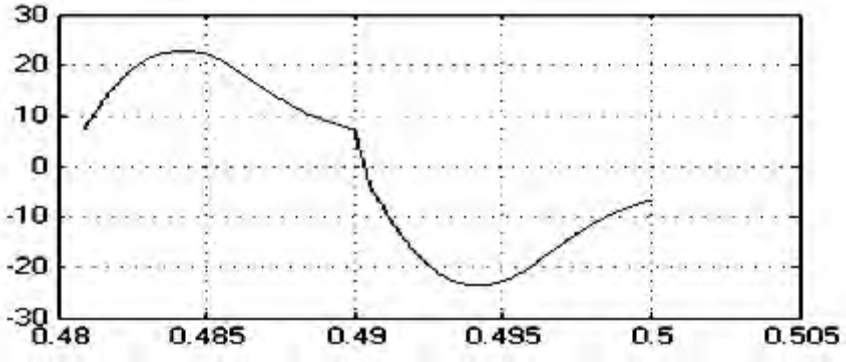

Figure 6.24: PV Output Current

The distortions on the signals are as a result of the harmonics introduced by the three inverter circuit. As mentioned earlier, these harmonics can be removed by using the true sine wave inverter which is not covered in this dissertation.

6.9 Discussion

A step-by-step procedure for modelling a single-diode photovoltaic module is presented in this chapter. This serves as an aid to induce more people into photovoltaic research and gain a closer understanding of I-V and P-V characteristics of PV module. The objective of the method is to fit the mathematical I-V equation to the experimental remarkable points of the I-V curve of the practical array. The method obtains the parameters of the I-V equations by using the following nominal information from the array datasheet: open-circuit voltage, short-circuit current, maximum output power, voltage and current at the

maximum power point, current/temperature and voltage/temperature co-efficient. This chapter gives a closed solution for the problem of finding the parameters of the single-diode model equation of a practical photovoltaic array.

Equation 5.5 is used to express the dependence of the diode saturation current I_o on the temperature was discussed and used in the model. The result obtained in the modelling of a practical photovoltaic array has demonstrated that the equation is effective. Moreover the same equation was able to adjust the I-V curve at the open-circuit voltages as well as temperatures different from the nominal temperature.

A Matlab codes in appendix A are used to plot the current-voltage and power-voltage characteristics of the panel hence the performance of the PV at different solar intensities are illustrated.

Apart from the PV panel, power electronic devices such as the MPPT, DC-DC converters, transformers and inverters were also modeled and coupled to the PV panel to ensure good quality ac output signal.

Chapter 7
Economic Modelling of CSP/PV Using SAM

The input parameters used in these simulations are based on the draft document of the Review of Renewable Energy Feed-in-Tariff (REFIT) of the National Energy Regulator of South Africa (NERSA) consultation paper March 2011 [245]. The exchange of R8.60 to $1 is used.

7.1. Variable names and Abbreviations

The following table lists the variable names used in this manual. For each variable, a letter in italics indicates the type of quantity the variable represents, and the subscript describes the quantity.

Table 7.1: Variable Names and Units

Name	Description	Units
A	Area	m^2
C_p	Heat capacity	J/kg-m^3
D	Length	m
E	Electric output	W_e
F	Multiplier factor	-
H	Enthalpy	Joules per kilogram
H	Hour	h
M	Mass flow rate	Kg/s
N	Number or quality	
[N]	Nearest integer greater than or equal to the quantity enclosed in brackets	
P	Power rating	W_e

Q	Thermal energy	W_h
T	Degrees Celsius	$^{\circ}C$
T	Time	hr
V	Velocity	m/s
V	Volume	gallons
Y	Year	y
Θ	Angle (theta)	Degrees $^{\circ}$
P	Density (rho)	Kg/m^3

7.2. Climate Input

In 2007, the terms of the Act, the energy regulator commissioned a study on the Renewable Energy Feed-in-tariffs (REFITs) to support renewable energies in South Africa. The Feed-in tariffs (FITs) would be based on the levelized cost of electricity (LCOE). The term of the Power Purchase Agreement (PPA) is to be twenty years and is to be reviewed every year for 5 years of implementation and every 3 years thereafter and the resulting tariffs will apply to new projects only [245].

In March 2009, the first REFIT tariffs were announced for wind, small hydro, landfill-to-gas and CSP (parabolic trough with 6hr storage [245]. In October 2009, the second REFIT tariffs were announced for CSP (without storage), PV, solid biomass, biogas and CSP (with 6hrs storage). On March 2011, the REFIT tariffs were revised, and it was proposed to reduce tariffs between 7.3 to 41.5 %. In August 2011, the 'REBID' was announced with 5 bidding windows: November 2011, March/August 2012, and March/August 2013. The initial total renewable energy allocation (RE) was increased from 1250 to 3725 MW [245], [246].

7.3. Financial Assumptions of the Analysis

Because of the absence of the specific case studies on renewable energy projects in South Africa, the following assumptions have been made

- 50 % of the equipment is imported,
- 50 % of the equipment is sourced locally,
- 45 % of the material is sourced locally,
- 55 % of the construction labour is sourced locally.

The US-based costs from SAM are used and the results are converted to the South African Rand for the simplicity. Inflation is assumed to be constant because inflation forecasting is not covered in this dissertation. Table 7.2 shows the summary of the financial assumptions.

Table 7.2: Financial Inputs

Financial Parameters	Value
Discount Rate	8 %
Debt fraction	70 %
Equity fraction	30 %
Real Cost of Debt before tax	6 %
National Tax Rate	28 %
Exchange Rate	8.6 %
Project Lifetime	20 Years

7.4. Climate Input

The climate input page shows detailed weather information of the location on the plant. In this case, Cape Town weather data is selected. The weather data of Cape Town is shown in table 7.3.

Table 7.3: Weather Data of Cape Town

Location Details	
City	Cape Town
Time zone	GMT+2
Elevation (m)	47 m
Latitude (deg)	-33.98
Longitude (deg)	18.6 deg.
Annual Weather Data Information	
Direct Normal Irradiance (DNI) kWh/m^2	1923.9
Global Horizontal Irradiance kWh/m^2	1900.7
Dry-bulb temperature $^{\circ}$C	16.5
Wind speed (m/s)	5.1

The graph in figure 7.1 shows annual DNI of the Cape Town weather from Oct 4 to Oct 8. Figure 7.2 is the annual DNI chart.

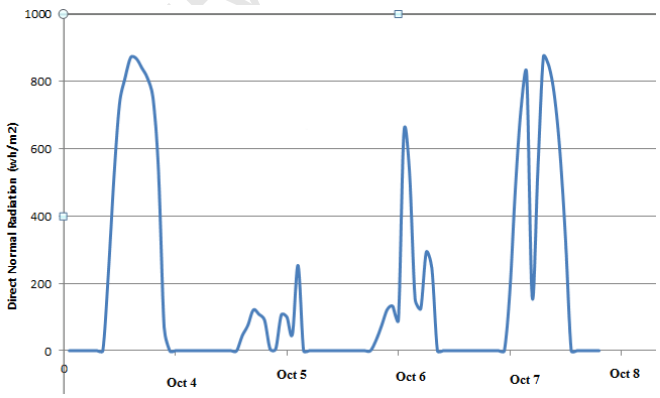

Figure 7.1: Direct Normal Radiation of Cape Town Weather

The DNI is minimal in winter which coincides with the months of April to September afterwards it peaks between the months of October to March which are the summer months of South Africa. The temperature profile of Cape Town shown in figure 7.3 also fluctuates between 0 and 35 $^{\circ}$C. The minimum temperature occurs in the winter around July while the maximum temperature is felt in March.

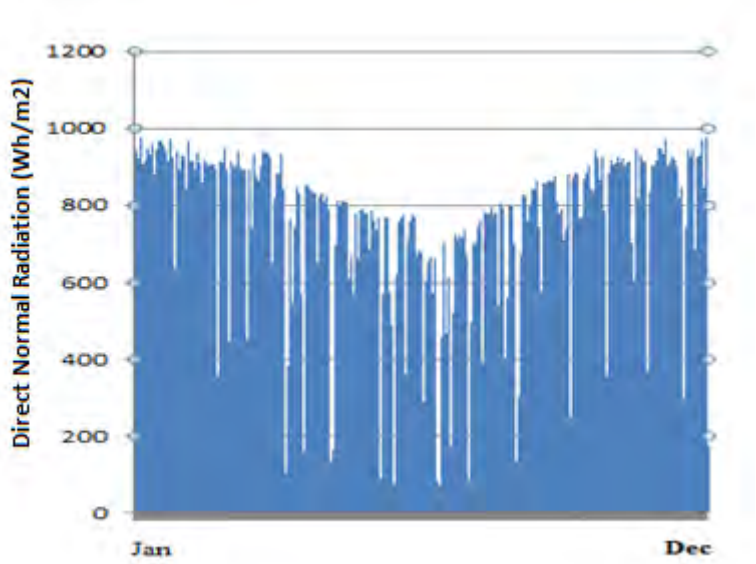

Figure 7.2: Hourly DNI chart of the Cape Town weather

The dry bulb temperature (DBT) is the temperature of air measured by a thermometer freely exposed to the air but shielded from radiation and moisture.

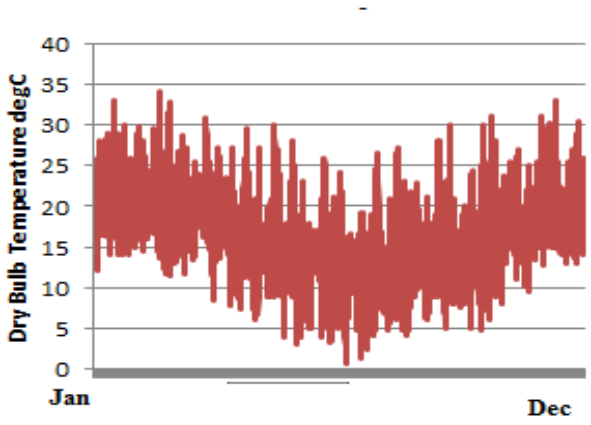

Figure 7.3: Dry bulb temperature hourly time series

It is the temperature that is usually thought of as air temperature and it is the true thermodynamic temperature. Other weather data such as dew point temperature, relative humidity, opaque sky are available in the Dview window of the weather data information of SAM.

7.5. Inflation/Interest Rates

On the financing page, the 50 year chart of South African Consumer Price Inflation (CPI) rate is 6 % which is the current inflation figure of South Africa is shown in figure 7.4 [247], [248].

Figure 7.4: Consumer Inflation Chart of South [247]

The CPI fluctuates within the range of -1 and 21 %. Using this range of inflation, we plot the expected levels of LCOE of our plant.

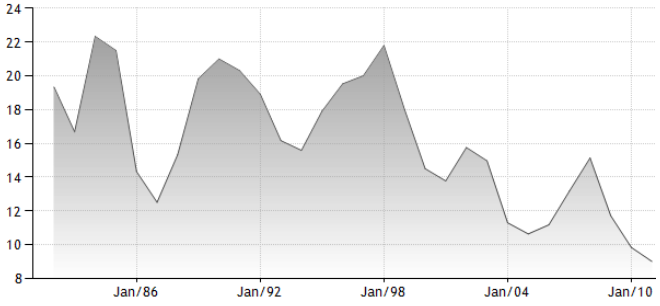

Figure 7.5: The South Africa interest rate 30 yr chart [248]

Figure 7.5 shows the interest rate chart of SA between 1986 and 2010. The interest rate fluctuated between 5 and 22 %. Increased rate of inflation reduces the cost of the energy produced using this plant.

7.6. Power Purchase Agreement (PPA)

The first year PPA price is the electricity sale price for the projects with Utility or commercial-third party ownership. Here in South Africa this is sale price is called REFIT tariff. The PPA escalation rate is an annual escalation rate that SAM uses to calculate future electricity sale prices based on the first PPA price. This value was discussed in the section 7.9.1; operation and maintenance. NERSA approved term is 20 years. The tax rate is fixed at 28 %. The REFIT escalation is given by the formula

$$\mathrm{REFIT_{j+1}} = \mathrm{Capex_{2011}} + \left(\mathrm{FOM_j} + \mathrm{VOM_j} + \mathrm{FUEL_j}\right)\mathrm{X}\left(1 + \mathrm{RSA_{CPI_j}}/100\right) \quad . \qquad (7.1)$$

Where:

j = calendar year ≥ 2011

$\mathrm{REFIT_j}$= PPA tariff in tear j

$CAPEX_{2011}$ = capital expenditure, Capex, R/kWh

FOM = Fixed Operation and Maintenance in year j, R/kWh

VOM = variable operation and Maintenance in year j, R/kWh

RSA_CPI_j= Actual South Africa CPI for year j [245]

7.7. REFIT escalation comments

The REFIT escalation exclusively reduced to the operation and maintenance hence the non-escalated part of the tariff losses value in real terms ZAR inflation proceeds over the REFIT lifetime. The investors and lenders would have to enter into long term currency hedges like ZAR-USD or ZAR-EUR. The ZAR-USD exchange rate benchmark used by NERSA is ZAR7.4 to $1 while the cost of hedging would be included in the operation and maintenance cost [245]. The tariff should balance the forex shock thereby enabling and mobilizing both local and foreign debt finance and equity investment. The Southern African Solar Thermal and Electricity Association (SASTELA) is an umbrella that unites solar companies in the Southern African region. Some their participants are EMVELO,

DBSA, IDC, SIEMENS, Exxaro, Areva, University of Stellenbosch, EARTH, quartile capital, Sol Africa, Abengoa Solar, Group five, Sessa, Standard bank, Alstom, Bridge capital and Built Africa [249].

7.8. Real Discount Rate

The real discount rate refers to the factor used in the present value calculation that indicates the time value of money thereby equating current and future costs. According to the Energy Department document on the input parameters, the discount rate should be set at real (after inflation) rate of 8 % per annum [250].

Other technical inputs are the Tower system costs like the direct capital costs which include the site improvements, heliostat field etc. The indirect capital costs are owners equity, land costs and the rest. The total installed cost and the operation, annual performance and maintenance cost are worked out by SAM.

7.9.Economic Model of 100 MW Concentrated Solar Power

All the inputs discussed up to this point are used for the simulations of both the concentrated solar power and the photovoltaic systems. The input parameters will be discussed from this point are used for CSP while those of the PV would be discussed in section 7.10.

7.9.1. Operation and Maintenance

Table 7.4 shows the REFIT adjustments of the CSP with 6 hrs storage from 2011 to 2013. The adjustments are based on the South African consumer price index. On the total the adjustments added R0.01 yearly on the REFIT price from 2011 through to 2012. VOM is the variable operations and maintenance, CAPEX is the capital expenditure while FOM is the fixed expenditure. REFIT escalation is therefore calculated as the ratio of increase in

LCOE from 2011 to 2012 which is equal to 1.006 % as shown in page 29 of NERSA REFIT document [249].

Table 7.4: **REFIT Adjustments with CPI [249]**

CSP CPI adjustments	2011	2012	2013
CAPEX R/kWh	1.24	1.24	1.24
FOM R/kWh	0.15	0.16	0.17
Fuel R/kWh	0.0027	0.0029	0.0030
VOM	0.00	0.00	0.00
Total (ZAR)	1.39	1.40	1.41

7.9.2. Solar Multiple

Solar Multiple (SM) is the ratio of the receiver`s design thermal output to the power block`s design thermal input. For systems with no storage, the solar multiple should be close to or equal to one.

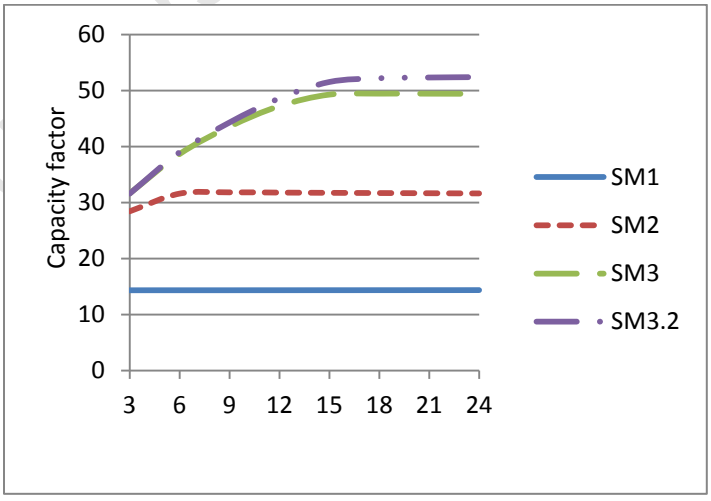

Figure 7.6: TES versus capacity factor

NERSA specifies a capacity factor of 40 % which corresponds to the solar multiple of 3.2 and thermal energy storage (TES) of 6 hrs. Figure 7.6 shows the chart of capacity factor against solar multiple. It can be seen that as the solar multiple increases, the capacity factor increases as well as shown in figure 7.7. Hence, the plant produces more energy annually and the overall cost of installation increases. The capacity factor of a plant is the ratio of the actual amount of energy produced over the maximum energy that it can produce if the plant was to operate at full load hourly round the year (i.e. 8760 hrs).

The chart of capacity factor against solar multiple is shown in figure 7.6. As the solar multiple increases the capacity factor increases as well. Hence the plant produces more energy annually and the overall cost of installation also goes up.

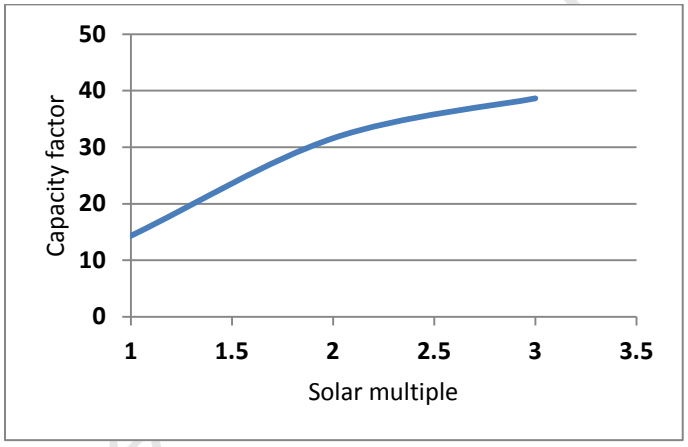

Figure 7.7: Solar multiple versus capacity factor TES=6 hrs

7.9.3. Optimization of the Power Tower

The power tower optimization simplifies the task of choosing values for the relatively large number of input parameters required to specify the power tower solar field and receiver. Because the heliostat field is typically the most capital intensive part of the power tower project, often accounting for 30-40 % of the total installation cost, optimizing the heliostat field is a critical step in minimizing overall project cost. The optimization wizard searches for a set of optimal system parameters. The optimal system is defined as a set of parameters that results in the lowest levelized cost of energy. In this

case, the solar multiple of 3.2 produces the capacity factor of over 50 % the solar multiple tab in the optimization wizard is set to 3.2 and run the optimization. Then set the thermal energy storage to 15 hrs and then run the rest of the simulation to obtain the results shown section 7.17.

7.9.4. Analysis Period

The analysis period is the number of years covered by the analysis. This is typically equivalent to the project or investment life and it is the number of years in the project`s cash flow. The term of the Power Purchase Agreement (PPA) is a legal contract between an electricity generator (provider) and a power purchaser. The duration of the contract is the analysis period and in this case, it is 20 years [245]. Figure 7.8 shows the general relationship between the LCOE and the analysis period. Longer analysis period results in lower the LCOE.

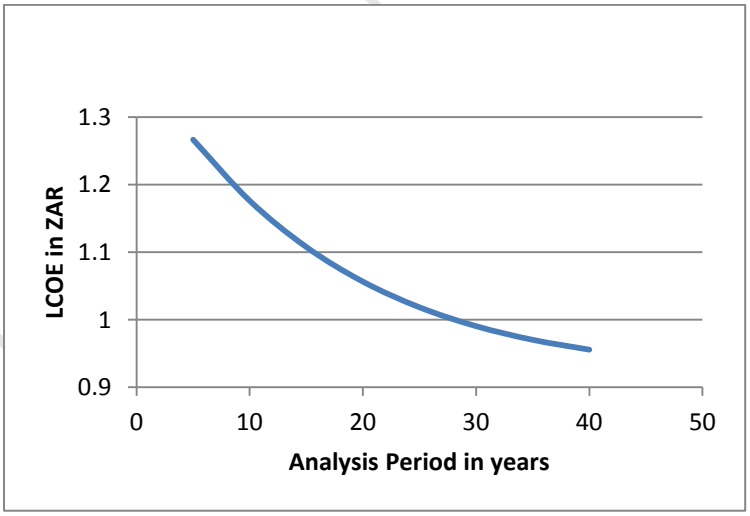

Figure 7.8: The variation of LCOE with the analysis period

7.9.5. Capacity factor

The capacity factor (CF) is the ratio of the system`s predicted electrical output in the first year of operation to the output had the system operated at its nameplate capacity.
Figure 7.9 shows the variation of the capacity factor with the thermal energy storage and LCOE. At a certain TES in this case 15 hrs, the capacity factor reaches the maximum, 52 % and remains there. Likewise the LCOE bottoms at the same value of TES (15 hrs) and remains there.

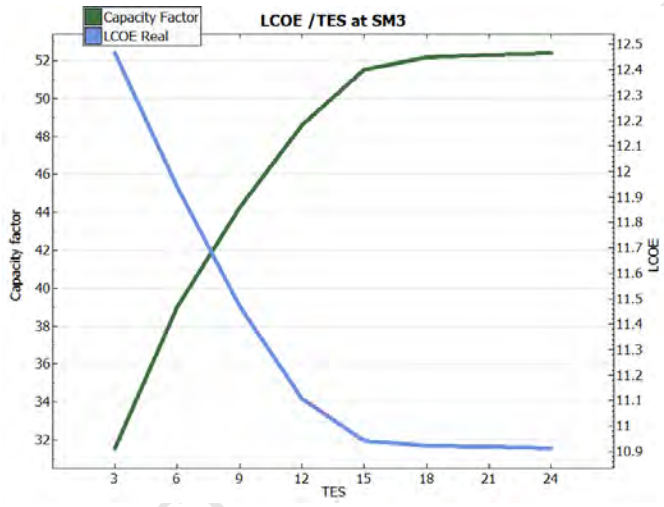

Figure 7.9: Capacity factor versus TES and LCOE

7.9.6. Debt Fraction

Figure 7.10 is the graph of the variation of the LCOE with the debt fraction. LCOE is minimal a debt fraction of 50 %. To achieve the cheapest cost of electricity, a debt fraction of 50 % must be maintained. The other 50 % of the capital should be sourced through partners/equities. However, selecting the second option which specifies the first PPA (or REFIT) price which in this case is R1.41 or $0.162 SAM does not use debt fraction in the calculations of LCOE under this plan.

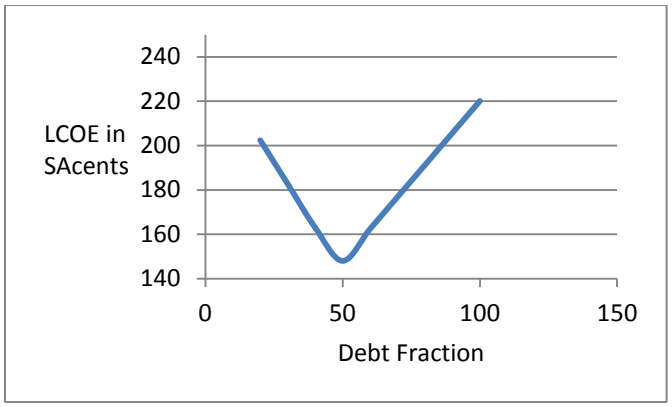

Figure 7.10: Debt fraction /LCOE

7.9.7. Condenser Type

Three types of condensers are supported by SAM. They are the evaporation type, the air-cooled type, and the hybrid type. In place with enough water, the evaporation type is the most economical as shown in figure 7.11. However, the difference between the cost of dry cooling and evaporative cooling is very little, to save fresh water air cooled condenser is recommended.

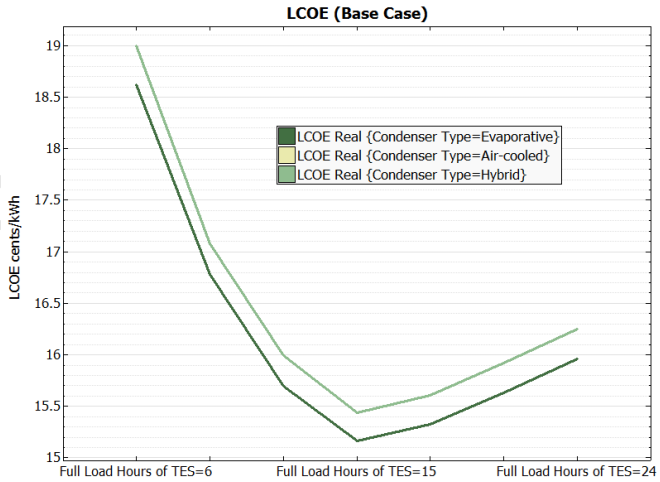

Figure 7.11: Variations of LCOE with the Condenser Type

7.9.8. Estimated Net Output at Design (Name Plate) Capacity

This is the power cycle`s nominal capacity , calculated as the product of the design gross output and estimated gross to net conversion factor. This is given by the equation 7.2

Estimated Net Output at Design (MW_e) = Design Gross Output (MW_e) x Estimated Gross to Net Conversion Factor (7.2)

SAM uses estimated gross to net conversion to calculate the system`s rated capacity related calculations, which includes the estimated total cost per net capacity value of the system cost page and the capacity factor reported in the result [221]. The sensitivity of the LCOE to the sizing of the CSP plant (Nameplate capacity) is shown in figure 7.12. It is worth noting that at different predetermined levels of thermal energy storage the CSP power tower LCOE shows no sensitivity to the changes in the nameplate capacity which was increased from 10 to 1000 MW. This is particularly important when determining the economic size of the CSP plant.

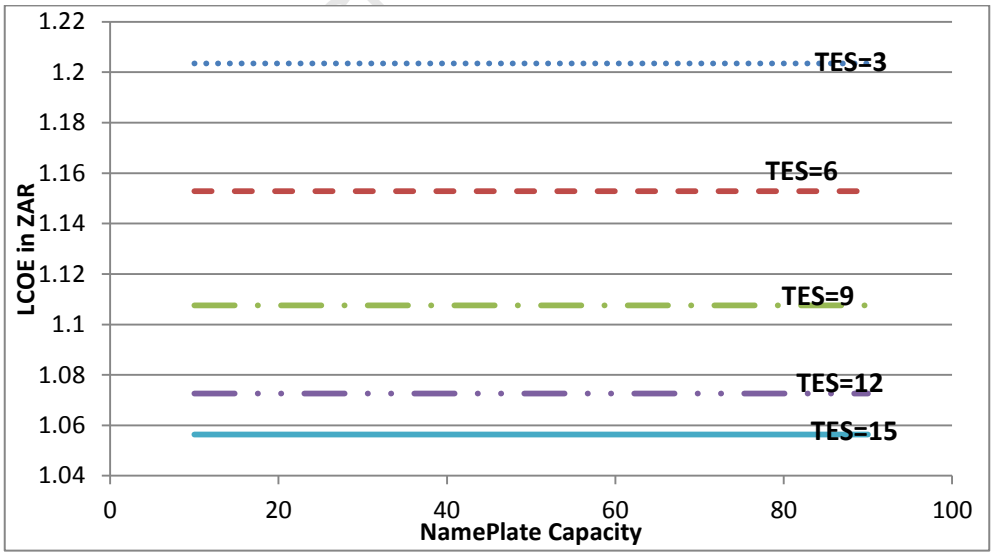

Figure 7.12: Relationship of LCOE with Nameplate Capacity

7.9.9. The Base Case (First Scenario)

The base case used in this simulation is CSP whose inputs are derived from the REFIT. However this case targets the internal rate of return (IRR) of 17 % [245]. Table 7.5 gives the summary of the base case input parameters.

Table 7.5: Summary of the Base Case Inputs

Inputs	Values
Climate	Cape Town
Nameplate Capacity	100 MW
Inflation Rate	5 %
Real discount rate	8 %
Loan Term	20 yrs
Debt Fraction	50 %
Solar Multiple	3.2
Thermal Storage (TES)	15 hrs
First year PPA Price	0.162
PPA Escalation Rate	1.006 %
Condenser type	evaporation
Tax Rate	28 %
Internal Rate of Return (IRR)	17 %
Loan Rate	6 %
Operation and maintenance	R0.16/ kWh

Table 7.8 shows the result of the REFIT case. Again the 6 hrs benchmark given by REFIT does not result in the lowest LCOE. The lowest LCOE occurs when the thermal energy storage is 15 hrs which corresponds to R1.05/ kWh. This is about 40 % mark-up from R1.40/ kWh given by NERSA. The LCOE in this case is almost the same as the REFIT price. The profit is very marginal in this case.

Table 7.6: Base Case Results

Metric	**Cost in Rand** (1US$=ZAR8.6)
Total Direct Cost	R7, 077, 800,000
Total Installed Cost	R8, 003, 000,000
Total Installed Cost per Capacity	R80,000/ kW
Analysis Period	20 Yrs
Net Annual Energy	451, 000,000 kWh
First year PPA price	R1.54/ kWh
LCOE Real	R1.17/ kWh
After Tax Net Present value (NPV)	R318, 200, 000
Gross to Net conversion Factor	0.89
Debt Fraction	50 %
Capacity Factor	51.5 %
PPA price escalation	1.01 %
Annual Water Usage	1, 545, 095 m^3
Total Land Area	2711.89 acres

Figure 7.13 shows the variation of the LCOE with the TES at a solar multiple of 3.2 and an IRR of 17 %. The six hours storage with even though is the benchmark of REFIT does not result in the lowest LCOE.

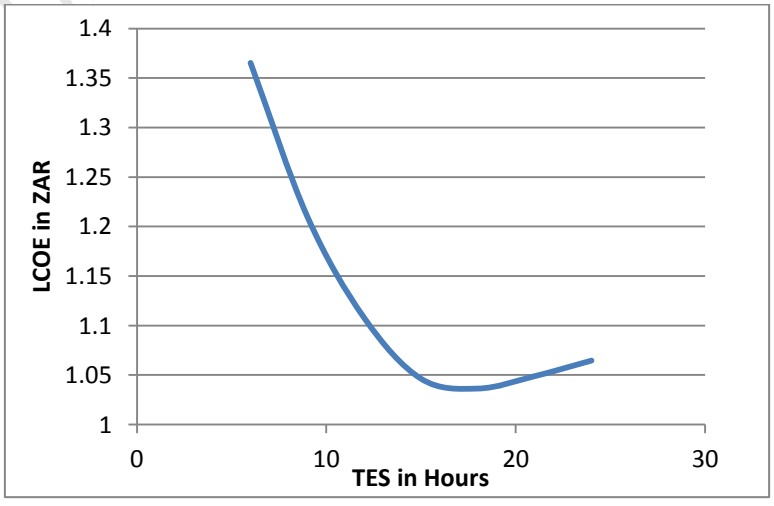

Figure 7.13: The LCOE/TES chart of the base case

7.9.10. Refit Case (Second Scenario)

In this case, the first year PPA price is set to the REFIT tariff (R1.40) and PPA escalation of 1.006 %/yr. SAM configures the plant to maximize IRR based on the given parameters. Table 7.7 shows the summary of the input parameters and table 7.8 shows the results.

Table 7.7: Input summary of the Refit Case

Inputs	Values
Climate	Cape Town
Nameplate Capacity	100 MW
Inflation Rate	5 %
Real discount rate	8 %
Loan Term	20 yrs
Debt Fraction	70 %
Solar Multiple	3.2
Thermal Storage (TES)	15 Hrs
First year PPA Price	0.162
PPA Escalation Rate	1.006 %
Condenser type	Evaporation
Tax Rate	28 %
Loan Rate	6 %

Table 7.6 shows the result of the REFIT case. Again the 6 hrs benchmark given by REFIT does not result in the lowest LCOE. The lowest LCOE occurs when the thermal energy storage is 15 hrs which corresponds to R1.05/ kWh of electricity. This is about 40 % mark-up from R1.40/ kWh given by NERSA. In this case, minimum LCOE is found at R1.00 per kWh (11.73 US cents) or which corresponds to TES of 15 hrs and it remains there up to TES of 24 hrs as shown in figure 7.14.

Table 7.8: **The Summary of the Refit Case Inputs**

Metric	**Cost (1USD=ZAR8.6)**
Total Direct Cost	R7, 077,000,000
Total Installed Cost	R8, 281,000,000
Total Installed Cost per Capacity	R82, 560/ kW
Net Annual Energy	451, 561, 665 kWh
First year PPA price	R1.39/ kWh
LCOE Real	R1.05/ kWh
After Tax Net Present value (NPV)	R197, 000,000
Gross to Net conversion Factor	0.89
Debt Fraction	70 %
Capacity Factor	51.6 %
Annual Water Usage	1, 217, 669 m^3
Total Land Area	2711.89 acres

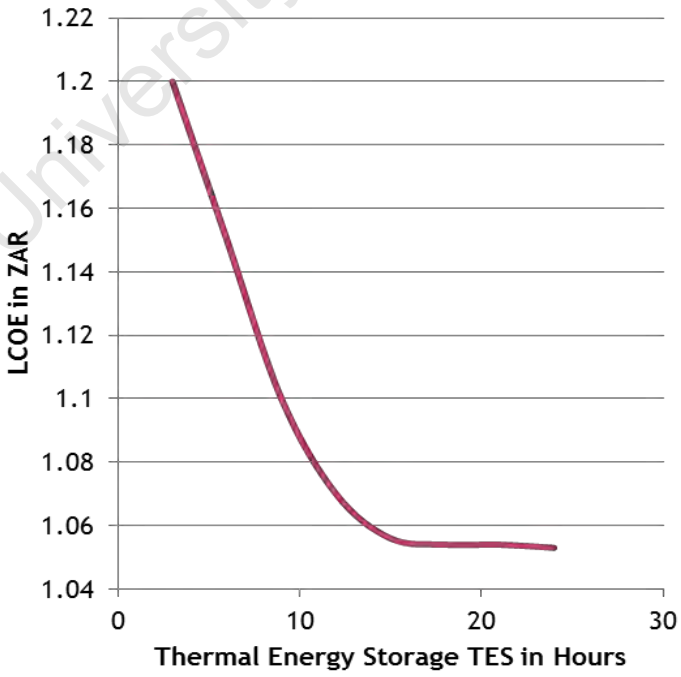

Figure 7.14: LCOE/TES for the REFIT case

7.9.11. Loan Rate

Loan rate is the annual loan interest rate. This value is used by SAM when the internal rate of return (IRR) is chosen and figure 7.15 shows its relationship with LCOE.

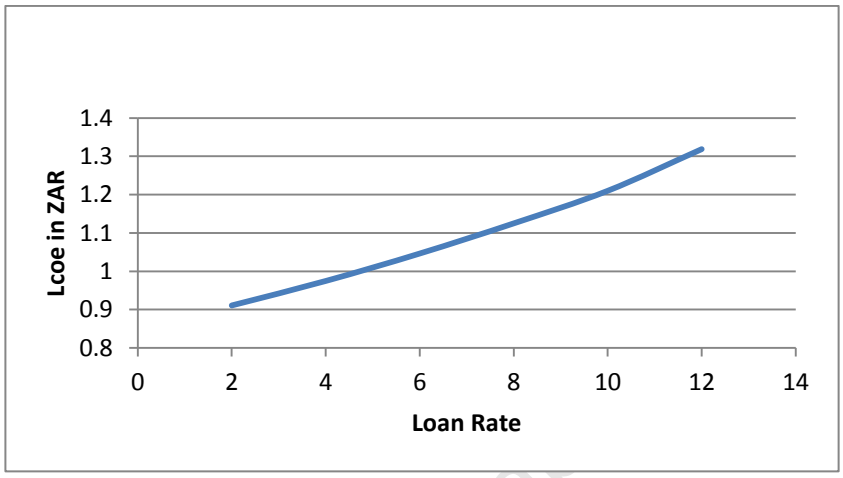

Figure 7.15: LCOE versus Loan Rate

7.9.12. Annual Energy Flow

Figure 7.16 shows the annual performance of the CSP plant with respect to the energy reaching the plant in the form of incident solar radiation. The incident energy to the solar field is 3,500 GWh. From the chart it can be seen that the solar field has an efficiency of 37.5 %. The annual energy output is about 500 GWh which accounts to about 11 % efficiency.

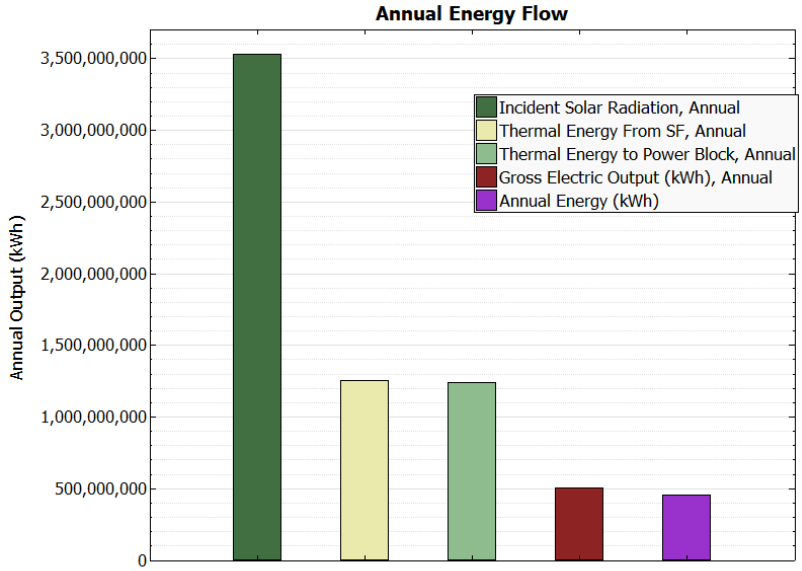

Figure 7.16: **Annual Energy Flow**

7.9.13. LCOE vs Tax Rate

The effects of the tax rate on the LCOE is shown in figure 7.17. The optimal tax rate occurring around 32 %. In this case, the tax rate of 28 % which is the South African tax rate as specified by the NERSA document is used.

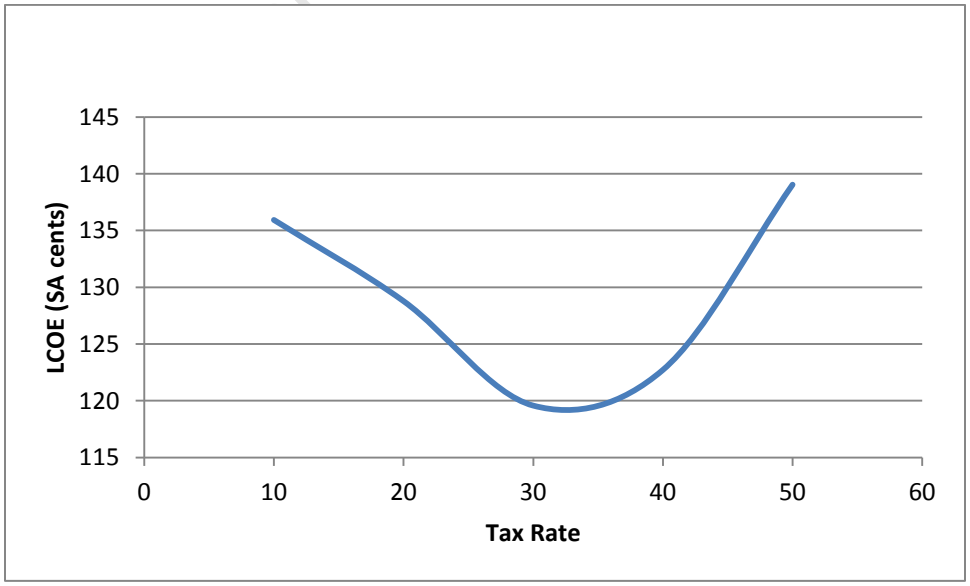

Figure 7.17: **Variation of the LCOE with the Tax Rate**

7.9.14. Discussion

The REFIT document recommends the sale price of electricity for each technology for the 20 year term. For the CSP with 6 hr storage, the REFIT price is R1.408 per kWh. NERSA on page 22 of the 2011 consultation document made an assumption of 17 % return on equity after tax, this value is used as the internal rate of return (IRR) in SAM [245] to obtain two exclusive scenarios.

The first scenario aims at 17% return on equity. Hence, a solar plant is modelled with SAM using the REFIT input parameters; however, in the financial page of the molten salt power tower, IRR and PPA escalation rate are fixed at 17 % and 1.006 % respectively. This configuration yielded an LCOE of R1.17/ kWh which is higher than that of the second scenario. This scenario would be very useful where loan could be secured from countries with lower loan rates. Figure 7.17 shows the dependence of the LCOE on the loan rates.

In the second scenario, we set the first year power purchase agreement (PPA) to R1.406/ kWh, escalation to 1.006 %/yr and the resulting LCOE is R1.00/ kWh. This is about a 40 % mark up from the REFIT price. The capacity factor is 50 % about 10 % higher than the recommended capacity factor which is 40 %. The thermal energy storage (TES) is set to 15 hrs. REFIT recommended TES is 6 hrs but this would mean a lower capacity factor and higher LCOE. The better way to increase the capacity factor would be by increasing the solar multiple from the default 1.9 to 3.2 as shown in figure 7.6 after which value of TES is increased to 15hrs which is the lowest point on the LCOE/TES curve in figures 7.13 and 7.14. This suggests that the plant should be run as a base load-generation. Both the annual energy produced and the total installed capacity would be increased but this would be better than constructing another solar plant.

Evaporation type condenser showed some savings in LCOE compared to the dry cooling type shown in figure 7.11 in locations where fresh water is available. However, fresh water resources supply being a global crisis is not always available. It is also worth noting that the switching from the evaporative cooling to dry cooling would add an extra 7 % to the LCOE. The plant LCOE showed no sensitivity to the nameplate capacity when the LCOE was simulated for nameplate capacities ranging from 10 to 100 MW.

This suggests that smaller plant sizes such as 10 MW could make more economic sense. Minimal LCOE was also found in the debt fraction of 50 %. The other 50 % could be sourced from equities. Another way the government could support the renewable energy generation is by creating special funding for the green projects. The round trip efficiency of the plant is about 13 % which is very low compared with that of the best photovoltaic panels (about 40 %).

7.10. Economic Modelling of 2.5 kW Photovoltaic System

Modeling and simulation of the 2.5 kW photovoltaic system was discussed chapters 5 and 6. In this section, the economic simulation of the grid-connected photovoltaic system using the same parameters used in the simulation of the 100 MW CSP is reported.

7.10.1. Module Characteristics

For the purposes of this simulation, SunPower SPR-210-BLK-U module is selected from the list of available PV modules. The standard reference conditions are total Irradiance of 1000 M/m^2 and cell temp of 25 $^{\circ}$C. The physical layout of the module array is shown in figure 7.18.

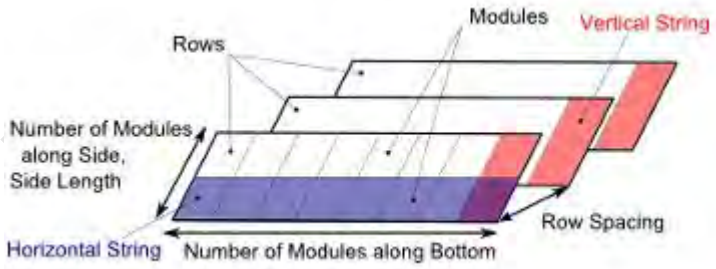

Figure 7.18: **The Physical PV Array**

The vertical strings and the horizontal strings of the PV modules are set up in parallel rows which define the tilt angle with the ground. At standard operating conditions the PV panel is tested and the I-V characterististics of the PV module is plotted as shown in figure 7.19. The chart shows that between 0 V and 40 V the output current is fairly stable

at 5.25 A which rapidly drops at 40 V because of the inherent PN junction characteristics of the panel.

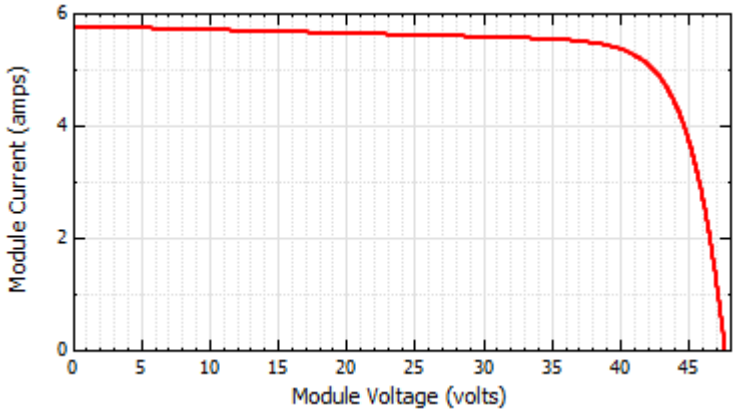

Figure 7.19: **IV characteristics of SunPower SPR-210-BLK-U**

The open circuit voltage and the short circuit current which are given by the manufacturer of the panel are 47.7 V_{dc} and 5.75 A_{dc} respectively. Other parameters supplied by the PV manufacturers are the panel efficiency, maximum power, max power current and Max Power voltage. These parameters are shown in Table 7.9.

Table 7.9: **Module Parameters**

Parameters	**Values**
Efficiency	17.30
Maximum Power (P_{mp})	215 W_{dc}
Max Power Voltage (V_{mp})	41 V_{dc}
Max Power Current (I_{mp})	5.25 A_{dc}
Open Circuit Voltage (V_{oc})	47.7 V_{dc}
Short Circuit (I_{sc})	5.75 A_{dc}
Material	Mono-c-Si
Module Area	1.244 m^2
Number of Cells	72

7.10.2. Inverter Characteristics

Inverter make/model: Sandia Inverters/SMA America: SB4000US 208V is chosen from the list of the available inverters. The efficiency and rated output power of the inverter are shown in figure 7.20. At 0 % rated power, the inverter efficiency is zero. The efficiency rises rapidly from zero to a peak value of 95 % and settles there for V_{dco}, MPPT-low and MPPT-hi [252]. MPPT-low (Vdc) is the manufacturer-specified minimum DC operating voltage as described in CEC test protocol [252]. MPPT-hi (Vdc) is the manufacturer-specified maximum DC operating voltage, as described in the CEC test protocol. The test protocol specifies that the inverter`s maximum DC voltage should not exceed 80 % of the array`s maximum allowable open circuit voltage [221].

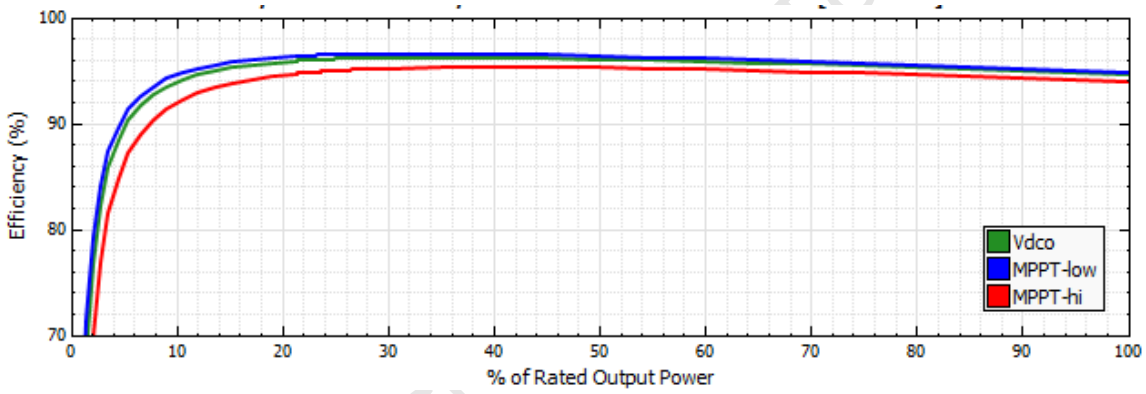

Figure 7.20: **The Efficiency/ Rated Output Power of the Inverter**

Table 7.10: **Inverter Parameters**

Parameters	Values
AC Voltage	208 V
Power AC_o	3500 W
Power DC_o	3700.17 W
Power S_o	17.36 W
Power n Tare	0.14 W
V_{dcmax}	0 V
I_{dcmax}	0 A

The manufacturer`s specification data of the SB4000US 208 V inverter which are included are AC voltage, AC output Power, DC output power DC maximum voltage etc. The inverter`s parameters are given in Table 7.10.

7.10.3. Array Layout

The size of the PV system is specified as follows;

- Desired array size is 2.5 kW_{dc}
- Number of modules per string is 9
- Number of strings in Parallel is 1
- Number of Inverters is 1

Note: Array DC capacity is 47 % of inverter DC capacity.

Actual Layout

The SAM software uses the desired array size to compute the actual layout of the panel which includes the nameplate capacity, number of modules, modules per string as shown in table 7.11.

Table 7.11: **Parameters of the Actual Layout of the panel**

Parameters	Values
Nameplate Capacity	1.722 kW_{dc}
Number of Modules	8
Modules per String	8
Strings in Parallel	1
Total Module Area	9.952 m^2
V_{OC} (String)	381.6 V
V_{mp} (String)	328 V

Other inputs which include the location climate, inflation rate and loan rate are same as in the CSP model. Table 7.12 shows the summary of the inputs.

Table 7.12: **Financial Input Parameters of the PV System**

Inputs	**Values**
Climate	Cape Town Climate
Inflation Rate	5 %
Discount Rate	8 %
Loan Rate	6 %
Analysis period	20 %
Debt Fraction	70 %

7.10.4. Economic Simulation Results

The cost of electricity generated by the photovoltaic systems includes the cost of generating electricity at the point of connection to the load or grid and it includes capital, discount rate as well as the costs of continuous operation, fuel and maintenance. The levelized cost of electricity (LCOE) is given by the equation (4.10) of Section 4.1.5.

Table 7.13; Summary of the PV Outputs

Total Installed Cost	R97, 200
Total installed cost per capacity	R56.7/ W_{DC}
Annual Energy Output	3,275 kWh
Capacity factor	14.9 %
Annual Cost of Energy	R7, 041
LCOE	R2.15
Payback Period	18.33 years

The monthly electrical energy output of the panel is shown in figure 7.21. The electrical energy output of the photovoltaic panel is best (about 400 kWh) in summer period than in the winter because during this period, sunlight is at its peak and shines for longer hours of the day. Cloud cover is also minimal. Net metering is available on application at the City of Cape Town. This means that for the months of Nov. to Feb., where energy production is at its peak, excess energy could be fed into the grid using the grid as storage. In winter

months between April and September when PV output is minimal and demand is highest the stored energy from the grid would be recovered. Hence the net energy is what is owed to the utility. Figure 7.21 shows the estimated monthly electrical energy output of the PV system.

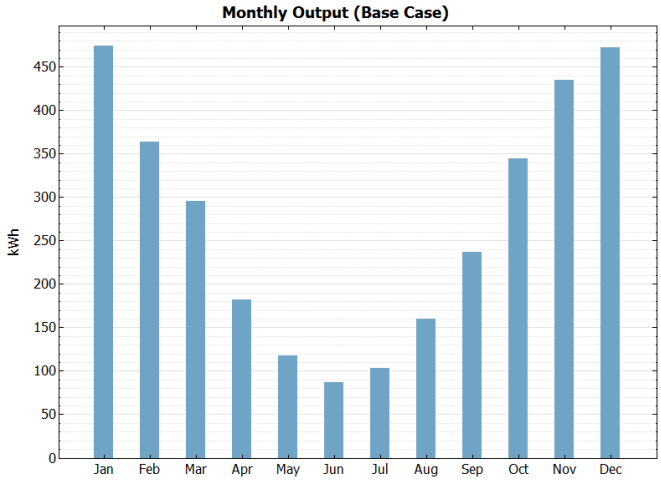

Figure 7.21: Monthly electrical energy output of the PV system

7.10.5. City of Cape Town Domestic Energy Tariff

The City of Cape Town is the utility that provides electricity to the Cape Town area.

Table 7.14: Domestic Energy Charges

Domestic Energy Charge	
Blocks	Energy Charge R/kWh plus vat
Block 1 (0 – 150) kWh	1.29
Block 2 (150 – 350) kWh	1.34
Block 3 (350 – 600) kWh	1.34
Block 4 (>600) kWh	1.60

The schedule of electricity tariff which became effective from July 2012 classified domestic electricity consumer in four blocks as shown in table 7.14 [253]. The blocks represent the average measured energy usage over any period of twelve consecutive months.

7.10.6. Discussion

The cost of the PV panel from the simulation result in section 7.10.4 is about R2.15 which shows a substantial mark-up from the NERSA REFIT price of R3.94 (i.e. 83 %) [245]. This shows that for an independent power producer whose main purpose is to produce and sell electricity, the PV system is economically viable. For a residential consumer, the City of Cape Town utility charges up to R1.60 shown in Table 7.14 which is a lot cheaper than the cost of PV electricity generation in this simulation.

If a household whose monthly consumption is 350 kWh (i.e. Block 3 consumer shown in Table 7.14) is considered, then the yearly consumption is 4200 kWh (or 350 x 12). From Table 7.14, the total yearly electricity cost without the PV system is R5, 628 (or 4200 x R1.34). From Table 7.13, the total cost of PV installation is R97, 200 (or R7, 041 yearly) hence it will take approximately 17 years (or R97, 200/R5, 628) to payback the cost of PV system with the electricity bill. It can be categorically stated that PV systems are still not economical compared with the present grid electricity at least for now. However with the steady rise in the price of utility electricity and the steady fall of the cost of the PV systems it will not take long for both prices to converge. Government and utility incentives are therefore required to motivate consumers to invest in the residential photovoltaic systems. On the interim research efforts which are aimed at the development of materials and novel manufacturing methods that will bring down the cost of photovoltaic modules as well as power electronics should be encouraged

Chapter 8

Conclusions and Recommendations

The economic simulations of the concentrated solar power and photovoltaic systems using Systems Advisor Model (SAM) presented in this dissertation give insight into the planning and prediction of the performance of the solar plants. The parametric analysis suggests ways of maximizing the performance of a solar power plant by varying the input parameters such as analysis period, capacity factor and condenser type. Depending on the goal of the investor, the plant can be configured to maximize the amount of energy produced thereby maximizing the return on investment. The results obtained are based on 2011 NERSA consultation paper which is already two years old at time of this work. However, 2013 NERSA version is expected to be released this month. Based on data used, the levelized cost of electricity (LCOE) for the CSP plant modelled was R1.05 at 50 % capacity factor. The NERSA electricity tariff for the same CSP plant is R1.45. The levelized cost of electricity for a PV panel using the same parameters is R2.15 while NERSA tariff is R3.94 and the city of Cape Town charges up to R1.34/unit of electricity used. It can be inferred based on the simulation results obtained that CSP is economically viable for the Independent power producer and it is cheaper than the PV technology. These results are only indications and may be different if other parameters such as operations and maintenance for the current year are taken into considerations.

It is recommended that utilities and governments should invest in the Concentrated Solar Power technology while research efforts should be aimed at reducing the cost and increasing the efficiencies of the photovoltaic technologies. Furthermore, the cost of the PV system could be reduced further by the use of the current source inverters (CSIs) that require fewer components. More research is needed towards the development of the CSIs. For the CSPs, further research into the development of the solar fuels would boost the profitability of the CSP which is essentially a thermal plant.

Appendix

Appendix A

```
open_system('pv50')
nvals = 0;
figure
for gval = 0.2:0.2:1
    nvals =  nvals +1;
    gvalStr = num2str(gval,3);
    set_param('pv50/G1','Gain',gvalStr);
    sim('pv50');
  plot(v,i);
  hold on
end
hold off
```

Figure A.1: The Matlab code in script file that iterates irradiation levels

```
open_system('pv50')
nvals = 0;
figure
for gval = 0.2:0.2:1
    nvals =  nvals +1;
    gvalStr = num2str(gval,3);
    set_param('pv50/G1','Gain',gvalStr);
    sim('pv50');
  plot(v,p);
  hold on
end
hold off
```

Figure A.2: Iteration code for Power/Voltage characteristics

```
open_system('pv50')
nvals = 0;
figure
for gval = 25:25:75
    nvals =  nvals +1;
    gvalStr = num2str(gval,3);
    set_param('pv50/G2','Gain',gvalStr);
    sim('pv50');
  plot(v,i);
  hold on
end
hold off
```

Figure A.3: V-I characteristics at temperatures between 25 to 75°C

```
open_system('pv50')
nvals = 0;
figure
for gval = 25:25:75
    nvals =  nvals +1;
    gvalStr = num2str(gval,3);
    set_param('pv50/G2','Gain',gvalStr);
    sim('pv50');
  plot(v,p);
  hold on
end
hold off
```

Figure A.4: Iteration code of the P-V chart at changing temperatures

```
function y = MPPT(u,i,u0,i0,D)
m=0;
du=u-u0; di=i-i0;
if du==0
    if di==0,m=D;
    else
        if di>0, m=D-0.01;
        else
            m=D+0.01;
        end
    end
elseif di/du==-(i/u)
else
   if di/du>-(i/u),m=D-0.01;
   else
    m=D+0.01;
   end
 end
  y=m;
end
```

Figure A5: Incremental Algorithm (IC) code of the MPPT [238]

Appendix B

True Sine wave Inverters

Multilevel inverters

In recent years, industry has begun to demand higher power requirement which now reaches the megawatt level. Controlled ac drives in the megawatt range are usually connected to medium-voltage network. Today, it is hard to connect a single power semiconductor switch directly to medium voltage grids (such as 2.3, 3.3, 4.16, or 6.9KV). For these reasons, a new family of multilevel inverters has emerged as the solution for working with higher voltage levels

Advantages of a Multilevel Converter

- They give a better quality signal which is closer to true sinusoid
- They can increase the inverter operating voltage without increasing the device rating
- They minimize the THD with low switching frequencies,
- They reduce the EMI due to lower voltage steps

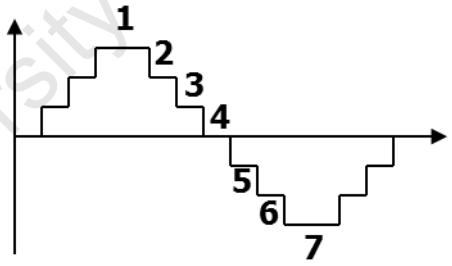

Figure B1: Seven-level inverter

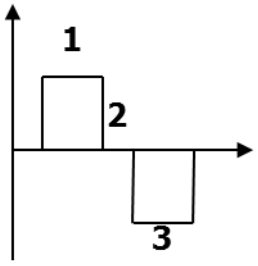

Figure B.2: Three-level inverter

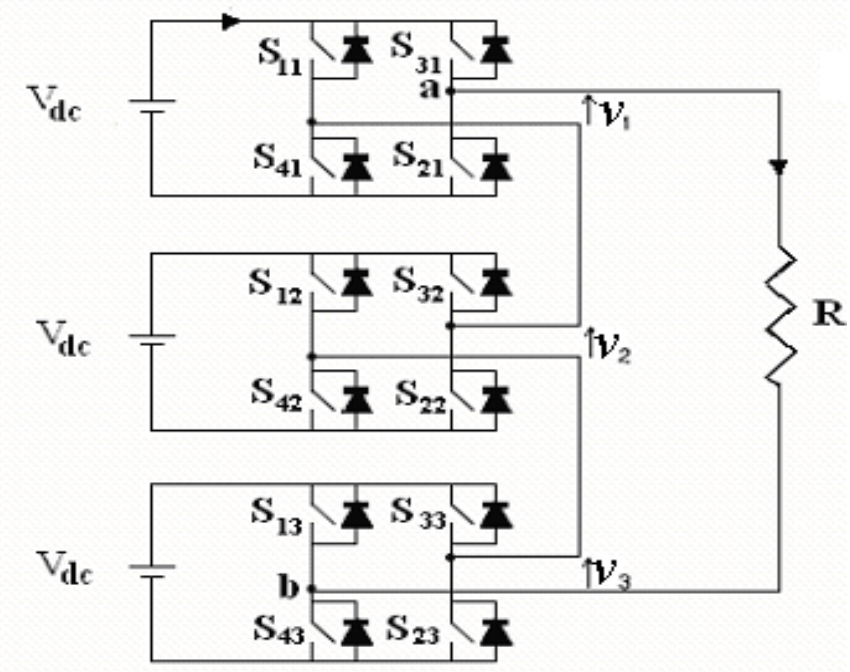

Figure B.3: cascaded inverter

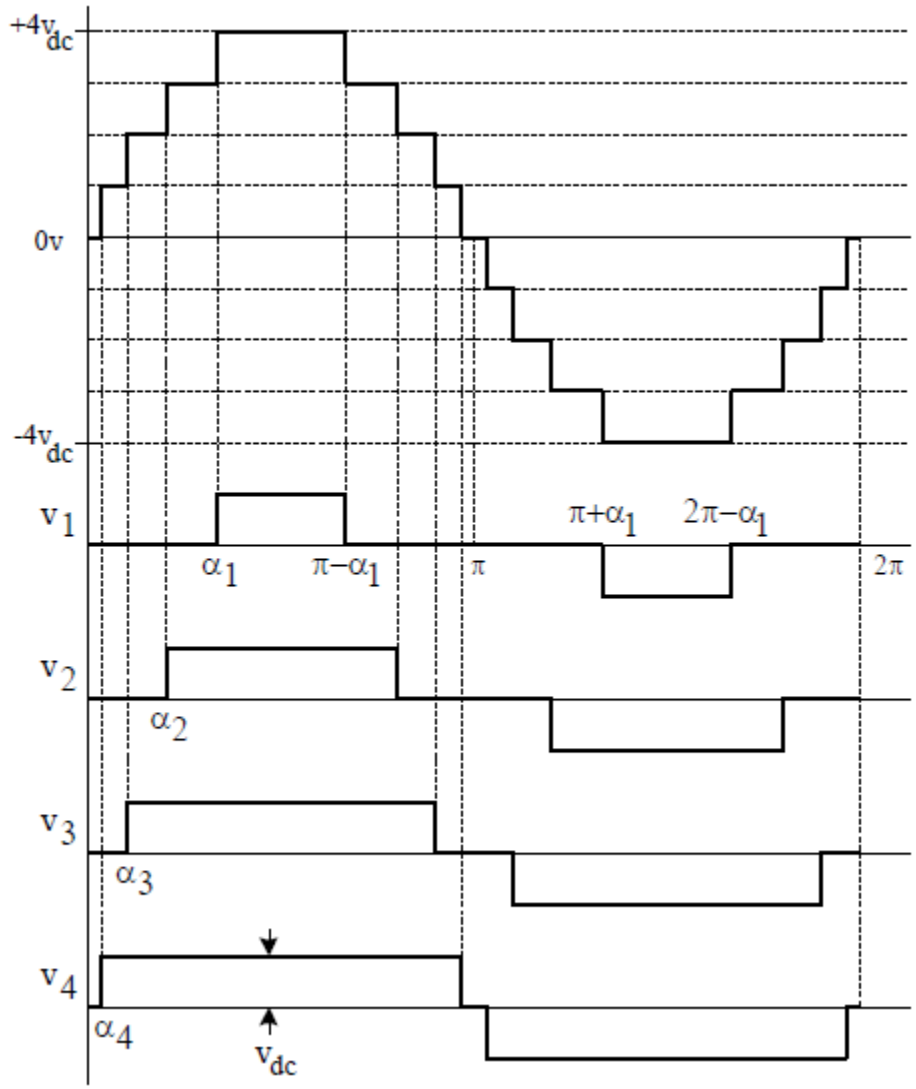

Figure B.4: The synthesized voltage waveform of seven-level inverter

A multilevel converter has several advantages over a conventional three-level converter for the purpose of achieving increased voltage current ratings, the quality of the waveform and harmonics cancellation. The quality of the inverter output voltage waveform can be expressed by using the Fourier analysis data to calculate the total harmonic distortion (THD).

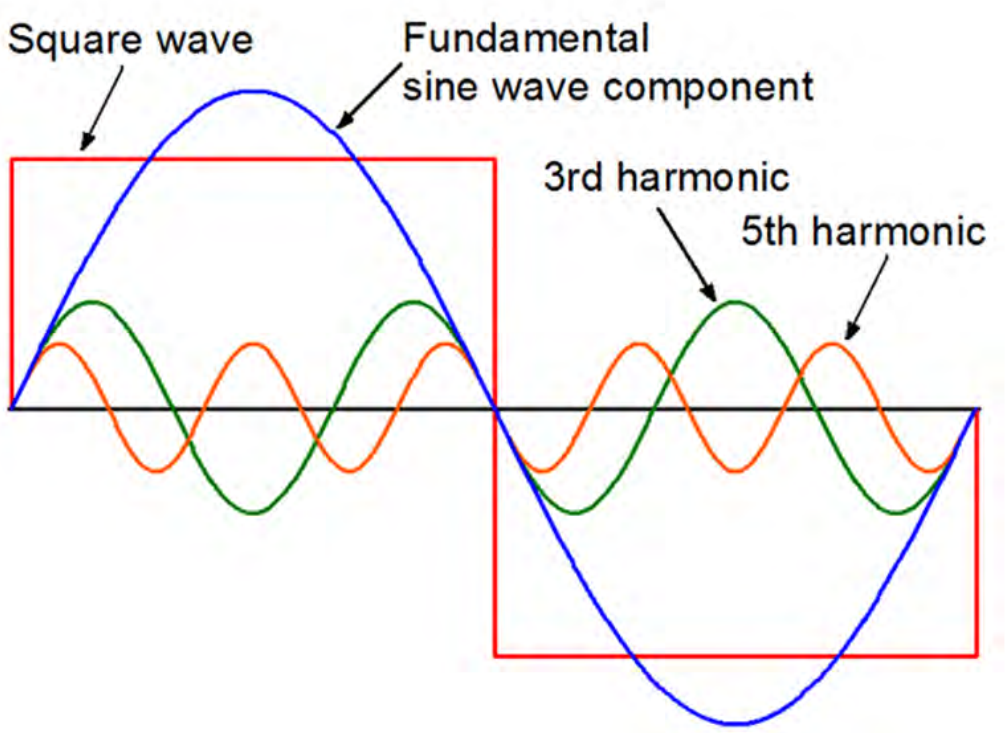

Figure B.5: Harmonics defined

The total harmonic distortion (THD) is the square root of the sum of the squares of the harmonic voltages divided by the fundamental voltage:

$$THD = \frac{\sqrt{V_2^2+V_3^2+V_4^2+\cdots+V_n^2}}{V_1} \quad \text{(A1)}$$

The quality of the output waveform that is needed from an inverter depends on the characteristics of the connected load. While some loads need a nearly perfect sine wave, others may work well with a square wave voltage [S. Jeevananthan].

Three-Phase Inverters

Three-phase inverters are used for variable-frequency drive applications and for hjgh power applications such as HVDC power transmission. A basic three-phase inverter consists of three single-phase inverter switches each connected to one of the three load terminals. For the most basic control scheme, the operation of the three switches is coordinated son that one switch operates at each 60 degree point of the fundamental output waveform. This creates a line-to-line output waveform that has six steps. The six-

step waveform has a zero-voltage step between the positive and the negative sections of the square-wave such that the harmonics that are multiples of three are eliminated as described above.

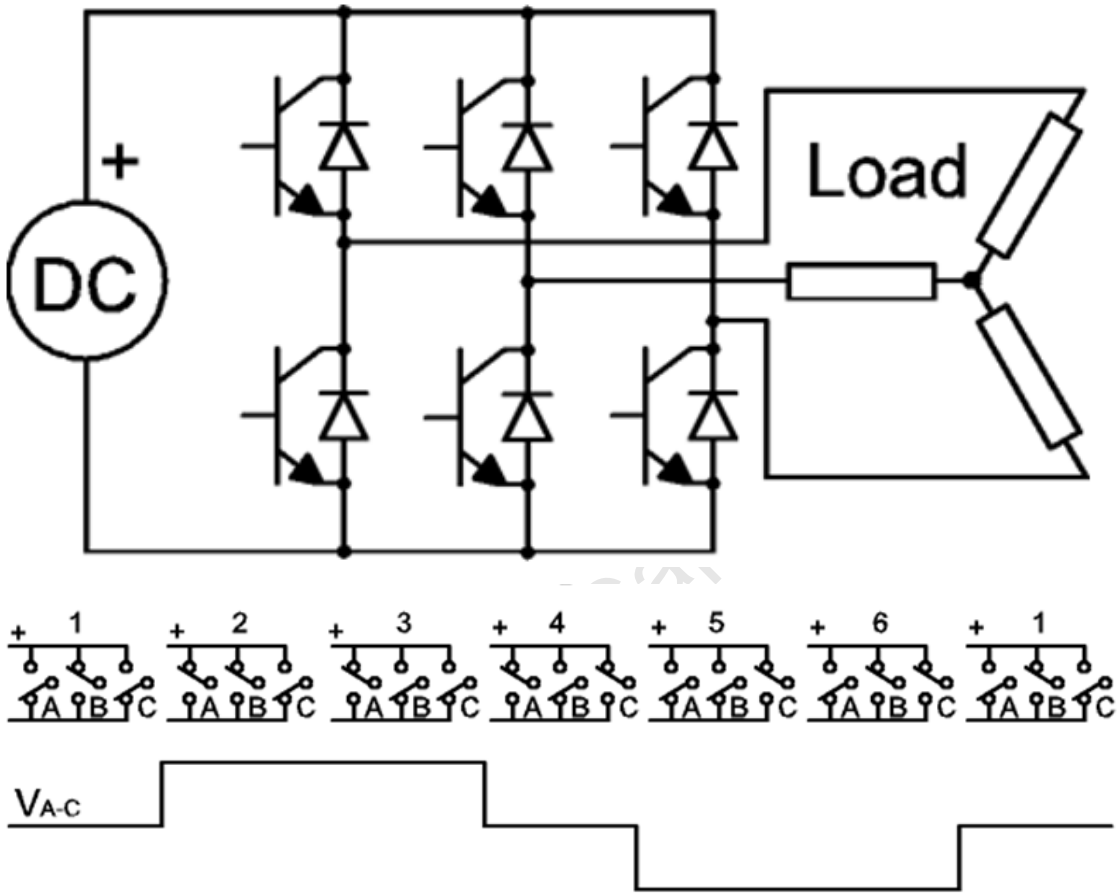

Figure B6: 3-phase inverter circuit showing six-step switching sequence and voltage between terminals A and C

To construct inverters with higher power ratings, two six-step three-phase inverters can be connected in parallel for a higher current rating or in series for a higher voltage rating. In either case, the output waveforms are phase shifted to obtain a 12-step wave form. If additional inverters are combined, an 18-step inverter is obtained with three inverters etc. Although inverters are usually combined for the purpose of achieving increased voltage or current ratings, the quality of the wave form is improved as well.

True or Pure Sine wave Inverters

A pure sine wave inverter produces a nearly perfect sine wave output (less than 3% total harmonic distortion) that is essentially the same as utility-supplied grid power thus it is compatible with all AC electronic devices. The design is more complex hence it costs more per unit power. If you operate the following equipment chances are that you would require a pure sine wave inverter

- Microwave
- Roof Fans
- Air conditions
- High precision chargers
- Swimming pool pumps
- Fridges fitted with compressors
- Fridge/Freezers
- Washing Machines
- Camera equipment which use the line signal for sinc
- Timing devices such as bed alarm clock which use the power signal as a timing base
- Tropical fish tank pumps

APPENDIX C

Validating the DC-DC Boost Converter

In order to determine the performance of the DC-DC boost converter, a steady state dc signal from the battery source is used as the input of the converter while the output is measured across a 50-ohm resistor. The following parameters are used:

Series inductance, Capacitance, pulse generator frequency and a battery voltage are 0.4mH, 25µF, 10 kHz and 10V respectively [236]. The duty cycle (D) of the signal generator which is the fraction of the pulse width with respect to the period is given by

$$D = 1 - \frac{V_{out}}{V_{in}} \qquad \text{(C1)}$$

$$D = 1 - \frac{10}{22} = 0.54$$

Or 54%

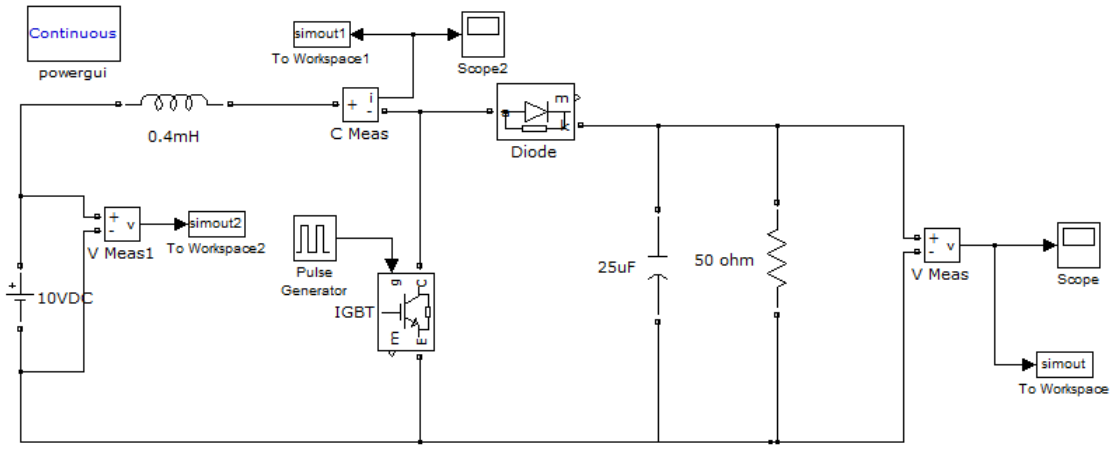

Figure C1: Boost Converter Circuit

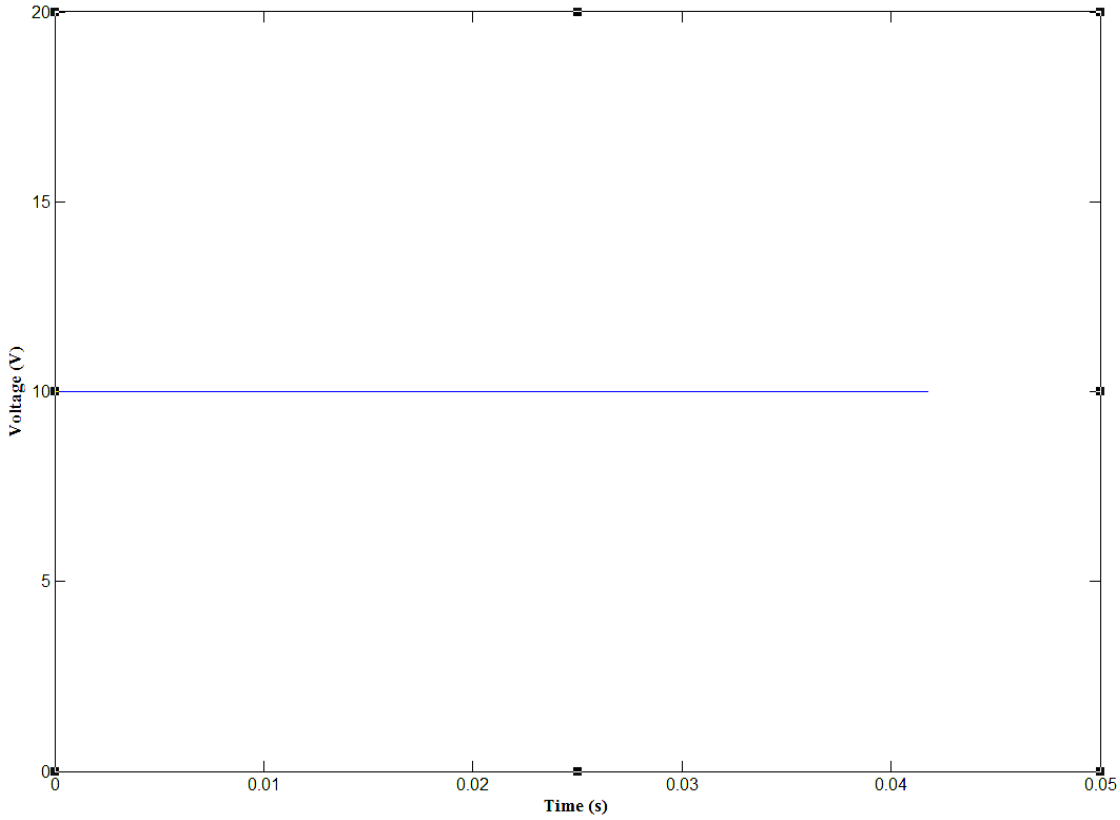

Figure C2: Boost Converter Input Voltage

The output voltage shown in figure C3 is characterized by ripples which is a function of the resistive and the capacitive components of the circuit and the value of the ripple voltage is given by

$$\frac{\Delta V}{V_0} = \frac{D}{RCf} \qquad \text{(C2)}$$

$$\Delta V = \frac{0.3*22}{50*25*10^{-6}*10*10^{3}} = 0.5281 \text{ V}$$

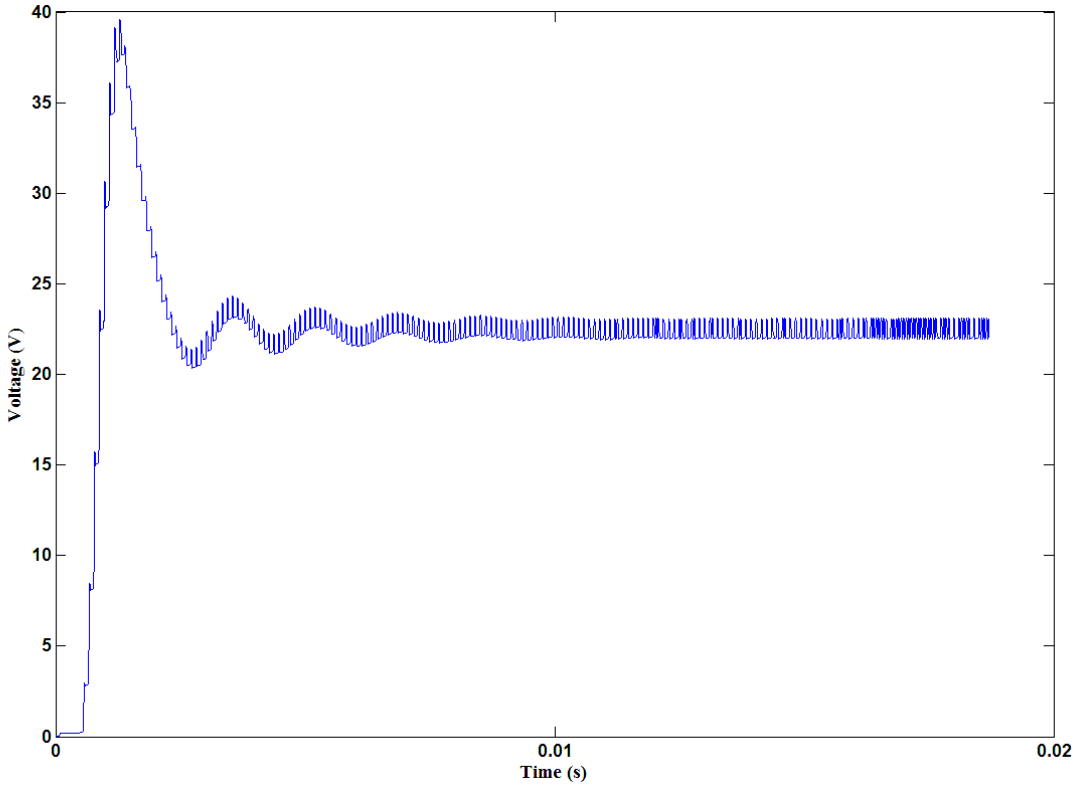

Figure C3: Output Voltage of the Boost Converter

The inductor current is shown in figure C4

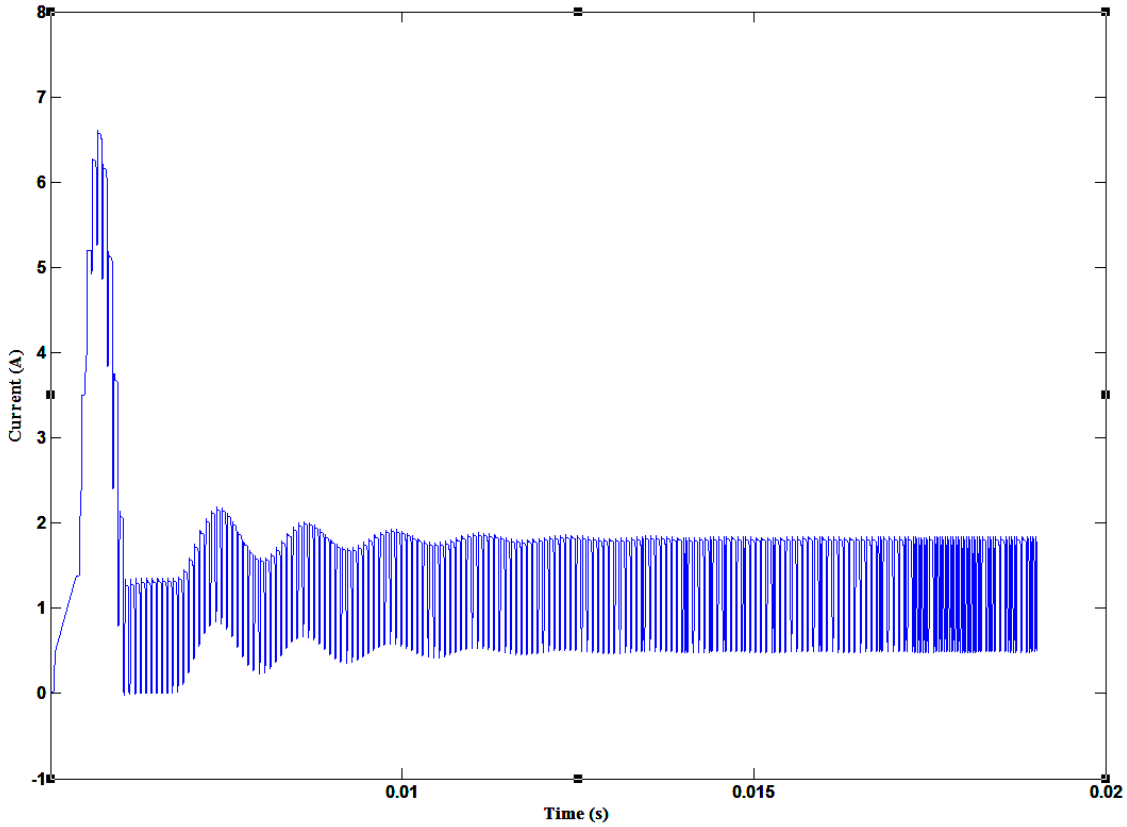

Figure C3: Inductor Current

References

[1] G. Marland, T.A Boden, R.J. Andreas, "Global, regional, and national CO_2 emissions," In Trends: A Compendulum of Data on Global Change, Carbon Dioxide information Analysis Center, Oak Ridge National Laboratory, U.S. Department of Energy. Oak Ridge, Tenn, U.S.A; 2003.

[2] Du Plessis, Pieter; "The potential of solar process heat for South African industry", University of Cape Town Energy Research Centre, pp. 4; 2011.

[3] T. Cebecauer, A. Skoczek, J. Betak, & M. Suri, "Solar fuel for the energy systems'; *GeoModel Solar*, Slovakia; pp. 5, June 2011.

[4] A.S. Sambo, B. Garba, I.H. Zarma, & M.M. Gaji, "Electricity generation and the present challenges in the Nigerian power sector," *Journal of Energy and Power Engineering*, *6*(7), 1050-1059, 2012.

[5] D.K. Kotter, S.D. Novack, W.D. Slafer, & P. Pinhero, " Solar nantenna electromagnetic collectors," In *Proc. Int'l Conf. Energy Sust,* vol. 1, no. 1, pp. 409-415, August 2008.

[6] S. Grover, & G. Moddel, "Applicability of metal/insulator/metal (MIM) diodes to solar rectennas," *IEEE Journal of Photovoltaics, 1*(1), 78-83, 2011.

[7] R.B. Schainker, "Executive overview: energy storage options for a sustainable energy future," *IEEE Transactions* in *Power Engineering Society General Meeting,* pp. 2309-2314, 2004, June 2004.

[8] D. Kottick, M. Blau, & D. Edelstein, "Battery energy storage for frequency regulation in an island power system," *IEEE Transactions on Energy Conversion, 8*(3), 455-459, 1993.

[9] Y.C. Chiao, K.P. Yang, & C.M.J. Yu, "Performance, internationalization, and firm-specific advantages of SMEs in a newly-industrialized economy," *Small Business Economics*, *26*(5), 475-492, 2006.

[10] K.H. An, W.S. Kim, Y.S. Park, J.M. Moon, D.J. Bae, S.C. Lim,... & Y.H. Lee, "Electrochemical properties of high-power supercapacitors using single-walled carbon nanotube electrodes," *Advanced functional materials*, *11*(5), 387-392, 2001.

[11] S.M. Hasnain, "Review on sustainable thermal energy storage technologies, Part I: heat storage materials and techniques," *Energy Conversion and Management*, *39*(11), 1127-1138, 1998.

[12] D. Banks, & J. Schäffler, "The potential contribution of renewable energy in South Africa", *Draft Update Report, 2006.*

[13] G. Wang, R. Hu, H. Wai, H. Zhang, Y. Yang, X. Xiong, G. Lui and S. Luo, "The effect of temperature changes on electrical performance of the betavoltaic cell," *Applied Radiation and isotope*, vol. 68, issue 12, pp. 2215-2217, 2010.

[14] S.C. Hao, Z.M. Lu, X.M. Fu, & T.X. Liang, "Nuclear Battery Materials and Application of Nuclear Batteries," *Nuclear Physics Review*, *3*, 018, 2006.

[15] G.N. Yakubova, "Nuclear Batteries with Tritium and Promethium-147 Radioactive Sources," *Doctoral dissertation, University of Illinois*, 2010.

[16] L. Popa-Simil, "Meta-material based nuclear structure applications in beamed thrust and space energy harvesting," In *47th AIAA Joint Propulsion Conference and 9th International Energy Conversion Engineering Conference,* pp. 1-3, 2011

[17] L.C. Olsen, L. C. "Review of betavoltaic energy conversion," In *NASA Conference Publication* (pp. 256-256). NASA, 1993.

[18] M.A. Ryan, "The alkali metal thermal-to-electric converter for solar system exploration," Jet propulsion laboratory, pasadena; 1999.

[19] M. Duduta, B.Ho, V.C. Wood, P. Limthongkul, V.E. Brunini, W.C. Carter and Y.M. Chiang, "Semi-solid lithium rechargeable flow battery," *Advanced Energy Materials,* volume1, issue 4, pp.511-516, 2011.

[20] C. Ponce de Leon, A. Frias-Ferrer, J. González-García, D.A. Szánto, & F.C. Walsh, "Redox flow cells for energy conversion," *Journal of Power Sources*, *160*(1), 716-732, 2006.

[21] A.A. Shah, M.J. Watt-Smith, & F.C. Walsh, "A dynamic performance model for redox-flow batteries involving soluble species," *Electrochimica Acta*, *53*(27), 8087-8100, 2008.

[22] A. Price, "Technologies for energy storage-present and future: flow batteries," In *Power Engineering Society Summer Meeting, IEEE,* Vol. 3, pp. 1541-1545, 2000.

[23] C.F. Schonbein, "Complete Dictionary of Scientific Biography," Encyclopedia.com, 2008.

[24] www.1eere.energy.gov

[25] O. Yamamoto, "Solid oxide fuel cells: fundamental aspects and prospects," *Electrochimica Acta*, *45*(15), 2423-2435, 2000.

[26] J. Suntivich, K.J. May, H.A. Gasteiger, J.B. Goodenough and Y. Shao-Horn, "A perovskite oxide optimized for oxygen evolution catalyst from molecular orbital principles," *Nature Chemistry*, issue 3, pp. 546-550, 2001.

[27] Y. Shao, G. Yin, Z. Wang, & Y. Gao, "Proton exchange membrane fuel cell from low temperature to high temperature: material challenges," *Journal of power sources*, *167*(2), 235-242, 2007.

[28] F. Yildiz, & K. Baltaci, "Challenges of EVs and HVs to the US Electrical Power Grid," *International Journal of Engineering Research & Innovation*, 68, 2011.

[29] O. Bohnke, C. Bohnke, & J.L. Fourquet, "Mechanism of ionic conduction and electrochemical intercalation of lithium into the perovskite lanthanum lithium titanate," *Solid State Ionics*, *91*(1), 21-31, 1996.

[30] G. Girishkumar, B. McCloskey, A.C. Luntz, S. Swanson, & W. Wilcke, "Lithium− air battery: Promise and challenges," *The Journal of Physical Chemistry Letters*, *1*(14), 2193-2203, 2010.

[31] M. Wakihara, & O. Yamamoto, "*Lithium ion batteries,"* John Wiley & Sons, 2008.

[32] B.E. Conway, "Electrochemical supercapacitors: scientific fundamentals and technological applications (POD)," *Kluwer Academic/plenum*, New York, 1999.

[33] M. Roberts, D. Wheeler, B. McKenzie and B. Bunker, "High Specific Capacitance conducting polymer supercapacitor electrodes based on Poly (tris (thiophenylphenyl) amine)", *Journal of Material Chemistry*, vol.19, issue 38, pp. 6977-6979, 2009.

[34] H.D. Abruna, Y.Kiya and J.C. Henderson, "Batteries and Electrochemical Capacitors," *Feature Article, ECEE Colorado*, 2008.

[35] G. Wang, L. Zhang, & J. Zhang, "A review of electrode materials for electrochemical supercapacitors," *Chemical Society Reviews*, *41*(2), 797-828, 2012.

[36] N. Khan, N. Marium, M. Zaki and L. Dinesh, "Transient analysis of pulsed charging in supercapacitors," *IEEE TENCON Proceedings*, vol. 3, pp.193-199, 2000.

[37] L.I. Zhongxue and W. Fu, "Diagnostic Identification of self-discharge mechanisms for carbon-based Supercapacitors with high energy density*," IEEE conferences on Power and Energy Engineering Conference (APPEEC), Asia Pacific,* pp.1-5, 2011.

[38] E. Frackowiak, V. Khomenko, K. Jurewicz, K. Lota and F. Beguin, "Supercapacitor based on conducting polymers/nanotubes composites," *Journal of Power Sources*, vol.153, issue 2, pp. 413-418, 2006.

[39] D. Pavel and S. Lubos, "The energy storage system with supercapacitor for public transport"; *IEEE conference on Vehicle Power and Propulsion (VPPC`09),* pp.1826-1830, 2009.

[40] P. Drabek, L. Straits, M. Los, "The Energy storage system with supercapacitor," *14th IEEE conferences on Power Electronics and Motion and Control (EPE/PEMC)*, pp.T9-39, 2010.

[41] Generation Communication; "Concentrating Solar Power (CSP)"; **www.eskom.co.za**, RW 0003 Revision, June 2010.

[42] S. Flueckiga; Z. Yang and S.V. Garimella, "An integrated thermal and mechanical investigation of molten salt thermocline storage," *Applied Energy*, vol. 88, issue 6, pp. 2098-2105, 2011.

[43] A. Gil, M. Medrano, I. Martorell, A. Lázaro, P, Dolado, B. Zalba, & L.F. Cabeza, "State of the art on high temperature thermal energy storage for power generation. Part 1—Concepts, materials and modellization," *Renewable and Sustainable Energy Reviews*, *14*(1), 31-55, 2010.

[44] R.W. Bradshaw, N.P. & Siegel, "Molten nitrate salt development for thermal energy storage in parabolic trough solar power systems," *Energy Sustainability Proceedings of ES2008,* pp. 10-14, 2008.

[45] K. Oikawa, L. Wulff, T. Iijima, F. Gejima, T. Ohmori, A. Fujita, ... & K. Ishida, "Promising ferromagnetic Ni–Co–Al shape memory alloy system," *Applied Physics Letters*, *79*(20), 3290-3292, 2001.

[46] R.S. Sokolowski, "Power transmission and distribution cables and transformers," *Power Applications of Superconductivity in Japan and Germany*, vol. 27, 1997.

[47] O.H. Al-Sakaf, "Application possibilities of solar thermal power plants in Arab countries", *Renewable energy*, vol. 14, issue 1, pp. 1-9, 1998.

[48] M. Park, S. Kwak, W. Kim, J. Lee, J. Han, K. Choi and S. Hanh, "Conceptual design of HTS magnet for a 5 MJ class SMES," *IEEE Transactions on Applied Superconductivity*, Vol.18, issue 2, pp. 750-753, 2008.

[49] T. W. Scheike, W. Bohlmann, P. Esquinazi, J. Barzola-Quiquia, A. Ballestar and A. Setzer, "Can doping graphite trigger room temperature superconductivity? Evidence for granular high-temperature superconductivity in water-treated graphite powder," *Advanced Materials,* vol. 24, issue 43 pp. 5826-5831, 2012.

[50] P.J. Hall, & E.J. Bain, "Energy-storage technologies and electricity generation," *Energy policy*, *36*(12), 4352-4355, 2008.

[51] T. Hamajima, M. Shimada, S. Hanai, Y. Wachi, M. Tezuka, & H. Takano, "SMES coil configurations with reduced stray field," *Applied Superconductivity,*" *IEEE Transactions,* 9(2), 346-349, 1999.

[52] Z. Jiahui, Y. Weijia, T.A. Coombs and Q. Ming, "Simulation and experiment of an YBCO SMES prototype in voltage sag compression," *Physica C: Superconductivity*, vol. 471, issue 5, pp.199-204, 2011.

[53] R. Radebaugh, "Cryocoolers: the state of the art and recent developments," *Journal of Physics: Condensed Matter*, *21*(16), 164219, 2009.

[54] M. Masuda, T. Shintomi, H. Sato and A. Kabe, "Superconducting energy storage magnets," *IEEE transactions*, vol.15, issue 2, pp. 766-799, 2008.

[55] M.P. Mitchell, K.J. Wilson, and L. Bauwens, "Comparative simulation of Stirling and Sibling cycle cryocoolers with two codes," *IEEE Proceedings of 24th intersociety Energy Conversion Engineering Conference*, vol.5, pp. 2205-2211, 1989.

[56] M.A. Green, "The effect of low temperature cryocoolers on the development of low temperature superconducting magnets," *IEEE journals on Applied Superconductivity*, vol.11, issue 1, part 2, pp. 2615-2618, 2001.

[57] Z. Zhang, Z. Guo and G. Gu, "The research of room temperature magnetic refrigeration technology," *8th IEEE conferences on Electrical machines and systems, ICEMS,* vol. 1, pp.769-771, 2005.

[58] M.H. Ali, B. Wu, & R.A. Dougal, "An overview of SMES applications in power and energy systems," *Sustainable Energy, IEEE Transactions, 1*(1), 38-47, 2010.

[59] J. Wang, J. Skiles, R. Kustoma, T. Ise, F. Tsang and J. Cleary, "Studies of power conditioning circuits for superconductive magnetic energy storage," *IEEE conferences on Power Electronics Specialist Conference*, pp. 307-312, 1988.

[60] C.A. Luongo, "Superconducting storage systems; an overview," *Magnetics, IEEE Transactions, 32*(4), 2214-2223, 1996.

[61] J. Zui, W. Yuan, T. Coombs and Q. Ming, "Simulation and experiment of YBCO, SMES prototype in voltage sag compensation," *Physica of Superconductivity* vol.471, issue 5-6, pp. 199-204, 2011.

[62] R.F. Giese, T.P. Sheehan, A.M. Wolsky and D.K. Sharma, "High- Temperature Superconductors: their potential for utility applications," Argonne Nat. Lab, IL; *IEEE transactions on Energy Conversion*, vol.7, issue 3, pp.589, 1992.

[63] R.J. Lloyd, T.E. Walsh, E.R. Kimmy and B.E. Dick, "An Overview of the SMES ETM Program, The Bechtel Teams Perspective," *IEEE Transactions on magnets*, vol.25, No.2, pp.1569-1575, 1989.

[64] C.S. Hsu, & W.J. Lee, "Superconducting magnetic energy storage for power system applications," *IEEE Transactions* in *Industry Applications, 29*(5), 990-996, 1993.

[65] M.H. Ali, W. Bin and R.A. Dougal, "An Overview of SMES Applications in Power and Energy Systems," *IEEE transaction on sustainable energy*, issue 1, vol.1, pp. 37-47, 2010.

[66] D.N. Palmer, "Downsized superconducting magnetic energy storage systems," *Proceedings of the 24th intersociety Energy conversion Engineering Conference, IECEC*, pp.453-458, vol. 1, 1989.

[67] V. Karasik, K. Dixon, C. Weber, B. Batchelder, G. Campbell, & P. Ribeiro, "SMES for power utility applications: a review of technical and cost considerations," *Applied Superconductivity, IEEE Transactions on*, *9*(2), 541-546, 1999.

[68] B. Wong, A. Snijders and L. McClung, "Recent Interseasonal Underground Thermal Energy Storage Applications in Canada," *IEEE, EIC climate change Technology*, pp.1-7, 2006.

[69] D. Banks, "An introduction to 'thermogeology' and the exploitation of ground source heat. *Quarterly Journal of Engineering Geology and Hydrogeology*, *42*(3), 283-293, 2009.

[70] F.J. Molz, J.O. Melville, A.D. Parr, D.A. King, & M.T. Hopf, "Aquifer thermal energy storage: A well doublet experiment at increased temperatures," *Water Resources Research*, *19*(1), 149-160, 1983.

[71] L. Ming, G. Qing, J. Yan, G. Qin, "Thermal Analysis of underground Thermal Energy storage under different load mode," International conference on Energy and Environmental Technology, ICEET, pp. 912-916, 2009

[72] I. Dincer, "On thermal energy storage systems and applications in buildings," *Energy and Buildings*, *34*(4), 377-388, 2002.

[73] L. Ming, G. Qing, J. Yan, G. Qin, "Thermal Analysis of underground Thermal Energy storage under different load mode," International conference on Energy and Environmental Technology, ICEET, pp. 912-916, 2009.

[74] R. Williams, "Becquerel Photovoltaic Effect in Binary Compounds," *The journal of Chemical Physics*, issue 32, volume 5, pp. 1505-1514, 1960.

[75] H. Becquerel, "Lachaire de physique du Museum," *Revue Scientifique* volume 49, pp. 674- 678, 1892.

[76] S.Y. Yang, L.W. Martin, S.J. Byrnes, T.E. Conry, S.R. Basu, D. Paran,... & R. Ramesh, "Photovoltaic effects in< equation>< font face='verdana'> BiFeO< sub> 3</sub></equation>," *Applied Physics Letters*, *95*(6), 062909-062909, 2009.

[77] J.Y. Kim, S.H. Kim, H.H. Lee, K. Lee, W. Ma, X. Gong, & A.J. Heeger, "New Architecture for High-Efficiency Polymer Photovoltaic Cells Using Solution-Based Titanium Oxide as an Optical Spacer," *Advanced materials*, *18*(5), 572-576, 2006.

[78] J. Perlin, "From space to earth: the story of solar electricity*," Earthscan*, 1999.

[79] D.M. Chapin, "Solar energy converting apparatus," United States Patent Office no. 2780765, 1957.

[80] J.D. Patterson and B. Bailey, "Solid-state Physics: Introduction to the theory," *Springer-Verlag Berlin Heidelberg,* chapter 6.3.9, pp. 349, 2007.

[81] D.G.S. Chuah, "A General Introduction of Photovoltaic Solar System," *US Asean Conference on Comparitive Technology Water Pumping* Penang, Malasia, 1988,

[82] C. Schmiga, H. Nagel, & J. Schmidt, "19% efficient n-type Czochralski silicon solar cells with screen-printed aluminium-alloyed rear emitter," *Progress in Photovoltaics: Research and Applications*, *14*(6), 533-539, 2006.

[83] D.P. Redon, "Microcrystalline silicon obtained by hot-wire chemical vapour deposition for photovoltaic applications," Department De Fisica Aplicada I` Optica, Universitat De Barcelonia, pp. 11-20, 1999.

[84] F. Meilland, A. Feltrin, M. Despeisse, F.J. Haug, D. Domine, M. Python and C. Ballif, "Realization of high efficiency micromorph tandem silicon solar cells on glass and plastic substrates: issues and potential," *Solar Energy Materials and Solar Cells,* volume 95, issue 1, pp. 127-130, 2011.

[85] G.C. Schwartz, & P.M. Schaible, "Reactive ion etching of silicon," *IEEE Journal of Vacuum Science and Technology,* vol. 16, issue 2, pp. 410-413, 1979.

[86] H.C. Yuan, V.E. Yost, M.R. Page, P. Stradins, D.L. Meier and H.M. Branz, "Efficient black silicon solar cell with a density-graded nano-porous surface: Optical properties, performance limitations, and design rules," *Applied Physics Letters*, vol. 95, issue 12, pp. 123501, 2009.

[87] J. Yoon, L. Li, A.V. Semichaevsky, J.H. Ryu, H.T. Johnson, R.G. Nuzzo and J.A. Roger, "Flexible concentrator photovoltaics based on micro-scale silicon solar cells embedded in luminescent waveguides," *Nature communications*, vol. 2, article 343, 2011.

[88] G.A. Aberle, "Thin film solar cells," *Thin Solid Film*, volume 517, issue 17, pp. 4706-4710, 2009.

[89] A. Mavrokefalos, S.E. Han, S. Yerci, M.S. Branham, & G. Chen, " Efficient light trapping in inverted nanopyramid thin crystalline silicon membranes for solar cell applications," *Nano letters*, *12*(6), 2792-2796, 2012.

[90] K. Takahashi, and M. Konagai, "Amorphous silicon solar cells," *Wily-interscience*, New York, NY, pp. 10, 1986.

[91] A. Madan, "Thin film amorphous silicon solar cells," *Solar Energy*, volume 29, issue 3, pp. 225-233, 2003.

[92] P.V. Meyers, "Design of the thin film solar cells," *Solar Cells,* volume 23, issue 1 & 2, pp. 59-67, 1988.

[93] K. Zweibel, & A. Hermann, "Cadmium Telluride (CdTe) Solar Cells," *International Society for Optics and Photonics Technical Symposium*, pp. 119-126, 1985.

[94] S. Lancy, "First Solar shatters previous record for cadmium telluride thin film efficiency," *Climate Progress*, July 2011.

[95] M. Hadrich, H. Metzner, U. Reislohner and C. Kraft, "Modelling the quantum efficiency of the cadmium telluride solar cells," *Solar Energy materials and Solar Cells*, volume 95, Issue 3, pp. 887-893, 2011.

[96] M.E. Beck, & M. Cocivera, "Thin-film copper indium diselenide prepared by selenization of copper indium oxide formed by spray pyrolysis," *Thin Solid Films*, *272*(1), 71-82, 1996.

[97] K. Kushiya, M. Tachiyuki, & T. Kase, *U.S. Patent No. 5,981,868*. Washington, DC: U.S. Patent and Trademark Office, 1999.

[98] E. Lee, S.J. Park, J.W. Cho, M.K. Oh and B.K. Min, "Nearly carbon-free printable CIGS thin film for solar cell application," *Solar Energy Materials and Solar Cells*, volume 95, issue 10, pp. 2928-2932, 2011.

[99] Dustin Mulvaney, "Thin Film - Green Technology," *Google books*, pp. 118-121, 2011.

[100] L. Eldada, "Design, development and manufacture of high- efficiency low-cost solar modules based on CIGS PVICs," In *Proc. SPIE* Vol. 7605, p. 76050F, 2010.

[101] M. Gratzel, "Dye-sensitized solar cells," *Journal of Photochemistry and Photobiology C: Photochemistry Reviews*, 4, issue 2, pp. 145-153, 2000.

[102] Y. Chiba, A. Islam, Y. Watanabe, R. Komiya, N. Koide, & L. Han, "Dye-sensitized solar cells with conversion efficiency of 11.1%," *Japanese Journal of Applied Physics, Part 2, Letters*, *45*(24/28), L638, 2006.

[103] J. Drechsel, B. Mannig, F. Kozlowski, M. Pfeiffer, K. Leo, & H. Hoppe, "Efficient organic solar cells based on a double< equation> pin</equation> architecture using doped wide-gap transport layers," *Applied physics letters*, *86*(24), 244102-244102, 2005.

[104] C. Brabec, U. Scherf and V. Dyakonov, "Organic Photovoltaics: Materials, Device Physics, and Manufacturing Technologies," *Wiley Online Libraries*, hardcover pp. 597, 2008.

[105] S. Karg, W. Riess, W. Dyakonov and M. Schwoerer, "Electrical and optical characterization of poly (phenylene- vinylene) light emitting diodes," *Synthetic Metals*, volume 54, Issues 1-3, pp. 427-433, 1993.

[106] C.W. Tang, "Two-layer organic photovoltaic cell," *Applied Physics Letters*, *48*, 183, 1986.

[107] J.J.M. Halls, K. Pichler, R.H. Friend, S.C. Moratti and A.B. Holmes, "Exciton diffusion and dissociation in a poly (p-phenylenevinylene)/C60 heterojunction photovoltaic cell," *Applied Physics Letters* Volume 68, issue 22, pp. 3120-3122, 1996.

[108] P.R. Somani, S.P. Somani, & M. Umeno, "Toward organic thick film solar cells: three dimensional bulk heterojunction organic thick film solar cell using fullerene single crystal nanorods," *Applied Physics Letters*, *91*(17), 173503-173503, 2007

[109] S.E. Shaheen, C.J. Brabec, N.S. Sariciftci, F. Padinger, T. Fromherz, & J.C. Hummelen, "2.5% efficient organic plastic solar cells," *Applied Physics Letters*, *78*, 841, 2001.

[110] Y. Jia, "Achieving High Efficiency Silicon–carbon Nano-tube Hetero-junction Solar Cell by Acid Doping," *Nano-letters* vol. 11, issue 5, pp. 1901-1905, 2011.

[111] W.J. Beek, M.M. Wienk, & R.A. Janssen, "Efficient hybrid solar cells from zinc oxide nanoparticles and a conjugated polymer," *Advanced Materials*, *16*(12), 1009-1013, 2004.

[112] J. Lee, J. Kong, H. Kim, S.O. Kang and K. Lee, "Direct observation of internal potential distributions in bulk hetero-junction solar cell," *Organic Electronics and Photonics, Applied Physics Letters,* volume 99, Issue 24, pp. 243-301, 2011.

[113] R. Holmes and R. Pandey; "Organic photovoltaic cells based on continuously graded donor-acceptor hetero-junctions," *IEEE Journal of Selected Topics in Quantum Electronics,* vol. 16, issue 6, pp. 7, 2011.

[114] J. Liu, T. Tanaka, K. Sivula, A.P. Alivisatos and J.M. Frechet, "End-functional polythiophene to control the morphology of nano-crystal-polymer composites in hybrid solar cells," *Journal of American Chemical Society* vol. 126, issue 21, pp. 6550-6551, 2004.

[115] A. Morales-Acevedo, "Comment on "35% efficient non-concentrating novel silicon solar cell,"" *Applied Physics Letters*; volume 63, issue 6, pp. 1-6, August 1993.

[116] I. Chambouleyron, "Multiple-gap amorphous solar cells reconsidered," *Institute of Physics, University de Campinas, Elsevier* volume 12, issue 4, pp. 393-400, 1984.

[117] S.W. Zeng, B.P. Zhang, J.W. Sun and J.F. Cai et al, "Substantial photo-response of InGaN p-i-n homo-junction solar cells," *Semiconductor Science and Technology*, vol. 24, issue 5, pp. 055009, 2009.

[118] S.W. Zeng, "Demonstration and study of photovoltaic performances of InGaN p-i-n homo-junction solar cells," *IEEE Journal of Quantum Electronics* volume 46, Issue 5, pp. 783-787, 2010.

[119] K.M. Yu, W. Walukiewicz, J. Wu, W. Shan, J.W. Beeman, M.A. Scarpulla, …& P. Becla, "Diluted II-VI oxide semiconductor with multiple band gaps," *Physical Review Letters*, volume 91, number 24, 246403, 2003.

[120] G.J. Conibeer, C.W. Jiang, D. König, S. Shrestha, T. Walsh, & M.A. Green, "Selective energy contacts for hot carrier solar cells," *Thin Solid Films*, *516*(20), 6968-6973, 2008.

[121] M.C. Hanna, Z. Lu, & A.J. Nozik, "Hot carrier solar cells. In *AIP Conference Proceedings* Vol. 404, p. 309, 1997.

[122] E.S. Rittner and R.A. Arndt, "Comparison of silicon solar cell efficiency for space and terrestrial use", *Journal of Applied Physics*, vol. 47, issue 7, 2009.

[123] J. Park, "Nano-solar Cells: Solar Cells of the future with Nanotechnology," IEEE San Francisco Bay Area Nanotechnology Council, 2009.

[124] A.W. Bett, F. Dimroth, W. Guter, R. Hoheisel, E. Oliva, S.P. Philipps, ... & G. Strobl, "Highest efficiency multi-junction solar cell for terrestrial and space applications," *space*, *25*(25.8), 30-6, 2009.

[125] P.R. Sharps, A. Cornfeld, T. Varghese, F. Newman, & J. Diaz, *U.S. Patent No. 7,785,989*. Washington, DC: U.S. Patent and Trademark Office, 2010.

[126] G. Zubi, J.L. Bernal-Agustín, & G.V. Fracastoro, "High concentration photovoltaic systems applying III–V cells," *Renewable and Sustainable Energy Reviews*, *13*(9), 2645-2652, 2009.

[127] R.R. King, D.C. Law, K.M. Edmondson, C.M. Fetzer, G.S. Kinsey, H. Yoon, …& N.H. Karam, "40% efficient metamorphic GaInP/GaInAs/Ge multijuction solar cells," *Applied Physics Letters (AIP)*, vol. 90, 183516, 2007.

[128] R.R. King, A. Boca, W. Hong, X.Q. Liu, D. Bhusari, D. Larrabee,... & N.H. Karam, "Band-gap-engineered architectures for high-efficiency multijunction concentrator solar cells," In *24th European Photovoltaic Solar Energy Conference and Exhibition, Hamburg, Germany* (Vol. 21), 2009.

[129] F. Dimroth, S.P. Philips, G. Peharz, E. Welser, R. Kellenbenz, T. Roesener, V. Klinger, E. Oliva, M. Steiner, M. Meusel, W. Guter and A.W. Bett, "Promises of advanced multi-junction solar cells for the use in CPV systems", *35th IEEE Photovoltaic Specialists Conference* (PVSC), pp.001231, 2010.

[130] R.R. King, D.C. Law, K.M. Edmondson, C.M. Fetzer, G.S. Kinsey, H. Yoon, R.A. Sherif and N.H. Karam, "40% efficient metamorphic GaInP/GaInAs/Ge multi-junction solar cells", *Applied Physics Letters*, volume 90, issue 18, pp. 183516, 2007.

[131] D.S. Chemla, D. Miller, P. Smith, A. Gossard, & W. Wiegmann, "Room temperature excitonic nonlinear absorption and refraction in GaAs/AlGaAs multiple quantum well structures," *Quantum Electronics, IEEE Journal of*, *20*(3), 265-275, 1984.

[132] K. Barnham, I. Ballard, J. Barnes, J. Connolly, P. Griffin, B. Kluftinger ... & A. Zachariou, "Quantum well solar cells," *Applied Surface Science*, *113*, 722-733, 1997.

[133] N.J. Ekin-Daukes, K.W.J. Barnham, J.P. Cnnoly, J. Wohlgemuth, D. Cunningham, J. Shaner, A. Nguyen and S. Ransome, "Strain balanced GaAsP/InGaAs quantum well-solar cells," *Applied Physics letters*, vol.75, issue 26, pp. 4195-4197, 1999.

[134] A.G. Norman, J. Geisz, J. Olson, K. Jones, & M. Al-Jassim, "Electron Microscopy Studies of GaP (N, As) Grown on Si (No. NREL/CP-520-37035). *National Renewable Energy Laboratory (NREL),* Golden, CO., 2005.

[135] J.F. Geisz, J.M. Olson, D.J. Friedman, K.M. Jones, R.C. Reedy and M.J. Romero, "Lattice-matched GaNPAs-on-silicon tandem solar cells," *PVSC*, pp. 695-698, 2005.

[136] F. Shanhui, "Ultra high efficiency thermo-photovoltaic solar cells using metallic photonic crystals as intermediate absorber and emitter," *Stanford University: Global Climate and Energy Project (GCEP),* 2009.

[137] T.J. Coutts, "An overview of thermo-photovoltaic generation of electricity," *11th IEEE International Photovoltaics Science and Engineering Conference* (PVSEC-11) Sapporo, Japan, 1999.

[138] C.A. Wang, H.K. Choi, S.L. Ransom, and G.W. Charache, "High-quantum-efficiency 0.5eV GaInAsSb/GaSb thermo-photovoltaic devices," *Applied Physics Letters,* volume 75, issue 9, pp.1305, 1999.

[139] A. Shakouri, "Thermoelectric, thermionic and thermo-photovoltaic energy conversion," *IEEE International Conference on Thermoelectrics*, pp. 507-512, 2005.

[140] A.I. Boukai, Y. Bunimovich, J. Tahir-Kheli, and J.K. Yu, "Silicon nanowires as efficient thermoelectric materials," *Nature*; volume 451, pp. 168-171, 2008.

[141] A. Freundlich, "High Efficiency Thermo-photovoltaics," *Center for Advance Materials, University of Houston, Texas*, pp. 1-3, 2008.

[142] L.L Kazmerski, "Solar photovoltaics R&D at the tipping point: A 2005 technology overview," *Journal of Electron Spectroscopy and Related Phenomena*, *150*(2), 105-135, 2006.

[143] S.F. Feste, J. Knoch, D. Buca and S. Mantl, "Fabrication of uniaxially strained silicon nanowires," *Thin Solid Films*, vol. 517, issue 1, pp. 320-322, 2008.

[144] O. Dross, R. Mohedano, P. Benitez, J.C. Minano, J. Chaves, J. Blen, ... & F. Munoz, "Review of SMS design methods and real-world applications," In *Proceedings of SPIE*, Vol. 5529, pp. 35-47, 2004.

[145] W.T. Welford, R. Winston, & D.C. Sinclair, "The optics of non-imaging concentrators: light and solar energy," *Physics Today*, *33*, 56, 1980.

[146] W. Van Sark, K.W.J. Barnham, L.H. Sloof, and J. Amanda, "Luminescent solar concentrators- A review of recent results," *Optics Express*; vol. 16, issue 26, pp. 21773-21792, Dec. 2008.

[147] S. Horne, G. Couley, J. Gordon, D. Fork, P. Meada, E. Schrader and T. Zimmerman, "A solid 500sun compound concentrator PV design," *4th IEEE World Conference on Photovoltaic Energy Conversion,* vol. 1, pp. 694-697, 2006.

[148] G.V. Shcherbatyuk, R.H. Inman, C. Wang, R. Winston, & S. Ghosh, "Viability of using near infrared PbS quantum dots as active materials in luminescent solar concentrators," *Applied Physics Letters*, *96*(19), 191901-191901, 2010.

[149] G.V. Scherbatyuk, R.H. Inman, C. Wang, R. Winston and S. Ghosh, "Viability of using near infrared lead sulphide quantum dots as active material in

luminescent solar concentrator," *Applied Physics Letters,* vol. 96, issue 19, pp. 191901-191903, 2010.

[150] X. Wang and A. Barnett, "One lateral spectrum splitting concentrator photovoltaic architecture: Measurements of current assemblies and analysis of pathways to 40% efficient modules," *35th IEEE PVSC*, pp. 002745-002750, 2010.

[151] A. Mokri, & M. Emziane, "A Triple-Cell Concentrator PV System with No Current-Matching and No Lattice-Matching Constrains," *In Sustainability in Energy and Buildings*, pp. 193-200, Springer Berlin Heidelberg, 2012.

[152] L.M. Fraas, J.E. Avery, J.E. Strauch and G. Girard, "Dual focus cassegrain module can achieve >>45% efficiency," *34th IEEE Photovoltaic Specialists Conference (PVSC),* pp. 001169 – 001173, 2009.

[153] D. Pachon, I. Anton and G. Sala, "Rating and modeling of concentrator systems," 29th *IEEE Photovoltaic Specialists Conference*; pp. 1600-1603, 2002.

[154] J.H. Karp, & J.E. Ford, "Multiband solar concentrator using transmissive dichroic beamsplitting," In *Solar Energy+ Applications*. International Society for Optics and Photonics, pp. 70430F-70430F, 2008

[155] M. Yamaguchi and A. Luque, "High efficiency and high concentration in photovoltaic," *IEEE Transactions on Electron Devices*, volume 46, Issue 10; pp. 2139-2144, 1999.

[156] R.R. King, D. Bhusari, D. Larrabee, X.Q. Liu, E. Rehder, K. Edmondson, ... & N.H. Karam, "Solar cell generations over 40% efficiency," *Progress in Photovoltaics: Research and Applications*, *20*(6), 801-815, 2012.

[157] L. Fraas, J. Avery, H. Huang, L. Minkin and E. Shifman, "Demonstration of a 33% efficient cassagrainian solar module," *IEEE Conference Publications,* pp. 679-682, 2006.

[158] N. Singh, S.C. Kaushik, & R.D. Misra, R. D. "Exergetic analysis of a solar thermal power system," *Renewable energy*, *19*(1), 135-143, 2000.

[159] W. Nishikawa, & S. Horne, "Key advantages of concentrating photovoltaics (CPV) for lowering levelized cost of electricity (LCOE)," In *23rd European PV solar energy conference* pp. 3765-3767, 2008.

[160] S.P. Sukhatme, "Solar energy: principles of thermal collection and storage," Tata McGraw-Hill Education, 2008.

[161] R.J.C. Perez, *European Patent No. EP 1536189*. Munich, Germany: European Patent Office, 2005.

[162] D.Y. Goswami, & F. Xu, "Analysis of a new thermodynamic cycle for combined power and cooling using low and mid temperature solar collectors," *Journal of Solar Energy Engineering*, *121*(2), 1999.

[163] X. Zhou, M.A.D.S. Bernardes, & R.M. Ochieng, "Influence of atmospheric cross flow on solar updraft tower inflow," *Energy*, *42*(1), 393-400, 2012.

[164] J.B. Schlaich, R. Bergermann, W. Schiel, & G. Weinrebe, "Design of commercial solar updraft tower systems-utilization of solar induced convective flows for power generation," *Transactions of the ASME-N-Journal of Solar Energy Engineering*, *127*(1), 117-124, 2005.

[165] G.L. Morrison, & J.E. Braun, "System modeling and operation characteristics of thermosyphon solar water heaters," *Solar Energy*, *34*(4), 389-405, 1985.

[166] V. Kienzien, J.M. Gordon, & J.F. Kreider, "The reverse flat plate collector: A stationary, nonevacuated, low-technology, medium-temperature solar collector," *J. Sol. Energy Eng.; (United States)*, *110*(1), 1988.

[167] H. Price, E. Lüpfert, D. Kearney, E. Zarza, G. Cohen, R. Gee, & R. Mahoney, "Advances in parabolic trough solar power technology," *Journal of solar energy engineering*, *124*(2), 109-125, 2002.

[168] A. Skumanich, "CSP at a crossroads: The first solar electric power plants are still proving their worth after three decades, so why aren't we seeing more CSP reach the development stage?" *Renewable energy focus*, *12*(1), 52-55, 2011.

[169] www.eskom.co.za

[170] National Department of Environmental Affairs, Savannah Environment (Pty) Ltd, www.savannahsa.co.za.

[171] Y. Haffejee, "Renewable energy IPP program: South Africa IRENA Renewable energy policies," Eskom, 2013.

[172] D. Huang, and F. Wu, "Research of closed Brayton cycle solar thermal power system," *3rd IEEE Conference on Measuring Technology and Mechatronics Automation (ICMTMA)*, vol. 2, pp. 1065-1067, 2011.

[173] F. Winterbach, "*Life Cycle Assessment (LCA) of various solar heat technologies,"* Stellenbosch: Stellenbosch University, 2011.

[174] C. Wyman, J. Castle and F. Kreath, "A review of collector and energy storage technology for intermediate temperature application," *Solar Energy*, volume 24, issue 6, pp. 517-540, 1980.

[175] G.J. Kolb, S.A. Jones, M.W. Donnelly, D. Gorman, R. Thomas and R. Davenport, "Heliostat cost reduction study," Sandia Report, SAND 2007-3292, unlimited Release June 2007.

[176] V. Hejmandi, M. Shin, B. Kress and A. Gilberto, "Novel solar co- generation trough system based on stretched micro structure Mylar film," *NASA ADS, SPIE eco-photonics*, volume 8065, pp. 80650G-80650G-10, 2011.

[177] A. Segal, M. Epstein and A. Yogev, "Hybrid concentrated photovoltaic and thermal power conversion at different spectral bands," *Solar Energy*, volume 76, issue 5, pp. 591-601, 2004.

[178] D.A. Boyd, R. Gejewski and R. Shift, "Cylindrical blackbody solar energy receiver," *Solar Energy,* volume 18, issue 5, pp. 395-401, 1976.

[179] T. Melchior, C. Perkins, A.W. Weimer, & A. Steinfeld, "A cavity-receiver containing a tubular absorber for high-temperature thermochemical processing using concentrated solar energy," *International Journal of Thermal Sciences*, *47*(11), 1496-1503, 2008.

[180] T.M. Masaud, K. Lee, & P.K. Sen, P. K. "An overview of energy storage technologies in electric power systems: What is the future?" *IEEE In North American Power Symposium (NAPS), 2010* pp. 1-6, 2010.

[181] A. Phoenix, "Phoenix, Arizona Concentrating Solar Power Program Review," Sunshot, US. Department of Energy, 2013.

[182] S.M. Hasnain, "Review on sustainable thermal energy storage technologies, part I: heat storage materials and techniques," *Energy Conversion and Management*, *39*(11), 1127-1138, 1998.

[183] F. Agyenim, N. Hewitt, P. Eames, & M. Smyth, "A review of materials, heat transfer and phase change problem formulation for latent heat thermal energy storage systems (LHTESS)," *Renewable and Sustainable Energy Reviews*, *14*(2), 615-628, 2010.

[184] D. Brosseau, J.W. Kelton, D. Ray, M. Edgar, K. Chisman, and B. Emms, "Testing of thermocline filler materials and molten-salt heat transfer fluids for thermal energy storage systems in parabolic trough power plants," *Journal of Solar Engineering,* vol. 127, issue 1, pp. 109-116, 2005.

[185] J.W. Raade, and D. Padowitz, "Development of molten salt heat transfer fluid with low melting point and high thermal stability," *Transactions of the ASME-N-Journal of Solar Energy Engineering*, vol. 133, issue 3, pp. 031013, 2011

[186] A. Sharma, V.V. Tyagi, C.R. Chen, & D. Buddhi, "Review on thermal energy storage with phase change materials and applications," *Renewable and Sustainable energy reviews*, *13*(2), 318-345, 2009.

[187] G. Ervin, "Solar heat storage using chemical reactions," *Journal of solid state chemistry*, *22*(1), 51-61, 1977.

[188] R. Fox, "Watt`s expansive principle in the work of Sadi Carnot and Nicolas Clement," *Notes and Records of the Royal Society of London*, vol. 24, issue 2, pp. 233-253, 1970.

[189] C.C. Gillispie, & R. Pisano, R. "On Principles in Sadi Carnot's Thermodynamics," In *Lazare and Sadi Carnot*, Springer Netherlands, pp. 191-225, 2013.

[190] B. Saleh, G. Koglbauer, M. Wendland, & J. Fischer, "Working fluids for low-temperature organic Rankine cycles," *Energy*, *32*(7), 1210-1221, 2007.

[191] H. Ibrahim Acar, "Second law analysis of the reheat-regenerative Rankine cycle," *Energy conversion and management*, *38*(7), 647-657, 1997.

[192] A. Poullikkas, "An overview of current and future sustainable gas turbine technologies. *Renewable and Sustainable Energy Reviews*, *9*(5), 409-443, 2005.

[193] J.L. Kerrebrock, "Magnetohydrodynamic generators with nonequilibrium ionization," *AIAA Journal*, *3*(4), 591-601, 1965.

[194] J. Grul, "Coal-fired open cycle magneto-hydrodynamic power plant emissions and energy efficiencies," *MIT Energy Lab. Report*, #MIT-EL 78-018, 1977.

[195] A.I. Hochbaum, R. Chen, R.D. Delgado and W. Liang, "Enhanced thermoelectric performance of rough silicon nanowires," *Letters (nature),* vol. 451, pp. 06381, 2008.

[196] J. Sol, "Theory and Manufacturing Processes of Solar Nano-antenna Electromagnetic Collectors," *Energy Engineering*, volume 132, issue 1, pp. 9, 2010.

[197] J. Dersch, M. Geyer, U. Herrmann, S.A. Jones, B. Kelly and R. Kistner, "Trough Integration into power plants-A study on the performance and economy of integrated solar combined cycle system," *Energy,* issue 29, pp. 947-1013, 2004.

[198] J. Servert, G. San Miguel and D. Lopez, "Hybrid solar-biomass plants for power generation; technical and economic assessment," *Global NEST Journal*, vol. 13, No. 3, pp. 266-276, 2011.

[199] A. Kribus, "A high-efficiency triple cycle for solar power generation," *Solar Energy,* Vol. 72, issue 1, pp.1-11, 2002.

[200] R. Hargraves, "Triple reheat closed Brayton cycle thermal/electric power conversion," *American Scientist,* volume 98, issue 4, pp. 304, August 2009.

[201] World Bank Group /GEF, "Strategy for the market development of concentrating solar thermal power," The international bank for Reconstruction and Development, World Bank, vol. 1, 2006.

[202] C. Turchi, N. Langle, R. Bedilion and C. Libby, "Solar-augment potential of U.S. fossil-fired power plants," National Renewable Energy laboratory and Electric Power Research Institute, pp. 1-25, February 2011.

[203] E.E. Anyanwu, & C.I. Ezekwe, "Design, construction and test run of a solid adsorption solar refrigerator using activated carbon/methanol, as adsorbent/adsorbate pair," *Energy Conversion and Management*, 44(18), 2879-2892, 2003.

[204] A. Ambrosio, M. Ambrosio, G. Ambrosone, V. Carillo, U. Coscia, V. Grossi, ... & S. Santucci, "A new radiation detector made of multi-walled carbon nanotubes," *Nuclear Instruments and Methods in Physics Research Section A: Accelerators, Spectrometers, Detectors and Associated Equipment*, *589*(3), 398-403, 2008.

[205] R.I. Bailey and J.C. Fletcher, "Electromagnetic wave energy converter," United States Patent 3,760,257, September 1973.

[206] T. Young, "Experiments and Calculations Relative to Physical Optics," *Philosophical Transactions of the Royal Society of London*, Vol. 94, pp. 1-16; 1803.

[207] S. Kocsis, B. Braverman, S. Ravets, M.J. Stevens, R.P. Mirin, L.K. Shalm and A.M. Steinberg, "Observing the average trajectories of a single photons in a two-slit interferometer," *Science 3,* vol. 332, no. 6034, pp. 1170-1173, 2011.

[208] A.R. Carter, "Stephan-Boltzmann`s Law," *Department of Physics, College of Wooster, Ohio,* USA; May, 2004.

[209] G.B. Rybicki, and A.P. Lightman, "Radiative processes in astrophysics," *John Wiley & Sons, New York;* vol. 25, 1979.

[210] P. Bharadwaj, B. Deutsch, and L. Novotny, "Optical antennas," *Advanced Optical Photon,* volume 1, pp. 438-483, 2009.

[211] P. Mittelstaedt, A. Prieur, & R. Schieder, "Unsharp particle-wave duality in a photon split-beam experiment. *Foundations of physics*, *17*(9), 891-903, 1987.

[212] S. Novak, "Microscopic antenna technology provides potential energy supply on flexible materials," *Solar Nanotechnology*, Idaho National Laboratories, 2008.

[213] R. Corkish, M.A. Green T. Puzzer, "Solar energy collecting by antennas," *Solar Energy*, volume 73, issue 6, pp. 395-401, 2002.

[214] J. Liu, Y.T. Kuo, K.J. Klabunde, C. Rochford, J. Wu, & J. Li, "Novel dye-sensitized solar cell architecture using TiO2-coated vertically aligned carbon nanofiber arrays," *ACS applied materials & interfaces*, *1*(8), 1645-1649, 2009.

[215] B.A. Munk, "Frequency selective surfaces: Theory and design," New York: Wiley, pp.2-23, 2000.

[216] G.C. Wang, T.M. Lu, M. Shur, S. Kalyanaraman, X.C. Zhang, V. Lakshminarayanan and M. Arjona, "Educational training program for THz science and technology at Rensselaer," In Education and Training in Optics and photonics. *Optical Society of America*, 2003.

[217] M. Gallo, L. Mescia, O. Losito, M. Bozzetti, F. Prudenzano, "Design of optical antenna for solar energy collection," *Energy*, vol. 39 issue 1; pp. 27-32, 2012.

[218] D.Y. Goswami, S. Vijayaaraghavan, S. Lu and G. Tamm, "New and Emerging Developments in Solar Energy," *Solar Energy;* volume 76, issues 1-3, pp. 33-43, 2004.

[219] J. Sol, "Theory and manufacturing processes of solar nantenna electromagnetic collectors," *Energy Engineering*, volume 132, issue 1, pp. 9, 2010.

[220] Matlab Help files version 7.9.0.2601, (R2009b)

[221] National Renewable Energy Laboratory (NREL); "Systems Advisor Model, Sam 2011.12.2," *BiblioBazaar,* 2012.

[222] M.A. Green, "Solar cells: operating principles, technology, and system applications," *Englewood Cliffs, NJ, Prentice-Hall, Inc., issue 288, p. 1*, 1982.

[223] P.T. Landsberg, "An introduction to the theory of photovoltaic cells," *Solid-State Electronics*, *18*(12), pp. 1043-1052, 1975.

[224] B.A. Gregg, & M.C. Hanna, M. C. "Comparing organic to inorganic photovoltaic cells: Theory, experiment, and simulation," *Journal of Applied Physics*, *93*(6), 3605-3614, 2003.

[225] M.A. Green, & R.B. Godfrey, "MIS solar cell—General theory and new experimental results for silicon," *Applied Physics Letters*, *29*(9), 610-612, 1976.

[226] D. Cahen, G. Hodes, M. Grätzel, J.F. Guillemoles, & I. Riess, "Nature of photovoltaic action in dye-sensitized solar cells," *The Journal of Physical Chemistry B*, *104*(9), 2053-2059, 2000.

[227] A.C. Melissinos, "Principles of modern technology," *Cambridge University Press,* 1990.

[228] J.S. Lai, & F.Z. Peng, "Multilevel converters-a new breed of power converters," *IEEE Transactions on Industry Applications, 32*(3), 509-517, 1996.

[229] R.D. Middlebrook, & S. Cuk, "A general unified approach to modelling switching-converter power stages," In *Power Electronics Specialists Conference* Vol. 1, pp. 18-34, 1976.

[230] F.Z. Peng, "Z-source inverter," *IEEE Transactions on Industry Applications, 39*(2), 504-510, 2003.

[231] J. Dixon, S. Tepper, & L.U.I.S. Moran, "Practical evaluation of different modulation techniques for current-controlled voltage source inverters," *IEE Proceedings* In *Electric Power Applications,* Vol. 143, No. 4, pp. 301-306 IET, 1996.

[232] S.B. Kjaer, J.K. Pedersen, & F. Blaabjerg, "A review of single-phase grid-connected inverters for photovoltaic modules. *IEEE Transactions on Industry Applications*, *41*(5), 1292-1306, 2005.

[233] T.C. Wang, Z. Ye, G. Sinha, & X. Yuan, "Output filter design for a grid-interconnected three-phase inverter," *IEEE 34th Annual Power Electronics Specialist Conference, PESC'03,* Vol. 2, pp. 779-784, 2003.

[234] J. Kitchen, W.Y. Chu, I. Deligoz, S. Kiaei, & B. Bakkaloglu, "Combined linear and Δ-modulated switched-mode PA supply modulator for polar transmitters." *IEEE International Solid-State Circuits Conference, ISSCC, Digest of Technical Papers.* pp. 82-588, 2007.

[235] Q. Zhao, & F.C. Lee, "High-efficiency, high step-up DC-DC converters," *IEEE Transactions on Power Electronics*, *18*(1), 65-73, 2003.

[236] K. PremKumar, M.E., "Fundamentals of Power Electronics and Power System with Matlab," Lecture EEE, SVCET, Tirunelveli, pp.6, 2001.

[237] N. Pandiarajan, & R. Muthu, "Mathematical Modeling of Photovoltaic Module with Simulink," *1st IEEE International Conference on Electrical Energy Systems,* pp. 257-263, 2011.

[238] S. Jeevananthan, "Matlab/Simulink-A tool for power electronic circuits"; Pondicherry Engineering College, Pondicherry; February, 2012.

[239] S. Panwar, & R.P. Saini, "Development and Simulation of Solar Photovoltaic model using Matlab/Simulink and its parameter extraction," *International Conference on Computing and Control Engineering*, pp. 1-8, April, 2012.

[240] E. Chikane, O.I. Okoro, M.T.E. Khan, & O.I. Okoro, "Concise higher electrical engineering," *Juta and Company Ltd,* pp. 379-400, 2008.

[241] Z. Xuesong, S. Daichun, M. Youjie, & C. Deshu, "The Simulation and design for MPPT of PV system based on Incremental Conductance Method," *IEEE WASE International Conference on Information Engineering*, pp. 341-317, 2010.

[242] T. Salmi, M. Bouzguenda, A. Gastli, & A. Masmoudi, "Matlab/Simulink based modeling of solar photovoltaic cell," *International Journal of Renewable Energy Research*, vol. 2, No. 2, 2012.

[243] M.G. Villalva, J.R. Gazoli, & E.R. Filho, "Modeling and Circuit-based Simulation of Photovoltaic Arrays," *IEEE Trans.*, pp. 1244-1254, 2009.

[244] Weatherization Works, "Solar Retroifs for weatherization and Remodels," *EERE Lesson 7, Photovoltaic (PV) System Basics;* www1.eere.energy.gov*;* 2012.

[245] NERSA Consultation Paper, "Review of Renewable Energy feed-in Tariffs," *National Energy Regulator of South Africa* (NERSA), pp. 1-32, 2011.

[246] R. Meyer, "The South African REFIT: Solar Resource Assessment options for Solar Developers," *Centre for Renewable and Sustainable Energy Studies, University of Stellenbosch,* pp. 3, 2010.

[247] Nedbank, "Economic Commentary," March 2012.

[248] Statistics South Africa, "Monetary Policy Review," *South Africa Reserve Bank*, pp. 3, May 2012.

[249] P. Ndebele, "REFIT REVIEW Consultation Hearing," Southern Africa Solar Thermal and Electricity Association (SASTELA), pp. 15, May 2011.

[250] S3: Discount rate-Integrated Resource plan, IRP 2010 Parameter, pp.1, 2010.

[251] P. Du Plessis, "The Potential of solar process heat for South African industry," *Energy Research Centre University of Cape Town*, pp. 53-54, 2011.

[252] D.L. King, S. Gonzalez, G.M. Galbraith, & W.E. Boyson, "Performance model for grid-connected photovoltaic inverters," *Sandia National Laboratories Report# SAND2007-5036*, 2007.

[253] City of Cape Town, "Electricity Tariff," **www.capetown.gov.za/en/electricity/Pages/ElectricityTariff.aspx**, Apr 28, 2013.

Research Publications

1. C. Chukwuka, and K. A. Folly, "Overview of Solar Power Generation," *South African Universities Power Engineering Conferences, SAUPEC*, University of Cape Town, South Africa, pp. 1-7, July, 2011
2. C. Chukwuka, and K. A. Folly, "Overview of four Energy Storage Devices," IEEE Publications, *45th Universities Power Engineering Conference, UPEC,* Soest, Germany, pp.1-7, September 2011
3. C. Chukwuka, and K. A. Folly, "Overview of Concentrated Photovoltaic Cells," *IEEE African Conferences, AFRICON*, Zambia, pp.1-7, September 2011.
4. C. Chukwuka, and K. A. Folly, "Batteries and Super Capacitors," *IEEE Power Africa,* University of Witswatersrand, Johanesburg, pp. 1-7, July 2012.
5. C. Chukwuka, and K. A. Folly, "Economic Assessment of Molten Salt Power Tower Concentrated Solar Power with National Renewable Energy Feed-in Tariff Scheme," *South African University Power Engineering Conference (SAUPEC),* North West University Potchefschroom, pp. 1-6, Jan. 2013.
6. C. Chukwuka, and K.A. Folly, "Technical and Economic Modeling of the 2.5 kW Grid-Tie Residential Photovoltaic System", *International Journal of Renewable Energy Research (IJRER)*, 3(2), pp. 412-419, 2013.

Appendix B

True Sine wave Inverters

Multilevel inverters

In recent years, industry has begun to demand higher power requirement which now reaches the megawatt level. Controlled ac drives in the megawatt range are usually connected to medium-voltage network. Today, it is hard to connect a single power semiconductor switch directly to medium voltage grids (such as 2.3, 3.3, 4.16, or 6.9KV). For these reasons, a new family of multilevel inverters has emerged as the solution for working with higher voltage levels

Advantages of a Multilevel Converter

- They give a better quality signal which is closer to true sinusoid
- They can increase the inverter operating voltage without increasing the device rating
- They minimize the THD with low switching frequencies,
- They reduce the EMI due to lower voltage steps

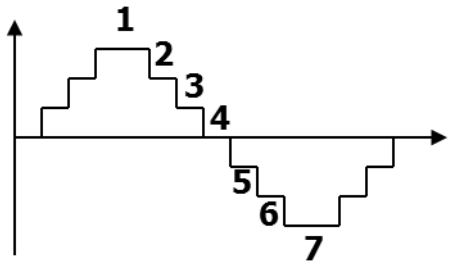

Figure B1: Seven-level inverter

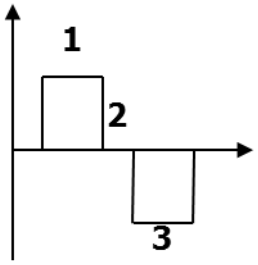

Figure B.2: Three-level inverter

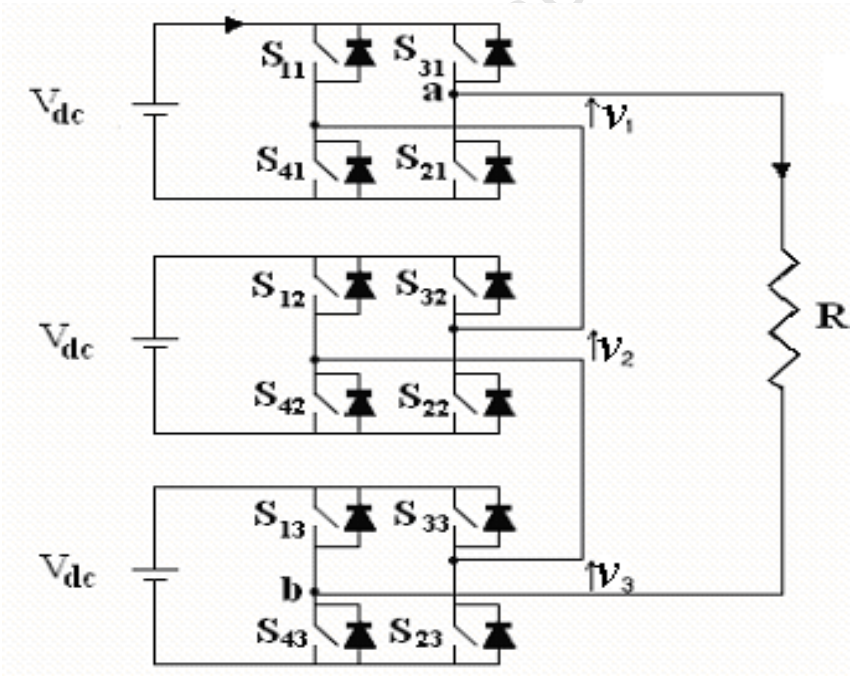

Figure B.3: cascaded inverter

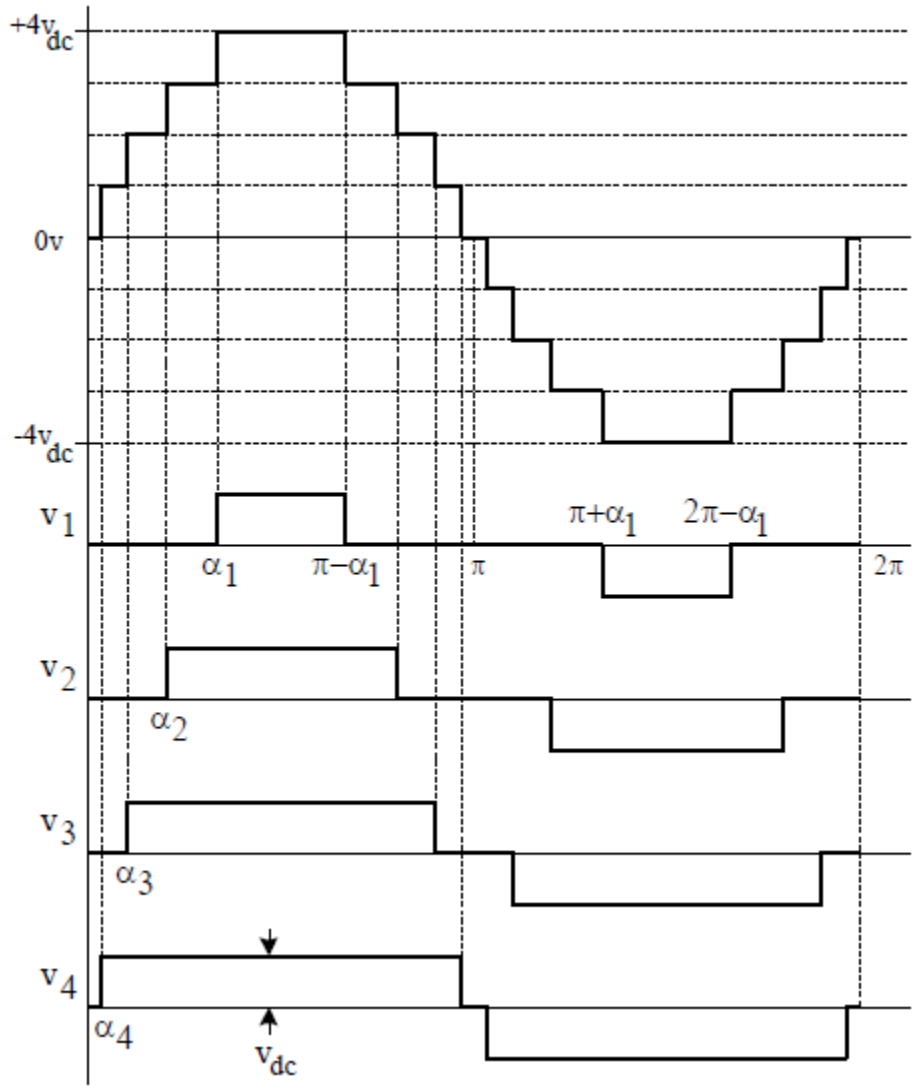

Figure B.4: The synthesized voltage waveform of seven-level inverter

A multilevel converter has several advantages over a conventional three-level converter for the purpose of achieving increased voltage current ratings, the quality of the waveform and harmonics cancellation. The quality of the inverter output voltage waveform can be expressed by using the Fourier analysis data to calculate the total harmonic distortion (THD).

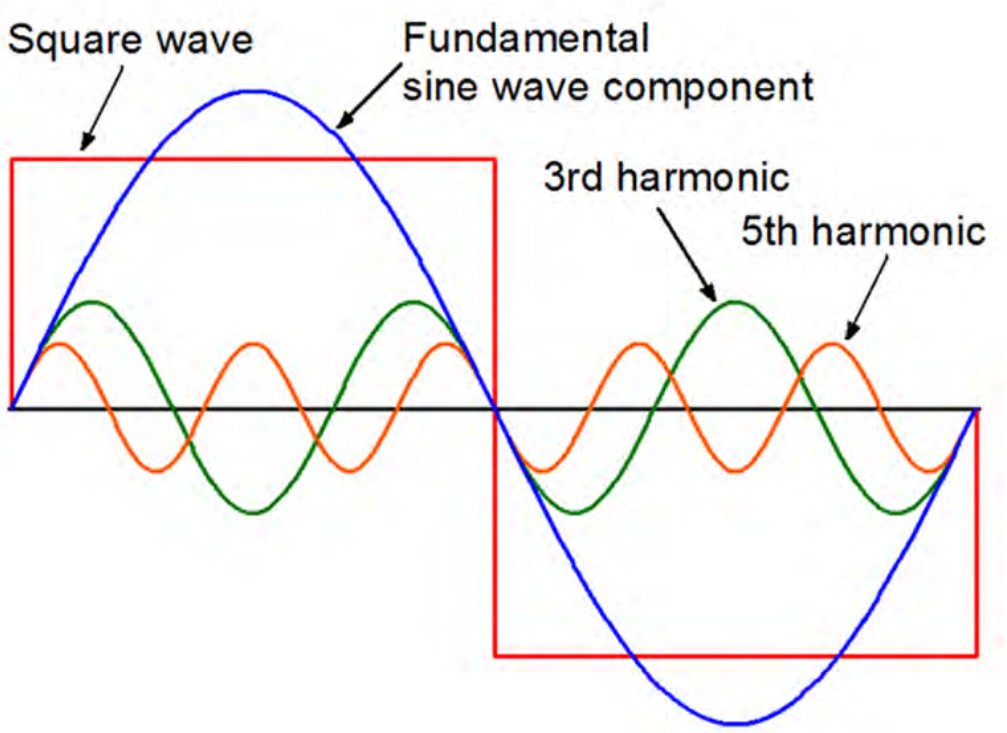

Figure B.5: Harmonics defined

The total harmonic distortion (THD) is the square root of the sum of the squares of the harmonic voltages divided by the fundamental voltage:

$$THD = \frac{\sqrt{V_2^2+V_3^2+V_4^2+\cdots+V_n^2}}{V_1} \quad \text{(A1)}$$

The quality of the output waveform that is needed from an inverter depends on the characteristics of the connected load. While some loads need a nearly perfect sine wave, others may work well with a square wave voltage [S. Jeevananthan].

Three-Phase Inverters

Three-phase inverters are used for variable-frequency drive applications and for hjgh power applications such as HVDC power transmission. A basic three-phase inverter consists of three single-phase inverter switches each connected to one of the three load terminals. For the most basic control scheme, the operation of the three switches is coordinated son that one switch operates at each 60 degree point of the fundamental output waveform. This creates a line-to-line output waveform that has six steps. The six-

step waveform has a zero-voltage step between the positive and the negative sections of the square-wave such that the harmonics that are multiples of three are eliminated as described above.

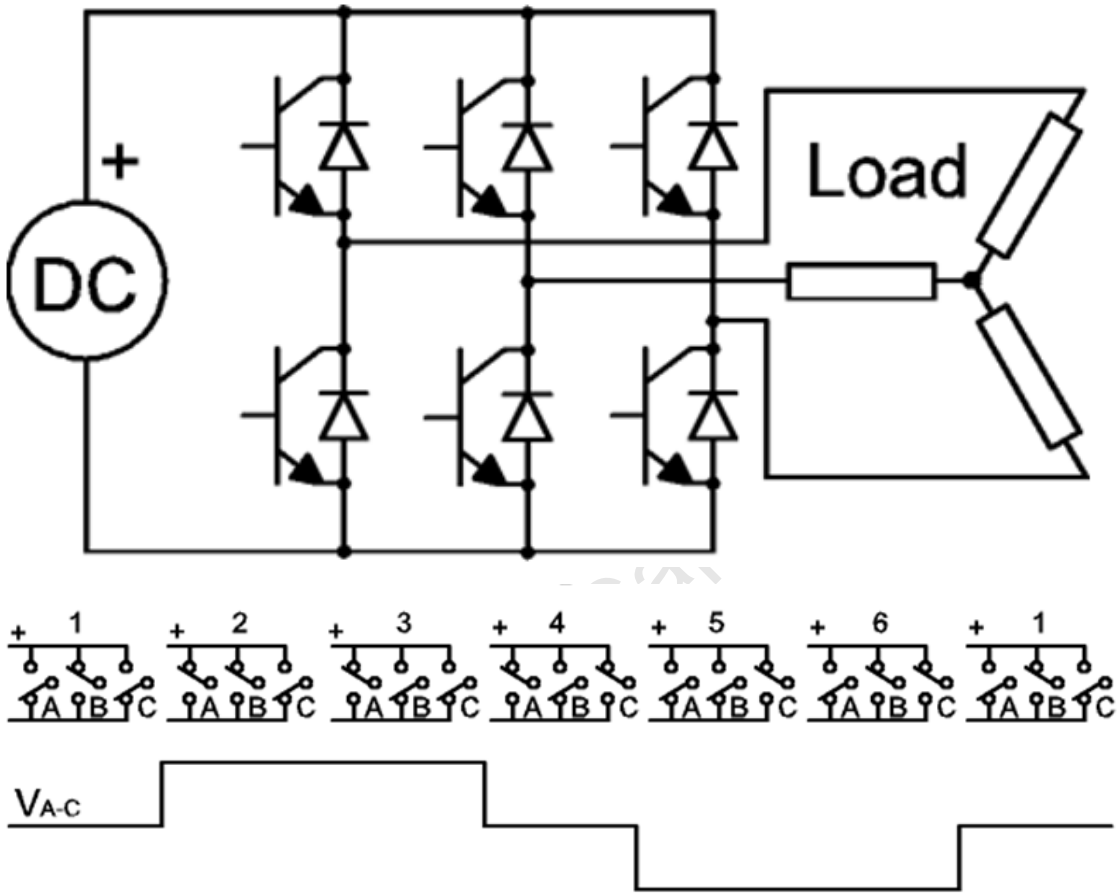

Figure B6: 3-phase inverter circuit showing six-step switching sequence and voltage between terminals A and C

To construct inverters with higher power ratings, two six-step three-phase inverters can be connected in parallel for a higher current rating or in series for a higher voltage rating. In either case, the output waveforms are phase shifted to obtain a 12-step wave form. If additional inverters are combined, an 18-step inverter is obtained with three inverters etc. Although inverters are usually combined for the purpose of achieving increased voltage or current ratings, the quality of the wave form is improved as well.

True or Pure Sine wave Inverters

A pure sine wave inverter produces a nearly perfect sine wave output (less than 3% total harmonic distortion) that is essentially the same as utility-supplied grid power thus it is compatible with all AC electronic devices. The design is more complex hence it costs more per unit power. If you operate the following equipment chances are that you would require a pure sine wave inverter

- Microwave
- Roof Fans
- Air conditions
- High precision chargers
- Swimming pool pumps
- Fridges fitted with compressors
- Fridge/Freezers
- Washing Machines
- Camera equipment which use the line signal for sinc
- Timing devices such as bed alarm clock which use the power signal as a timing base
- Tropical fish tank pumps

APPENDIX C

Validating the DC-DC Boost Converter

In order to determine the performance of the DC-DC boost converter, a steady state dc signal from the battery source is used as the input of the converter while the output is measured across a 50-ohm resistor. The following parameters are used:

Series inductance, Capacitance, pulse generator frequency and a battery voltage are 0.4mH, 25µF, 10 kHz and 10V respectively [236]. The duty cycle (D) of the signal generator which is the fraction of the pulse width with respect to the period is given by

$$D = 1 - \frac{V_{out}}{V_{in}} \qquad \text{(C1)}$$

$$D = 1 - \frac{10}{22} = 0.54$$

Or 54%

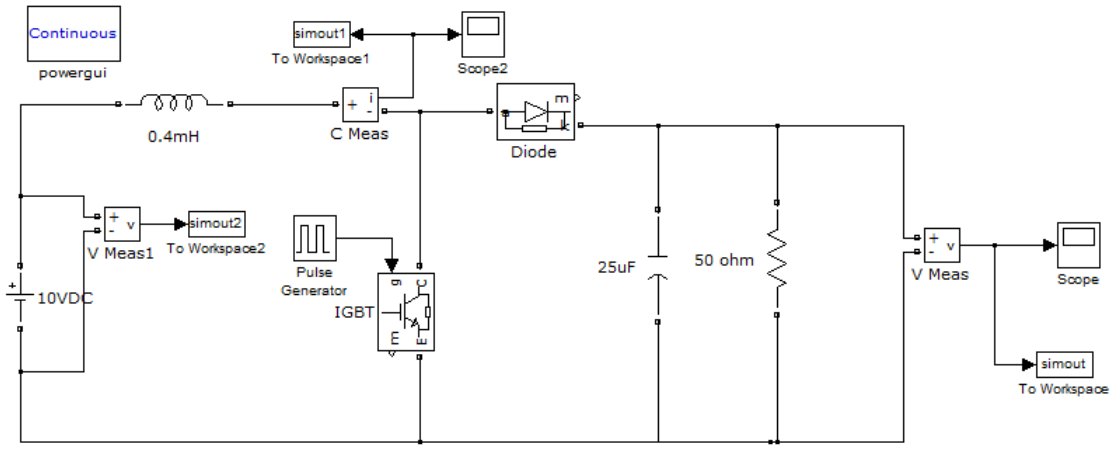

Figure C1: Boost Converter Circuit

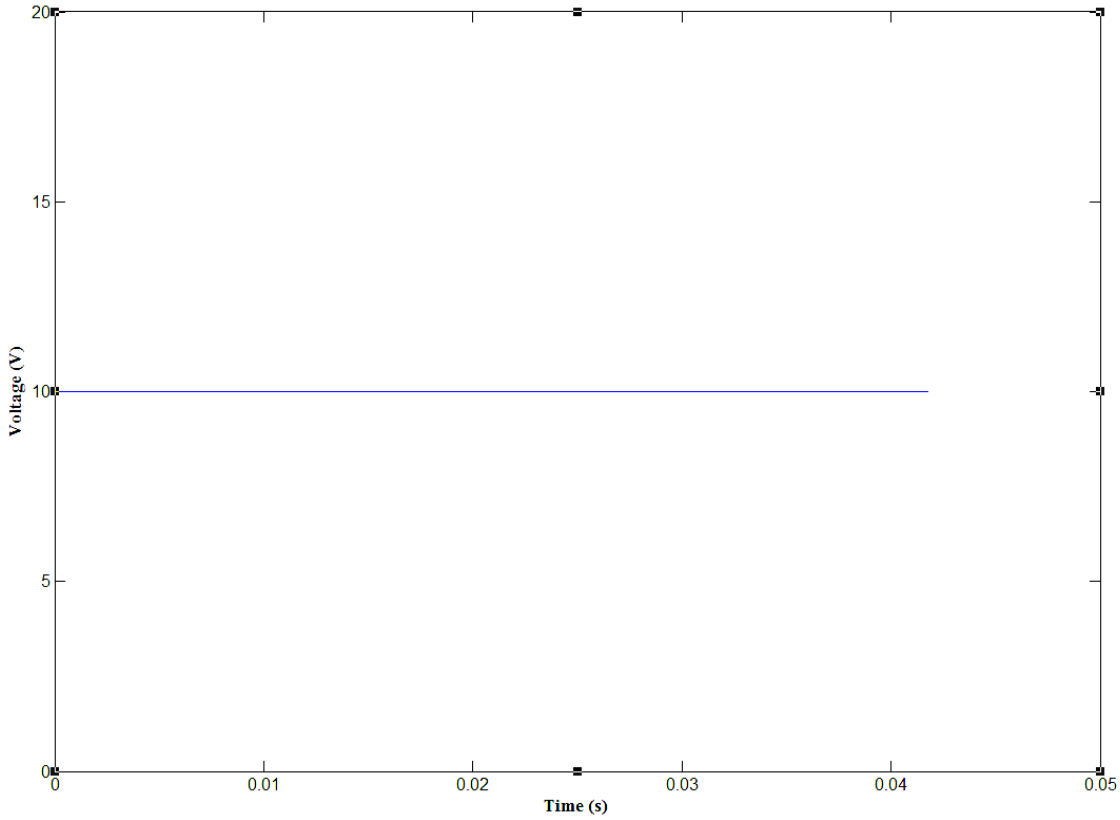

Figure C2: Boost Converter Input Voltage

The output voltage shown in figure C3 is characterized by ripples which is a function of the resistive and the capacitive components of the circuit and the value of the ripple voltage is given by

$$\frac{\Delta V}{V_0} = \frac{D}{RCf} \qquad \text{(C2)}$$

$$\Delta V = \frac{0.3*22}{50*25*10^{-6}*10*10^{3}} = 0.5281 \text{ V}$$

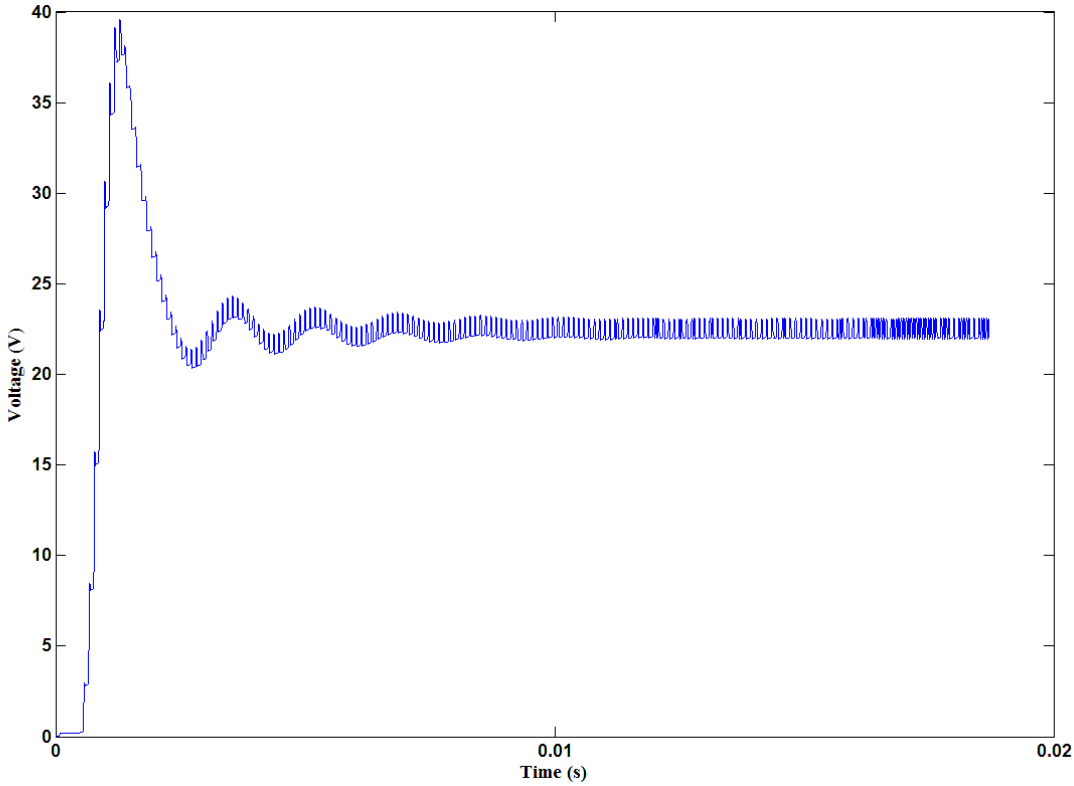

Figure C3: Output Voltage of the Boost Converter

The inductor current is shown in figure C4

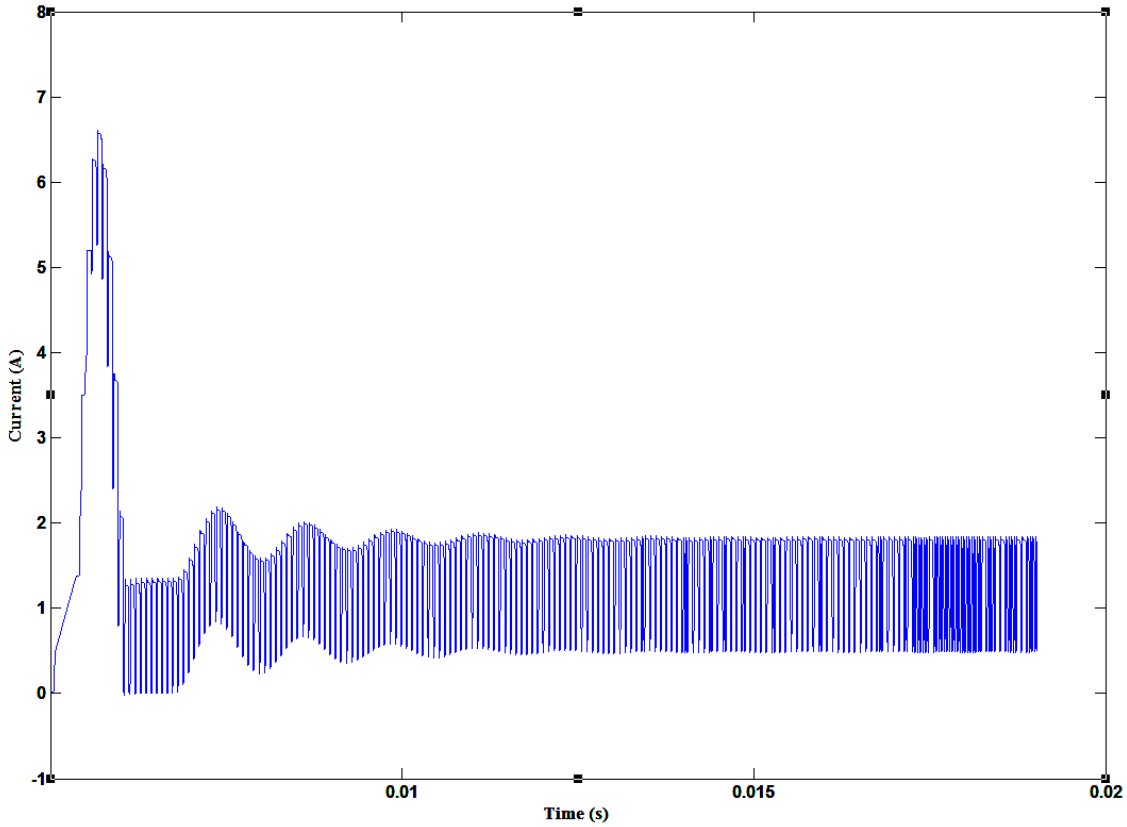

Figure C3: Inductor Current